Studies of photoinduced molecular dynamics using ion imaging and correlation analysis

Joseph W. McManus
Jesus College
University of Oxford

A thesis submitted for the degree of
Doctor of Philosophy
Trinity 2024

Abstract

Understanding the dynamics that connect the reactants and products of a chemical process is essential to be able to predict and potentially control the outcome. The aim of this thesis is to investigate the molecular dynamics of photoexcited polyatomic molecules in the gas phase. A range of studies are presented that use femtosecond laser pulses to probe the motion of atoms within molecules. Product kinetic energy and angular distributions are recorded simultaneously using ion imaging. A photochemical process of particular interest is the rapid multiple ionisation of a molecule in an intense laser field that causes dissociation into many fragment ions, known as a Coulomb explosion. One of the main topics of this thesis is how the laser-induced Coulomb explosion of a target molecule can be used to characterising its atomic structure, including being able to track structural change following photoexcitation.

Results are presented from four different experimental studies. Two of these investigated the fragmentation dynamics of molecules exposed to an intense laser field. The first is a study of the fragmentation dynamics of 1-iodopropane and 2-iodopropane polycations, prepared by site-selective ionisation of the iodine atom by an extreme-ultraviolet femtosecond laser pulse. The data analysis focuses on disentangling the competing fragmentation channels of doubly and triply charged parent ions. The second study examines the Coulomb explosion dynamics of the *cis* and *trans* isomers of 1,2-dichloroethene following strong-field ionisation by a near-infrared femtosecond laser pulse. The work explores how the parent ion charge states affects the Coulomb explosion dynamics, and hence the ability to determine structural information from the final fragment momenta.

The other two experimental studies investigated the photoinduced molecular dynamics of the *cis* and *trans* isomers of 1,2-dichloroethene, excited in their (π, π^*) absorption bands using an ultrafast pump-probe scheme. The photodissociation dynamics were monitored in real time using a near-infrared laser pulse to ionise the neutral photofragments. The time-resolved momentum distribution of atomic ions produced by Coulomb explosion of highly charged *trans*-1,2-dichloroethene reveals that the molecule undergoes ultrafast structural rearrangement prior to C–Cl bond cleavage. Early attempts to model the molecular dynamics suggest that torsion about the C–C bond axis is involved.

In order to establish which ions arise from the same photochemical process, experiments record all of the ions generated in each acquisition cycle and the data are processed using an analysis that measures correlation. This approach allows the fragmentation pathways of a molecule to be conclusively assigned. Taken further, it can be utilised to inspect the fragmentation dynamics of specific channels. The main correlation analysis method used in this thesis is covariance mapping. Several new techniques that expand the covariance mapping methodology are introduced and demonstrated. The other key aspect of the data analysis is the use of classical Coulomb explosion simulations to guide and support the interpretation of experimental data. Advancements in modelling the fragmentation dynamics of molecular polycations are discussed, in particular the modelling of sequential breakup mechanisms.

Acknowledgements

What a blast. These past three and a half years have been immensely fulfilling. I'd do it all over again. I am grateful to all those who made it possible and supported me throughout my studies. First and foremost, I must thank my supervisor Professor Mark Brouard. Your support and guidance throughout my time at Oxford have been all I could ask for in a supervisor. Thank you for always being so approachable, but also so trusting of me to let me work independently. I owe you more drinks than I can count.

The Brouard group has been wonderful company to me, both in the office and at the pub. To certain members I owe special thanks. To Dr Felix Allum, thank you for showing me the ropes and being a great source of insight throughout my studies. Your work ethic and efficiency are a marvel to me. I am also grateful to Dr Robert Mason for helping me in those early days. I wish I'd had the chance to work with you more. No thanks to Dr Robert Burleigh for leaving those fingernail clippings for me to find years later. To Dr Josh Featherstone, my partner in 'bodge-job' science, I owe huge thanks. You're the kindest and most selfless person I have ever had the pleasure to work with. Your computing help saved me countless hours - if only the IT department could be as helpful! My thanks also to Max McCrea for filling in the gaps of everything I forgot from undergraduate chemistry, and to Dr Martin Lam for teaching me so much over the many hours we spent in the lab together. To Harryson Skelly, I'm not sure you were the best scientist, but you were great company.

I am grateful to Dr Michael Burt and the members of his group I worked closely with. Michael, you were like a second supervisor to me in those months of my first year when I was working alone, still figuring things out. The diligent work of Dr Emily Warne kept the laser system in Oxford pulsing and the data rolling-in. Tiffany Walmsley was my closest collaborative partner who I worked side-by-side with on a portion of the data analysis presented here, and for this she deserves my special thanks. Discussions with you were my favourite. Our workflows completed each other perfectly.

I would also like to thank those who supervised me throughout my undergraduate project at the University of Bristol, who continued to be a presence throughout my postgraduate studies. Professor Andrew Orr-Ewing is the individual who introduced to the field of reaction dynamics, and the reason I undertook my DPhil with Mark. Professor Mike Ashfold, your insight is unmatched, and I'll always appreciate your input at a meeting. Thank you Dr Patrick Robertson for your very helpful, very cutthroat criticism, which I know never to take too seriously.

The experimental work conducted in the Brouard laboratory would not have been possible without the the exceptional teams of the mechanical and electronic workshops, as well as the CRL facilities staff. Particular thanks to Andrew Green, Steven Barry, Philip Hurst, John Adams, Ronald Tarry and Colin Mitchell. It might have just been your job, but it was magic to me.

I am grateful both to Jesus College and the Clarendon fund for jointly funding my studies. If you ask me, it was money well spent. An additional thank you to Jesus College for generously funding my many travels to beamtimes and conferences over the course of my studies. I am also grateful for the financial support of EPSRC which funded the experimental work conducted in Brouard laboratory.

Thanks to Ewan, Ryan, Sam, Ricky and Shamus whose music soundtracked so many coding and writing sessions. I might just be the top Sheepdogs listener worldwide. Thank you to Simon. Some might say your are sour, but its just what I like, and more than anything else, you have kept me energised through it all. To Ginge, I don't know where the future will take us, but you're along for the ride now, and there's no one else I'd rather spend it with.

Chapter 5

The experimental work presented in this chapter was conducted as part of a beamtime at the Spring-8 Angstrom Compact free-electron Laser in Hyogo, Japan, led by Dr Ruaridh Forbes. By their nature, large scale user facility beamtimes involve many more people than a typical in-house experiment (too many for me to individually thank here!) but I would specifically like to thank Ruaridh for giving me the opportunity to participate, and providing sage advice and insight on the analysis that followed. The beamtime took place in the spring of 2021, when strict travel restrictions remained in place due to the ongoing COVID-19 global pandemic, and as such I am indebted to local members of the collaboration who performed all of the on-site experimental work. Data analysis was conducted jointly with Tiffany Walmsley.

Chapter 8

The experiments performed in the James R. MacDonald laboratory at Kansas State University were carried out in collaboration with the research group of Professor Daniel Rolles. Thank you Daniel for giving me the opportunity to come and work with your group on this project. Your wonderful hospitality made it my favourite trip of DPhil (Kansas is far better than ‘not that bad’). Your enthusiasm, optimism and problem solving have kept many experiments going long after I had given up hope. The experimental work was conducted jointly with Dr Avijit Duley, but I am also indebted to Dr Huhyn Lam and Anbu Venkatachalam for their hard work in ensuring the project’s success. Thank you also Keyu Chen simply for driving me to the supermarket so I could eat during the hardest working week of my life.

No generate artificial intelligence was used in the writing of this thesis, or as part of the work presented within.

Contents

Appendices

List of publications

This thesis is based upon the following publications:

Chapter 5

1. **J. W. McManus**,* T. Walmsley,* K. Nagaya, J. R. Harries, Y. Kumagai, H. Iwayama, M. N. Ashfold, M. Britton, P. H. Bucksbaum, B. Downes-Ward, T. Driver, D. Heathcote, P. Hockett, A. J. Howard, E. Kukk, J. W. L. Lee, Y. Liu, D. Milesevic, R. S. Minns, A. Niozu, J. Niskanen, A. J. Orr-Ewing, S. Owada, D. Rolles, P. A. Robertson, A. Rudenko, K. Ueda, J. Unwin, C. Vallance, M. Burt, M. Brouard, R. Forbes, and F. Allum, “Disentangling sequential and concerted fragmentations of molecular polycations with covariant native frame analysis”, Phys. Chem. Chem. Phys. **24**, 22699–22709 (2022).
   *These authors contributed equally to this work.

2. T. Walmsley,* **J. W. McManus**,* Y. Kumagai, K Nagaya, J. R. Harries, H. Iwayama, M. N. Ashfold, M. Britton, P. H. Bucksbaum, B. Downes-Ward, T. Driver, D Heathcote, P Hockett, A. J. Howard, J. W. L. Lee, Y. Liu, E. Kukk, D. Milsesevic, R. S. Minns, A. Niozu, J. Niskanen, A. J. Orr-Ewing, S. Owada, P. A. Robertson, D. Rolles, A. Rudenko, K. Ueda, J. Unwin, C. Vallance, M. Brouard, M. Burt, F. Allum, and R. Forbes., “The role of momentum partitioning in covariance ion imaging analysis”, J. Phys. Chem. A, **128**, 4548-5460, (2024).
   *These authors contributed equally to this work.

Chapter 6

3. **J. W. McManus**, F. Allum, J. Featherstone, C. Lam, and M. Brouard, “Two-dimensional projected-momentum covariance mapping for Coulomb explosion imaging”, J. Phys. Chem. A, **128**, 3220-3229, (2024).

Contributions were made to following publications:

4. F. Allum, **J. McManus**, O. Denby, M. Burt, and M. Brouard, “Photoionization and photofragmentation dynamics of I_2 in intense laser fields: a velocity-map imaging study”, J. Phys. Chem. A **126**, 8577–8587 (2022).

5. I. Gabalski, F. Allum, I. Seidu, M. Britton, G. Brenner, H. Bromberger, M. Brouard, P. H. Bucksbaum, M. Burt, J. P. Cryan, T. Driver, N. Ekanayake, B. Erk, D. Garg, E. Gougoula, D. Heathcote, P. Hockett, D. M. P. Holland, A. J. Howard, S. Kumar, J. W. L. Lee, S. Li, **J. McManus**, J. Mikosch, D. Milesevic, R. S. Minns, S. Neville, Atia-Tul-Noor, C. C. Papadopoulou, C. Passow, W. O. Razmus, A. Röder, A. Rouzée, A. Simao, J. Unwin, C. Vallance, T. Walmsley, J. Wang, D. Rolles, A. Stolow, M. S. Schuurman, and R. Forbes, "Time-Resolved X-ray Photoelectron Spectroscopy: Ultrafast Dynamics in CS$_2$ Probed at the S 2p Edge", J. Phys. Chem. Lett. **14**, 7126–7133 (2023).

6. J. Unwin, F. Allum, M. Britton, I. Gabalski, H. Bromberger, M. Brouard, P. H. Bucksbaum, T. Driver, N. Ekanayake, D. Garg, E. Gougoula, D. Heathcote, A. J. Howard, P. Hockett, D. M. P. Holland, S. Kumar, C.-s. Lam, J. W. L. Lee, **J. McManus**, J. Mikosch, D. Milesevic, R. S. Minns, C. C. Papadopoulou, C. Passow, W. O. Razmus, A. Röder, A. Rouzée, M. Schuurman, A. Simao, A. Stolow, A. Tul-Noor, C. Vallance, T. Walmsley, D. Rolles, B. Erk, M. Burt, and R. Forbes, "X-ray induced Coulomb explosion imaging of transient excited-state structural rearrangements in CS$_2$", Commun. Phys. **6**, 309 (2023).

7. F. Allum, Y. Kumagai, K. Nagaya, J. Harries, H. Iwayama, M. Britton, P. H. Bucksbaum, M. Burt, M. Brouard, B. Downes-Ward, T. Driver, D. Heathcote, P. Hockett, A. J. Howard, J. W. L. Lee, Y. Liu, E. Kukk, **J. W. McManus,** D. Milsesevic, A. Niozu, J. Niskanen, A. J. Orr-Ewing, S. Owada, P. A. Robertson, A. Rudenko, K. Ueda, J. Unwin, C. Vallance, T. Walmsley, R. S. Minns, D. Rolles, M. N. R. Ashfold, and R. Forbes, "Direct momentum imaging of charge transfer following site-selective ionization", Phys. Rev. A **108**, 043113 (2023).

8. W. O. Razmus, F. Allum, J. Harries, Y. Kumagai, K. Nagaya, S. Bhattacharyya, M. Britton, M. Brouard, P. H. Bucksbaum, K. Cheung, S. W. Crane, M. Fushitani, I. Gabalski, T. Gejo, A. Ghrist, D. Heathcote, Y. Hikosaka, A. Hishikawa, P. Hockett, E. Jones, E. Kukk, H. Iwayama, H. V. S. Lam, **J. W. McManus**, D. Milsesevic, J. Mikosch, S. Minemoto, A. Niozu, A. J. Orr-Ewing, S. Owada, D. Rolles, A. Rudenko, D. Townsend, K. Ueda, J. Unwin, C. Vallance, A. Venkatachalam, S. Wada, T. Walmsley, E. M. Warne, J. Woodhouse, M. Burt, M. N. R. Ashfold, R. S. Minns, and R. Forbes, "Exploring the Ultrafast and Isomer-Dependent Photodissociation of Iodothiophenes via Site-Selective Ionization", Phys. Chem. Chem. Phys., **26**, 12725-12737 (2024).

9. J. Unwin, W. O. Razmus, F. Allum, J. Harries, Y. Kumagi, K. Nagaya, M. Britton, M. Brouard, P. Bucksbaum, M. Fushitani, I. Gabalski, T. Gejo, P. Hockett, A. J. Howard, H. Iwayama, E. Kukk, C. S. Lam, **J. McManus**, R. S. Minns, A. Niozu, S. Nishimuro, J. Niskanen, S. Owada, J. D. Pickering, D. Rolles, J. Somper, K. Ueda, S. Wada, T. Walmsley, J. Woodhouse, R. Forbes, M. Burt, and E. M. Warne, "Time-resolved probing of the iodobenzene C-band using XUV-induced electron transfer dynamics", ACS Phys. Chem. Au, *Accepted.*

10. T. Walmsley, F. Allum, J. Harries, Y. Kumagai, S. Lim, **J. W. McManus**, K. Nagaya, M. Britton, M. Brouard, P. H. Bucksbaum, R. Forbes, M. Fushitani, I. Gabalski, T. Gejo, P. Hockett, A. J. Howard, H. Iwayama, E. Kukk, C. Lam, R. S. Minns, A. Niozu, S. Nishimuro, J. Niskanen, S. Owada, W. O. Razmus, D. Rolles, J. Somper, K. Ueda, J. Unwin, S. Wada, J. Woodhouse, R. Forbes, M. Burt and E. M. Warne, "Distinguishing the XUV-induced Coulomb explosion dynamics of iodobenzene using covariance analysis", J. Phys. B, *Submitted.*

List of abbreviations

1D	One-Dimensional
2D	Two-Dimensional
3D	Three-Dimensional
AM	Auger-Meitner
ATI	Above-Threshold Ionisation
a.u.	Atomic units of momentum
BBO	Beta Barium Borate
CCD	Charge-Coupled Device
CDF	Cumulative Distribution Function
CEI	Coulomb Explosion Imaging
CFD	Constant Fraction Discriminator
COLTRIMS	COLd Target Recoil-Ion Momentum Spectroscopy
CoM	Centre-of-Mass
CPA	Chirped Pulse Amplification
DCE	DiChloroEthene
DLA	Delay-Line Anode
FEL	Free-Electron Laser
FROG	Frequency-Resolved Optical Gating
FWHM	Full Width at Half Maximum
ISI	Inner-Shell Ionisation
IP	IodoPropane
KE	Kinetic Energy
KER	Kinetic Energy Release
LIF	Laser-Induced Fluorescence
MCP	MicroChannel Plate

NIR	Near InfraRed
OAR	Open Area Ratio
OPA	Optical Parametric Amplifier
PES	Potential Energy Surface
PImMS	Pixel Imaging Mass Spectrometry
PULSAR	Prairie Ultrafast Light Source for Attosecond Research
RVP	Rotary Vane Pump
SACLA	Spring-8 Angstrom Compact free-electron LAser
SASE	Self-Amplified Spontaneous Emission
SFI	Strong-Field Ionisation
SHG	Second Harmonic Generation
TMP	TurboMolecular Pump
ToF	Time-of-Flight
TR	Time-Resolved
UHV	Ultra-High Vacuum
UV	UltraViolet
VMI	Velocity-Map Imaging
XUV	eXtreme UltraViolet

1
Introduction

Contents

1.1 Photochemistry

Photochemistry is concerned with chemical processes induced through interaction with light. Many photochemical processes are of paramount importance in nature. The most well known is photosynthesis, the process exploited by plants to convert carbon dioxide into useful sugars, which is driven by the absorption of sunlight.[1] Much of the chemistry in the Earth's upper atmosphere is dictated by photochemical mechanisms. For example, the Chapman cycle,[2] which is responsible for the regeneration of ozone from molecular oxygen, is initiated by UltraViolet (UV) light. Photochemistry is also widely utilised in technological applications, a topical example being energy generation by solar cells.[3]

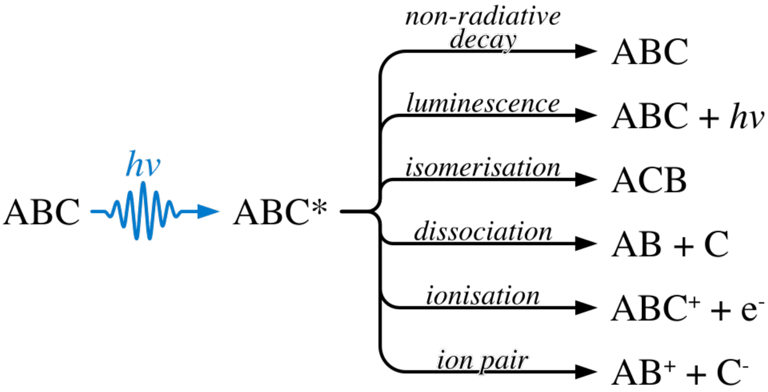

Figure 1.1: Some of the possible photochemical processes for a molecule ABC induced by absorption of a photon with energy $h\nu$.

At the molecular level, the absorption of a photon of light resonant in energy with a transition between two energy levels of a molecule will promote the molecule to an energetically excited state. From this state, the manner in which the system evolves will depend upon the properties of the molecule and the exact nature of the excitation. A wide variety of outcomes are possible, a selection of which are outlined for a prototypical molecule ABC in Figure 1.1. This thesis is concerned exclusively with photochemical processes, and the remainder of this chapter is dedicated to describing the processes of key interest. To begin, the approach taken in this work for studying photochemistry is outlined.

1.2 Photoinduced molecular dynamics

This thesis comprises a range of studies into photochemical processes in small molecules, using ultrafast lasers to probe their structural dynamics on the natural timescale of nuclear motion. The goal of these studies is to probe the photochemistry of simple systems in detail to gain a greater understanding of the underlying mechanisms at play. This is a 'bottom-up' approach, where the insight gained into the behaviour of elementary systems can be extended to more complex chemical systems with practical applications. A focus on small molecules that exhibit relatively simple molecular dynamics allows the fundamental principles of photochemistry to be interrogated in model systems. Furthermore, these studies are carried out exclusively in the gas phase, where molecules can be isolated from outside interactions, *e.g.* from the solvent.

Understanding molecular dynamics following photoexcitation is often complicated by coupling between the electronic and nuclear degrees of freedom of a system. It is common to invoke the Born-Oppenheimer approximation, which assumes that the motion of the electrons and nuclei can be treated separately.[4] This allows the molecular wave function ψ to be factorised into an electronic component (ψ_{elc}) and a nuclear component (ψ_{nuc}):

$$\psi(\vec{r}, \vec{R}) \approx \psi_{\mathrm{elc}}(\vec{r}, \vec{R})\psi_{\mathrm{nuc}}(\vec{R}), \tag{1.1}$$

where $\vec{r}$ and $\vec{R}$ refer to the electronic and nuclear coordinates, respectively. The basis for this approximation is that the electrons move on a much faster timescale than the heavy atomic nuclei. Hence, for any change in nuclear structure the electrons adjust essentially instantaneously to their lowest energy configuration.

The Born-Oppenheimer approximation leads directly to the concept of the Potential Energy Surface (PES),[5] which is a map of the electronic energy as a function of the nuclear coordinates. Although referred to as a 'surface', a PES is typically multi-dimensional as its dimensionality is equal to the number of nuclear coordinates, which is $3N - 6$ for a polyatomic molecule comprised of N atoms.

This means that PESs quickly increase in complexity for larger molecules. A different PES exists for each electronic state of a molecule. Within the Born-Oppenheimer approximation, it is the topography of the populated PES or PESs that directly determines the molecular dynamics, and therefore the ultimate outcome of photoexcitation. Experimental studies of molecular dynamics can be viewed as directly probing the PESs of a system.

It must be acknowledged that instances where the Born-Oppenheimer approximation breaks down are well catalogued. Particularly significant are conical intersections – points at which two or more PESs intersect and crossing between the surfaces can occur.[6–8] In the vicinity of a conical intersection, electronic and nuclear motion are strongly non-adiabatically coupled and the two can no longer be treated separately. Non-adiabatic effects are uncommon in thermal reactions, which commonly take place exclusively on the ground electronic state, but are ubiquitous in photochemistry.

1.2.1 Photodissociation

If a molecule gains sufficient energy through photoabsorption to transfer to an excited electronic state, the dynamics on that excited state may result in the cleavage of a chemical bond. This is known broadly as photodissociation. The exact nature of the process will depend of the topography of the PES associated with the excited state, and those of any close-lying excited states which may non-adiabatically couple to the initially populated state.[9] Figure 1.2 illustrates several photodissociation scenarios for a diatomic molecule AB.

If dissociation occurs on the electronic state populated by photoabsorption, either because there is no barrier to dissociation, or because the barrier is exceeded by energy gained through photoabsorption, it is referred to as direct photodissociation. These two mechanisms are shown in panels (i) and (ii). If the electronic state populated by photoabsorption is bound and dissociation occurs via transfer to a different electronic state, it is known as predissociation. In the case shown in panel (iii) this proceeds via non-adiabatic coupling to a dissociative state. In panel (iv) photoexcitation populates a quasi-bound state and dissociation occurs by tunneling through the barrier. These two scenarios are known as Hezberg type I and II predissociation, respectively. Direct dissociation is a rapid process, often complete within 100 fs.[10]. The timescale of predissociation varies considerably depending on the exact nature of process, but it is generally much slower, *i.e.* picoseconds.[11,12] Finally, dissociation on the ground electronic state can also take place if a radiationless decay leaves the molecule in a highly excited vibrational state, as seen in panel (v).

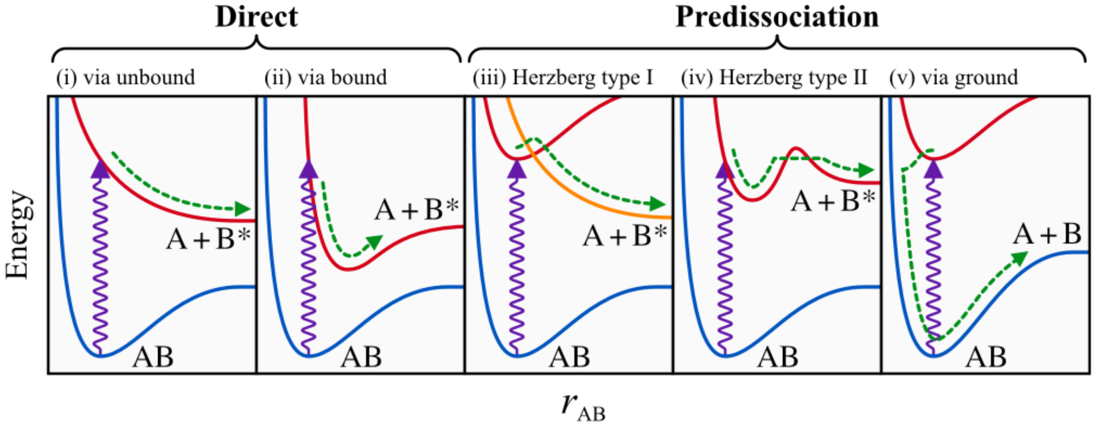

Figure 1.2: Some of the possible photodissociation mechanisms for a diatomic molecule AB following photoexcitation from its ground electronic state (*blue*) to an excited electronic state (*red*). The potential energy for each electronic state is plotted as a function of the separation of the two atoms. The dashed green line in each panel is the trajectory followed on the potential energy curve(s). (i) Direct photodissociation via a unbound excited state; (ii) direct photodissociation via a bound excited state; (iii) Herzberg type I predissociation; (iv) Herzberg type II predissociation; (v) predissociation via radiationless transfer to a highly excited vibrational state of the ground electronic state.

The dynamics of UV photoinduced C–I bond cleavage in methyl iodide are discussed briefly in Section 2.8.3. A thorough interrogation of the UV photodissociation dynamics of 1,2-dichloroethene is presented in Chapters 7 and 8. The following section discusses an exceptional photodissociation process that is ubiquitous throughout the work in this thesis.

1.2.2 Coulomb explosion

Coulomb explosion is the process whereby multiple electrons are rapidly removed from a target molecule to produce a highly charged and highly unstable molecular polycation, which subsequently 'explodes' into many fragment ions:

$$\mathrm{ABC} \xrightarrow{nh\nu} \mathrm{ABC}^{(p+q+r)+} \rightarrow \mathrm{A}^{p+} + \mathrm{B}^{q+} + \mathrm{C}^{r+}. \tag{1.2}$$

It is termed as such because the forces governing the dissociation are primarily Coulombic. This means that the fragment momenta are sensitive to the internuclear separation of the fragment ions at the instant of dissociation.

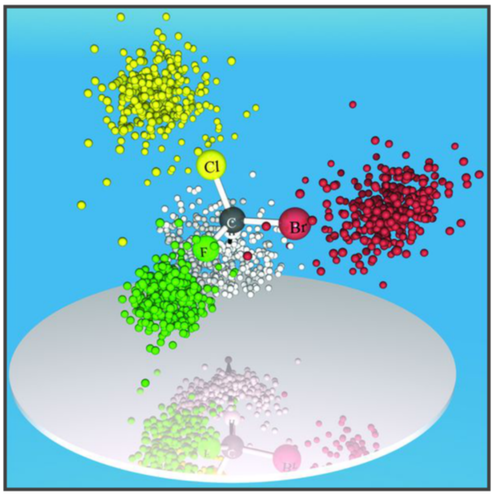

Figure 1.3: Correlated momenta of H^+ (*white*), Br^+ (*red*), Cl^+ (*yellow*) and F^+ (*green*) from the Coulomb explosion of (S)-$CHBrClF^{5+}$. Momenta are normalised with respect to the momentum of C^+ (not shown). H^+ momenta have been scaled by a factor of 2 for visibility. Adapted from Reference [13].

Provided that multiple ionisation and subsequent fragmentation occurs on a short timescale relative to nuclear motion, the initial atomic positions in the parent molecule are mapped onto the final fragment momenta. Recording the momenta of the fragments of a Coulomb explosion therefore offers a direct route to probe nuclear structure. This approach is known as Coulomb Explosion Imaging (CEI)[14] and is central to the work presented in this thesis. As an example, results from a pioneering CEI study by Pitzer *et al.*[13] are shown in Figure 1.3. The relative momenta of ions of the substituent atoms from the Coulomb explosion of a halogenated methane molecule are plotted. These strongly resemble their nuclear positions in the parent molecule. Crucially, this study relied upon being able to measuring the relative, correlated momenta of multiple fragments, techniques for which are discussed in Section 1.5.

Coulomb explosion was first demonstrated in experiments that projected molecules at high speed through thin metal foil to rapidly strip electrons.[14,15] The experiments described in this thesis use a more contemporary method of inducing Coulomb explosion through interaction with an intense laser pulse.[13,16–20] Relevant ionisation mechanisms in intense laser fields are described in Section 1.4. Laser-induced CEI has been extensively used to determine static nuclear structure, such as distinguishing structural[21–23] and chiral[13,24] isomers, and identifying different conformations of molecular clusters.[25–27] It is of particular interest when combining with pump-probe spectroscopy to examine time-evolving nuclear structure.[16,17] This approach is discussed in Section 1.3.1, demonstrated in Section 2.8.3, and applied in the experimental work presented in Chapters 7 and 8.

1.2.3 Photoisomerisation

Photoisomerisation refers to a structural rearrangement induced by photoabsorption that transform one molecule into another. Two major examples are ring opening/closing processes[28] and the interconversion of *cis-trans* isomers.[29] The latter of these is the primary interest of the work presented in Chapters 7 and 8. *cis-trans* isomerisation occurs in chemical compounds with a double bond that is reduced to a single bond upon photoexcitation, enabling free rotation and hence isomerisation between *cis* and *trans* forms. This is a straightforward form of molecular photoswitching – a process which is important in nature for the conversion of photons to mechanical energy. For example, the isomerisation of a chromophore in rhodopsin forms the molecular basis for vision.[7,30]

Photoisomerisation is initiated by transfer to an excited electronic state, followed by relaxation, possibly via other excited electronic states, to the ground state of a structural isomer. For the experiments in Chapters 7 and 8 1,2-dichloroethene was selected as the target molecule because it is expected to exhibit similar *cis-trans* isomerisation dynamics to ethene. Being the simplest possible photoswitch, ethene has received substantial attention, and its dynamics are well characterised. Photoexcitation to the lowest excited state of the molecule (π, π^*) removes the restriction on rotation about the C–C axis and the molecule undergoes ultrafast torsion to a twisted geometry. Subsequent relaxation to the ground state reimposes the planar geometry. This occurs via pyramidalisation of one of the CH_2 groups, which accesses a conical intersection between the excited and ground electronic states.[31,32]

1.3 Femtochemistry

Because nuclear motion within molecules occurs on the order of tens of femtoseconds, to investigate such processes in real time it is necessary to make measurements on a femtosecond timescale. This is often refereed to as the ‘ultrafast’ timescale. Such experiments were made reality in the 1980s with the advent of mode-locked laser sources capable of producing sub-100 fs pulses.[33,34] The principle behind mode-locked lasers is expanded upon in Section 2.1.1.

Time-Resolved (TR) studies of molecular photodynamics using ultrafast lasers are generally performed in a pump-probe scheme.[35,36] A ‘pump’ pulse initiates the photochemical process of interest, followed by a delayed ‘probe’ pulse that transfers population to a state which can be measured in some way. This represents a snapshot of the system at a certain point in the reaction. By repeating the measurement at a series of pump-probe delays it allows the full temporal evolution of the dynamics to be captured. Such experiments were first explored by Ahmed Zewail, who was later awarded the Nobel Prize in Chemistry in 1999 for his pioneering work in establishing the field of femtochemistry.[37]

An important consideration of ultrafast studies is that the gain in time resolution must necessarily come with a sacrifice in energy resolution, and hence state selectivity. The energy-time uncertainty relation:

$$\Delta E \Delta t \geq \frac{\hbar}{2}, \tag{1.3}$$

dictates that a laser pulse that is narrow in the time domain must necessarily be broad in the frequency domain, *i.e.* a pulse with a short time duration pulse will have a broad spectral bandwidth.[38] The spectral bandwidth of a ultrafast laser pulse is broad enough to excite multiple eigenstates of a system. Though individual eigenstates are stationary, the coherent population of several eigenstates creates a non-stationary, localised wave packet. An ultrafast pump pulse therefore prepares a wave packet that evolves in time.

The experiments of Zewail and coworkers which examined the photodissociation dynamics of sodium iodide provide an excellent demonstration of wave packet dynamics.[39,40] The two PECs relevant to the dynamics are illustrated schematically in Figure 1.4(a). These asymptotically correlate to dissociation into neutral Na + I and ionic $Na^+ + I^-$, and so are referred to as the covalent and ionic curves, respectively. In the region where the PECs intersect they interact to produce a curve crossing. Photoexcitation at 310 nm prepares a wave packet that is bound within the potential well formed by the two PECs and oscillates back and forth, *i.e.* the Na-I bond vibrates. Whenever the wave packet traverses the curve crossing some fraction is transmitted and continues to propagate along the covalent PEC, forming dissociated Na + I. This is what was tracked experimentally using Laser-Induced Fluorescence (LIF).

Figure 1.4(b) displays the TR-LIF trace at a probe wavelength of 590 nm, which measures the quantity of dissociated Na. The signal increases in regular steps with a period equal to the time taken for each oscillation of the wave packet in the potential well. The oscillations are clear in the trace recorded at a probe wavelength of 615 nm, shown in panel (c). This off-resonance wavelength probes Na in a transition state, hence signal is only observed each time the wave packet is in the vicinity of the curve crossing. The signal decays with increasing delay, indicating that the population in the potential well has decreased each time the curve crossing is traversed. As it continues to oscillate, the wave packet gradually dechoeres due to the anharmonicity of the potential well, causing successive peaks in the trace to become broader.

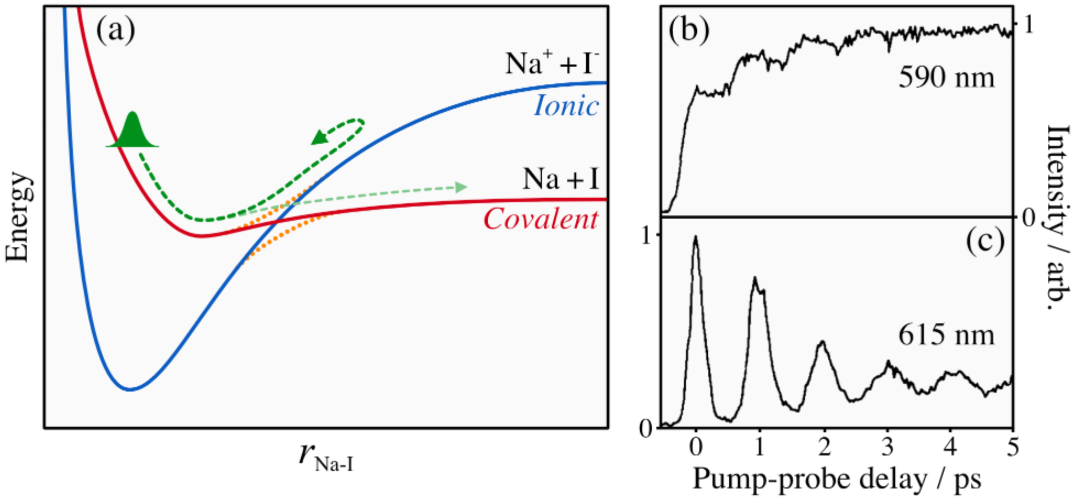

Figure 1.4: (a) Schematic representation of the dynamics of NaI following single photon excitation at 310 nm. The covalent (*red*) and ionic (*blue*) adiabatic PECs interact to produce an avoided crossing (*orange*), giving rise to a pair of diabatic PECs. The excited wave packet oscillates in the potential well of upper diabatic PEC. Each time it traverses the region of the curve crossing, a fraction is transmitted and escapes the well to form dissociated Na + I. The right hand panels show the TR-LIF signal at a wavelength of (b) 590 nm and (c) 615 nm, which probe dissociated Na and transition state Na, respectively. Adapted from Reference [40].

In addition to LIF, the ultrafast pump-probe methodology pioneered by Zewail and coworkers has been combined with a variety of experimental probe techniques. This includes: mass-spectrometry,[41] ion imaging,[10–12] photoelectron spectroscopy,[42] transient absorption spectroscopy,[43,44] X-ray diffraction and scattering,[45] electron diffraction[46] and, the topic of the next section, Coulomb explosion imaging.[16,17]

1.3.1 Time-resolved Coulomb explosion imaging

The femtosecond pump-probe methodology developed by Zewail and coworkers was first combined with CEI to probe time-evolving nuclear structure by Stapelfeldt *et al.* in the 1990s.[16,17] Their original experiment that investigated the photodissociation dynamics of molecular iodine is a valuable example of the principles of Time-Resolved Coulomb Explosion Imaging (TR-CEI). The pump-probe scheme is depicted in Figure 1.5(a). Excitation of the ground state by a 80 fs, 625 nm pump pulse prepares a wave packet on the dissociative $\mathrm{A}\,^3\Pi_{1u}$ PES. Following a delay (Δt) the wave packet is projected onto a Coulombic PES by a second 625 nm pulse with triple the peak intensity.

The momenta of the fragments from the ensuing Coulomb explosion provide a snapshot of the nuclear structure immediately prior to ionisation. Measurements at several pump-probe delays can be used to construct a picture of the molecular dynamics. Varying Δt samples the dissociation process at different stages of progression, therefore the pump-probe delay effectively controls the separation of the iodine fragments upon ionisation and subsequent Coulomb explosion. This manifests as a decreasing Kinetic Energy Release (KER) of the Coulomb explosion with increasing Δt, shown by the I^+ Kinetic Energy (KE) spectra in panel (b), which were measured using Time-of-Flight (ToF) mass spectrometry. The timescale at which the peak in the spectra shifts is characteristic of the real-time nuclear motion during photodissociation.

Since this initial demonstration of TR-CEI on a simple, direct photodissociation process in a diatomic molecule, the technique has been extended to study photoinduced molecular dynamics in larger, more complex systems. Examples include photoinduced molecular vibration of a biphenyl molecule;[47] photoinduced rotational dynamics of OCS;[48] UV-induced photodissociation of various halomethanes[49–51] and halobenzenes;[52] photoisomerisation via hydrogen migration in cationic actylene,[53,54] methanol,[55] and ethanol;[56] and even roaming dynamics during the photodissociation of formaldehyde.[57] The seventh and eighth chapters of this thesis apply TR-CEI to study the UV photoexcitation dynamics of 1,2-dichloroethene.

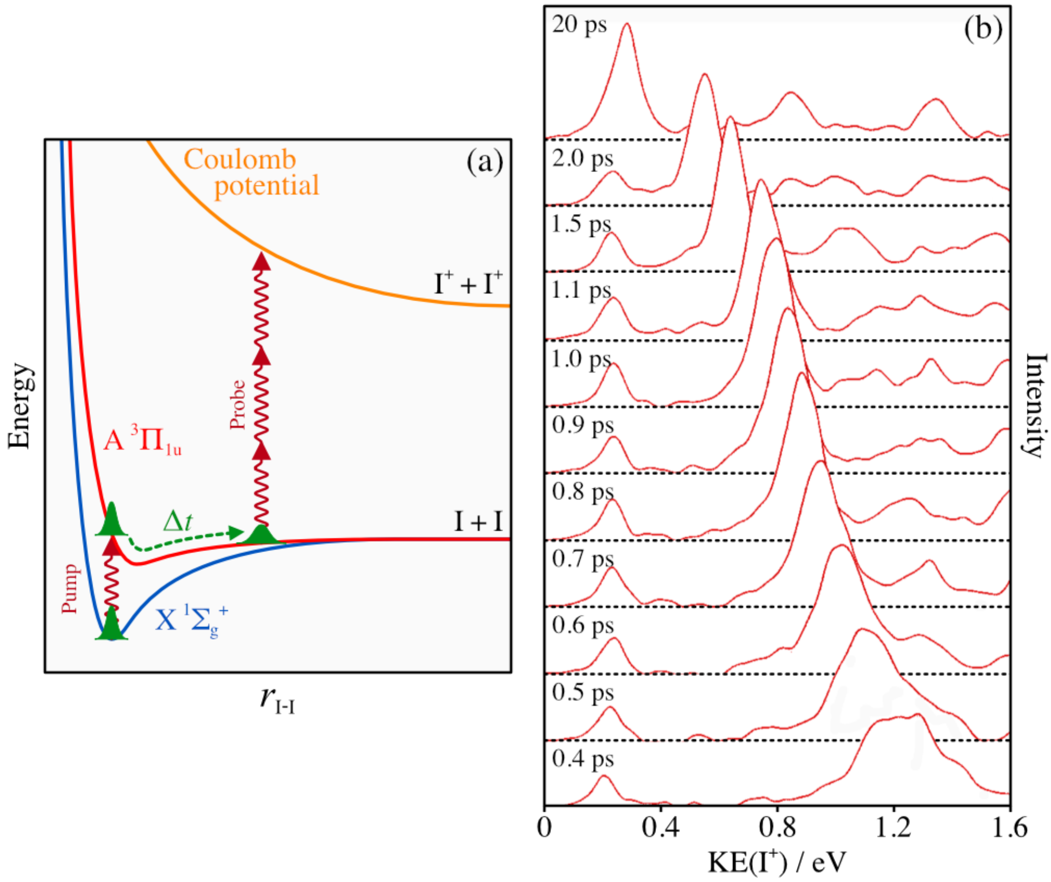

Figure 1.5: (a) Schematic illustration of the wave packet dynamics involved in the TR-CEI of I_2 photodissociation. The pump pulses prepares a wave packet (*green*) on the dissociative $A\,^3\Pi_{1u}$ PES (*red*). The wave packet evolves for some time period (Δt) before being projected by multiphoton ionisation onto a repulsive Coulomb potential (*orange*), resulting in prompt Coulomb explosion into $I^+ + I^+$. (b) I^+ kinetic energy spectra recorded at different Δt. Adapted from Reference [17].

It is important to consider whether CEI is a suitable probe of molecular structure, especially for larger molecular targets. The technique relies on understanding the mapping between the initial atomic positions within the parent molecule and the final fragment momenta. To ensure a straightforward mapping, ionisation and any subsequent charge redistribution must occur on a fast timescale compared to nuclear motion, such that the molecular structure is not meaningfully perturbed prior to explosion. It is also the case that ‘complete’ fragmentation into exclusively atomic ions results in more direct mapping – a topic that is explored in Chapter 6. Photoionising large molecules to a high enough charge state to produce complete Coulomb explosion can often be a challenge.

TR-CEI is not unique in its capability to probe time-evolving molecular structure. X-ray[45] and electron diffraction[46] techniques can also be combined with pump-probe methodology to examine real-time nuclear motion. Whilst CEI relies upon inferring molecular structure from the relative fragment momenta, diffraction techniques are capable of directly determining structural parameters. However, structural information must be retrieved from the measured diffraction patterns, which is difficult, especially for more complex molecules.[58] By comparison, TR-CEI offers a more straightforward method of probing molecular dynamics.

1.4 Photoionisation

The CEI experiments described in this thesis exclusively used intense laser pulses to prepare the precursor polycations by photoionisation. A distinction can be made between the experiments that employed an optical laser system, presented in Chapters 6, 7 and 8, and those conducted at a Free-Electron Laser (FEL) facility, discussed in Chapter 5. The principal difference being that these laser sources induce ionisation of the target molecule through different mechanisms.

1.4.1 Ionisation in intense laser fields

The most widespread contemporary method of performing CEI is using a Ti:Sapphire laser system. These are tabletop instruments that are suitable for most conventional laboratories, widely commercially available, and can induce substantial multiple ionisation of a target molecule almost universally. Ti:Sapphire laser systems are capable of producing pulses of Near-InfraRed (NIR) light with a duration of tens of femtoseconds. The duration of pulses can be reduced to sub-10 fs through other means, such as spectral broadening in a hollow core fiber and pulse compression.[59] The operating principles of these systems are described in Section 2.1.1.

Although the photon energy of a Ti:Sapphire laser is low, the peak intensity of individual pulses is high enough to achieve Strong-Field Ionisation (SFI). The onset of SFI occurs around a laser field intensity of 10^{14} W cm^{-2} where the strength of the electric field of the ionising radiation becomes comparable to the Coulombic attraction between the electrons and nuclei in the target molecule. The laser field distorts the potential experienced by bound electrons, leading to different ionisation mechanisms depending on the extent of the distortion.[60] These are illustrated schematically in Figure 1.6.

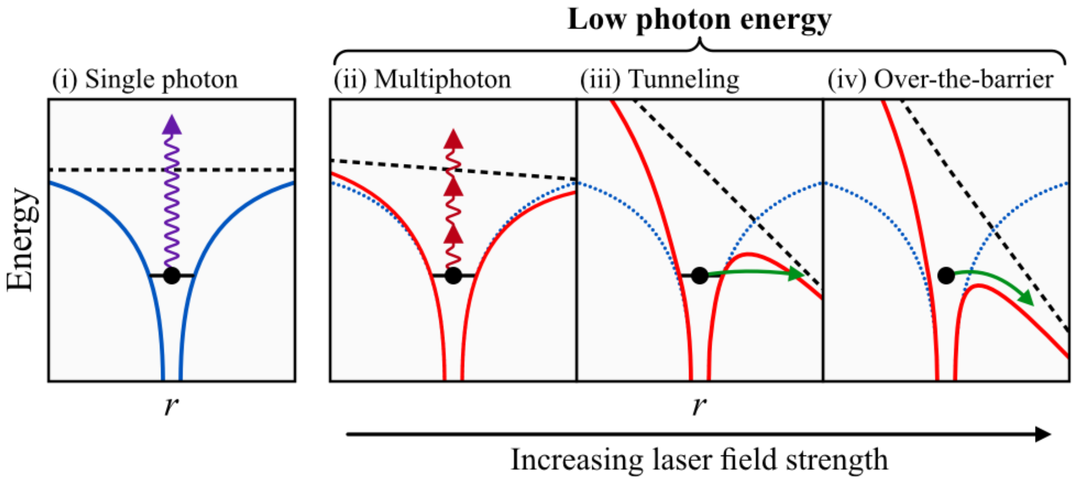

Figure 1.6: Different possible ionisation mechanisms with increasing laser intensity. Single photon ionisation in a weak laser field that does not distort the binding potential (*blue*) is shown in panel (i), where the photon energy exceeds the electron binding energy. Panels (ii–iv) illustrate the distortion of the potential experienced by the electrons (*red*) with increasing external field strength, when the photon energy is much less than the electron binding energy. This results in multiphoton, tunneling, and over-the-barrier ionisation, respectively.

The first panel display the simple case of single photon ionisation when the laser field does not perturb the binding potential of the electrons. If the photon energy is substantially less than the electron binding energy, but the external field strength remains low, ionisation can occur by prompt absorption of multiple photons until the ionisation potential is exceeded. See panel (ii). The absorption of photons above the number required for ionisation is known as Above-Threshold Ionisation (ATI)[61] and manifests as a series of photoelectron peaks separated by the photon energy $h\nu$. As the magnitude of the external field increases, the potential experienced by the electrons is eventually distorted such that the barrier to ionisation is reduced sufficiently for bound electrons to tunnel through, as depicted in panel (iii). Finally, panel (iv) displays the high field limit, where the potential is distorted to the extent that the barrier to ionisation is absent.

SFI is in essence a 'blunt-hammer' method of photoionisation, which indiscriminately strips valance electrons from all molecules. This proceeds via a sequential mechanism where electrons are removed in a step-wise fashion. It is crucial that the pulse duration is kept as short as possible for CEI, in order to minimise internuclear motion within the time window of the ionisation process. Otherwise it can complicate the interpretation of the fragmentation dynamics. For example, decreasing the pulse duration from 40 to 10 fs for the SFI ionisation of D_2O was found to drastically reduce distortions in the molecule's internuclear geometry before dissociation.[62] Fortunately, the effect is less significant for heavier species.[18]

It is worth noting that whilst many treat SFI purely as a tool for preparing molecular polycations (the author of this thesis being no exception), it is a complex and fascinating process in itself, and the subject of its own active field of research.[63]

1.4.2 Inner-shell ionisation

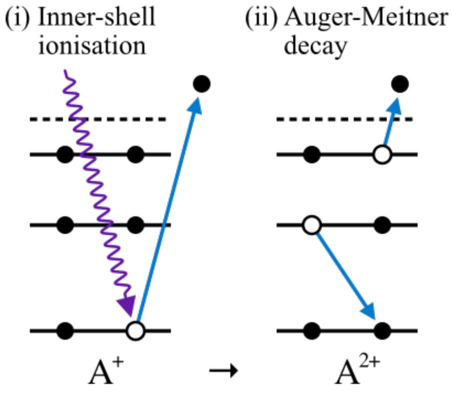

Figure 1.7: (i) ISI by a high-energy photon, resulting in a singly charged ion in a highly excited state. (ii) Subsequent AM decay, where an electron from a higher-lying state drops down to refill the inner-shell vacancy, and the residual energy is released in the KE of a secondary electron. This process yields a dication.

At very high photon energy, in the eXtreme UltraViolet (XUV) or X-ray regime, ionisation can occur from deeply bound orbitals within a molecule. Compared to valence orbitals, which tend to be delocalised across a molecule, inner-shell orbitals are highly localised to a single atom. This makes Inner-Shell Ionisation (ISI) a much more precise method of photoionisation than SFI, as ionisation can be performed selectively at a specific atomic site. Following ISI, the vacancy is rapidly repopulated by a higher-lying electron. The excess energy is released either by emitting a photon or ejecting a secondary electron. A diagram for this second process, called Auger-Meitner (AM) decay,[64,65] is presented in Figure 1.7.

Higher charge states can be reached by multiphoton inner-shell absorption that creates multiple inner-shell vacancies and triggers a cascade of AM decay processes. This is beyond the capabilities of most conventional synchroton sources and requires a FEL – a source of intense femtosecond pulses of short wavelength radiation (see Section 2.1.2 for details). Most CEI studies that utilise ISI rely on multiphoton absorption by a heavy atom within the molecule, as these species have a large X-ray absorption cross section. A prevalent example is ionisation of iodine above the 4d edge.[51,52,66–68] This produces a localised build up of charge on the heavy atom that redistributes throughout the molecule to initiate Coulomb explosion. The initial charge localisation has even been exploited to study processes such as charge transfer dynamics during dissociation.[51,52,66–68]

Though X-ray induced CEI necessarily relies on successive steps of photoionisation, AM decay and charge redistribution prior to breakup, the cumulative time taken can be remarkably short. Experiments conducted at FEL facilities are now pushing the boundaries for the complexity of molecules that can be studied using CEI. A recent study recorded momentum images for all fragments from the complete Coulomb explosion of 2-iodopyridine with unprecedented clarity, which was attributed to rapid charge up of all 11 atoms within only a few femtoseconds.[20] The downside is that there is a limited number of FEL facilities worldwide, so securing ‘beamtime’ is a highly competitive process. Even then the time allocated is very restrictive, meaning that experiments are inevitably the result of compromise.

1.5 Multi-particle correlations

In many studies of reaction dynamics, measuring not only the properties of individual products, but also the correlations between them can unlock additional insight.[69] At the most basic level, this approach allows products that arise from the same process to be identified. If correlated product angular and energy distributions are recorded they can be used to characterise the underlying process.

Within the context of CEI, the structural dynamics of a diatomic molecule can be followed by measuring the momentum of only one of the fragment ions, because the momentum of the second fragment must necessarily be equal and opposite. For example, in the original experiments of Stapelfeldt *et al.*[16,17] nuclear motion during the photodissociation of I_2 was tracked by measuring the kinetic energy of individual I^+ ions. When investigating the Coulomb explosion of a polyatomic molecule yielding more than two fragments, the momenta of the fragments can no longer be easily related. Indeed, if the ensemble of ionised molecules is randomly orientated there will be no relation between the fragment momenta in the laboratory frame. In order to extract structural information the momenta must be measured in correlation so that the relative recoil of fragments can be inspected in the molecular frame.

Two methods have been developed for determining the correlated properties of fragment ions: coincidence analysis and covariance analysis. Both are applied in the experimental work reported in this thesis. To begin, the older of these two techniques is outlined.

1.5.1 Coincidence analysis

The concept behind coincidence measurements is to probe individual molecular fragmentation events against a near-zero background, such that in any measurement where multiple ions are generated they can be confidently assigned to the breakup of the same molecule. The first application of coincidence analysis in the field of reaction dynamics was by McCulloh *et al.* in the 1960s.[70] They studied the Coulomb explosion of small gas phase molecules induced by electron impact by the coincident detection of two ions. In the decades since, ion-ion coincidence spectroscopy has been extensively applied to characterise the Coulomb explosion of triatomic molecules,[18,71,72] including the identification of sequential and concerted breakup mechanisms.[73–75] More recently, recording the momenta of several fragment ions from Coulomb explosion under coincidence conditions has proven to be a powerful tool for structural determination[13,20,21,23,76–78] (see the example given in Section 1.2.2).

In the context of laser-induced CEI, conducting an experiment under coincidence conditions requires that on average $\ll 1$ molecule is ionised per laser shot. Because experimental signal is low, it is also essential to minimise background signal due to ionisation of species other than the target molecule. These experiments have a reputation for taking a very long time to collect data, though in recent years certain studies have been to able to offset the low count rate with a higher experimental cycle speed through the use of new high repetition rate laser sources. The experiments reported in Chapter 8 were conducted under coincidence conditions, but employed a unique 10 kHz laser system to greatly expedite data acquisition.

In reality, coincidence studies of Coulomb explosion are not so ‘pure’ as the initial description would imply. False coincidence events between uncorrelated ions are inevitable, either due to generation of background ions simultaneous to the Coulomb explosion of a target molecule, or from the breakup of multiple target molecules in the same laser shot. Hence, such studies rely heavily on applying appropriate filters to remove false coincidence events from the dataset.[13,20,21,76,78,79] A common approach is to focus on ‘complete’ coincidence events where the detected fragments together constitute the original molecule. True coincidences can then be isolated by selecting only those combinations of ions whose momenta sum to zero. These filtering techniques are explored fully as part of the data analysis in Chapter 8.

1.5.2 Covariance analysis

If the count rate in a laser induced CEI study is increased, suitable conditions for coincidence measurements are quickly lost. Contributions from ions generated from the breakup of separate molecules in the same laser shot begin to dominate. The true coincidence events remain, but are hidden amongst an overwhelming background of false coincidences. In the late 1980s Frasinski *et al.* developed a statistical method for capturing and removing this background to isolate the correlations between fragment ions using covariance analysis.[80] Their approach is able to extract equivalent information to coincidence analysis, whilst operating at orders of magnitude higher ion count rates.[81]

There are two scenarios where covariance analysis is better suited for CEI than coincidence analysis. The first is when operating with a limited repetition rate which makes it impractical to conduct experiments at a low count rate, as it would take an excessive amount of time to collect sufficient data. This is what motivated the experiments reported in Chapters 5 and 6 to be performed at higher count rates, necessitating covariance analysis. The former was limited to 60 Hz by the repetition rate of the laser, and the latter to 10 Hz by the capabilities of the detection system.

The second scenario is when count rates are unavoidably high. As the target system is increased in size the fragment ions from a single molecule become too numerous to all be captured in coincidence. It is more practical to measure the correlated momenta of anchor species on the molecule that provide a good representation of its structure. For example, Christensen *et al.* applied covariance analysis to examine the torsional motion of a biphenyl molecule in a TR-CEI study by tracking the relative momenta of pairs of halogen substituents.[47] On the other hand, if the ion detector has limited multi-hit capabilities (see Section 2.5) it is infeasible to operate at a high count rate, and experiments must be conducted under coincidence conditions.

The application of covariance analysis to CEI data is a core aspect of this thesis. In addition, a significant portion of the work of this thesis constituted the development of new covariance analysis techniques that provide deeper insight into the many-body dissociation dynamics of molecular polycations. For these reasons, Chapter 3 is dedicated to covariance analysis, including outlining the fundamental principles, numerous variations, and many applications of the technique.

1.6 Thesis outline

This thesis is concerned with the investigation of photoinduced molecular dynamics, including the fragmentation dynamics of molecular polycations, and isomerisation and dissociation in small molecules. A number of experimental studies using ultrafast laser pulses are described, conducted in three different laboratories across the globe. All of them utilise CEI in some form and, critically, rely on measuring the correlated momenta of fragment ions in order to extract information about molecular structure. This initial chapter has introduced the central photochemical processes, CEI as a method to track molecular structure, and the key observables that need to be measured experimentally. The following chapter outlines the host of different practical techniques that are combined in a laser-induced CEI, as well as the data processing routines that convert the raw experimental signals into measured properties of the ions.

Chapter 3 provides a detailed overview of covariance mapping applied to the fragmentation of molecular polycations. The multiple variations of this analytical technique used throughout the later chapters are discussed, including new variants developed to examine the dynamics of three-body fragmentation processes. After that, Chapter 4 describes a classical model of the Coulomb explosion process that is heavily relied upon to guide and support the interpretation of experimental data. The focus is on how this simple model can be modified to replicate the dynamics of a number of different molecular processes, as appropriate. The remaining chapters present results from various experimental studies.

In Chapter 5, results from a experimental study conducted at a FEL facility are presented. Data were collected for the isomers of iodopropane irradiated with intense XUV femtosecond laser pulses. This dataset is used to demonstrate the potential of a tailored covariance mapping approach, which employs extensive filtering on the relationship between fragment momenta to isolate and interrogate specific fragmentation channels in detail.

Chapters 6 and 7 report a series of experiments conducted in the laboratory in Oxford. The first of these two chapters investigates the Coulomb explosion of the *cis* and *trans* isomers of 1,2-dichloroethene, following SFI by intense NIR femtosecond laser pulse. This lays the ground work for the second, which describes a TR-CEI study of the UV photoexcitation dynamics of *trans*-1,2-dichloroethene, intended to probe photoinduced *cis-trans* isomerisation dynamics in this molecular system. Chapter 8 follows on directly by presenting results from a second round of TR experiments on the UV photoexcitation dynamics of the *cis* and *trans* forms of 1,2-dichloroethene, carried out using a more technically advanced experimental apparatus. The marked improvement in the quality of the data provides much deeper insight into the photoinduced molecular dynamics.

2

Experimental principles and apparatus

Contents

This chapter details the various practical techniques that are combined in a modern, laser-induced Coulomb explosion imaging experiment. The experimental work presented in this thesis was carried out on three different time-resolved Coulomb explosion imaging instruments. All three operate on the same fundamental principles. Target molecules are introduced into a vacuum chamber by means of a molecular beam, which is intersected by a femtosecond laser pulse, or pulses if preforming TR-CEI. The resulting ions are focused by a set of ion optics down a ToF tube, and onto a time and position sensitive detector.

To begin, each component part is reviewed individually. Following this an explicit description is provided for each spectrometer. The instrument in the Brouard group laboratory at the University of Oxford (referred to as the Oxford spectrometer) is given the most attention, as this was by-far the instrument that the author spent the longest time on its operation, upkeep and maintenance. The data processing routines used to extract physical properties of measured ions from their raw experimental signals are described. Finally, an account is given of the preliminary experiments used to characterise the TR-CEI capability of the Oxford spectrometer, following the recent installation of a Ti:Sapphire laser system.

2.1 Femtosecond laser sources

The most important feature that sets each experimental instrument apart is the accompanying femtosecond laser source. Two of the instruments are coupled to a Ti:Sapphire laser system, which is a conventional optical laser system, and the third to a free-electron laser, which operates on a fundamentally different principle. As already covered in Section 1.4, Ti:Sapphire lasers systems and FELs produce ultrafast pulses of substantially different wavelength light, responsible for distinct photoionisation mechanisms. Here, the working principles for each type of laser are discussed.

2.1.1 Ti:Sapphire laser systems

A Ti:Sapphire laser system is capable of producing intense, ultrafast pulses of light in the NIR wavelength region. It is a laser *system* because it is composed of several lasers which together produce the final output. Broadly, this can be understood as an oscillator or seed laser, which generates weak femtosecond laser pulses that are raised in pulse energy inside an amplifier. Energy is dumped into the amplifier by a pump laser and picked up by the seed pulses.[38] Both the oscillator and amplifier uses a Ti:Sapphire lasing medium, whilst the pump laser typically uses a Nd:YLF lasing medium.

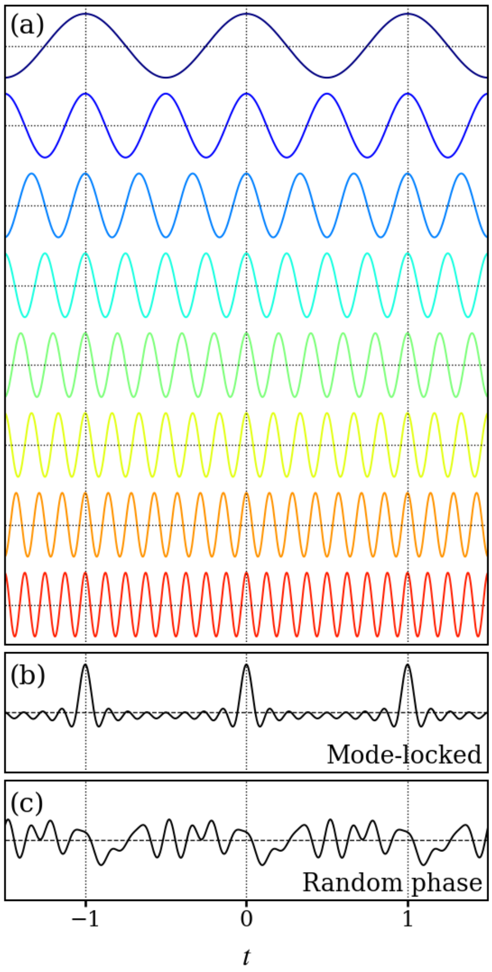

Figure 2.1: A demonstration of the principle of mode-locking. Panel (a) displays eight different frequency components which are summed either in-phase, *i.e.* mode-locked, in (b) or with random phases in (c).

There are two key technologies behind a Ti:Sapphire laser system. The first is mode-locking, demonstrated by Hagrove, Fork and Pollack in 1964.[82] This refers to the process of inducing a fixed-phase relationship between the longitudinal modes of a laser cavity, such that they interfere constructively to produce a series of pulses. As a demonstration, Figure 2.1 displays the result of adding the first eight cavity modes in-phase, versus with random phases. The greater the number of mode-locked frequencies that are summed, the shorter the resulting pulse. Practically, this means a laser medium with a large spectral bandwidth is needed to support the generation of femtosecond pulses. Ti:Sapphire is a particularly good example.

Methods to achieve mode-locking are categorised as either active or passive. Active mode-locking techniques use an external modulator placed within the cavity and driven with an electric signal. For example, an acousto-optic modulator. On the other hand passive mode-locking or self-mode-locking relies on the light in the cavity itself driving modulation through some physical process, *e.g.* Kerr lens mode-locking.[83] Generally, active mode-locking produces a more stable series of pulses, but passive mode-locking is able to generate narrower pulses. For the reader looking to learn more, Reference [38] is a good starting point, and the references therein offer much greater detail.

To be of practical use for many applications, the low energy ultrafast pulses from a mode-locked oscillator must be amplified. However, this poses a significant technical challenge. The very high intensity of ultrafast pulses easily damages a gain medium through unwanted non-linear effects such as self-focusing. The amplification technique utilised in a Ti:Sapphire laser system is known as Chirped-Pulse Amplification (CPA), developed by Mourou and Strickland in 1985.[84] Their solution was to temporally stretch pulses prior to amplification to reduce the peak power to a level that does not damage the gain medium. Amplified pulses are then re-compressed to femtosecond duration. This is shown pictorially in Figure 2.2. In a Ti:Sapphire laser system pulses are stretched to several hundred picoseconds, and can then safely be amplified from nJ up to mJ.

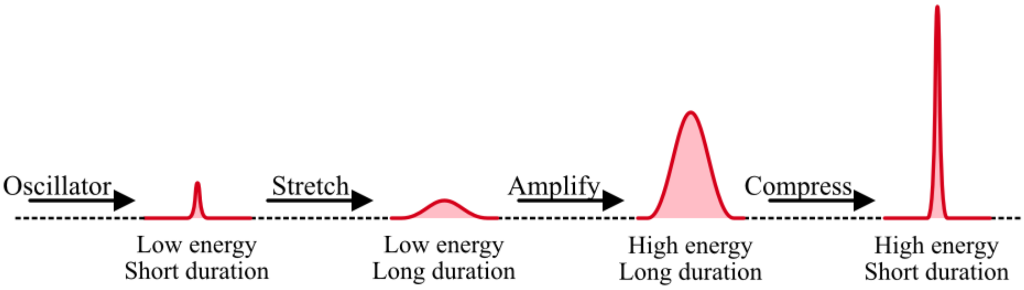

Figure 2.2: The CPA scheme. Weak femtosecond seed pulses from an oscillator are temporally stretched prior to amplification, and then subsequently re-compressed. This avoids issues faced with amplifying these pulses directly.

For the development of CPA, Mourou and Strickland jointly received the Nobel Prize in Physics in 2018.[85,86] The term 'chirped' refers to the fact the pulses are temporally stretched. An ultrafast pulse is said to be transform limited when all of its constituent frequency components have a consistent phase, giving the minimum possible duration for the spectral bandwidth. A pulse is chirped when its frequency components are dispersed. Chirp can be either positive or negative depending on whether the red or blue frequencies lead. During CPA, first positive chirp is induced, typically using a pair of diffraction gratings arranged so that the lower frequency components travel a shorter distance. Afterwards, a grating compressor working on the opposite principle (lower frequency components travel a longer distance) applies an equal and opposite negative chirp to re-compress pulses.

2.1.2 Free-electron lasers

Free-electron lasers are sources of extremely intense, ultrafast pulses of short wavelength, tuneable radiation. They are an entirely different class of instrument to tabletop lasers as they are accelerator based light sources. Due to their scale and cost, only a handful are in operation worldwide. Obtaining beamtime at one is a highly competitive process. FELs can access wavelengths in the XUV to X-ray regime[87–90] making them excellent sources of radiation for ISI. Their tuneability allows the wavelength of radiation to be adjusted to selectively ionise a specific inner shell of a species.

Though referred to as a laser, a FEL is not a laser in the traditional sense. The properties of the generated radiation are similar to that of a laser, but light amplification does not occur by stimulated emission of radiation. Instead, photons are generated by synchroton radiation[91] – the physical phenomena where a charged particle moving at relativistic velocity (*i.e.* a significant fraction of the speed of light) emits radiation when accelerated perpendicular (radial) to its direction of travel.

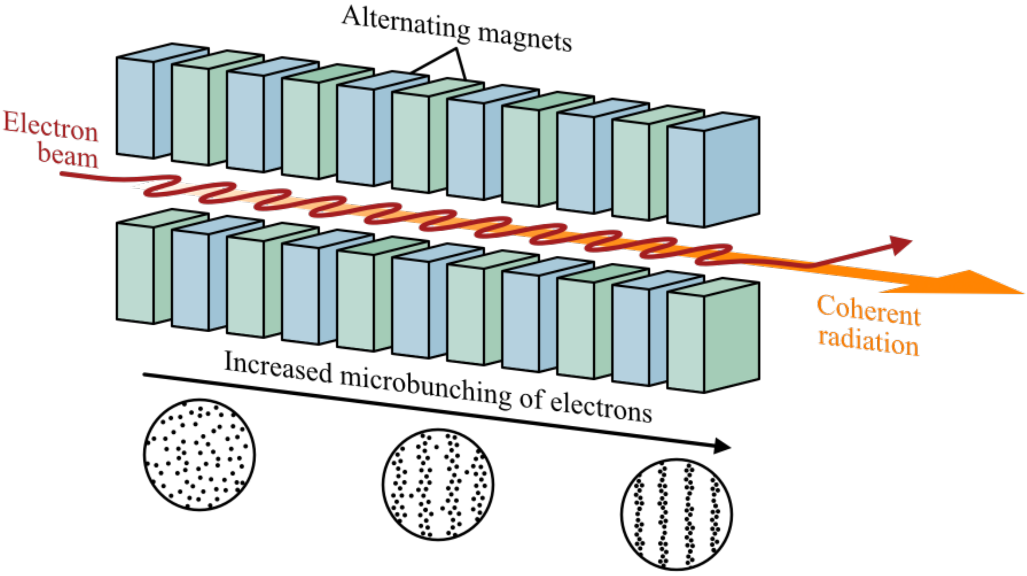

Figure 2.3: The undulator of an FEL, which produces coherent radiation through SASE. A beam of electrons that travels through the undualtor is forced to oscillate by the alternating magnetic field, leading to emission of synchroton radiation. This begins a feedback loop where the radiation interacts with electron beam to cause microbunching, resulting in coherent radiation emission, which further enhances microbunching.

In a FEL, an electron beam is accelerated in a linear accelerator and then injected into an undulator, depicted in Figure 2.3. The undulator consists of a long arrangement of dipole magnets with alternating polarity. The alternating magnetic field causes the emission of synchroton radiation, which then re-interacts with the electrons, causing them to coalesce into bunches separated by the radiation wavelength, known as microbunching.[92] A feedback loop commences wherein bunched electrons emit coherent radiation as they continue to oscillate, which in turn induces a greater degree of mircobunching. This results in an exponential rise in the intensity of coherent radiation as the electrons traverse the undulator.

The central wavelength of the radiation can be tuned by adjusting the properties of the alternating magnetic field and the KE of the electron beam.

Some initial bunching of the electrons in the beam is required to start the microbunching process. Most FELs rely on Self-Amplified Spontaneous Emission (SASE),[92,93] where whatever small, random initial bunching is present in the electron beam is amplified. As a result SASE sources are inherently stochastic. Significant shot-to-shot variation occurs in spectral properties including pulse energy and arrival time. Free-electron lasing schemes that use seeding to provide the initial bunching of electrons can have drastically improve pulse stability and coherence properties. For example, using an external laser.[94]

2.2 Vacuum technology

Laser-induced CEI experiments must be conducted under Ultra-High Vacuum (UHV) conditions, characterised by a pressure below 1×10^{-7} mbar. This serves two purposes. The first is to obtain essentially collision-free conditions, allowing the photochemistry of a molecule to be studied in isolation from external interactions. It also ensures that nascent ions travel the distance from the interaction region to the detector undisturbed. Under UHV conditions, the mean free path is at least several hundred meters.

The second purpose is to limit the background signal due to photoionisation of species other than the target molecule. Due to the non-selective nature of ionisation by intense laser pulse, residual gas molecules in the vacuum chamber will also be ionised. Background signal is particularly problematic for coincidence imaging experiments, which operate under conditions where on average $\ll 1$ target molecule is ionised per laser shot. Signal from the ionisation of background gases can easily overwhelm the low signal from the target system. Therefore, such studies often pursue additional measures to further reduce the pressure, allowing them to reach base pressures on the order of 10^{-10} mbar.

Achieving UHV conditions requires the combination of two kinds of vacuum pump designed to operate in different flow regimes.[95] From atmospheric pressure down to ∼1 mbar is the viscous flow regime. Under these pressures the mean free path of particles is significantly less than the dimensions of the chamber, *i.e.* collisions between particles are far more frequent than collisions with the chamber walls. The gas acts like a conventional fluid, with the flow behaviour dictated by the interactions between particles. Pumps designed to operate in the regime are called 'roughing' pumps and are effective down to $\sim 10^{-3}$ mbar.

As the pressure decreases the mean free path of particles increases and, when the mean free path exceeds the dimensions of the chamber, the system is in free molecular flow. Interactions between particles become negligible and the gas no longer 'flows' in the macroscopic sense. Rather it is characterised by individual particles moving in straight lines. TurboMolecular Pumps (TMPs) are designed to operate exclusively in the molecular flow regime and bring the pressure down to UHV.[96] A TMP must be coupled in series with a roughing pump which maintains a low backing pressure. The subsequent sections explore the functionality of TMPs and the two types of roughing pump used on the Oxford spectrometer.

2.2.1 Roughing pumps

When the work of thesis commenced, the Oxford spectrometer was equipped with a pair of oil-sealed Rotary Vane Pumps (RVPs). The mechanism of a RVP is illustrated in Figure 2.4.[97] It consists of a rotor mounted off-centre inside a circular cavity. A pair of vanes is installed inside slots cut into the rotor so they can slide radially. Centrifugal force and often a spring set between the vanes forces them outwards, such that they maintain contact with the walls of the cavity as the rotor rotates. This divides the cavity into two separate chambers. The mechanism is best understood by focusing on the action of a single chamber, highlighted in the consecutive panels of the figure. The chamber is initially connected to the inlet, whilst the outlet is sealed by a valve. As the rotor turns the volume of the chamber expands, causing gas to flow in. As it continues to rotate the chamber is sealed by the rear vane. The volume begins to decrease and the enclosed gas is compressed. Eventually, the chamber is connected to the outlet valve and the gas is forced out.

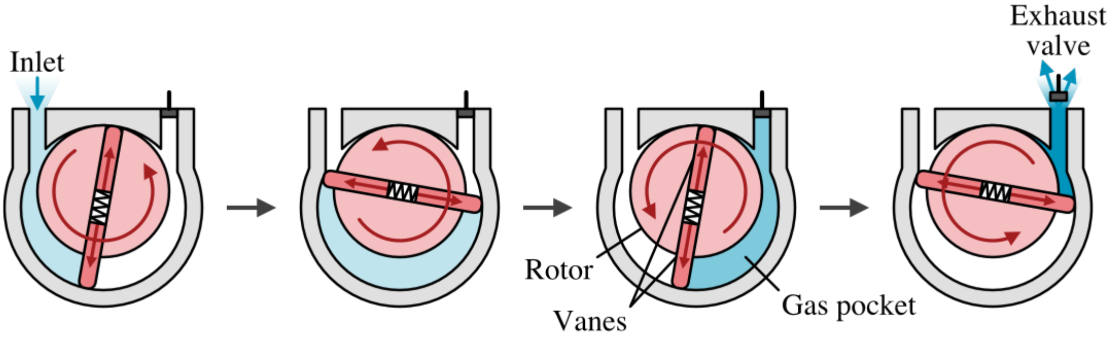

Figure 2.4: The mechanism of a RVP. The contacts between the pair of vanes and the cavity walls divides the cavity into two separate chambers. Successive panels show how the rotation of the rotor changes the volume of one of the chambers (*blue*). The chamber first expands, causing molecules to flow in from the system being pumped. Then the volume is decreased to force the gas out through the outlet.

The diagram displays the simplest case of an RVP with two working chambers created by a pair of vanes. Working models often incorporate more vanes to divide the cavity into several chambers. The oil helps to maintain the seal between the vanes and the cavity walls, as well as serving the general purpose of lubricating the moving parts. RVPs are robust, reliable and easy to maintain, but their dependence on oil makes them unsuitable for an experiment requiring a clean background. Indeed, oil contamination was a persistent issue for the Oxford spectrometer. This motivated the replacement of the oil-sealed RVPs with oil-free or dry scroll pumps following the conclusion of the experimental work.

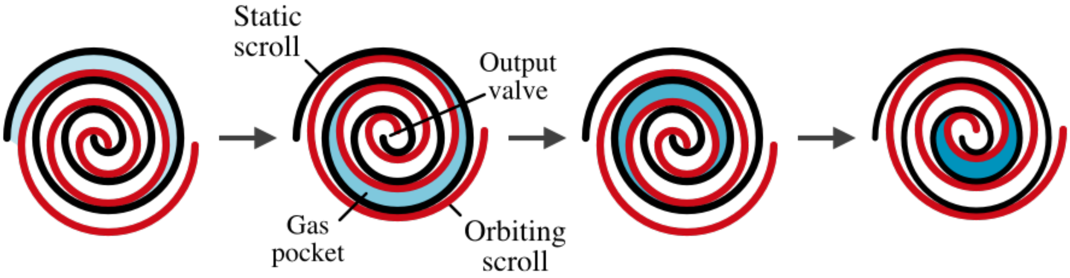

Figure 2.5: The mechanism of a scroll pump. Consecutive panels show how the orbit of one spiral relative to the other compresses a pocket of gas (*blue*) as it is transported towards the outlet valve located at the centre of the assembly.

A scroll pump is similar to an RVP in that it relies on trapping and compressing pockets of gas. This is achieved using a pair of wound spirals or scrolls, shown in Figure 2.5.[95] One spiral is fixed whilst the other orbits eccentrically against it, without rotating. The relative motion traps pockets of gas between the two spirals, which are squeezed as they are transported towards the outlet valve at the centre of the assembly. Static images struggle to do this mechanism justice, so the reader is encouraged to go online to find one of the many animations. In addition to requiring no oil lubrication, these pumps are distinctly quieter and more energy efficient than RVPs.

2.2.2 Turbomolecular pumps

In appearance, a turbomolecular pump is similar to a turbine. It consists of a series of rapidly rotating ‘rotors’, interposed with static ‘stators’. However, a TMP serves the opposite function to a turbine. Rather than extracting KE from a system, a TMP transfers KE to the particles of a gas.[97] The blades of each rotor are titled with respect to the direction of rotation, so that particles impacted by the rotor receive an impulse in the required direction of flow. The blades of each stator are angled oppositely to funnel particles deflected off the blades towards the next rotor, where the process continues. This principle is illustrated in Figure 2.6.

Each rotor-stator pair forms a stage, so that a TMP is composed of multiple stages. The stages become smaller towards the outlet so that the gas is successively compressed to level of the backing pressure. Turbomolecular ‘pump’ is therefore a misnomer as the device operates as a compressor. The key parameter for TMPs is the compression ratio, which governs the pumping speed. Compression ratio is determined by the physical properties of the pump, *e.g.* rotation rate, but also depends on molecular mass.[96] As a result TMPs are far more effective at pumping heavier species than lighter ones. At base pressure, the residual gas in a chamber is mainly composed of H and He.[95]

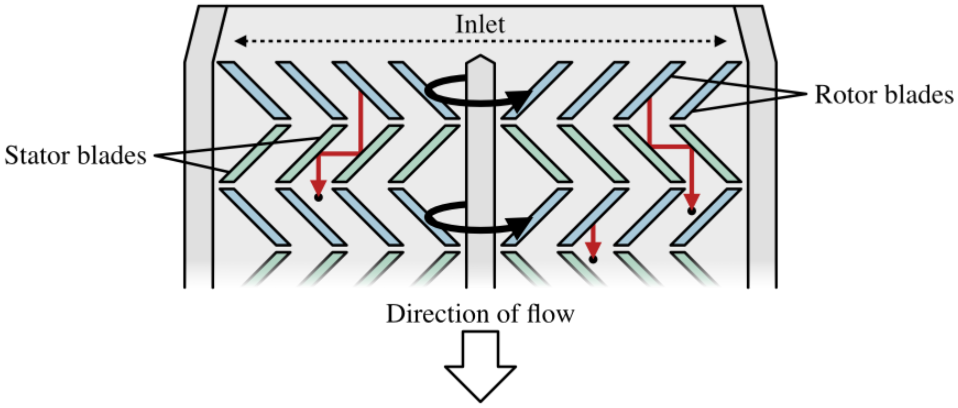

Figure 2.6: Diagram of how particles 'flow' within a TMP. Particles that enter the area swept out by the upper rotor receive a downwards impulse when struck. They deflect off the blades of the stator beneath, and towards the second rotor. By this process, particles progressively 'flow' in one direction. A TMP consists of ∼10 stages of rotor-stator pairs that decrease in size towards the outlet to compress the gas to the backing pressure.

2.3 Molecular beams

A molecular beam is a localised density of molecules, all moving in the same direction with approximately equal velocities, such that there are very few collisions between molecules. Molecular beams are used to introduce target molecules into an UHV chamber in sufficient quantity for study without substantially raising the pressure. Such a beam can then easily be intersect with a laser beam to induce photochemistry of the constituent molecules. A molecular beam is generated simply by expanding high-pressure gas into a region of UHV through a narrow orifice, and then skimming the resulting supersonic expansion to create a linear profile.

Collisions are common in a high-pressure gas, so in order for molecules to escape through an aperture, collisions parallel to the direction of travel are favoured. Through this process, molecules convert the majority of their thermal energy into translational energy along a common direction, producing significant rotational cooling. Cooling of the vibrational degrees of freedom is typically far less efficient. Collimation is used to select out the 'zone of silence' – the section of the expansion that is supersonic and where molecules are internally coldest. The resulting molecular beam has a narrow longitudinal velocity distribution, minimal transverse velocity, and rotational temperature on the order of 10 K.

A starting ensemble of molecules that is internally cold is ideal for investigations of photochemical dynamics. By minimising the number of molecules that are internally excited prior to interaction with light, it ensures that the available energy comes primarily from photoabsorption, so that any ensuing dynamics are dictated by photoexcitation. For the specific context of an experiment that seeks to measure photofragment momenta, such as CEI, an internally cold molecular ensemble with a narrow velocity distribution will yield photofragments with sharp, well-resolved momentum distributions, making it easier to disentangle different dissociation channels.

Several factors influence the degree of internal cooling in a molecular beam, as well as the longitudinal and transverse velocity distributions of the beam. For a detailed discussion the reader is referred to the seminal work of G. Scoles.[98] The key factor exploited in the experimental work of this thesis is co-expansion of the molecular species with a noble gas, commonly referred to as seeding. Seeding with a carrier gas that is lighter than the molecular species causes molecules to be buffeted by collisions with the faster moving carrier gas atoms. This both enhances the degree of cooling and increasing the terminal velocity of the beam. Seeding can also be advantageous for preventing unwanted clustering of the target molecule in the molecular beam expansion. It is common to use a $\leq 10\%$ mixture of the target molecule diluted in noble gas, in which case the properties of the molecular beam approaches that of a beam of the pure noble gas. This comes at the expense of signal from the target molecule, however.

2.4 Ion imaging

Ion imaging is an umbrella term used to describe a class of experimental techniques that measure the properties of ions by using an electric field to project them onto a Two-Dimensional (2D) position sensitive detector. The centrepiece of an ion imaging instrument is the ion optics, which generate the electric field. In the original incarnation of ion imaging, introduced by Chandler and Houston in 1987,[99] the ion optics consisted of three electrodes: a repeller plate held at positive voltage, and a pair of grounded grids mounted in front. A molecular beam enters the ion optics through a hole in the centre of the repeller plate, where it is intersected by one or more focused laser pulses, producing photofragment ions. The electric field maps a convolution of the initial ion position and velocity onto the detector.

An additional benefit of using an electric field to extract ions is that the time taken for ions to reach the detector (t) is dependent on their mass-to-charge ratio (m/q):

$$t \propto \sqrt{\frac{m}{q}\frac{1}{V_{\mathrm{R}}}}, \tag{2.1}$$

as well as the voltage applied to repeller plate (V_{R}). This approximates a ToF mass spectrometer, where ion species are separated temporally at the detector. In the experiments of Chandler and Houston this was exploited by pulsing the central grid of the ion optics to a positive voltage $> V_{\mathrm{R}}$ after the ion species of interest had passed to repel any higher mass ions. If the arrival time of ions at the detector is measured alongside their positions a ToF spectrum can be produced, allowing the chemical identity of ions to be determined.

2.4.1 Velocity-map imaging

Various improvements have been made to the original ion optics design of Chandler and Houston in the years since. Without doubt the largest step forward was made a decade later by Eppink and Parker when they developed Velocity-Map Imaging (VMI).[100] Today, VMI is the most popular variant of ion imaging and has become part of the standard apparatus for studying molecular photodynamics. Their ion optics design incorporates three electrodes, shown in Figure 2.7. The repeller plate is essentially unchanged from Chandler and Houston's design, but the grid-based electrodes have been replaced by open annular electrodes. The extractor electrode is held at a positive voltage below that of the repeller plate, whilst the final electrode is still grounded.

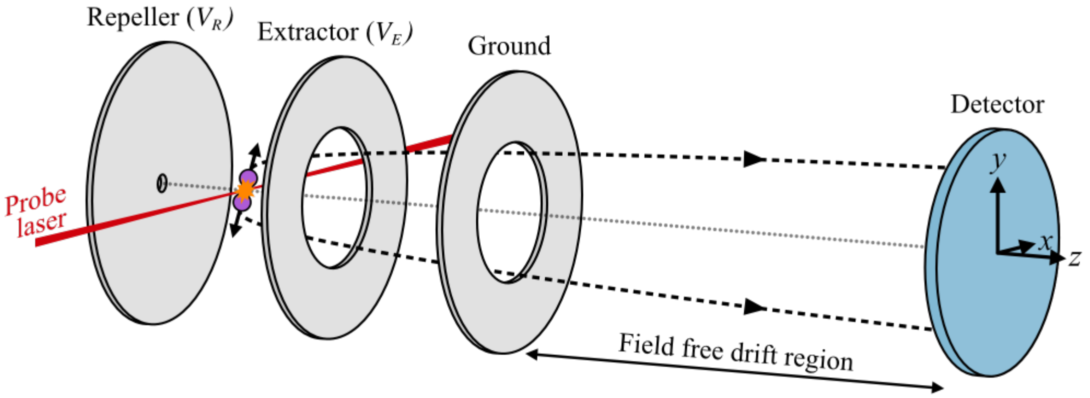

Figure 2.7: Schematic diagram of the ion optics for VMI. Photofragment cations formed in the region between the repeller and extractor electrodes are focused onto the detector in such a manner that the impact position of each ion is related to its nascent velocity vector, and is independent of its position of formation.

The use of open rather than grid-based electrodes means 100% of ions are transmitted. But the principal advantage is that by precisely tuning the ratio of the extractor voltage relative to the repeller voltage, ions are focused onto the detector such that the impact position of each is uniquely determined by its initial velocity vector in the detector plane. Crucially, the impact coordinate is independent of the position at which the ion is formed. This eliminates the blurring of ion images caused by the velocity distribution being convoluted with the spatial distribution of ions within the interaction region (the volume where the overlap of the molecular beam and ionising laser pulse generates ions).

The result is a 2D velocity map of the asymptotic velocities of the fragments from the photochemical process under investigation projected onto the detector. Figure 2.8(a) displays an example image from the work of Eppink and Parker[100] of ions focused using their improved ion optics design. The image maps the velocity distribution of O^+ produced from the photodissociation of molecular oxygen following two-photon excitation around 225 nm. The distribution consists of several sharp concentric rings, each of which corresponds to a different dissociation and ionisation pathway.[101] For comparison, the image in (b) was recorded with grid based electrodes, akin to the original design of Chandler and Houston.

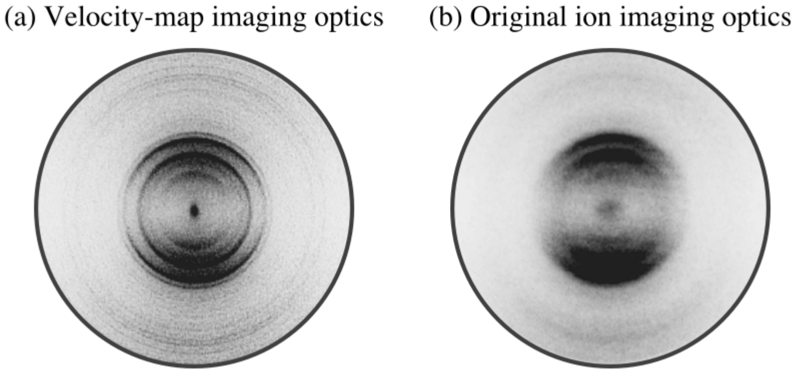

Figure 2.8: O^+ ion images from the photodissociation of O_2 following two-photon excitation around 225 nm, recorded with (a) open annular electrodes and (b) grid-based electrodes. Adapted from Reference [100].

If the distribution on the detector in (a) is expressed in polar coordinates, the angle from the centre is representative of the direction of travel, whilst the radius is directly proportional to the magnitude of velocity/momentum in the detector plane. (Henceforth, ion imaging will be described in terms of the measurement of ion momenta rather velocities, for reasons that will become apparent in Chapter 3). The impact radius is also inversely proportional to $\sqrt{V_\mathrm{R}}$. Changing the extractor and repeller voltages whilst maintaining their ratio therefore provides control over the image size on the detector. If their precise ratio is disturbed, the mapping once again becomes a convolution of initial ion position and velocity – note that spatial mapping occurs at a different precise ion optics voltage ratio. This can be useful in certain scenarios for visualising the volume of the interaction region.

2.4.2 Three-dimensional ion imaging

A traditional VMI experiment, such as the original experimental configuration of Eppink and Parker,[100] records a 2D projection of the ion momenta. This is because the Three-Dimensional (3D) distribution of ions, commonly called the Newton sphere, is flattened onto the detector along the ToF axis. This has earned it the name ‘crush’ imaging. In the current work it is also referred to as 2D projected-momentum imaging, in contrast to 3D momentum imaging, where all three components are measured with comparable precision.

If the experimental momentum distribution possesses cylindrical symmetry, it is a straightforward process to retrieve the 3D fragment momentum distribution from its 2D projection using an inverse Abel transform.[102] For the case of CEI induced by polarised laser light, the momentum distribution of individual fragments do possess the necessary symmetry to perform an inverse Abel transform. However, relative fragment momentum distributions (the key observable in CEI) typically do not.

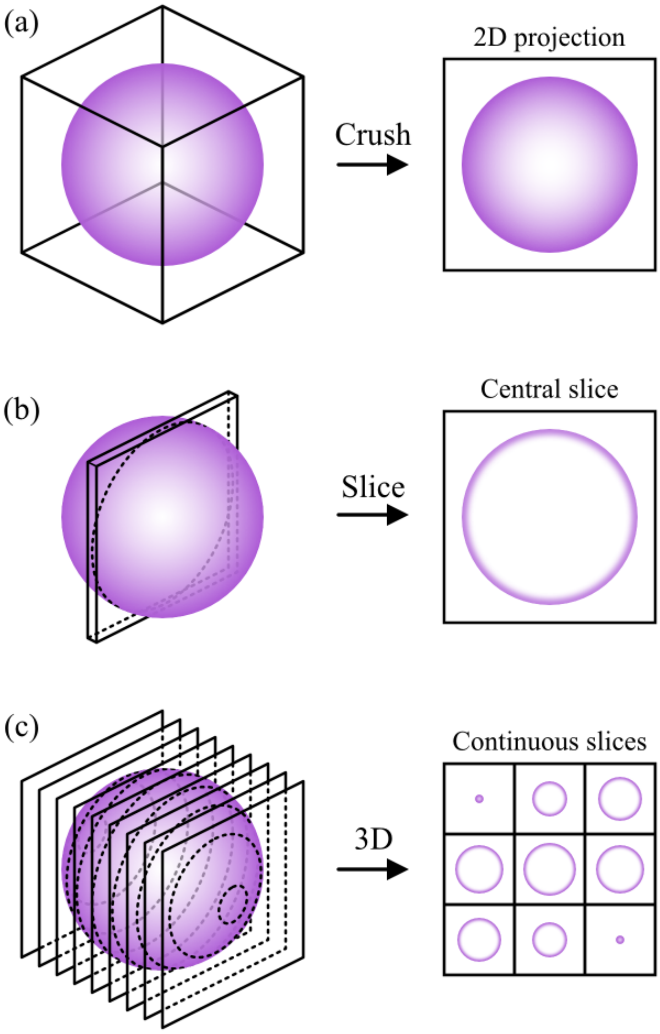

Figure 2.9: The conceptual difference between (a) crush imaging where the entire Newton sphere is projected onto detector, (b) slice imaging where only a narrow central slice along the ToF axis is measured through physical means, and (c) 3D imaging where the complete Newton sphere is captured as a sequence of slices along the ToF axis by a detector with suitably high timing resolution.

Slice imaging was developed to circumvent the need for image inversion by directly measuring only the central slice of the distribution,[103,104] as for many applications the central slice contains all the desired information. Figure 2.9 portrays the conceptual difference between crush and slice imaging. From an isotropic distribution, slice imaging records a sharp ring as only those ions whose momenta are approximately parallel to the detector plane are detected. The momentum distribution measured via crush imaging is smeared towards lower radius due to how the out-of-plane component of each ion's momentum is projected.

To perform slice imaging, the detector is 'gated' over a narrow time window so that only a thin slice around the centre of the Newton sphere is recorded. This is facilitated by temporally stretching the Newton sphere along the ToF axis to spread the arrival time of the ions at the detector. The same width time gate can then capture a narrower potion of the distribution. To stretch the Netwon sphere, a third electrode is introduced into the ion optics, allowing a smaller potential difference to be employed in the interaction region whilst maintaining velocity-mapping.

Unfortunately, slice imaging is not a practical approach for CEI. This is only a valid approach if fragment ions recoil in plane. Even then, several slices would need to be recorded per experimental cycle, one for each fragment species. Ultimately, it is not possible to obtain the relative 3D fragment momentum distribution in a CEI experiment that measures the 2D projected fragment momenta. The 3D momenta of the ions must be measured directly. The impact that recording 2D projected relative fragment momenta has on the structural information that can be deduced is addressed in Section 3.5.1.

3D momentum imaging can be achieved by temporally stretching the Newton sphere, in the same way as slice imaging, but using a detection system capable of recording multiple slices in quick succession[67,105–107], as depicted in Figure 2.9(c). A calibration can then be established between ToF relative to the centre of the ion packet and out-of-plane (z) ion momentum. This means p_z resolution is determined by the timing resolution of the detection system. True 3D momentum imaging requires that the p_z resolution is comparable to that of the in-plane momentum components p_x and p_y. At this point, rather than taking discrete slices along the ToF, an effectively continuous distribution is captured.[108–112] Recording the ion ToF with sufficient resolution to perform this reconstruction can be a challenge. This is the reason why the experiments reported in Chapters 6 and 7 were limited to 2D projected-momentum imaging, whilst those in Chapters 5 and 8 could use 3D momentum imaging.

2.4.3 COLTRIMS

COLd Target Recoil-Ion Momentum Spectroscopy (COLTRIMS) is an alternative charged particle momentum imaging technique.[113] It uses a familiar arrangement of a molecular beam intersected by one or more laser pulses, but a different detection scheme explicitly designed to perform 3D momentum imaging. For this purpose, a COLTRIMS spectrometer employs a pair of high timing resolution delay-line anode detectors (see Section 2.5.2). These are arranged facing one another either side of the interaction region, as shown in Figure 2.10. Rather than a velocity-mapping field, a weak homogeneous electric field is used to guide nascent ions onto one detector, and electrons in the opposite direction onto the other.

The weak extraction field results in a greater momentum resolution, but it can cause high speed particles to be focused outside the radius of the detector. Often a weak magnetic field is also applied, which does not meaningfully perturb the ion trajectories, but forces electrons into spiral trajectories so that they remain confined within the radial span of the detector. To accurately determine the particle ToF, a reference time for the interaction is provided by a photodiode triggered by the arrival of the laser pulse.

COLTRIMS was originally developed for kinematically complete measurements of molecular fragmentation processes in which the momenta of all products are measured to fully interrogate the breakup dynamics.[114] This is the reason these instruments are designed with the capability to record ions and electrons simultaneously, and why they are tailored towards conducting experiments under coincidence conditions. In recent years, COLTRIMS spectrometers have become the ‘gold standard' for CEI due to their ability to measure the 3D momenta of fragment ions with high resolution, yielding correlated momentum images of unprecedented quality.[13,20,78,115]

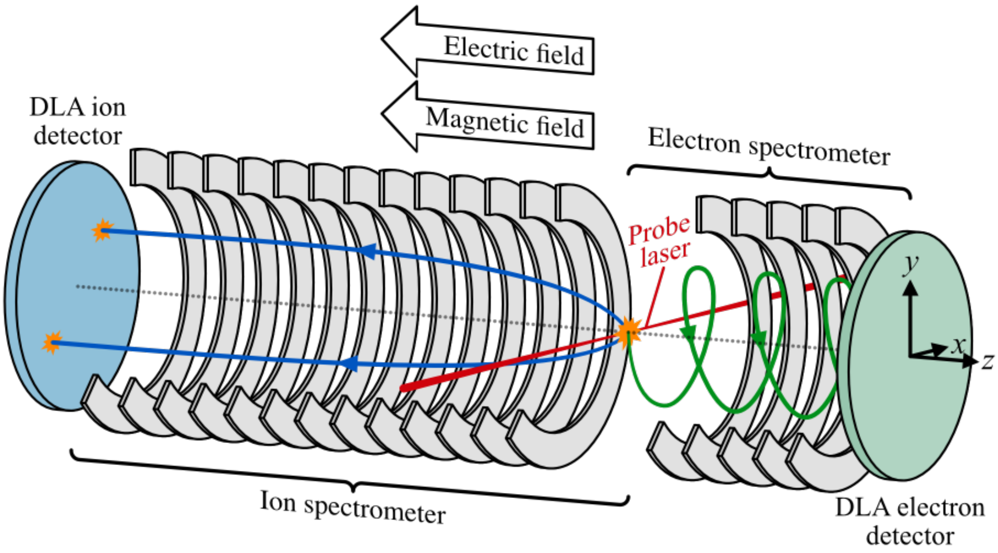

Figure 2.10: Schematic diagram of the ion optics for COLTRIMS. A homogenous electric field is used to focus ions (*blue*) and electrons (*green*) formed by the same process in opposite directions, onto separate detectors. This is overlapped with a homogenous magnetic field that confines electrons closer to the central axis of the spectrometer by forcing them onto spiral trajectories. The magnetic field does not meaningfully perturb the trajectories of ions.

The electron detector of a COLTRIMS spectrometer is not normally used for CEI experiments. The electrons retain information about the photoionisation process, but ionisation is often treated only a tool to trigger fragmentation, and is not of interest for many studies. If a CEI experiment employs SFI, it is true that, due to the nature of the ionisation process, the photoelectron spectrum does not offer significant insight. For experiments that utilise ISI, the electronic information reveals which excited electronic states are accessed by the ionisation process. Hence, measuring the fragment ions and photoelectrons in correlation allows the relationship between ionisation and fragmentation dynamics to be explored.[116]

2.5 Ion detection

The detection scheme for ion imaging has several key requirements. First, it must be position sensitive. This is achieved using a 2D detector plate able to record both the x and y spatial coordinates of each ion impact. Second, the detector must be able to detect individual ions. This requires a method of signal amplification. Finally, it is also highly desirable to be sensitive to the arrival time of ions. The ions arrive at the detector temporally separated according to their m/z. This means it is possible to selectively acquire data for a single species by gating the detector over its arrival time. Although it is far more efficient to record the complete dataset of all ions, including $(x,\ y,\ t)$ information for each. The chemical identity of each ion can then be determined from its arrival time by performing a ToF calibration.

A more powerful advantage of this method lies in the ability to measure correlations between several ions generated in the same pulses, which arrive at different times. This is what enables measurement of the relative momenta of the various ion fragments from a molecular Coulomb explosion, providing information about the original molecular structure.[13,19–22,24] The arrival time of an ion can also be used to reconstruct the component of its momentum perpendicular to the detector plane if the timing sensitivity is high enough. This is how 3D momentum imaging is performed,[108,110–113] as discussed in the previous section.

Two types of time-sensitive detector were used to collect the ion imaging data presented in this thesis. The first is delay line anode detectors, which belong to the family of anode readout detectors. This is by-far the older technology and has been the traditional choice for TR ion imaging for many years. The second is an example of a fast time-stamping camera. These devices have grown rapidly in popularity over the last decade, driven by ongoing developments in the technology. In either case, the ion signal is initially amplified using microchannel plates.

2.5.1 Micro-channel plates

The first stage in a ion imaging detection scheme is to amplify the signal using Micro-Channel Plates (MCPs). An MCP is a thin plate of resistive material, typically a few millimeters thick and several centimeters in diameter, covered by millions of micron-size pores. When a high potential is applied across the MCP, each pore or channel acts as an independent particle amplifier. An ion that impacts inside one of the pores will liberate secondary electrons which are accelerated down the channel. This begins a cascade by which the original signal is amplified by several orders of magnitude. If a second MCP is coupled to the first, the spray of electrons emitted from a single channel in the first will trigger cascades in multiple channels of the second, further increasing amplification. This principle is illustrated in Figure 2.11.

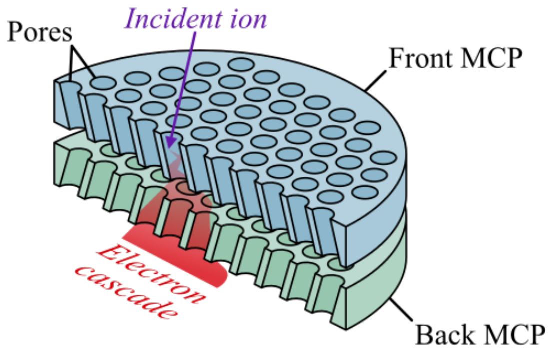

Figure 2.11: Illustrated cross section of a dual-chevron MCP detector (size and number of pores is not to scale). The impact of an ion inside one of the channels produces a localised spray of electrons from several channels on the opposite side.

The gain of an MCP is dependent on how far down an ion travels down a channel before it impacts the wall. To reduce this distance on average, channels are angled slightly with respect to the surface. To further increase the gain in a dual MCP detector, the second plate is rotated by 180°, such that two channels facing each other in the different plates form a chevron (V) shape. Using this configuration, the impact of a single ion produces roughly one million electrons from the opposite side[109] (depending on the applied voltage). The electrons are subsequently detected using one of the methods described in the following sections.

An important characteristic of an MCP is the ratio of its surface area to the area occupied by pores, known as the Open Area Ratio (OAR). Any ion incident between the channels of an MCP will not generate an electron cascade, hence the detection efficiency (η) is limited by the OAR. The close-packed arrangement of pores gives typical OARs between 50-60%. In applications where several particles must be measured in correlation it is desirable to make the OAR as large as possible. Because the probability of detecting n particles in coincidence is given by η^n, if $\eta = 60\%$ the probability of detecting two particles in coincidence is only 36%, for detecting three it is 22%, and so on. For this purpose 'funnel' MCPs with tapered pores have been developed which have an OAR close to 90%.[117,118]

Whilst practically the OAR limits the detection efficiency, in order to achieve an efficiency close to the OAR other factors are important. This includes operating the MCPs at suitably high voltage and ensuring the KE of incident ions is high enough to trigger the detector. This latter condition can be satisfied by raising the ion optics voltages to accelerate nascent ions onto the detector with greater velocity.

2.5.2 Delay-line anode detectors

Delay-Line Anode (DLA) detectors are renowned for their high spatial (tens of μm) and temporal (hundreds of ps) resolution, which makes them ideal for 3D momentum imaging.[13,20,21,78,79,115] The first position-sensitive detectors based on DLA technology were developed by Eland in the 1990s for conducting coincidence imaging.[119,120] This remains the primary application of DLA detectors today, as despite advancements in the years since, they have severely limited multi-hit capabilities. This makes them unsuitable for operation at anything but very low ion count rates.

A DLA is essentially a wire terminated by amplification and timing electronics. A standard DLA detector assembly consists of two delay lines tightly interwoven at right angles,[121] as shown in Figure 2.12(a). The detector is mounted directly behind the MCPs and the delay lines are held at constant voltage. When secondary electrons expelled from the rear MCP impinge onto the DLA detector it generates an electrical pulse in each delay line, which propagates towards both ends of the wire. The difference in the time taken for the signal to reach both ends of the wire is related to its position of origin. The two perpendicular delay lines determine the position of ion impact along independent axes (see Section 2.7.1 for details).

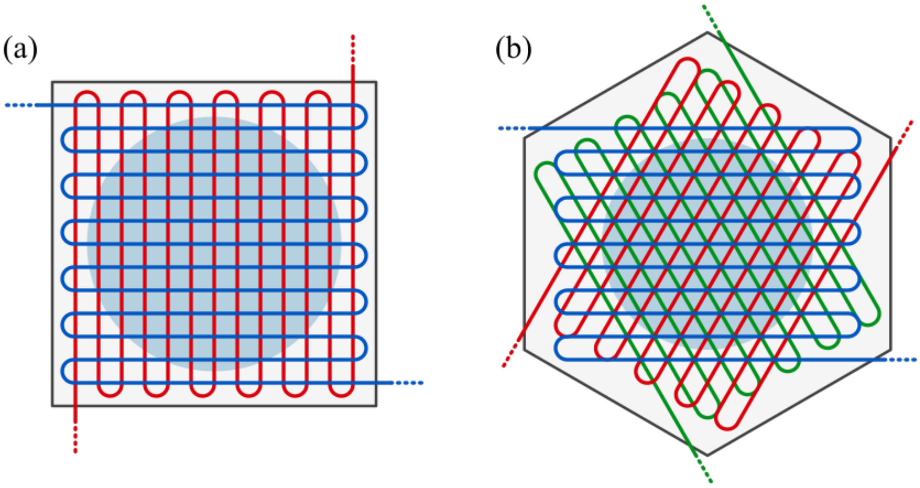

Figure 2.12: Schematic of (a) a conventional DLA detector comprised of two delay lines (*red* and *blue*) and (b) a hexagonal DLA comprised of three delay lines (*red*, *blue* and *green*).

The reason why conventional DLA detectors struggle to record multiple hits simultaneously is because when two or more ion events occur in quick succession, it becomes difficult to disentangle the electrical signals corresponding to the different events. The most notable advancement in this area is the development of hexagonal delay lines anodes which incorporate a third layer into the design.[122] The three delay lines are wound in a hexagonal geometry, pictured in Figure 2.12(b). These detectors are capable of recording two ions simultaneously, and larger numbers under specific conditions. This remains far inferior to the multi-hit capability of other technologies, however.

2.5.3 Fast time-stamping cameras

Whilst the limited multi-hit capability of DLA detectors is not an inherent disadvantage when conducting coincidence imaging experiments, there are scenarios where it is not feasible or even possible to operate at a low count rate. This was mentioned earlier in Section 1.5.2. If an experiment functions at a low repetition rate it is sometimes necessary to operate at higher count rate to avoid excessively long data acquisition times. When studying the Coulomb explosion of larger molecules, inherently higher numbers of fragment ions are generated per laser shot, so it is highly likely that multiple ions will reach the detector simultaneously.

Fast time-stamping cameras are a relatively new type of time-sensitive detector capable of recording multiple simultaneous ion events. They build on the traditional (time-insensitive) method of performing ion imaging, which relies on using a screen coated with phosphorescent material to convert the localised electron spray from the MCPs into a flash of light that can be imaged by camera.[100] Electrons are accelerated onto the phosphor screen through a few kV potential, resulting in excitation and subsequent fluorescence of the material. Historically, experiments have used charge-coupled device (CCD) cameras which do not record timing information.

A fast time-stamping camera also records the flashes of light from a phosphor screen, but is able to time stamp them with high timing precision. As opposed to a conventional frame-based camera, which records complete images of the full pixel array, each pixel in a time-stamping camera acts as independent detector. When the intensity measured by a pixel exceeds a certain threshold it records the value of an internal timer. Each event recorded by the camera is therefore a set of $(x,\ y,\ t)$ coordinates, where $(x,\ y)$ are the unique coordinates of each pixel. In addition, because each pixel functions independently, the limit on the number of simultaneous events is practically eliminated.

This is an event-orientated data acquisition approach, where only the data relevant to each event is recorded, similar to the DLA detectors previously discussed. This mode of operation is fundamental to a high time precision camera which needs to acquire data at high frequency. If the camera was to continuously capture complete frames, the massive amount of data generated could not be read out at an equal rate. This is unnecessary as the large majority of frames contain no events, and in those few that do, the signal is confined to only a small number of the total pixels. An event-orientated approach is much more efficient as it circumvents saving an overwhelming number of null values which otherwise choke the data throughput.

Because each pixel functions independently in a time-stamping camera, the number of events that can be recorded simultaneously is restricted only by the rate at which data can be read out from the camera. Unlike a DLA detector, it is not fundamentally limited by the physical characteristics of the detector. Practically, this amounts to a multi-hit capacity that is orders of magnitude higher. Fast time-stamping cameras typically cannot equal the spatial and temporal precision of a DLA detector, though.

The fast time-stamping camera of principal interest to this thesis is the Pixel Imaging Mass Spectrometry (PImMS) camera,[123,124] developed jointly by researchers at the University of Oxford and the Rutherford Appleton laboratory. The second and most recent generation of this camera (PImMS2) houses a 324 x 324 pixel array sensor and has a timing precision of 25 ns. Photos of the camera and sensor are displayed in Figure 2.13. The camera must be triggered and nominally operates at a repetition rate of 10 Hz. Each pixel can independently record up to 4 events per cycle, with a dead time of ∼100 ns following one event before the next can be recorded.

Figure 2.13: (*Left*) Photo of the PImMS camera. (*Right*) Photo of the PImMS2 sensor.

A direct competitor to the PImMS2 camera is the Tpx3Cam equipped with a Timepix3 chip.[112,125–127] It has a smaller 256 x 256 pixel array, but boasts a significantly shorter 1.6 ns timing resolution, which makes it better suited for 3D momentum imaging. In addition, the Tpx3Cam sensor runs continuously and can therefore support a much higher experimental repetition rate. By contrast, the 10 Hz repetition rate of the PImMS2 camera is nearly always the limiting factor of an experiment.

At the time of writing, the third generation of PImMS camera is currently under testing. It utilises the same PImMS2 sensor, but faster supporting circuitry that enables it to operate at a much higher repetition rate – initial tests suggests at least four times greater. Nevertheless, this cannot match the capabilities of the Tpx3cam, and a new generation of Timepix chip is currently in late development which promises even more impressive specifications.[128] This includes a larger 448 x 512 pixel array and sub-200 ps timing resolution.

The readout chip from a fast time-stamping camera can also be mounted in vacuum to detect the electrons from the MCPs directly.[127] The advantage of this approach is that it bypasses the phosphor screen, which can limit the achievable time resolution due to the finite rise time of the phosphorescent material.[112,129] It is less versatile than having a camera mounted outside of the vacuum though, which is easily interchangeable. In the future, a fast time-stamping sensor equipped with single photon avalanche diodes[130] should, in principle, be able to directly detect individual ions. This would remove the need for MCPs for signal amplification.

2.6 Spectrometers

This section breaks down the specific operating principles of each of the TR-CEI instruments used to collect the data presented in this thesis. Naturally, the instrument in the laboratory at the University of Oxford is the one that the author spent the most time working with. A detailed break down of the functionality of this experiment is given and only brief descriptions are provided for the other two instruments, which the author had less hands-on experience with.

2.6.1 Oxford

The Oxford spectrometer is the name given to the instrument located in the Brouard group laboratory in the Chemistry Research Laboratory at the University of Oxford. This apparatus was used to to collect the data presented in Chapters 6 and 7. The instrument is a conventional on-axis VMI spectrometer, meaning the molecular beam travels along the ToF axis. A diagram is shown in Figure 2.14.

The experiment is divided into three vacuum chambers: the source, reaction and detection. Target molecules are introduced into the source chamber by expansion through a pulsed solenoid valve (Parker Series 9 Pulse Valve). The standard gaseous mixture is ∼10% sample diluted in He, provided at a backing pressure of 2 bar. A 1 mm diameter skimmer (Beam Dynamics Inc.) that separates the source and reaction chambers produces a collimated molecular beam from the supersonic expansion. The pulsed valve is mounted onto the source chamber via a stage that allows the nozzle to be translated in 3D relative to the skimmer to optimise the section of the expansion that is sampled. A large TMP with a capacity of $510\,\mathrm{l s^{-1}}$ pumps the source chamber (Pfeiffer Vacuum TMH 521 P), backed by a RVP (Leybold Trivac D 25 B). This achieves a base pressure of $\sim 1 \times 10^{-7}$ mbar, which rises to $\sim 10^{-6}$ mbar when the pulsed valve is in operation. The laboratory is air conditioned but otherwise none of the TMPs require additional cooling.

The reaction chamber houses the ion optics, consisting of four circular stainless steel plates which fulfil the roles of repeller, extractor, lens and ground electrodes. These are mounted onto the reaction chamber by four stainless steel rods and insulated from one another, as well as the rods, by ceramic spacers (MACOR). Each plate is 1 mm thick, 92 mm in diameter, and has an aperture of carefully selected size. A narrow 2 mm diameter hole in the centre of the repeller electrode is sufficient for the molecular beam to pass through. The apertures in the extractor, lens and ground electrodes are 12, 32 and 40 mm across, respectively. From repeller to ground the separation between each pair of plates is 15, 22 and 30 mm. Voltages are applied to the electrodes via high voltage feedthroughs mounted onto the reaction chamber.

Laser pulses enter the reaction chamber through a 1 mm thick, 10 mm diameter CaF_2 window (Crystran), and intersect the molecular beam in a perpendicular geometry in the region between the repeller and extractor electrodes. Nascent ions are accelerated by the velocity-mapping field of the ion optics. They fly through

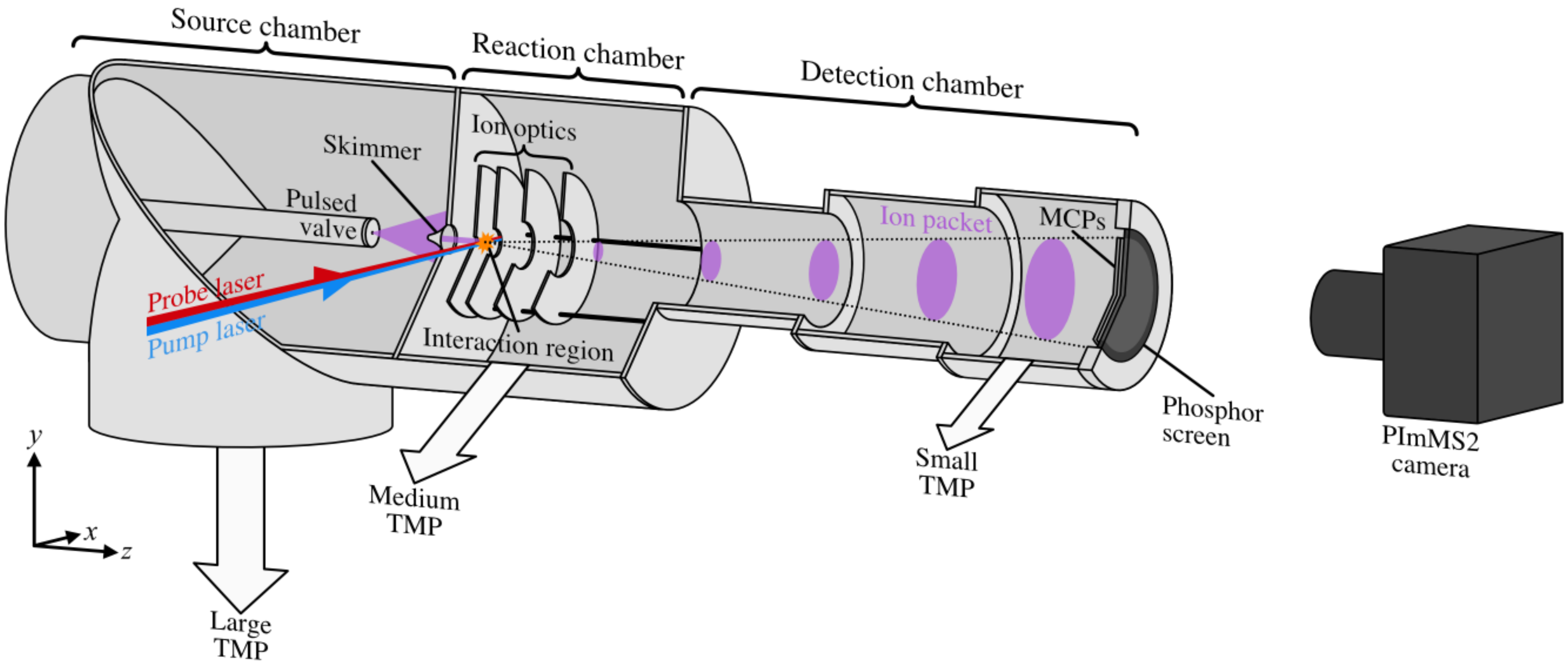

Figure 2.14: Schematic illustration of the Oxford VMI spectrometer with a cutaway to show the interior. This design is referred to as 'on-axis' because the molecular beam is directed parallel to the ToF or z-axis and perpendicular to the plane of the detector. Details are provided in the text.

the field-field drift region of detection chamber and impact the detector. Further details on the optical laser system and ion detector are given below.

The reaction chamber is pumped by a $400\,\mathrm{l\,s^{-1}}$ TMP (Alcatel ATP 400) and the detection chamber by a small $65\,\mathrm{l\,s^{-1}}$ TMP (Leybold Turbovac Sl 80 H), mounted adjacent to the detector. Both are backed by the same RVP (a second Leybold Trivac D 25 B). This maintains a base pressure of 8×10^{-8} mbar across the detection and reaction chambers. A gate valve allows the detection chamber to be isolated from the reaction chamber so that the dual MCP detector can be kept under UHV whilst the other two chambers are vented for maintenance. Minimising exposure to the atmosphere helps to prolong the lifetime of the MCPs and circumvents the need to recondition – a lengthy procedure where the MCPs are raised to operating voltages over multiple hours to slowly desorb any species bound to their surfaces.

Following the conclusion of the experimental work presented in this thesis, the pair of Leybold Trivac D 25 B oil-sealed RVPs were replaced by a pair of Pfeiffer Vacuum HiScroll 18 dry scroll pumps.

Optical laser system

Until recently the Oxford spectrometer was coupled to a dye laser system pumped by a Nd:YAG laser, primarily used to perform resonance enhanced multi-photon ionisation.[105,107] Immediately prior to the beginning of the work of this thesis the nanosecond laser system was replaced by a femtosecond Ti:Sapphire laser system, intended to perform TR-CEI. The system is manufactured by Spectra Physics and consists of a Solstice Ace Ti:Sapphire regenerative amplifier, pumped by a Ascend Nd:YLF laser, which is used to amplify seed pulses from a Mai:Tai active mode-locked oscillator. The amplifier produces pulses with a temporal duration of 35 fs, an average pulse energy of 5 mJ, a central wavelength of 800 nm and a bandwidth of 60 nm, at a repetition rate of 1 kHz.

A diagram of the optical setup is shown in Figure 2.15. A sequence of beamsplitters is used to share the 5 W output power of the amplifier between various experiments. Ultimately, 0.45 W is focused into the spectrometer to drive

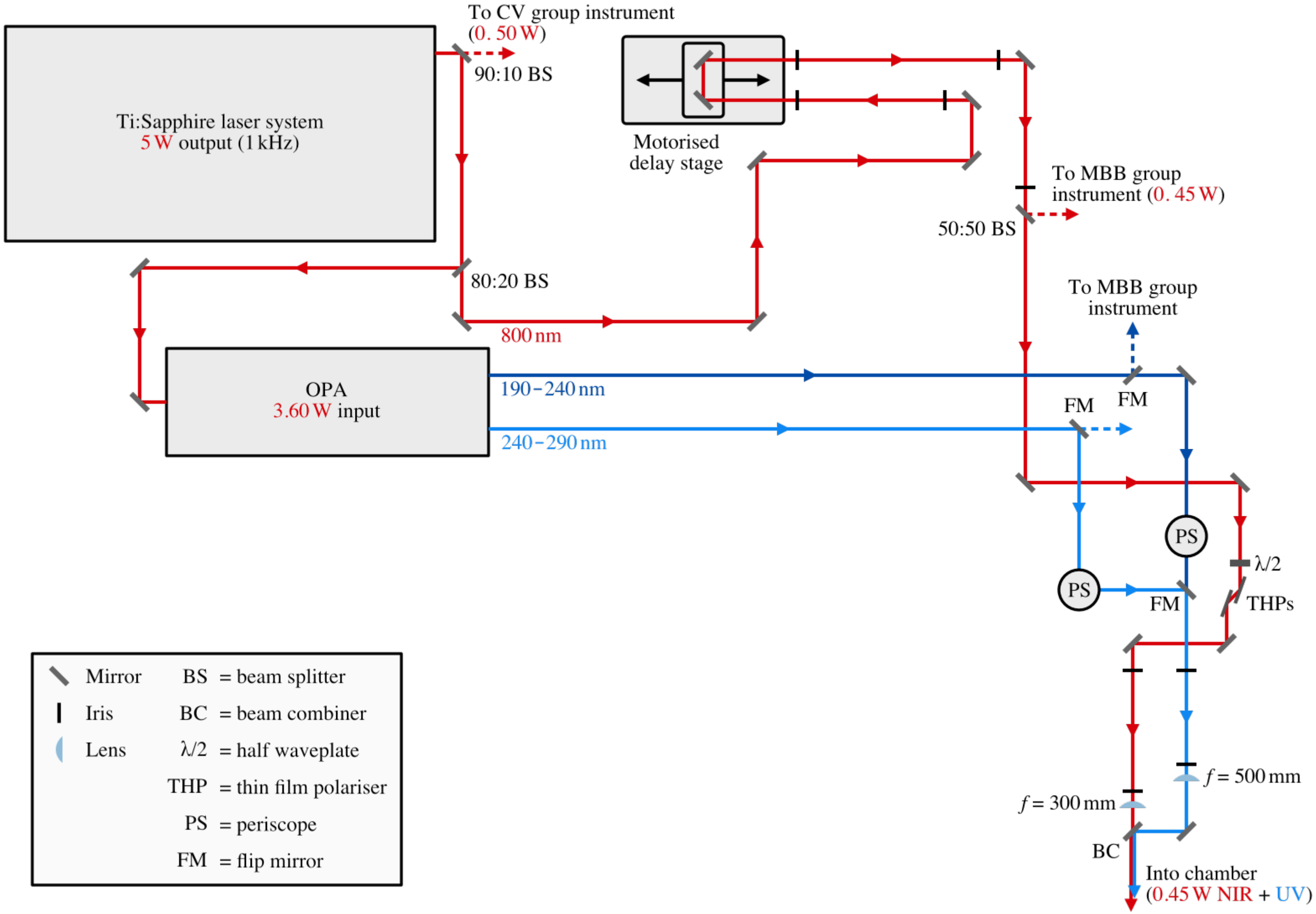

Figure 2.15: Schematic of the ultrafast laser system and the optical setup that couples it to the Oxford spectrometer. The output beam of the OPA originates from one of two ports depending on the selected wavelength, hence there are two parallel UV beam lines, with only one in use at any time.

SFI. The bulk of the NIR beam (3.6 W) is used to pump an Optical Parametric Amplifier (OPA) (Spectra Physics TOPAS Prime), a tunable light source that can generate wavelengths from 190–2600 nm through non-linear frequency mixing.

Inside the OPA, the input beam is split and a small section is used to drive white light generation by focusing into a piece of glass to produce self-phase modulation. In the pre-amplifier the white-light beam is overlapped with another section of the input beam in a non-linear crystal. Selective amplification of a specific wavelength is achieved by changing the relative delay of the two beams and adjusting the angle of the crystal for optimum phase-matching. This process produces a weakly amplified signal beam and an idler beam. A second amplifier follows, pumped by the bulk of the input beam. The signal beam is tunable from 1160-1600 nm, and accordingly, the idler beam from 1600-2600 nm. A tunable output in the UV/visible wavelength region is attained by non-linear frequency mixing of the signal, idler and residual input beams. Tuning of the output wavelength is done entirely by motorised stages within the OPA, controlled by proprietary software. Select optical elements must be interchanged manually to access different wavelength ranges.

To adjust the time delay between the UV and NIR pulses, the path length of the NIR beam is varied using a computer-controlled delay line stage (Newport DL125). NIR pulses are focused into the spectrometer by a 300 mm focal length, 2 mm thick plano-convex UV fused silica lens (Eksma Optics). Control over the pulse energy is provided by a variable attenuator (Eksma Optics), comprising a half waveplate and a pair of thin-film polarisers. Rotation of the waveplate provides continuous variation of the beam's polarisation direction. The thin-film polarisers reflect horizontally polarised light whilst transmitting the vertically polarised light. A calibration between NIR pulse energy and peak intensity was established based on the observed ponderomotive shift of the ATI peaks in the photoelectron spectra of Ar, recorded at a series of pulse energies. This procedure is described in Appendix A.

UV pulses are focused into the spectrometer by a 500 mm focal length, 2.4 mm thick plano-convex CaF_2 lens (Thorlabs). Because focal length is a function of wavelength, the CaF_2 lens is mounted on a linear translational stage so that the focus can be shifted to overlap spatially with the focal point of the NIR beam. Depending on the frequency mixing process required, output pulses either come out of one port of the OPA horizontally polarised, or a second port vertically polarised. Vertically polarised pulses are directed through a linear periscope which leaves their polarisation unchanged, whilst horizontally polarised pulses are transmitted through a right-angle periscope which swaps their polarisation. The two beam lines then converge onto the same path before the focusing lens.

UV and NIR pulses are overlapped through use of a dichroic mirror (Eksma Optics) by transmitting the NIR beam through the rear face, and reflecting the UV beam off the front face. Finally, the overlapped beams pass into the vacuum chamber via a 1 mm thick CaF_2 window (Crystran). In Section 2.8 measurements carried out to characterise the ultrafast pulses inside the chamber are described. This includes the spectral and temporal widths of the NIR pulses, and the cross-correlation of the NIR and UV pulses, which corresponds to the time resolution of the instrument for probing molecular dynamics.

Ion detector

The detection assembly comprises a pair of 75 mm diameter chevron-stacked MCPs coupled to a P47 phosphor screen (Photonis USA). The MCPs pores are 25 μm in diameter with a centre-to-centre spacing of 32 μm, for an OAR of 55%. Each ion impact on the detector generates a flash of light which is imaged by a PImMS2 camera. This stores the 2D position and time of each event with a timing precision of 25 ns. The PImMS2 camera operates at 10 Hz with all four memory registers of every pixel enabled, allowing each to record up to four events per acquisition cycle. By reducing the number of memory registers per pixel to 3, 2 or 1 the camera can be run at 20, 25 or 40 Hz.

The current from the back face of the rear MCP is measured using an oscilloscope (Lecroy DDA260) to provide a high resolution ToF trace. In order to separate the high frequency signal due to ion impacts from the high voltage DC current given to the MCP, a custom built decoupler with a high bandpass filter is used.[131]

Fundamentally, the time resolution of this measurement should correspond to the subnanosecond resolution of the MCPs. Practically, it remains limited by the response time of the electronics and the analogue to digital converter of the oscilliscope.

A high voltage pulse generator (DEI PVM-4150) connected to the front face of the front MCP allows it to be pulsed from ground to several hundred volts within 25 ns. By decreasing the gain across the front MCP the detection efficiency of ions is drastically reduced. This is used to selectively 'gate' the detector off at the time of arrival of undesired species, either to avoid saturation of the PImMS2 camera, or simply to prevent deterioration of the MCPs.

Relative timing control

The operation of the instrument requires numerous devices to be precisely coordinated with one another. This includes the timings of the Ti:Sapphire laser system, the pulsed solenoid valve, the front MCP pulse and the PImMS2 camera. The timeline of events that occurs upon every experimental cycle is outlined in Figure 2.16. The relative timings are controlled by a delay pulse generator (Quantum Composer 9520 series). The laser system acts as the 'clock' for the experiment which triggers the delay pulse generator each time it pulses. It therefore also controls the repetition rate for the experiment. The 1 kHz repetition rate of the Solsitce Ace must be divided to accommodate for the limited capabilities of the other components. The pulsed solenoid valve operates at a maximum rate of 250 Hz, but the limiting component is the PImMS2 camera which tops out at 40 Hz under special conditions. Regularly, it is run at 10 or 20 Hz.

The delay pulse generator first triggers the pulsed valve so that the molecular beam intersects with the laser pulse(s). The precise timing offers control over what section of the molecular beam is photoexcited. Towards the front of the expansion molecules are internally coldest, but the experimental signal is less due to lower density, and fluctuates more due to the timing jitter of the pulsed valve. Second the delay pulse generator turns on the PImMS2 camera in time for the arrival of the ions at the detector. Finally, the front face of the front MCP is pulsed to gate the detection of any unwanted ion species. The pulse on-set and duration dictates the time window over which the detector is inactive, allowing for either a single ion species or several to be gated out.

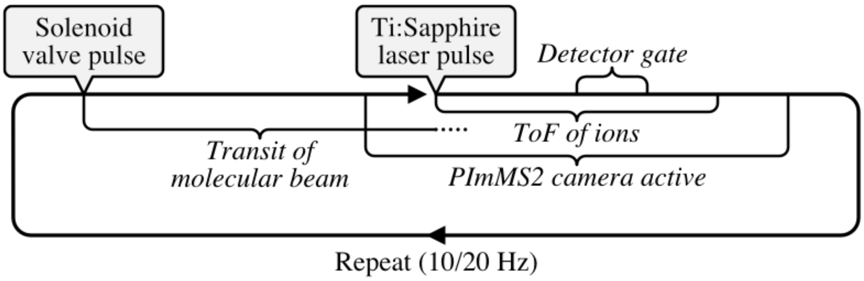

Figure 2.16: The sequence of events that occurs on every experimental cycle. The relative timing of events is controlled by a delay pulse generator. The 'clock' for the experiment is provided by the laser system, which triggers the delay pulse generator on each cycle.

In general, electronic devices such as the delay pulse generator are only capable of precisely controlled timing down to the nanosecond timescale. This is why the delay between the pump and probe femtosecond laser pulses needs to be independently controlled by an analogue method, *i.e.* a delay line stage.

2.6.2 PULSAR

The eighth chapter of this thesis reports work carried out in the James R. Macdonald Laboratory at Kansas State University, in collaboration with the research group of Prof. Daniel Rolles. Experiments made use of the Prairie Ultrafast Light Source for Attosecond Research (PULSAR), a state of the art custom Ti:Sapphire laser system that pulses at a repetition rate of 10 kHz.[132] This negates the issue of how long data collection can take at a low ion count rate, allowing otherwise prolonged coincidence imaging experiments to be conducted on a practical time scale.

The laser system is coupled to a COLTRIMS spectrometer. A schematic slice of the apparatus perpendicular to the ToF axis is shown in Figure 2.17. A continuous supersonic molecular beam is produced by expanding neat gaseous sample through a 30 μm diameter nozzle, followed by a 0.2 mm skimmer. The molecular beam is then further collimated by two downstream apertures of 1 and 2 mm diameter. Finally, a pair of externally adjustable slits, used to 'cut' the molecular beam, provide control over the width of the molecular beam in the interaction region.

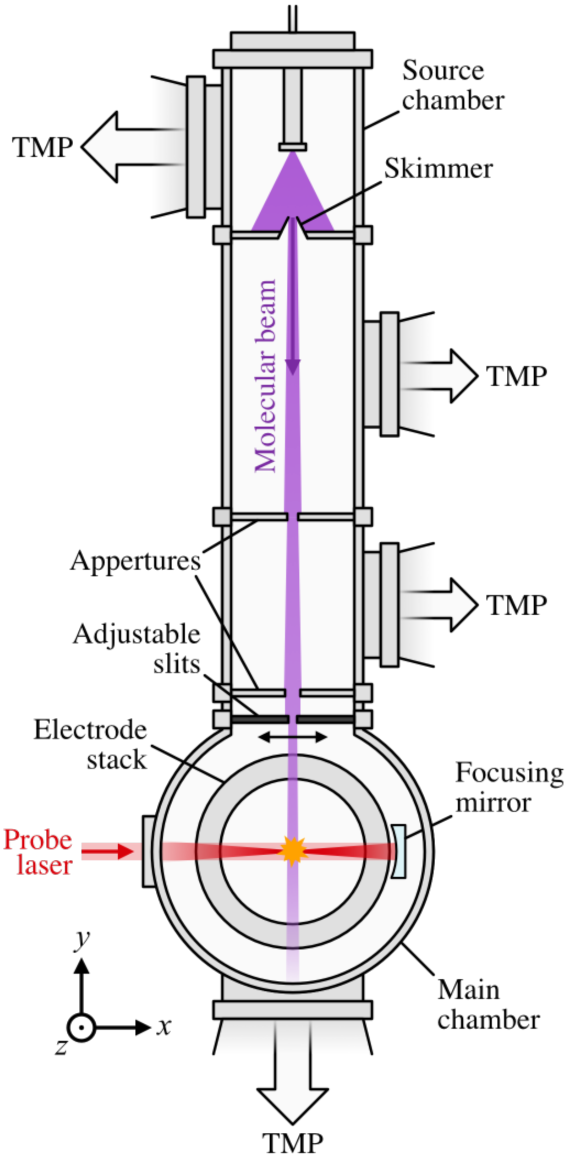

Figure 2.17: Schematic cross section of the COLTRIMS spectrometer in the James R. Macdonald laboratory. The electrode stack is not fully illustrated and the twin detectors are omitted as these components lie along the axis normal to the page. Details are provided in the text.

The combination of the skimmer and two apertures divides the instrument up into four differentially pumped regions. This is necessary to maintain UHV in the main chamber when gas is being expanded through the nozzle, raising the pressure in the source chamber to $\sim 10^{-5}$ mbar. The pressure is reduced to $\sim 10^{-7}$ mbar and then ∼10^{-9} mbar across the two intermediate chambers, and is maintained at a base pressure of 4×10^{-10} mbar in the main chamber. To reach such a low base pressure special tactics are adopted. The walls of the chamber are heated to >100°C for several days to desorb strongly bound species, such as H_2O. The TMPs mounted on the instrument are backed by a small $80\,\mathrm{l\,s^{-1}}$ TMP, which is in turn backed by a conventional roughing pump.

A 75 mm focal length concave mirror mounted inside the main chamber is used to focus laser pulses, which cross the molecular beam in a perpendicular geometry at the centre of the COLTRIMS spectrometer. The electrode stack is not fully illustrated and twin detectors are omitted in Figure 2.17 as these components lie along the axis normal to the page. An illustration from a side-on perspective is given in Figure 2.10. The uniform electric field generated by the electrode stack points out of the page and accelerates nascent ions in this direction onto one detector. Electrons are accelerated in the opposite direction (into the page) onto a second detector.

Optical laser system

PULSAR is a custom built Ti:Sapphire laser system. Seed pulses produced by a Kerr-lens passive mode-locked oscillator (KM Labs) are amplified in a two-stage multipass amplifier, pumped by a Nd:YLF laser. The system produces 2 mJ pulses at a repetition rate of 10 kHz with a nominal temporal duration of 21 fs and a central wavelength around 790 nm.[132] Characterisation of fundamental output pulses is performed using a Second Harmonic Generation (SHG) Frequency-Resolved Optical Gating (FROG),[133] as described in Section 2.8.1.

Harmonics of the NIR output are produced by sum frequency generation in Beta Barium Borate (BBO). The second harmonic (395 nm) is generated from doubling the fundamental. Mixing the second harmonic and fundamental produces the third harmonic (263 nm), and mixing the third harmonic and fundamental generates the fourth harmonic (198 nm). The duration of fourth harmonic pulses was characterised using a cross-correlation FROG,[134] which relies on a difference frequency generation process between the fourth harmonic and fundamental.

Ion detector

Only the ion detection system is described here as the electron detector was not used in the experiments presented in Chapter 8. The ion detector consists of a triple Z-stack of 80 mm funnel MCPs, mounted in front of a two-layer DLA detector. The analog signals from each of the four DLA terminals and the front MCP are first amplified and then fed into Constant Fraction Discriminators (CFDs). These devices are important for providing a timing output that is independent on the height of the original signal, *i.e.* the intensity of the ion event. The outputs of the CFDs are recorded by a multichannel time-to-digital converter which registers the timing information on an event-by-event basis. The signal from a photodiode triggered by the laser pulse provides a reference that all the other timing signals are measured with respect to.

The 2D spatial coordinates of an event are reconstructed from the DLA signals and the accurate arrival time determined from the MCP signal, permitting reconstruction of the complete 3D momentum information for each ion. Details on the calculation of the $(x,\ y)$ coordinates and 3D momentum calibration are given in Sections 2.7.1 and 2.7.2.

2.6.3 SACLA

Chapter 5 presents work conducted at the soft X-ray beamline (BL1) of the Spring-8 Angstrom Compact free electron LAser (SACLA) in Hyogo, Japan.[135] At this beamline users are required to provide their own instruments. For the beamtime, a double sided VMI spectrometer was provided by the group of Prof. Kyioshi Ueda.[136] Similar to a COLTRIMS spectrometer, this instrument is designed to image ions and electrons simultaneously by accelerating them in opposite directions onto two different detectors. A minimalist diagram of the key components is shown in Figure 2.18.

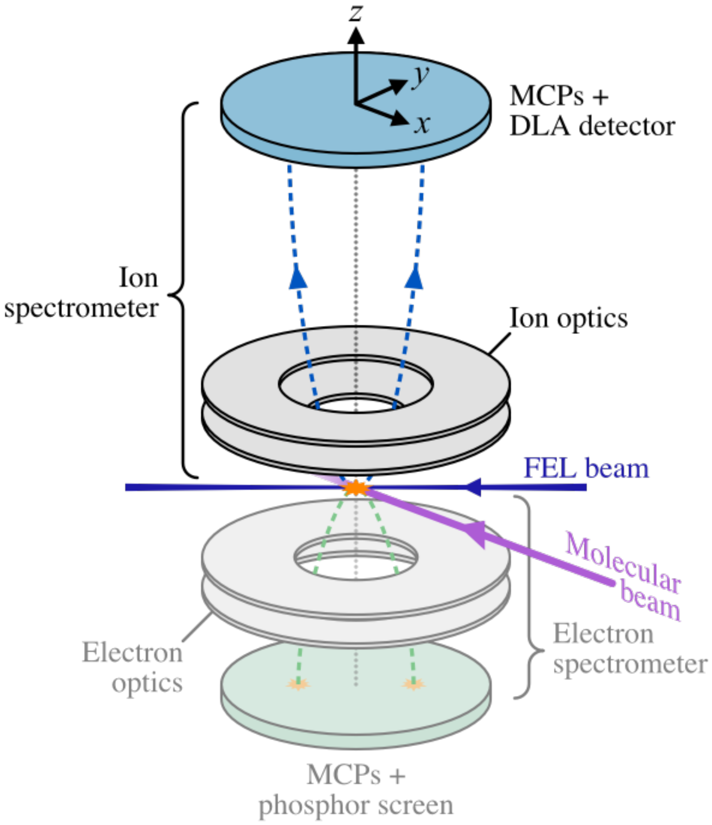

Figure 2.18: The key components of the experimental setup at SACLA. The molecular beam and FEL beam cross at 45° inside the spectrometer. The resulting ions (*blue*) and electrons (*green*) are accelerated in opposite directions and velocity mapped onto separate detectors. Note that the electron spectrometer side of the instrument (*faded*) was not used in the experiments described here.

Unseeded gaseous sample is expanded through a pulsed solenoid valve (Parker Series 9 Pulse Valve) and skimmed to form a supersonic molecular beam. In the centre of the spectrometer, the pulsed molecular beam is intersected at 45° by FEL pulses, focused using a pair of Kirkpatrick-Baez mirrors.[137] The instrument is orientated vertically with the ToF axis perpendicular to the direction of travel of the molecular beam. Ions are extracted upwards, fly through a long drift tube, and are velocity mapped onto a pair of MCPs coupled to a hexagonal DLA detector. Electrons are accelerated down a shorter drift tube and velocity mapped onto a second detector, comprising a pair of MCPs attached to a phosphor screen and a CCD camera.

Free-electron laser

The soft X-ray beamline at SACLA was commissioned in 2016 and produces XUV pulses with a photon energy ranging from 40-150 eV.[135] Pulses are produced at a rate of 60 Hz, have an average bandwidth of 2% of the photon energy, and a pulse duration of approximately 30 fs.[138] Owing to the SASE process, significant shot-to-shot variation occurs in various spectral properties of the pulses. An array of instrumentation is used to record different fluctuating parameters. Most relevant to the current experimental work is the gas intensity monitor, used to record the energy of each pulse. This is a chamber filled with a dilute quantity of rare gas that XUV pulses pass though en route to the spectrometer. Approximately 95% of the incident pulse energy is transmitted. The ion current due to photoionisation of the rare gas is measured and converted to pulse energy.

Ion detector

Only the ion detection system is described in detail here as electrons were not recorded in the experiments presented in Chapter 5. It consists of a pair of 120 mm diameter chevron-stacked MCPs mounted to a three-layer hexagonal DLA detector. This records the (x, y) spatial position and arrival time of ion hits with high precision, permitting reconstruction of the complete 3D momentum information for each ion.

Uniquely, the multi-hit capacity of the detection system is enhanced beyond the normal limit of a DLA detector using a combination of the redundant information and a sophisticated logic to increase the number of possible hit event extractions.[139] Instead of processing the signals from the DLAs using CFDs and a time-to-digital converter, the six signals from the three DLAs, as well as the current trace directly from the rear MCP, are read using a multichannel digitizer and processed using software resembling a CFD. This method increases the redundancy in the dataset. The signal for each hit event needs to be resolved in only four of the seven readouts to reconstruct the $(x,\ y,\ t)$ coordinates of the ion, allowing a virtually dead-time free measurement of up to 100 ions per FEL laser shot.

2.7 Post-processing

The raw experimental signals recorded by an ion imaging detector need to be processed in two stages to obtain the momenta of the measured ions. The first step is hit finding to determine the precise $(x,\ y)$ coordinates at which each ion impacted the detector. The second is to convert those 2D spatial coordinates to the components of the ion's transverse momentum, and if possible, its arrival time to longitudinal momentum.

2.7.1 Hit finding

Pixelated detectors

Each flash of light on a phosphor screen typically illuminates several pixels of a time-stamping camera. The result is a cluster of multiple $(x,\ y,\ t)$ events recorded by the camera which correspond to each ion event. An example is depicted in the first panel of Figure 2.19. To assign each ion event a single $(x,\ y,\ t)$ coordinate, a centroiding algorithm is applied that identifies all of the pixels illuminated in a cluster, and then calculates their centre. This process is illustrated in the subsequent panels of Figure 2.19.

Beginning from a single pixel event, the algorithm identifies all others belonging to the same cluster by a search of the eight nearest neighbours, as shown in blue. This is repeated for each pixel added to the cluster, until no more neighbours are found. As it searches, the algorithm works through events by ascending timebin and only includes those that occur within a specified timing window. Pixels are usually illuminated over a spread of timebins, due to the roughly Gaussian profile of flashes on the phosphor screen. Pixels close to the centre of the cluster receive a higher photon flux and therefore exceed the triggering threshold earlier than those at the fringes. For post-processing of data recorded on the Oxford spectrometer, a time window of 7 PImMS2 timebins (175 ns) was used, which approximates the decay time of the P47 phosphor screen.

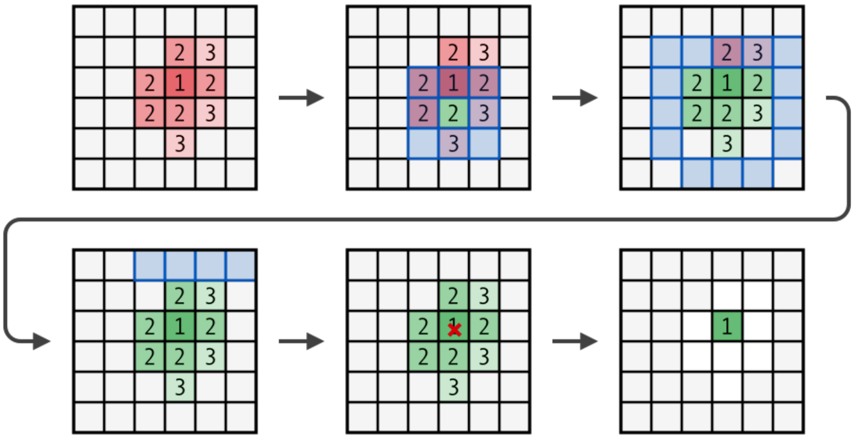

Figure 2.19: Simplified picture of the centroiding process applied to data recorded by a pixelated time-stamping camera, such as the PImMS2 camera. Each pixel is labelled by the relative timebin when it was triggered, where 1 refers to the earliest timebin in the cluster. A nearest neighbours search algorithm, shown in blue, is used to identify all of the pixels triggered by the hit event. The $(x,\ y)$ coordinates of the cluster is assigned using Equation 2.2 and t from the earliest timebin in the cluster.

Once all of the N events that make up a cluster have been identified, x and y centres are calculated using an average of the coordinates of each pixel, weighted by the time when they were triggered:

$$x = \frac{\sum_{i=1}^{N} x_i/t'_i}{\sum_{i=1}^{N} 1/t'_i}, \tag{2.2a}$$

$$y = \frac{\sum_{i=1}^{N} y_i/t'_i}{\sum_{i=1}^{N} 1/t'_i}. \tag{2.2b}$$

x_i and y_i are the spatial coordinates of the ith event and t'_i is its timebin, relative to the timebin of the earliest event in the cluster (t_0):

$$t'_i = t_i - t_0 + 1. \tag{2.3}$$

This method gives increased weight to the earliest events within a cluster, which are presumed to be closest to the centre of the ion impact. In this way, the timing information acts as a proxy for the absent intensity information. Since the earliest a pixel can detect an ion event is the actual time of the ion hit on the detector, the earliest time code within a cluster is necessarily the most accurate. Hence, t_0 is assigned as the timebin of the centroided event.

Delay-line anode detectors

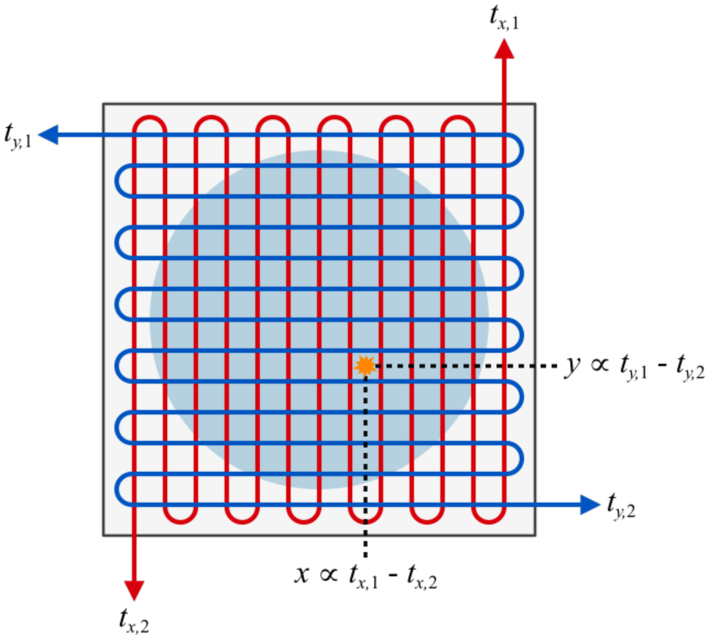

Figure 2.20: The conventional DLA detector comprising of two delay lines. The vertically wound (*red*) and horizontally wound (*blue*) delay lines determine the x and y spatial positions of an ion impact, respectively. $t(x_1), t(x_2)$ and $t(y_1), t(y_2)$ denote the time signals recorded at the four terminals.

For a conventional two-layer DLA detector of the type shown in Figure 2.20, the vertically (*red*) and horizontally (*blue*) wound delay lines are used to determine the position of a hit event along x and y, respectively. When an avalanche of secondary electrons from the back face of the rear MCP impacts the DLA detector it generates an electrical pulse in each delay line, which propagates towards both ends of the wire. The current measured at each terminal is processed using a CFD to determine an arrival time. The spatial coordinate of the event in each dimension can be uniquely determined from the difference between the arrival time at the terminals of each delay line:

$$x \propto t_{x,1} - t_{x,2}, \tag{2.4a}$$

$$y \propto t_{y,1} - t_{y,2}. \tag{2.4b}$$

In addition, the total time taken for the signal to travel to both ends of a delay line ($t_{x,1} + t_{x,2}$ or $t_{y,1} + t_{y,2}$) is proportional to the length of the wire. It should therefore be constant for each delay line. This restriction is used eliminate false events by discarding any with a time sum outside of a narrow predetermined range. The time of an event (t) can be calculated from the average of the timing signals:

$$t = \frac{t_{x,1} + t_{x,2} + t_{y,1} + t_{y,2}}{4}, \tag{2.5}$$

but is also often determined by measuring the current trace directly from the MCPs.

2.7.2 Momentum calibration

Two-dimensional velocity-map imaging

In a VMI spectrometer, the radius (r) at which an ion is focused onto the detector is related to the magnitude of its velocity in the detector plane (v_{xy}) by:

$$r \propto \sqrt{\frac{{}^{1}\!/_{2}\, m {v_{xy}}^2}{q V_{\mathrm{R}}}}. \tag{2.6}$$

Or in terms of a fragment's in-plane momentum (p_{xy}):

$$r \propto \sqrt{\frac{1}{2 m q V_{\mathrm{R}}}}\, p_{xy}, \tag{2.7}$$

where m and q are the ion's mass and charge, and V_{R} is the voltage on the repeller plate. The components of an ion's transverse momentum ($p_x,\ p_y$) can therefore be calculated from its 2D impact coordinates ($x,\ y$):

$$p_x = \alpha\sqrt{2mqV_\mathrm{R}}\,(x - x_0), \tag{2.8a}$$

$$p_y = \alpha\sqrt{2mqV_\mathrm{R}}\,(y - y_0), \tag{2.8b}$$

where $(x_0,\ y_0)$ is the coordinates of the centre of the velocity distribution for the ion species of interest, *i.e.* the position where an ion with zero in-plane momentum is focused, and α is a radius to momentum conversion factor with units of pixels^{-1}.

For the Oxford spectrometer, the absolute KE scale of the velocity-map images was calibrated based on the ATI peaks in the photoelectron spectra of Ar, which are spaced by the photon energy. Details are provided in Appendix A.

Three-dimensional velocity-map imaging

The calibration between $(x,\ y,\ t)$ coordinates and 3D momentum for the spectrometer employed in the experiments at SACLA was established using SIMION.[140] This is a software package specifically designed for calculating the electric fields produced by ion optics, and simulating ion trajectories in those fields. Using the fact that $t \propto \sqrt{m/qV_\mathrm{R}}$ for a VMI spectrometer, the equations for the components of an ion's momentum parallel to the plane of the detector can be expressed in terms of its $(x,\ y,\ t)$ coordinates:

$$p_x = \alpha m\left(\frac{x - x_0}{t - t_0}\right), \tag{2.9a}$$

$$p_y = \alpha m\left(\frac{y - y_0}{t - t_0}\right). \tag{2.9b}$$

t_0 is the centre of the ToF distribution for the ion species of interest, *i.e.* the ToF of an ion with zero momentum perpendicular to the plane of detector. α is a constant extracted from the SIMION calibration. The component of an ion's momentum perpendicular to the detector is determined directly from its ToF:

$$p_z = \beta q(t - t_0), \tag{2.10}$$

where β is another constant extracted from the SIMION calibration.

COLTRIMS

The uniform electric field in a COLTRIMS spectrometer is parallel to the ToF (z) axis, and so does not affect the transverse velocities of the nascent ions. The motion of the ions in the xy-plane is field free, hence the radius at which an ion impacts the detector is given by:

$$r - r_0 = v_{xy}(t - t_0), \tag{2.11}$$

or in terms of a fragment's in-plane momentum:

$$r - r_0 = \frac{p_{xy}}{m}(t - t_0), \tag{2.12}$$

where r_0 is centre of the distribution of the ion species of interest on the detector, *i.e.* the position where an ion with zero in-plane momentum will impact. Rearranging, the components of an ion's transverse momentum can be calculated from its (x, y, t) coordinates:

$$p_x = m\left(\frac{x - x_0}{t - t_0}\right), \tag{2.13a}$$

$$p_y = m\left(\frac{y - y_0}{t - t_0}\right). \tag{2.13b}$$

Perpendicular to the plane of the detector, the ions experience a constant acceleration under the electric field (E). The equation of motion in this direction is:

$$L - z_0 = v_z(t - t_0) + \frac{qE}{2m}(t - t_0)^2, \tag{2.14}$$

where L is the length of the spectrometer and z_0 is the initial displacement in the z-direction, which together define the distance from the interaction region to the detector. Substituting $E = V_\mathrm{R}/(L - z_0)$ and rearranging provides an equation for the z component of an ion's momentum in terms of its ToF, and various constants of the instrument:

$$p_z = \frac{m(L - z_0)}{t - t_0} - \frac{qV_\mathrm{R}}{2(L - z_0)}(t - t_0). \qquad (2.15)$$

2.8 Characterisation of a TR-CEI apparatus

This chapter finishes with an account of the preliminary experiments carried out as part of the commissioning of the new TR-CEI instrument at the University of Oxford. Though the Oxford spectrometer itself has been operational for many years, dedicated work with the Ti:Sapphire femtosecond laser system coincided with the start of the work of this thesis. First, the characterisation of the ultrafast laser pulses is described, before results from a first TR-CEI experiment are presented.

2.8.1 NIR pulse characterisation

Temporal characterisation of the laser pulse(s) is a crucial aspect of a TR experiment. The pulse duration(s) will determine the time resolution of the measurement and therefore the shortest timescale on which chemical change can be resolved. For the specific case of TR-CEI, it also important to characterise the duration of the probe pulse to assess how it might influence the Coulomb explosion dynamics. As discussed in Section 1.4.1, an extended probe pulse duration can complicate the extraction of nuclear structural information.

The fundamental issue with measuring the duration of an ultrafast laser pulse is that it requires a method with a femtosecond time resolution. This is beyond the capabilities of any electronic measurement technique, as even the fastest photodiodes available have a response time on the order of picoseconds. The solution is to use the ultrafast pulse to measure itself – an approach known as autocorrelation[38]. Fundamentally, this involves splitting the pulse into two halves, delaying one half relative to the other using a longer path length, and then recombining the two pulses in a rapidly responding non-linear medium to generate the second harmonic of the input pulse.

By scanning one pulse through the other, the intensity of the SHG signal will vary as a function of their relative delay. Provided the shape of the input pulse is known, the intensity profile of fundamental input pulse can be determined from the measured intensity profile of the second harmonic output pulse. The pulse duration is equal to the Full Width at Half Maximum (FWHM) of the intensity profile. If the input pulse has a Gaussian profile, the pulse duration of the input pulse (τ_i) and output pulse (τ_o) are related by:

$$\tau_o = \sqrt{2}\,\tau_i. \tag{2.16}$$

The instrument built specifically to characterise the NIR pulses from the Ti:Sapphire laser system is a SHG-FROG.[141] The non-linear medium used for SHG is a BBO crystal. In principle, a FROG measurement is a spectrally resolved autocorrealtion, *i.e.* rather than using a photodiode to measure to intensity of the delay-dependent SHG signal, a spectrometer is used to recorded the SHG spectrum as a function of delay. The result is an intensity map as a function of both delay and wavelength, as seen in Figure 2.21(a). The key advantage of a FROG measurement is that any chirp of the pulse is apparent in the shape of the trace. When the pulse is transform limited all of the wavelengths overlap in time (delay) to produce a symmetric trace. But if the pulse is chirped, the various frequency components do not arrive simultaneously, giving a diagonally distorted trace.

The SHG-FROG trace in Figure 2.21(a) was recorded for the fundamental output of the Ti:Sapphire laser system. The measurement must be performed on the laser table, so in order to accurately predict the pulse duration at the interaction region of the spectrometer, any optics in the beam path that are bypassed need to be emulated. The laser beam was picked off before the focusing lens and transmitted through three windows en route to the SHG-FROG. These were of the correct material and thickness to replicate the focusing lens, dichroic mirror and chamber window, respectively.

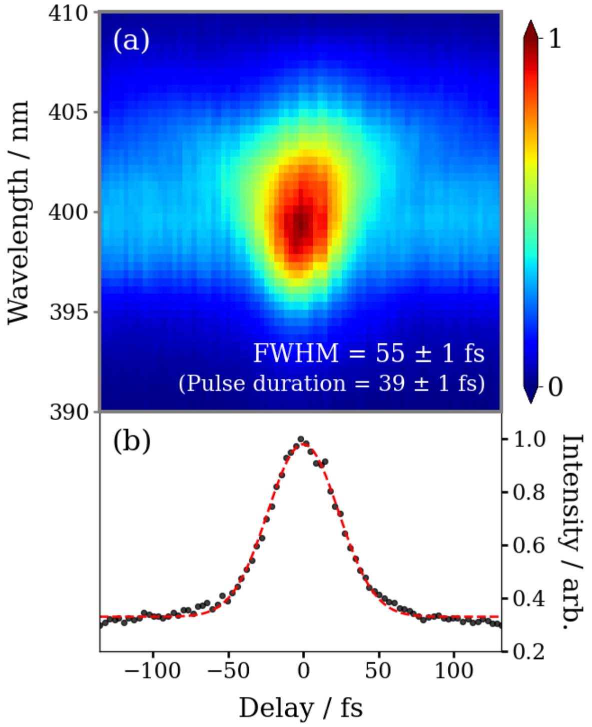

Figure 2.21: (a) SHG-FROG trace and (b) wavelength-integrated trace for the fundamental output of the Ti:Sapphire laser system coupled to the Oxford spectrometer. Measured using optics that emulate the beam path to the interior of the chamber. A Gaussian fit (*red dash*) to the wavelength-integrated trace yields a FWHM of 55 ± 1 fs, corresponding to a pulse duration of 39 ± 1 fs, where the error represents the standard error on the fitted parameter.

Figure 2.21(b) displays the intensity profile of the SHG signal, obtained by integrating the wavelength region of interest in panel (a). Fitting the transient enhancement to a Gaussian function yields a value of $\tau_o = 55 \pm 1\,\text{fs}$, where the uncertainty in the value reflects the standard error on the FWHM of the fitting. Using Equation 2.16, this corresponds to a pulse duration of the NIR pulse ($\tau_{800\,\text{nm}}$) of 39 ± 1 fs, slightly above the nominal 35 fs pulse duration for the amplifier.

2.8.2 UV pulse characterisation

To characterise the duration of the UV pulses generated by the OPA, a different method is required. It generally is not possible to measure a UV pulse using autocorrelation as the wavelength of second harmonic will be too short to measure, either because it is absorbed by the non-linear medium, or because it is not detectable by a conventional spectrometer. Several other methods have been developed to circumvent these issues, such as the cross-correlation FROG[134] and self-diffraction FROG.[142] In the present work, the duration of the UV pulse was characterised *in-situ* by performing non-resonant, two-colour multiphoton ionisation of H_2O with the UV and NIR pulses.

For the preliminary experiments described here, the OPA was tuned to generate light with a central wavelength of 258 nm. The TR yield of H_2O^+ measured directly by the spectrometer was recorded as a function of the time delay between the 258 nm and 800 nm pulses. The resulting cross-correlation trace is shown in Figure 2.22. Fitting the transient enhancement to a Gaussian function yields a cross-correlation width (τ_{xcor}) of 161 ± 7 fs, where the uncertainty in the value reflects the standard error on the FWHM of the fitting.

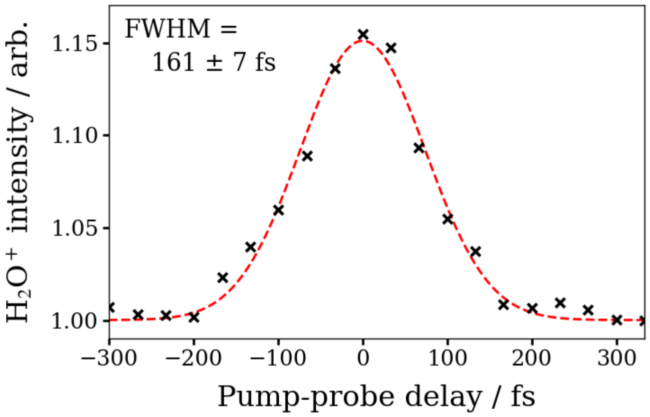

Figure 2.22: Cross-correlation trace of the UV (258 nm) and NIR (800 nm) pulses. Measured inside the Oxford spectrometer via two-colour multiphoton ionisation of H_2O^+. A Gaussian fit (*red dash*) to the time-dependent H_2O^+ signal yields a FWHM of 161 ± 7 fs, where the error represents the standard error on the fitted parameter.

A lower limit of the pulse duration of the UV pulse ($\tau_{258\,\mathrm{nm}}$) can be estimated based on the cross-correlation width and the pulse duration of the NIR pulse:

$$\tau_{\mathrm{xcor}}{}^2 = \tau_{800\,\mathrm{nm}}{}^2/n + \tau_{258\,\mathrm{nm}}{}^2, \tag{2.17}$$

where it is that assumed a single UV photon and n NIR photons are absorbed in the ionisation process. Based on the first ionisation potential of H_2O of 12.62 eV[143] and the 258 nm photon energy (4.81 eV), a further five 800 nm (1.55 eV) photons are required to create H_2O^+. Inputting $n = 5$ into Equation 2.17 yields a value of $\tau_{258\,\mathrm{nm}} = 160 \pm 7\,\mathrm{fs}$. This is nearly equal to $\tau_{\mathrm{x}cor}$, which reflects the fact that duration of the NIR pulse is significantly shorter than the duration of the UV pulse.

The extracted $\tau_{258\,\mathrm{nm}}$ slightly exceeds the range of 60-150 fs quoted for the output pulse duration in the manufacturer specifications for the TOPAS prime. Only a range can be provided as the transform limit of the output pulses from the OPA varies as a function of the central wavelength due to the different non-linear frequency mixing processes involved. The transform limit at the generated wavelength can be accurately determined be measuring the spectral bandwidth. Even so, the pulse duration of the UV pulse is expected to exceed the transform limit due to dispersion, mainly from propagation through the focusing lens and entrance window on the spectrometer.

2.8.3 Case study: Ultraviolet photodissociation dynamics of methyl iodide

Methyl iodide (CH_3I) is a model system for understanding gas phase molecular photodissociation dynamics. The molecule has been the focus of countless experimental and theoretical studies over a period spanning several decades.[10–12,99,144–150] More recently, the ultraviolet photodissociation of CH_3I has become a popular subject in the field of TR-CEI.[50,52,66,67,151,152] Previous studies have extensively characterised the dissociation dynamics, which makes it an excellent system for testing the functionality of the new TR-CEI apperatus in the laboratory at the University of Oxford.

The first absorption band of CH_3I (the A-band) results from excitation of a non-bonding valence electron of the iodine atom to the lowest anti-bonding molecular orbital, which prompts rapid C-I bond cleavage. The A-band spans from 220-350 nm and comprises three dipole-allowed transitions to repulsive electronic states, labelled $^1Q_1$, $^3Q_0$ and $^3Q_1$.[144,145] The pump wavelength selected for this study was 258 nm, at the absorption cross section maximum of the A-band. The dominant transition at 258 nm is to the $^3Q_0$ state, resulting in dissociation into a CH_3 radical and an iodine atom in its spin-orbit excited state ($^2P_{1/2}$). During dissociation, a fraction of the excited state population can transfer to the $^1Q_1$ state via a curve crossing, producing a CH_3 radical and an ground state iodine atom ($^2P_{3/2}$). The branching ratio between I*($^2P_{1/2}$) and I($^2P_{3/2}$) depends on the exact excitation wavelength.[144]

A ~10% mixture of CH_3I was prepared by diluting its room temperature vapour pressure in helium gas, up to a pressure of 3 bar. The resulting mixture was expanded into the Oxford spectrometer to produce a supersonic molecular beam, which was intersected by the 258 nm output of the OPA and 800 nm fundamental output of the Ti:Sapphire laser system. The spectrometer was operated in crush VMI mode, with voltages of 8.00 and 6.02 kV applied to the repeller and extractor electrodes, respectively, and the other two electrodes held at ground. Ion images were recorded for regular pump-probe delay steps of 66.7 fs across a range from −0.8 to 3.2 ps, where positive delay corresponds to the UV pulse arriving before the NIR pulse, and vice versa. The position of time zero was established based on the cross correlation peak in the yield of H_2O^+. At each pump-probe delay, data were acquired over ~500 laser shots.

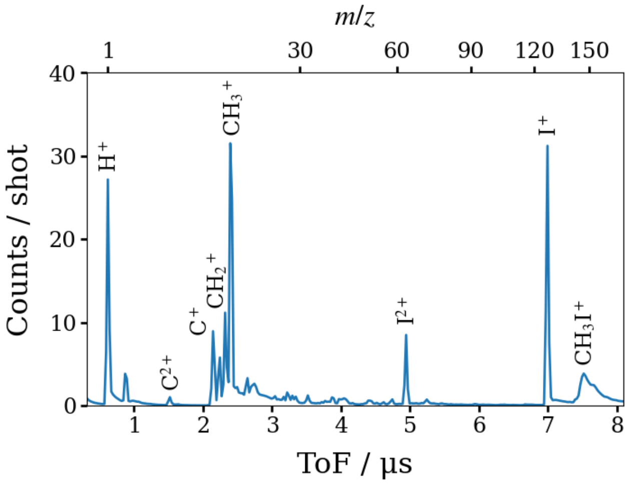

Figure 2.23: Ion ToF spectrum of methyl iodide exposed to an UV (258 nm) laser pulse and an intense NIR (800 nm) laser pulse. Summed over all relative delays of the two laser pulses. Unlabelled peaks are background gases.

Figure 2.23 shows the ion ToF mass spectrum recorded by the PImMS2 camera, summed over all relative delays of the two laser pulses. The analysis here will focus on the CH_3^+ and I^+ ions, which are the two most prominent fragments. Ion images are obtained by integrating the $(x,\ y)$ data over the ToF range of the peak of interest, and over the delay range of interest. Raw ion images of CH_3^+ and I^+ when the NIR pulse precedes the UV pulse (UV early), and when the UV pulse far precedes the NIR pulse (UV late), are presented in left column of Figure 2.24. In the adjacent column are Abel inverted ion images,[102] processed using the pBASEX algorithm.[153] Time-dependent features that arise from C-I bond dissociation by the UV pulse prior to ionisation by the NIR pulse are indicated by arrows. The features are more easily observed in the CH_3^+ images because the majority of KE released by dissociation is partitioned into this cofragment, rather than the much heavier iodine.

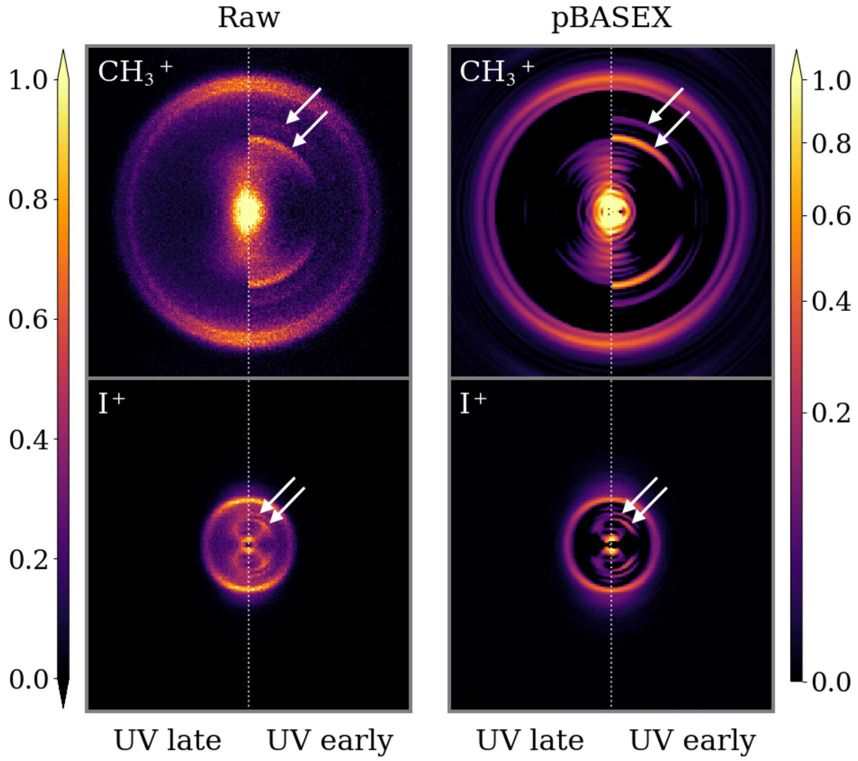

Figure 2.24: (*left column*) Raw and (*right column*) pBASEX inverted ion images for (*top row*) CH_3^+ and (*bottom row*) I^+. In the left half of each panel is the image when the NIR pulse precedes the UV pulse (−0.5 ps), and in the right half is the image when UV pulse far precedes the NIR pulse (3 ps). Arrows indicate features only present in the UV early images. The laser polarisation axis was vertical in these images. Each panel is normalised separately.

Plotting the fragment momenta as a function of pump-probe delay, shown in Figure 2.25, provides a complete picture of the delay-dependent effects. Each plot is produced by angular integration of the pBASEX inverted images for the ion of interest at each delay step, normalisation of each radial distribution by the number of laser shots, and finally calibration from radius to momentum. Fragment momenta are plotted in atomic units (a.u.). The same two-body dissociation channels contribute to the TR momentum distributions for CH_3^+ and I^+, so naturally, they match. Because the signal in the I^+ ion images is distributed over a smaller area of pixels, the I^+ momentum resolution is distinctly worse. For example, the splitting of the high momentum feature in panel (a) is unresolved in panel (b). Therefore, the discussion will focus on the CH_3^+ momentum distribution.

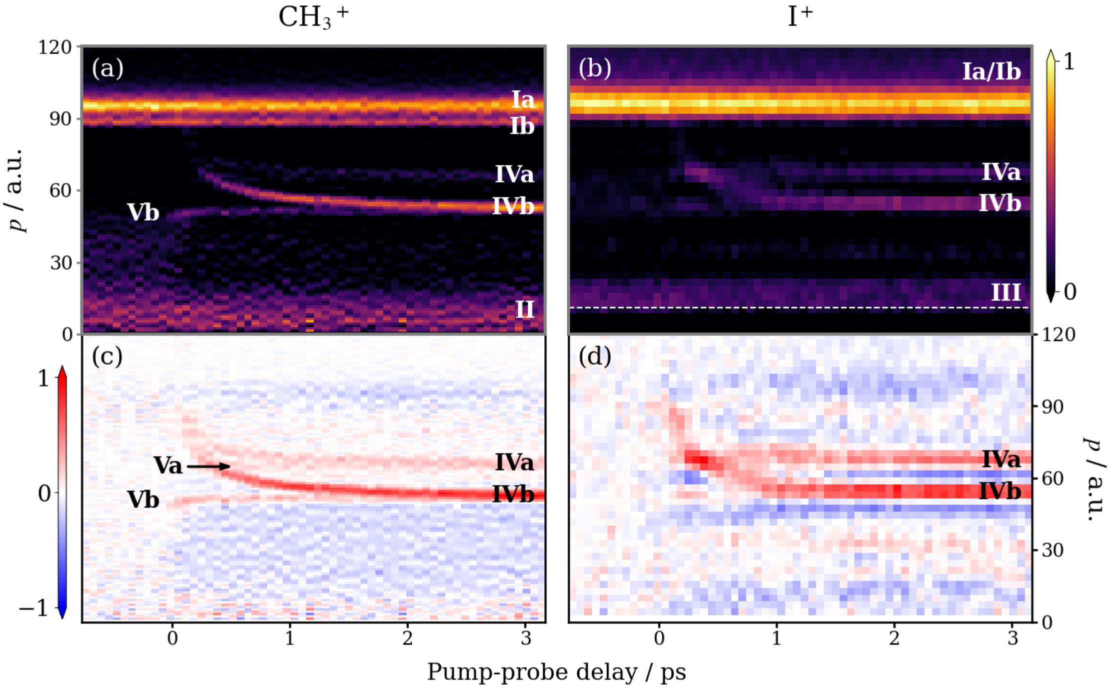

Figure 2.25: Time-resolved momentum distribution of (a) CH_3^+ and (b) I^+ obtained from pBASEX inverted ion images. Positive delay corresponds to the UV pulse arriving before the NIR pulse, and vice versa. The labelled features are discussed in the main text. The dashed line in (b) indicates a region of zero intensity due to saturation of the detector by preceding ion hits on each cycle. In panels (c) and (d) the average UV late signal has been subtracted from all delays in order to highlight which regions are enhanced (*red*) and which are depleted (*blue*) when the UV pulse precedes the NIR pulse. Each panel is normalised separately.

Those features in Figure 2.25(a) whose intensity do not change with pump-probe delay arise from the ionisation of molecules by the NIR probe pulse that have not been excited by the UV pump pulse.[50,152] The high momentum feature that is split into two channels, labelled Ia and Ib, can be assigned to the Coulomb explosion of doubly ionised CH_3I:

$$\mathrm{CH_3I} \xrightarrow{nh\nu_{800\,\mathrm{nm}}} \mathrm{CH_3I^{2+}} \rightarrow \mathrm{CH_3}^{+} + \mathrm{I}^{+}, \tag{Ia}$$

$$\mathrm{CH_3I} \xrightarrow{nh\nu_{800\,\mathrm{nm}}} \mathrm{CH_3I^{2+}} \rightarrow \mathrm{CH_3}^{+} + \mathrm{I}^{*+}. \tag{Ib}$$

The measured KERs for these channels are 5.0 ± 0.3 and $4.3 \pm 0.1\,\mathrm{eV}$, with uncertainties referring to the standard deviations of Gaussian functions fitted to the KER spectra. These values agree well with those previously reported by Banares and coworkers of 5.2 and 4.4 eV.[154] The very low momentum feature labelled II corresponds to dissociative ionisation that produces a methyl ion and a neutral iodine cofragment:

$$\mathrm{CH_3I} \xrightarrow{nh\nu_{800\,\mathrm{nm}}} \mathrm{CH_3I^{+}} \rightarrow \mathrm{CH_3}^{+} + \mathrm{I}. \tag{II}$$

A similar feature is labelled III in panel (b) and is attributed to fragmentation of the parent monocation, where the charge is instead retained by iodine:

$$\mathrm{CH_3I} \xrightarrow{nh\nu_{800\,\mathrm{nm}}} \mathrm{CH_3I^{+}} \rightarrow \mathrm{CH_3} + \mathrm{I}^{+}. \tag{III}$$

It is often informative to compute the differential signal by subtracting the average UV late signal from all delays. Doing so removes the delay-independent, probe-only signals, and isolates the delay-dependent features of interest. Here, and throughout this thesis, difference ion momentum distributions are plotted on a colour scale that displays enhancement in red and depletion in blue. The $CH_3{}^{+}$ difference momentum distribution in Figure 2.25(c) exhibits no strong regions of depletion, but four distinct features that appear at positive delay from photoexcitation by the UV pulse, subsequent dissociation, and then ionisation by the NIR pulse.

The two features in panel (c) whose momenta decreases with pump-probe delay, labelled IVa and IVb, are assigned to neutral photodissociation of CH_3I into a methyl radical and an iodine atom in either its excited or ground spin-orbit state, followed by ionisation of both cofragments:[50,152]

$$CH_3I \xrightarrow{h\nu_{258\,\mathrm{nm}}} CH_3 + I \xrightarrow{nh\nu_{800\,\mathrm{nm}}} CH_3{}^+ + I^+, \tag{IVa}$$

$$CH_3I \xrightarrow{h\nu_{258\,\mathrm{nm}}} CH_3 + I^* \xrightarrow{nh\nu_{800\,\mathrm{nm}}} CH_3{}^+ + I^{*+}. \tag{IVb}$$

The Coulomb repulsion between the ion pair decreases as the pump-probe delay increases because of the growing separation of the two dissociating, neutral fragments at the instant of ionisation. This manifests as a downward curve in time, known as a Coulomb curve.

At sufficiently long delay, Coulomb repulsion becomes negligible and the energies of the ions is solely due to the neutral dissociation. The momenta of the fragments from channel IVb is lower at long delay because, as a result of the neutral dissociation producing iodine in an excited state, less of the available energy is released as KE of the fragments.[145] Finally, the two features labelled Va and Vb in Figure 2.25(c) that correlate with channels IVa and IVb at long delay arise from ionisation of the methyl fragment in the absence of a charged iodine cofragment:

$$CH_3I \xrightarrow{h\nu_{258\,\mathrm{nm}}} CH_3 + I \xrightarrow{nh\nu_{800\,\mathrm{nm}}} CH_3{}^+ + I, \tag{Va}$$

$$CH_3I \xrightarrow{h\nu_{258\,\mathrm{nm}}} CH_3 + I^* \xrightarrow{nh\nu_{800\,\mathrm{nm}}} CH_3{}^+ + I^*. \tag{Vb}$$

The KERs of the (IVa + Va) and (IVb + Vb) channel pairs at the longest delay time used in the experiment (3.2 ps) are 2.4 ± 0.2 and 1.5 ± 0.1 eV, respectively. These values are in good agreement with the expected values of 2.40 and 1.45 eV, assuming the same energy partitioning as at 266 nm.[145]

The assignment of the features in Figures 2.25(a) and (c) can be confirmed using covariance analysis, which reveals the correlated properties of fragment ions (a full discussion of the topic is provided in the following chapter). Figure 2.26(a) is a covariance map of the TR 2D-projected momentum distribution of CH_3^+ that is produced in correlation with I^+. This was constructed by calculating the covariance map of CH_3^+ relative to the recoil direction of I^+ at each delay step, integrating each covariance map to obtain a radial distribution (Abel inversion does not apply), then normalising and calibrating the radial distributions in the same fashion as Figure 2.25.

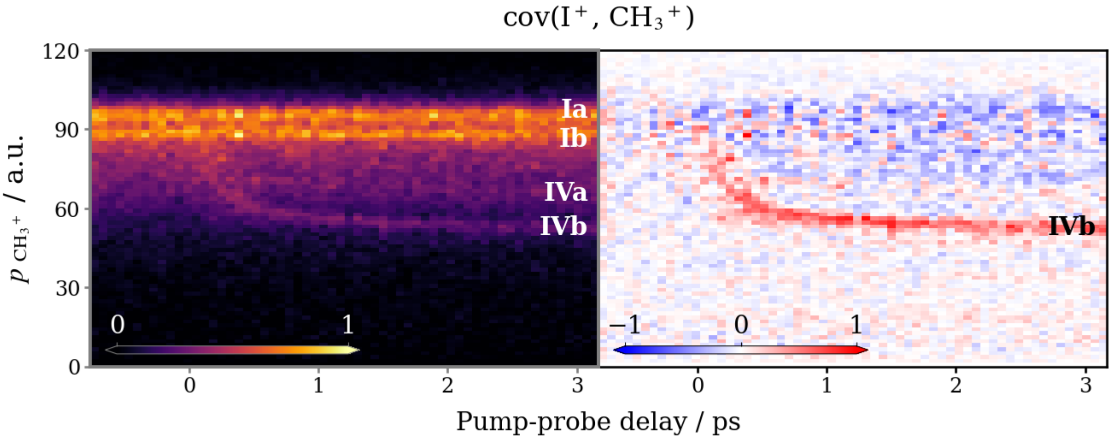

Figure 2.26: (a) Time-resolved two-fold covariance map of the 2D projected-momentum distribution of CH_3^+ from the two-body breakup of CH_3I^{2+} into $CH_3I^+ + I^+$. (b) UV late subtracted plot. Each panel is normalised separately.

The covariance map reveals which features are the result of channels that produce a $CH_3^+ + I^+$ ion pair. As expected, features II, Va and Vb are removed by this analysis. Because the map is constructed from 2D projected-momentum information, the features all appear smeared towards lower momentum (the full implications are examined in Section 3.5.1). As a result, the intense probe-only channels Ia and Ib mask the weak signal from channel IVa.

Overall, the results of this brief study are in good agreement with the findings of earlier TR-CEI experiments that employed a NIR probe pulse.[50,152] The only previously observed channels not reproduced in the current work involve ionisation of CH_3^+ by multiple UV photon absorption, *e.g.*, dissociative ionisation induced by the UV pulse, followed by ionisation of the neutral cofragment by the NIR pulse.[50] In the current study, the intensity of the pump pulse was low enough to avoid significant UV multi-photon excitation.

This preliminary work has demonstrated the capabilities of the new instrument, including following the correlated momenta of dissociating cofragments through TR covariance mapping. Moving forward, the apparatus shows great potential for exploring the structural dynamics of new systems of study. The discussion has also provided an introduction to how data are analysed and interpreted in a modern TR-CEI study. This is important groundwork for Chapters 7 and 8, which present TR-CEI data of more complex molecular dynamics.

3

Covariance mapping

Contents

In order to fully probe the dynamics of the Coulomb explosion of a polyatomic molecule and gain insight into the starting structure of the neutral molecule, the momenta of multiple fragments ions must be measured in correlation. The main method utilised in this thesis to determine the correlated properties of photofragment ions is covariance analysis. Covariance is a statistical measure of the correlation between two variables, denoted A and B, across a series of observations:[80]

$$\begin{aligned} \mathrm{cov}(A,\ B) &= \langle (A - \langle A \rangle)(B - \langle B \rangle) \rangle \\ &= \langle AB \rangle - \langle A \rangle \langle B \rangle, \end{aligned} \tag{3.1}$$

where $\langle A \rangle$ refers to the mean of the measured quantity A. In essence, this measures how relative changes in two random variables correlate.

The interpretation of the covariance from the first line of Equation 3.1 is as follows. If when A is above its mean value, B is also above its mean value, the quantities inside both brackets will be positive. This yields a positive covariance and A and B are said to be correlated. Conversely, if when A is larger than its mean value, B is lower than its mean value, the covariance will be negative and two variables are said to be anticorrelated. If independent of the value of A, B is equal to its mean value, the value of the second bracket is zero and the covariance too. In this case A and B are uncorrelated.

In the context of covariance analysis applied to laser-induced CEI, each laser shot represents a different observation, whilst the variables are the measured coordinates of the photofragment ions. It is common to express the covariance in terms of the difference of two terms, as seen in the second line of Equation 3.1. The first term ($\langle AB \rangle$) is the correlated product, calculated from all of the pairs of ion A and ion B detected in the same laser shot:

$$\langle AB \rangle = \frac{1}{N} \sum_{i=1}^{N} A_i \, B_i. \tag{3.2}$$

This corresponds to the coincidence measured in a coincidence spectroscopy experiment. Such experiments are conducted under conditions that minimise the possibility of multiple parent molecules being ionised in the same laser shot. If all of the ions detected in each laser shot originate from the same molecule, it ensures there are no pairs of ions from the separate Coulomb explosion events.

If the average number of parent of molecules probed per laser shot (λ) rises above 1, the correlated product will contain a significant portion of false coincidence events. The higher the value of λ is, the greater the proportion of detected ion pairs that will be falsely correlated. The uncorrelated term ($\langle A\rangle\langle B\rangle$) accurately captures this false coincidence event background. By subtracting the uncorrelated term from the correlated term, the true ion correlations are isolated.

The uncorrelated term is calculated from all of the pairs of ion A and ion B across the entire dataset, independent of whether they are detected in the same laser shot or not:

$$\langle A\rangle\langle B\rangle = \frac{1}{N^2}\sum_{i=1}^{N} A_i \sum_{i=1}^{N} B_i. \tag{3.3}$$

Due to the requirement to iterate over every pairwise combination across the entire dataset, calculating the uncorrelated term is very computational expensive. This is especially problematic when extending covariance analysis to higher dimensions as the total number of combinations scales with the power of the number of dimensions. A more efficient approach is to approximately calculate the uncorrelated term based on a smaller subset of the data. This is approach is explained in Appendix B.

This chapter offers a discussion of the various different covariance analysis techniques that have been developed to investigate the fragmentation dynamics of molecular polycations. Examples are provided from pioneering studies in the literature and experiments conducted as part of the work of this thesis. Simulations are used to demonstrate some of the key concepts. Emphasis is placed on recent developments in covariance analysis made during the course of this thesis. This includes new covariance mapping techniques, which are applied as part of the data analysis in later chapters.

3.1 Time-of-flight covariance mapping

Covariance analysis was first applied in the context of molecular fragmentation by Frasinski *et al.* to study the correlations between the ToF signals of fragment ions, measured using ToF mass spectrometry.[80] By calculating the covariance between the one-dimensional (1D) ToF spectrum and itself they produced a 2D covariance map, as shown in Figure 3.1(a). Mathematically, this corresponds to setting $A = B$ in Equation 3.1, where $A_i(t)$ is the value of the spectrum at time t on laser shot i.

Covariance is simply a scalar that measures the statistical relationship between two random variables. The technique of Frasinski *et al.* is therefore properly referred to as covariance mapping, as the result is a matrix that shows the statistical relationship between different regions of random functions. In the case of a laser-induced ionisation experiment, the number of molecules within the interaction volume obeys Poisson statistics. The signal therefore fluctuates significantly on a shot-to-shot basis, and covariance mapping identifies those regions of the spectrum that tend to fluctuate with one another, implying an underlying correlation.

Examining the ToF covariance map in Figure 3.1(a), the positive diagonal is autovariance, which reflects the necessarily perfect correlation of each ion with itself. The ToF covariance map is symmetric about this line. Of interest are the off-diagonal features, which identify the ion species that are formed together as cofragments, revealing the fragmentation pathways of the parent molecule. These data were measured for the Coulomb explosion of CO exposed to an intense laser field, hence the correlated ion pairs are combinations of C and O ions with different charges states. The ToF of key ions are labelled along the axes in the figure. As an example, the dotted lines indicates where the feature for the channel $\mathrm{CO}^{2+} \rightarrow \mathrm{C}_\mathrm{f}^{+} + \mathrm{O}_\mathrm{b}^{+}$ appears in both halves of the covariance map.

The correlated features between pairs of ions manifest as negatively sloped lines due to momentum conversation in the breakup of a diatomic molecule. If one fragment is projected away from the detector, increasing its ToF, the other is necessarily projected towards the detector, decreasing is ToF. The effect is particularly pronounced in this dataset because the laser pulse was polarised parallel

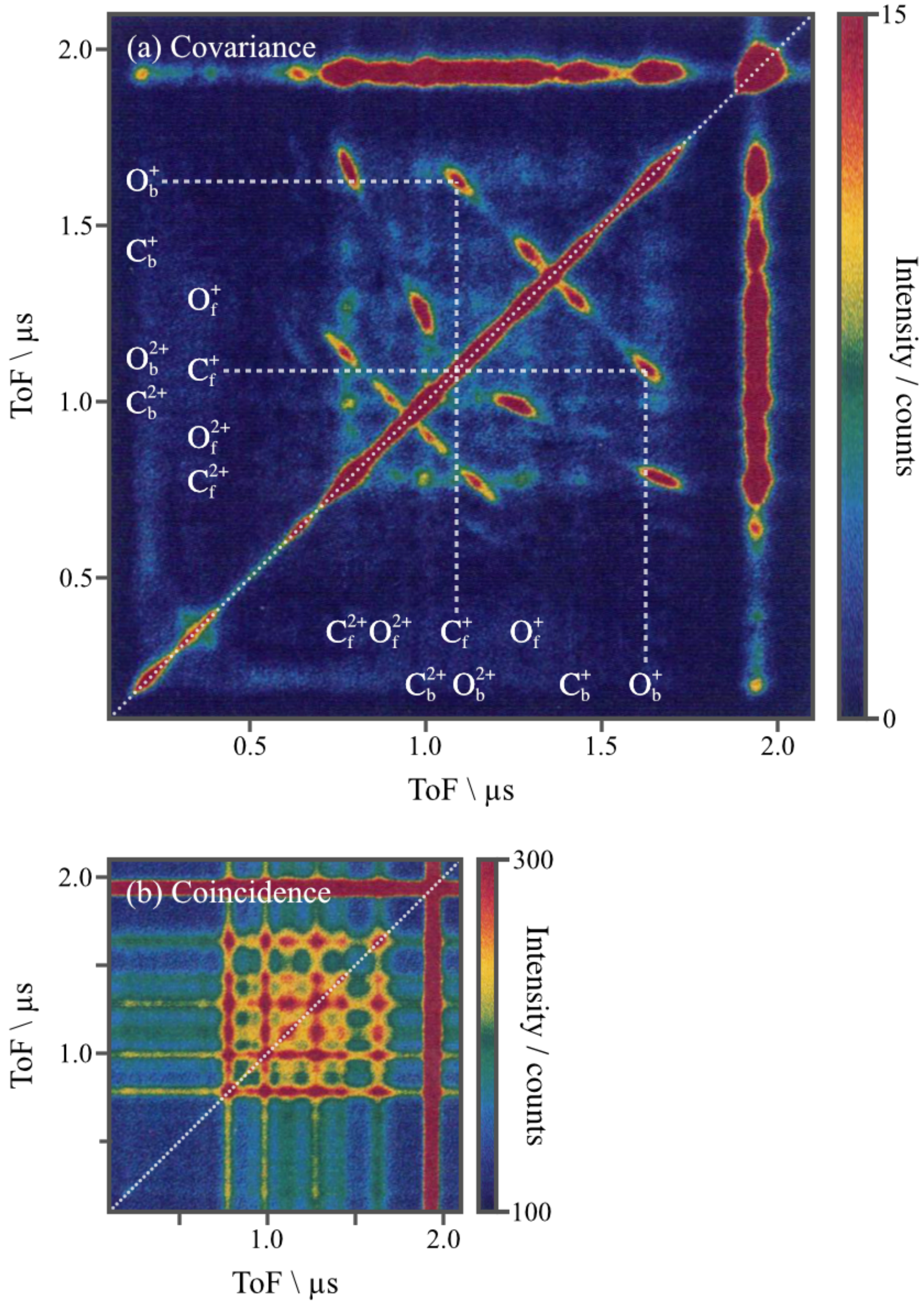

Figure 3.1: ToF (a) covariance and (b) coincidence maps for CO exposed to an intense sub-picosecond laser pulse. Note the difference in the range of the colour scale for the two panels. Maps are symmetric about the positive diagonal. Laser pulses were polarised parallel to the ToF axis, resulting in two peaks for each Coulomb explosion channel, depending on which ion species is ejected towards the detector ($_f$) and which is ejected away ($_b$). The dotted lines in (a) indicate the feature for an example channel: $CO^{2+} \rightarrow C_f^+ + O_b^+$. Adapted from Reference [80].

to the ToF axis. Two distinct peaks appear for each Coulomb explosion channel depending on which ion species is ejected towards the detector, and which is ejected away. For a two-body breakup, the exact gradient reflects the ratio of the charge on the fragments, *e.g.* if both have equal charge the gradient is -1.

For comparison, the ToF coincidence map (the $\langle AB \rangle$ term of the covariance calculation) is presented in Figure 3.1(b). This correlation map is dominated by false coincidence events that mask the true correlations in the dataset, making all pairs of ion species appear correlated. Clearly, a coincidence analysis is not appropriate for this dataset. Whether is it appropriate is largely determined by λ (the average number of parent of molecules probed per laser shot).[155] To demonstrate, a series of simulations have been performed.

An event array was generated based on the following reaction scheme for a triatomic molecule ABC:

$$\mathrm{ABC} \xrightarrow{h\nu} \begin{cases} \mathrm{ABC}^{+} \\ \mathrm{ABC}^{2+} \rightarrow \mathrm{AB}^{+} + \mathrm{C}^{+} \\ \mathrm{ABC}^{2+} \rightarrow \mathrm{A}^{+} + \mathrm{BC}^{+} \\ \mathrm{ABC}^{3+} \rightarrow \mathrm{A}^{+} + \mathrm{B}^{+} + \mathrm{C}^{+}, \end{cases} \tag{3.4}$$

where it is assumed that all channels are equally likely. Data were simulated for 1×10^4 ionisation events and then grouped into laser shots according to Poisson statistics, with a given λ. The model used to simulate Coulomb explosion data is described in the next chapter. For the purpose of calculating ToF correlation maps, simulated ions were assigned ToF values in arbitrary units based on their momentum along one axis.

Coincidence and covariance maps simulated for three different λ values, $0.1\,\mathrm{shot}^{-1}$, $1\,\mathrm{shot}^{-1}$, and $10\,\mathrm{shot}^{-1}$, are shown in Figure 3.2. It is worth noting the two distinct forms of the off-diagonal features observed in the correlation maps for this reaction scheme. Any feature that arises from a two-body breakup channel has the familiar form of a sharp negatively sloped line, but the correlation between any pair of ions produced by the three-body breakup has a broad oval shape.

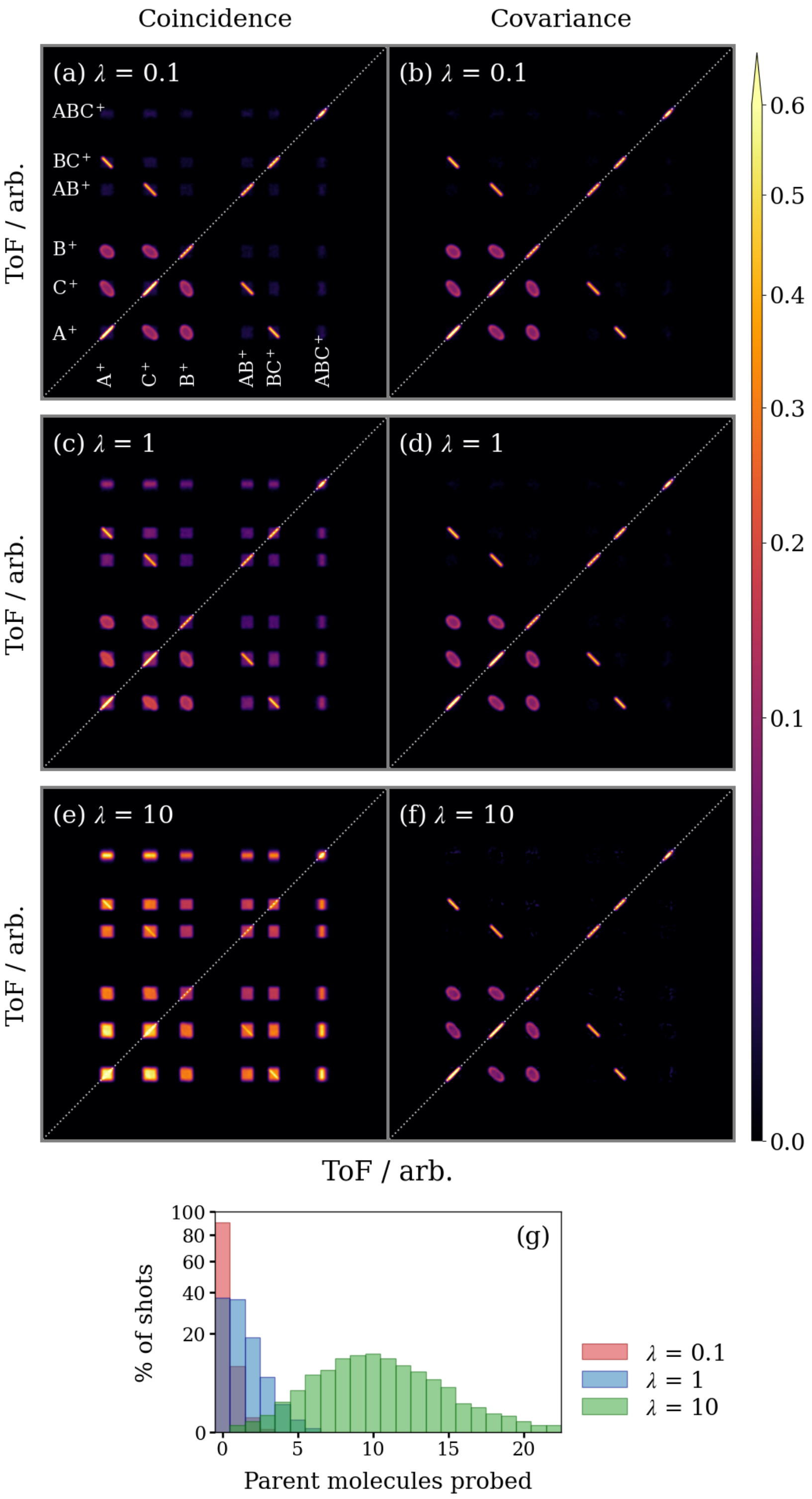

Figure 3.2: Simulated ToF (*left column*) coincidence and (*right column*) covariance maps for the reaction scheme presented in Equation 3.4. Each map is normalised separately. Data were simulated for 1×10^4 ionisation events and grouped into laser shots with an average number of parent molecules probed of (a, b) $0.1\,\text{shot}^{-1}$, (c, d) $1\,\text{shot}^{-1}$, and (e, f) $10\,\text{shot}^{-1}$. Corresponding parent molecules probed per laser shot distributions are shown in panel (g).

As can be seen in panels (a) and (b), the coincidence and covariance maps are virtually identical when λ is much less than one. The corresponding distribution of the number of parent molecules probed per laser shot for this dataset is displayed in red in panel (g). The vast majority of laser shots contain no ionisation events. As expected, a single molecule is ionised in roughly 10% of laser shots, and very few laser shots occur where more than one molecule is ionised. These experimental conditions are well-suited for performing coincidence measurements.

As λ is increased, the coincidence map becomes contaminated by falsely correlated events. For example, in panels (c) and (e) the parent monocation appears correlated with other ion species, despite the fact that it is not created with any cofragments. When $\lambda = 1$ the true correlations are higher in intensity than the background of false coincidence events. Once λ is as high as 10, the true correlations can no longer be distinguished. By contrast, the covariance map does not visibly change in appearance as λ rises. The implication is that under Poisson statistics covariance analysis is always appropriate, though not always necessary.

Ultimately, other factors including detection efficiency and the rate of background counts also play a role in determining whether coincidence or covariance analysis is more appropriate. For a discussion of these factors, see Reference [156].

3.2 Covariance imaging

ToF covariance mapping is primarily useful for identifying ions that are formed by the same dissociation channel.[80,157–159] To fully interrogate the Coulomb explosion dynamics of a polyatomic molecule, one must examine the correlations between the fragment ion momenta, as measured by ion imaging.[19,22,24,81] The resulting covariance maps contain the relative fragment recoil distributions, from which information about the nuclear structure at the instant of Coulomb explosion can be inferred.

Covariance imaging is the term used here to refer to calculating the covariance between the $(x,\ y)$ spatial coordinates of two or more ion images.[19,160] This is in contrast to covariant momentum mapping, which involves calculating a map of the covariance between fragment ion momentum vectors. That is the subject of a later section. In essence, covariance imaging extends the ToF covariance mapping approach to higher dimensions. The covariance map between the 2D spatial coordinates of a pair of ion images is a four-dimensional array. Because this is difficult to visualise, the covariance map is often transformed into a reference frame with a reduced number of dimensions.

Stapelfeldt and coworkers were the first to demonstrate covariance mapping applied to ion imaging data.[161] Their angular covariance mapping method does not strictly meet the definition of covariance imaging outlined here, however. They first transform the $(x,\ y)$ spatial coordinates of each detected ion into a single angular coordinate, producing a 1D angular distribution for each ion species. Calculating the covariance between a pair of angular distributions then yields a 2D matrix, similar to a ToF covariance map.

In subsequent work, Stapelfeldt, Brouard and coworkers developed recoil-frame covariance imaging.[160] Their procedure generates a 2D covariance map of the $(x,\ y)$ coordinates of one ion species in the so-called 'recoil frame' of another. It is particularly intuitive because the covariance map retains the outward appearance of an ion image. One species is selected as the 'reference' ion, then a 2D covariance map is calculated for each unique set of $(x,\ y)$ coordinates of the reference ion with the full space of $(x,\ y)$ coordinates of the 'partner' ion. The covariance maps for the different reference ion coordinates are then rotated such that the reference ion coordinates all lie along a common axis (conventionally the positive y-axis), and are summed together.

This process of constructing a recoil-frame covariance image is illustrated in Figure 3.3 on data simulated for the breakup of diatomic AB^{2+} into $A^+ + B^+$. Each panel in the central column of the figure is an example of a covariance map between a single set of $(x,\ y)$ coordinates of A^+, and the full coordinate space of B^+. The correlated feature is always observed at an angle of 180° relative to the fixed coordinate of A^+, showing that A^+ and B^+ recoil back-to-back. In the final covariance map, the recoil-direction of A^+ is fixed and the spatial distribution of B^+ on the detector is plotted relative to this direction.

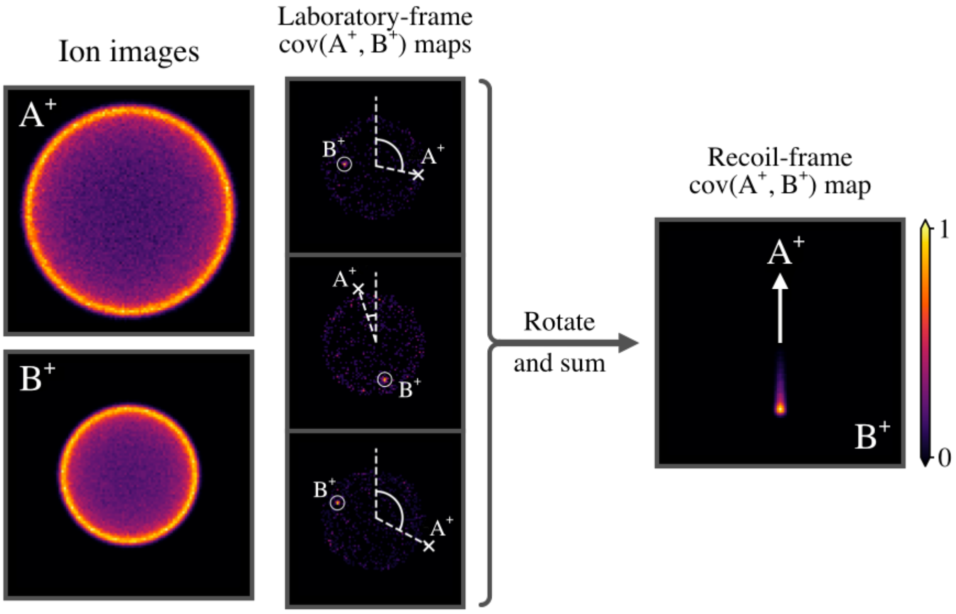

Figure 3.3: Demonstration of how a recoil-frame correlation map is constructed. Data were simulated for the two-body breakup of diatomic AB^{2+} into $A^+ + B^+$. Raw ion images are shown on the left. For each unique set of $(x,\ y)$ coordinates of A^+, a 2D covariance map with the full $(x,\ y)$ coordinate space of B^+ is calculated. Each covariance map is then rotated so that the reference ion coordinates align with the positive y-axis, and the set of rotated images is summed to give the recoil-frame correlation map on the right. Adapted from Reference [162].

Because each detector image is a 2D projection of a 3D fragment momentum distribution, only the 2D projection of the fragment momenta may be aligned in a recoil-frame covariance image. This means the molecular orientation prior to Coulomb explosion is not well defined. In the frame of the covariance map in Figure 3.3, AB^{2+} can lie anywhere in a plane defined by the y-axis and the axis pointing out of the page. Due to these out-of-plane contributions, the correlated feature extends across a radial range, even though the simulated dissociation has a well defined KER. The implications this has for the information that can be extracted are considered in Section 3.5.1.

Recoil-frame covariance imaging is particularly well-suited for studying the Coulomb explosion between a pair of ions, such as a two-body breakup,[50,163] or a three-body breakup involving a neutral cofragment.[163,164] Figure 3.4 presents example data for the Coulomb explosion of molecular iodine following SFI by intense NIR femtosecond laser pulse, acquired using the Oxford spectrometer. Ion images recorded for singly, doubly and triply charged iodine fragments are shown along the bottom edge of the figure. Each consists of several concentric rings that correspond to different dissociation channels. These features peak along the polarisation axis of the laser, which was vertical in these images, due to the dependence of the ionisation rate on the angle between the molecular axis and the laser polarisation axis, known as geometric alignment.[165,166].

Covariance maps between all possible reference and partner ion combinations of I^+, I^{2+} and I^{3+} are shown in Figure 3.4. Each isolates a different $I_2{}^{(p+q)+} \rightarrow I^{p+} + I^{q+}$ channel. Once again, the covariance signals are tightly focused around 180°, as dictated by momentum conservation. The radius of each covariance signal aligns with a different ring in the partner ion image from which it is derived. Hence, recoil-frame covariance imaging can be used to definitively assign the multiple Coulomb explosion channels that contribute to each ion image. The analysis is capable of isolating even very weak signals that are difficult to distinguish in the ion images, such as the Coulomb explosion of I^+ and I^{3+}. The innermost rings in the I^+ and I^{2+} ion images must correspond to dissociation with a neutral iodine cofragment. Several such channels contribute to the I^+ ion image, due to the multiple dissociative electronic states of $I_2{}^+$ populated by SFI.[167]

The breakup of a polyatomic molecule into a pair of ions typically is not a good probe of the molecular structure. To extract more detailed structural information, it is necessary to explore the relative recoil of fragments ions from the many-body breakup of a more highly charged parent polycation. This was the goal of the first application of recoil-frame covariance imaging to CEI data by Slater *et al.*[19,160] In a pioneering study, they investigated the Coulomb explosion dynamics of an axially chiral biphenyl molecule exposed to an intense NIR femtosecond laser pulse. It is infeasible to measure all of the ions in coincidence from the Coulomb explosion of such a large molecule into atomic fragments. Hence, this studied relied upon measuring the relative recoil direction of a number of substituent 'anchor' species.

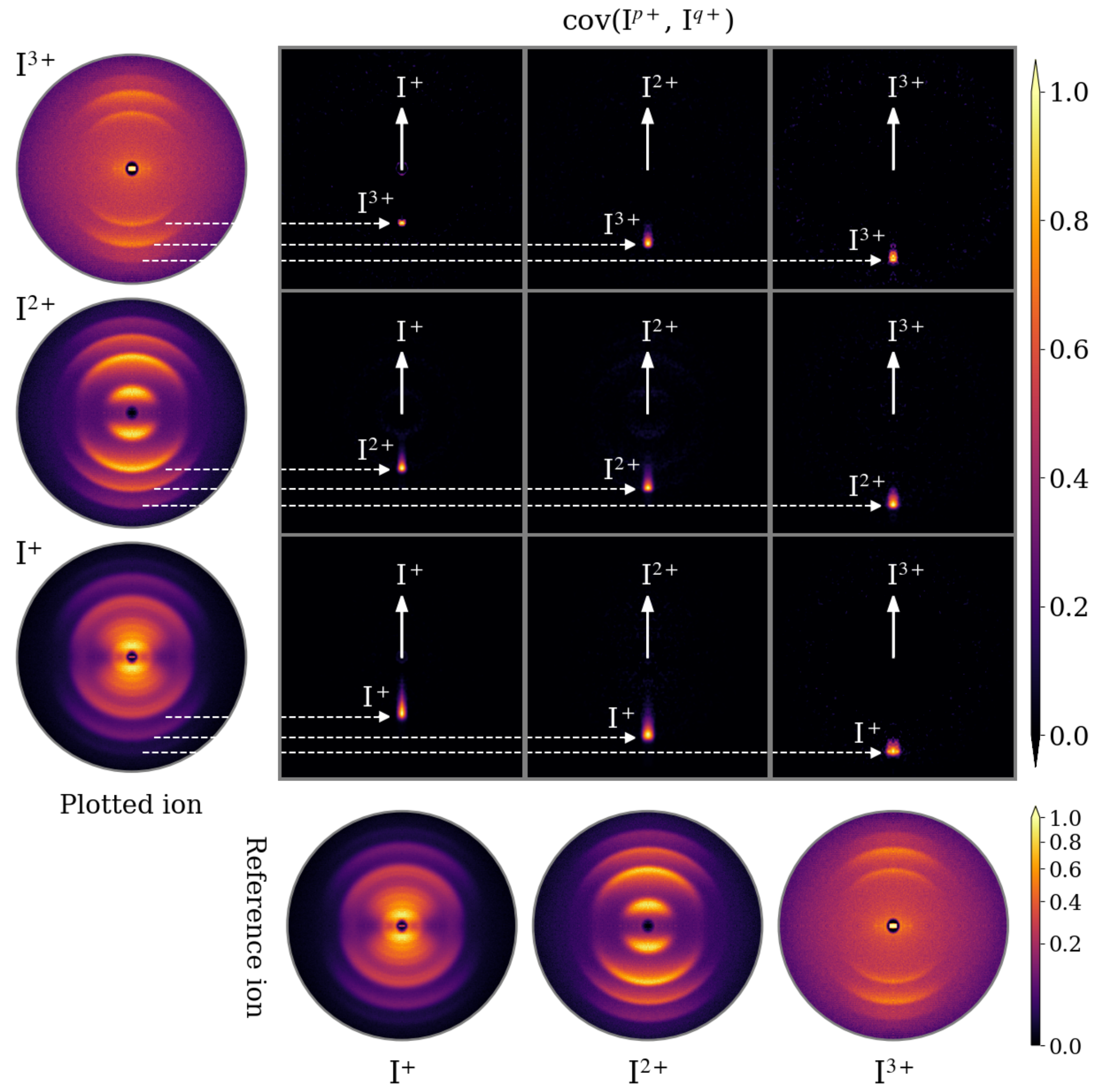

Figure 3.4: Recoil-frame two-fold covariance maps for the Coulomb explosion of strong-field ionised I_2. Ion images of the reference and partner ion for each plot are displayed along the *bottom row* and *left column*, respectively. Dashed arrows indicate which channel in the partner ion image is isolated in the covariance map. Each panel is normalised separately.

The raw ion images for key species are presented in the left column of Figure 3.5. A nanosecond laser pulse was used to adiabatically align molecules either perpendicular or parallel to the detector. The molecule is still free to rotate about the alignment axis. This gives rise to cylindrically symmetric distributions for F^+ and B^+ when the molecule is aligned head-on to the detector, shown in the upper left panels of the figure. Calculating a recoil-frame covariance map between F^+ and Br^+ transforms into a frame where the orientation about the alignment axis is fixed, as seen in the neighbouring panels. The four peaks in each covariance map resemble the four relative positions of F and Br in the molecule, when viewed head-on. The relative positions of these peaks is a good indicator of the dihedral angle between the two phenyl rings.

Turning now to the data recorded with the molecule aligned side-on to the detector, the position of the N, F and Br substituents within the molecule is reflected within the raw ion images. Due to the four-fold symmetry of the images it is not possible to identify, for instance, whether both Br atoms are located on the same phenyl ring. Using recoil-frame covariance imaging to calculate the covariance map of Br^+ with respect to the recoil direction of N^+, the data is transformed into a frame of reference where the orientation of the molecule along the alignment axis is fixed. Br^+ recoils exclusively in the opposite direction relative to N^+, confirming that both Br substituents are located on the same phenyl group.

This approach for molecular structure determination – combining Coulomb explosion of aligned molecules with recoil-frame covariance imaging – was pushed further by Burt *et al.*[22] They unambiguously identified four different isomers of difluoroiodobenzene by their recoil-frame covariance images, which were then used as references to identify two isomers in a mixed sample, and determine their ratio. The angular covariance mapping method of Stapelfeldt and coworkers, meanwhile, has been extensively used for identifying different conformations of molecular clusters.[25–27]

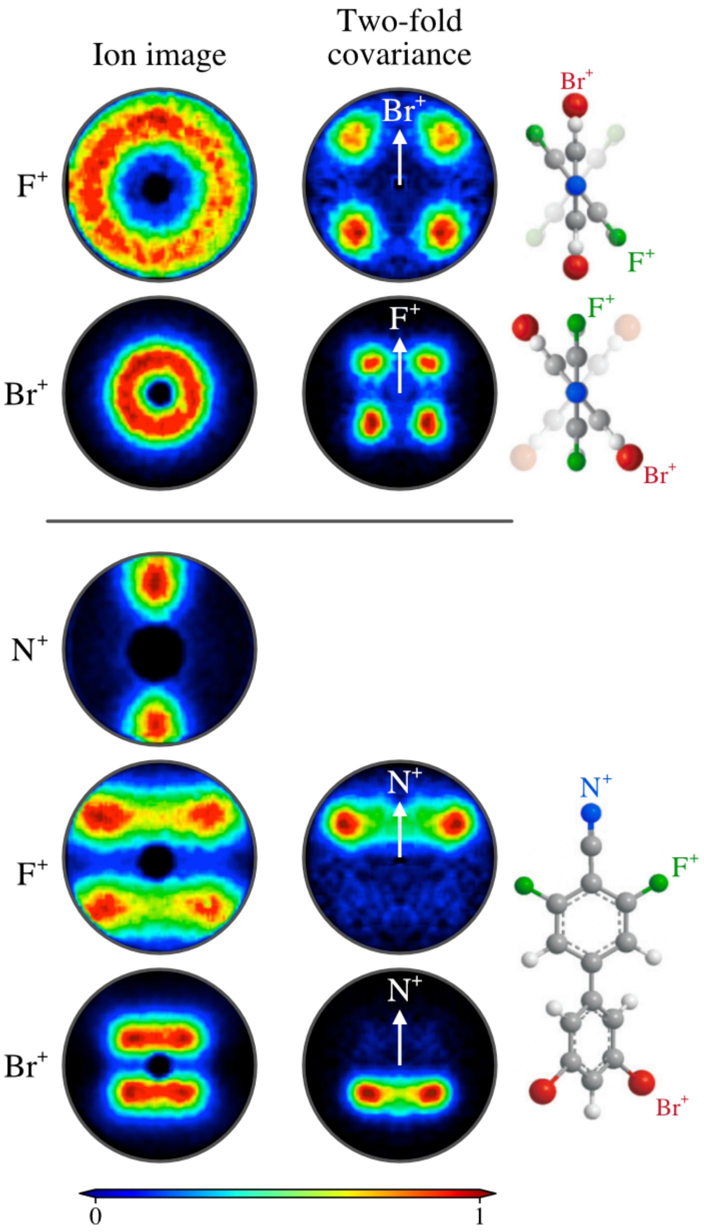

Figure 3.5: (*Left column*) Laboratory-frame ion images of fragments from the Coulomb explosion of 3,5-dibromo-3′,5′-difluoro-4′-cyanobiphenyl. Upper and lower images were recorded with the molecule aligned perpendicular and parallel to the detector, respectively. (*Right column*) Recoil-frame two-fold covariance maps where the reference ion is labelled, and the partner ion is the same as the adjacent ion image. Each panel is normalised separately. Adapted from Reference [19].

In a follow up study, Slater *et al.* investigated the torsional motion of the same biphenyl target molecule using TR-CEI.[24] Recoil-frame covariance imaging was used to track the recoil angle between F^+ and Br^+ ions – indicative of the dihedral angle between the two phenyl rings – as a function of delay following vibrational excitation by a weak NIR femtosecond 'kick' pulse. This represented the first application of recoil-frame covariance imaging, and covariance mapping in general, to study time-evolving nuclear structure. More recently, Allum *et al.* applied recoil-frame covariance imaging in a TR-CEI study of the photodissocation dynamics of methyl iodide to examine how the relative momentum of a pair of ions evolved as a function of pump-probe delay, *i.e.* separation upon Coulomb explosion.[50]

3.3 Three-fold covariance

Up until this point, the discussion has focused on covariance between two variables. In many scenarios, it is desirable to establish the correlation between a higher number of variables. Formulae for calculating the covariance (or an equivalent statistical measure of correlation) of up to six variables have been derived,[156] and the mathematics is understood for extending these formulae to still high numbers of variables (see Section 3.7). For clarity, from hereon the covariance between a pair of variables is referred to as two-fold covariance.

In this thesis, the highest order covariance considered is between three variables:

$$\begin{aligned}\mathrm{cov}(A,B,C) &= \langle (A-\langle A\rangle)(B-\langle B\rangle)(C-\langle C\rangle)\rangle \\ &= \langle ABC\rangle - \langle AB\rangle\langle C\rangle - \langle AC\rangle\langle B\rangle - \langle BC\rangle\langle A\rangle + 2\langle A\rangle\langle B\rangle\langle C\rangle,\end{aligned} \tag{3.5}$$

known as three-fold covariance. In the context of covariance mapping applied to ion imaging data, there are technical challenges associated with measuring the correlated properties of a higher number of ions. Foremost is that the probability of detecting n particles from a single dissociation event is proportional to η^n, and therefore the required data acquisition time increases exponentially. The topic is reviewed in Section 3.8.

The most obvious application of three-fold covariance analysis in the context of molecular fragmentation is to unequivocally assign the products of a three-body fragmentation channel. This is how three-fold covariance mapping was initially demonstrated by Frasinski *et al.*[157] They carried out a ToF mass spectrometry study of the dissociation of multiply ionised N_2O and calculated the covariance between three identical copies of the 1D ToF spectrum. The resulting ToF three-fold covariance map is 3D matrix, making it difficult to visualise.

Figure 3.6(a) displays 2D projections from a simulated ToF three-fold covariance map for the same reaction scheme introduced earlier in Section 3.1 to demonstrate two-fold covariance mapping. Each projection is a sum along the vertical axis of the 3D covariance map over the ToF range for a different ion species. As an example, the projection obtained by summing over the ToF range of C^+ is shown in full in panel (b). The result is a 2D covariance map of the correlations between pairs of ions that are *also* correlated with C^+.

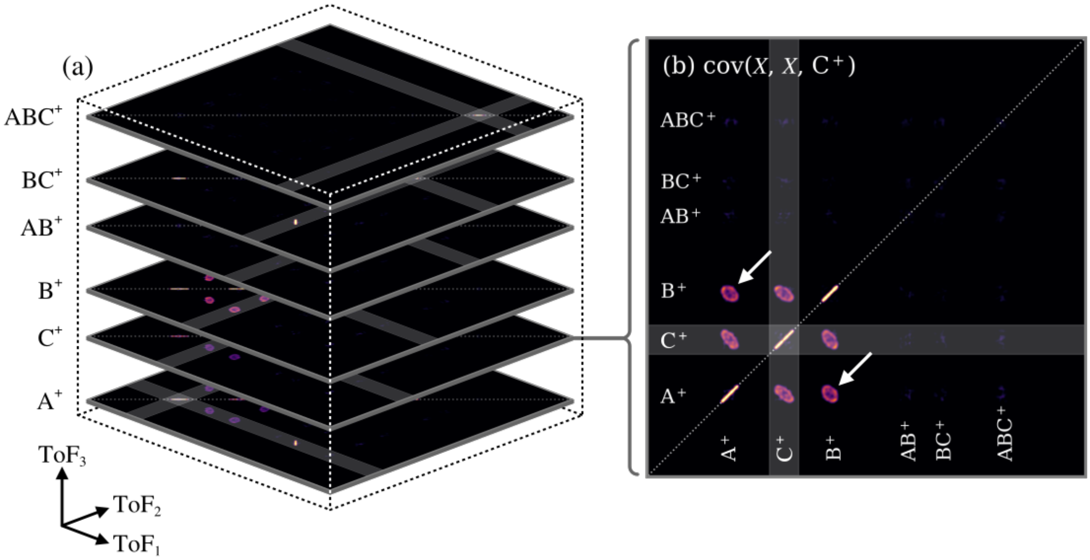

Figure 3.6: (a) 2D projections of the simulated ToF three-fold covariance map for the reaction scheme presented in Equation 3.4. Data were simulated for 1×10^4 ionisation events and grouped into laser shots with on average 5 parent molecules probed per shot. Each projection is summed over the ToF range for a different ion species. (b) The projection obtained by summing over the ToF range of C^+, showing the correlations between pairs of ions that are *also* correlated with C^+. The autovariance planes are highlighted in grey. Arrows indicate the feature for $ABC^{3+} \rightarrow A^+ + B^+ + C^+$.

In addition to autovariance along the positive diagonal, a 2D projection of the ToF three-fold covariance map contains autovariance planes. These planes correspond to the correlation of the ion species of interest with itself and another ion, *i.e.* two-fold correlations. The planes are highlighted in grey in Figure 3.6(b) and contain contributions from $AB^+ + C^+$, $A^+ + C^+$, and $B^+ + C^+$. Of interest are the features outside the autovariance planes, which identify combinations of three distinct ion species that are formed together. In Figure 3.6(b) there is only one, indicated by the arrows, which identifies the breakup of ABC^{3+} into $A^+ + B^+ + C^+$.

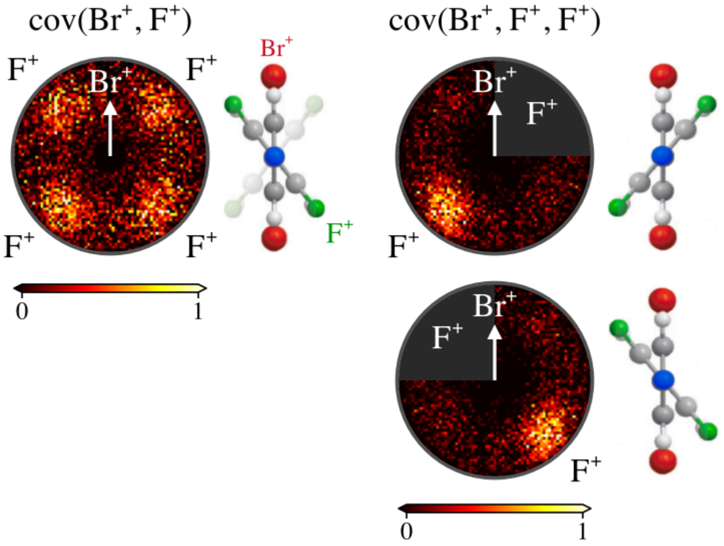

Figure 3.7: (*Left*) Recoil-frame two-fold covariance map of the distribution of F^+ ions relative to Br^+ from the Coulomb explosion of 3,5-dibromo-3′,5′-difluoro-4′-cyanobiphenyl, aligned perpendicular to the detector. (*Right*) Three-fold (Br^+, F^+, F^+) covariance maps in the same frame of reference, showing the distribution of one F^+ ion when the second is constrained to the region indicated by the grey quadrant. Each panel is normalised separately. Adapted from Reference [168].

The first application of three-fold covariance mapping to ion imaging data[168] was a re-analysis of the same CEI dataset examined by Slater *et al.* in their original demonstration of recoil-frame covariance imaging.[19,160] By expanding covariance imaging to three-particle correlations, the problem of dimensionality is only amplified. The covariance map between the 2D spatial coordinates of a trio of ion images is an eight-dimensional array. The approach of Pickering *et al.* was to re-purpose the recoil-frame representation by mapping the $(x,\ y)$ coordinates of one ion species in the recoil-frame of a second, whilst stipulating that the $(x,\ y)$ coordinates of the third ion must lie within a predetermined region of the image.

Three-fold covariance mapping was used to disentangle contributions from the Coulomb explosion of different axially chiral enantiomers of 3,5-dibromo-3′,5′-difluoro-4′-cyanobiphenyl. The left panel of Figure 3.7 displays the two-fold covariance map of F^+ relative to the recoil direction of Br^+. Four peaks are present due to the contribution of both enantiomers, as illustrated by the adjacent cartoon. By calculating the three-fold covariance between Br^+ and two F^+ ions, the signal from either enantiomer can be isolated based upon where the second F^+ ions recoils relative to Br^+, as shown in the right-hand panels of the figure.

More recently, Allum *et al.* applied three-fold covariance mapping in a 3D ion imaging study of the Coulomb explosion dynamics of strong-field ionised D_2O.[81] Figure 3.8(a) is a plot of the total KER as a function of the D^+ ion pair relative recoil angle for the Coulomb explosion of D_2O that yields a pair of D^+ ions, determined by a two-fold covariance analysis between $D^+ + D^+$. Two features are discernible in the covariance map. The low KER feature can sensibly be ascribed to three-body fragmentation of D_2O^{2+} to yield neutral oxygen, and the high KER feature to three-body fragmentation of D_2O^{3+} into three monocations. These assignments were confirmed by calculating a map of the three-fold covariance between $D^+ + D^+ + O^+$, shown in panel (b), in which only the high KER feature persists.

This study was a major step forward from the original covariance imaging experiments performed by Slater *et al.* By coupling 3D ion imaging with multi-particle covariance analysis, the method of Allum *et al.* is capable of fully interrogating many-body dissociation dynamics. This is a different approach from the work of Slater *et al.*, which sought to determine structural information by tracking the relative momenta of a few key substituents on a molecule. In general, to track structural dynamics in detail, especially via TR-CEI, obtaining a complete picture of the dynamics of fragmentation is vital. For polyatomic species, this can only be facilitated by three- and higher-fold correlation mapping.

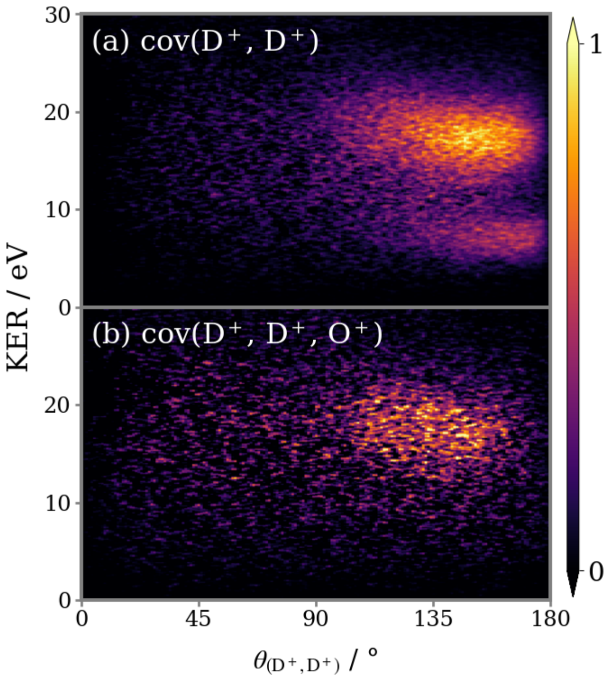

Figure 3.8: KER as a function of relative recoil angle of the D^+ ion pair for the three-body concerted breakup of $D_2O^{2/3+}$ into $2D^+ + O/O^+$. Panel (a) has been calculated using a two-fold covariance analysis between $D^+ + D^+$ and contains contributions from the breakup of both parent dications and parent trications. Panel (b) was calculated using a three-fold covariance analysis between $D^+ + D^+ + O^+$, which isolates signal exclusively from the breakup of the parent trication. The intensity of three-fold covariance map was normalised by dividing by the estimated detection efficiency of the O^+ ion. Adapted from Reference [81].

3.4 Unstable experimental conditions

As covariance analysis is based on a statistical analysis of signal fluctuations, it is essential to maintain stable experimental conditions. Variation of any experimental parameter that influences the total ion signal will cause the yield of all species to rise and fall as one, introducing false contributions to the calculated covariance map. The two parameters most prone to fluctuations in a laser-induced CEI experiment are the laser pulse intensity and the target molecule density in the interaction region.

For demonstration, it is once again instructive to consider the simulated ToF two-fold covariance map for the reaction scheme outlined in Equation 3.4. Figure 3.9(a) is the covariance map for a dataset with no shot-to-shot variation in λ. Fluctuating experimental conditions were emulated by multiplying λ by a random value between

0.25-1.75 on each laser shot. As expected, this causes the ion count distribution, shown in panel (h), to deviate from Poisson statistics, and induces false correlations in the calculated covariance map in panel (b), making all species appear correlated to some extent.

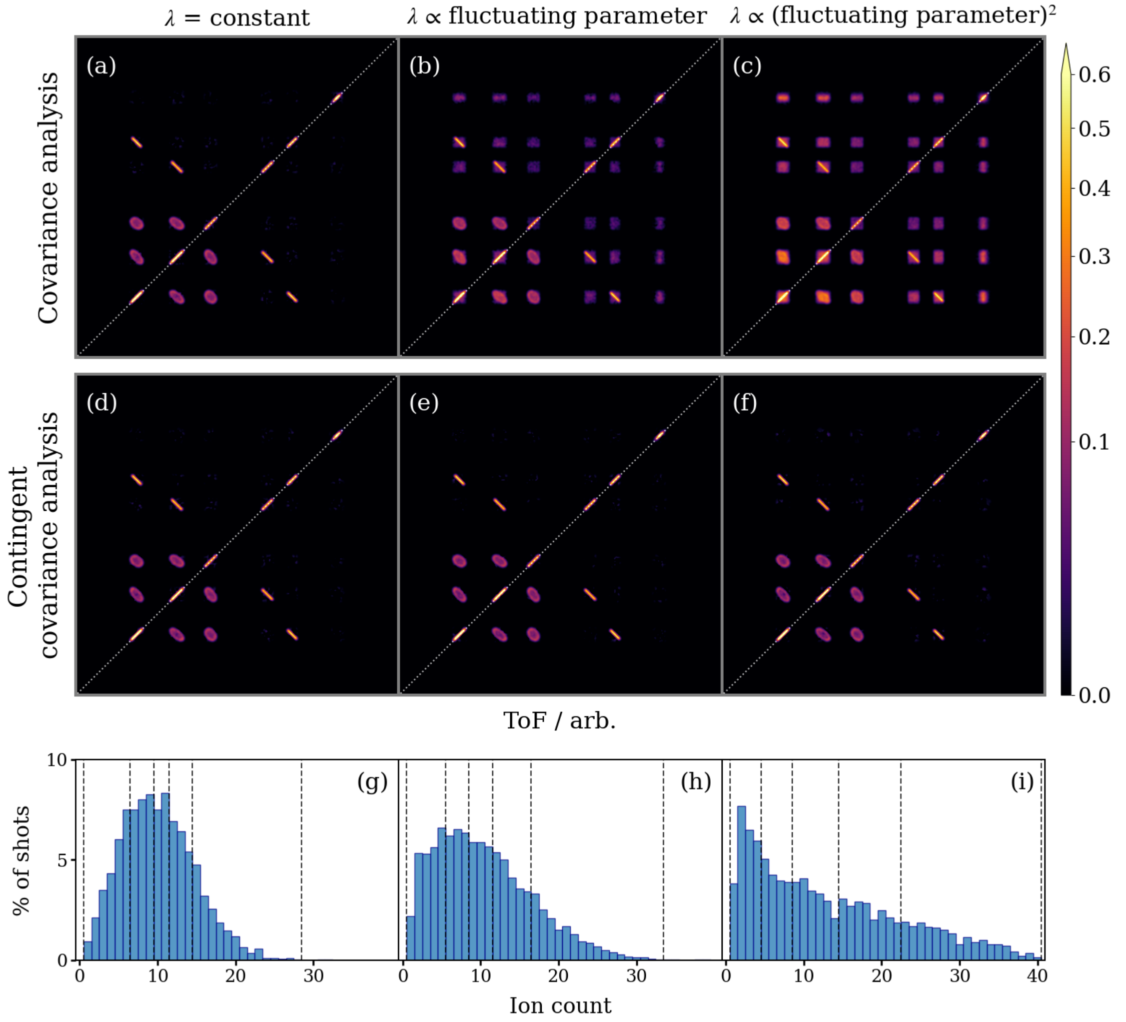

Figure 3.9: Simulated ToF (*top row*) covariance and (*centre row*) contingent covariance maps for the reaction scheme presented in Equation 3.4. Each map is normalised separately. Data were simulated for 1×10^4 ionisation events and grouped into laser shots with either (a, d) no dependence, (b, e) a linear dependence or (c, f) a quadratic dependence of the average number of parent molecules probed on a parameter that fluctuates 25-175%. The ion count distribution for each scenario is displayed in the *bottom row*. Vertical dashed lines indicate the boundaries of the bins used for the contingent covariance calculation.

3.4.1 Partial covariance analysis

Whilst efforts can be made to achieve stable experimental conditions, in some scenarios this is not possible. A notable example is when conducting laser-induced CEI experiments using a SASE FEL, as these light sources are inherently stochastic, and shot-to-shot variation in the pulse energy is unavoidable. Instead, one must turn to measures that correct for the false correlations induced in the covariance map. For this purpose, Frasinski *et al.* developed partial covariance analysis wherein the correlation between the fluctuating parameter (I) and the parameters of interest ($A,\ B$) is calculated.[169,170] This term is subtracted from the covariance map to isolate the correlation of the parameters of interest:

$$\mathrm{pcov}((A,B),I) = \mathrm{cov}(A,B) - \frac{\mathrm{cov}(A,I)\,\mathrm{cov}(I,B)}{\mathrm{cov}(I,I)}. \tag{3.6}$$

This analysis can also be extend to correct for the effect of several fluctuating parameters.[155]

Partial covariance mapping was first demonstrated for calculating ToF covariance maps from data collected at a FEL, where the fluctuating parameter considered was the XUV pulse energy.[170] The technique was partially successful. To completely suppress the false correlations the weighting of correction term had to be arbitrarily increased by 10%, implying that the technique had not fully captured the correlation between the fluctuating parameter(s) and total ion count. Perhaps this was because partial covariance analysis assumes that the ionisation rate is linearly dependent on the fluctuating parameter, whereas multi-photon ionisation processes typically scale non-linearly with pulse intensity.

Another disadvantage of partial covariance analysis is that it requires prior knowledge of any fluctuating experimental parameters, and relies on being able to measure those parameters on a shot-by-shot basis. Later, an alternative method of accounting for unstable experimental conditions was developed that circumvents these issues, known as contingent covariance analysis.[155]

3.4.2 Contingent covariance analysis

Contingent covariance analysis corrects for the effect of a fluctuating parameter that influences the total ion signal by dividing the dataset into smaller subsets, over which the fluctuating parameter is approximately constant.[155] The covariance map is calculated separately for each subset, for which the false correlations are minimal. The resulting set of covariance maps is then averaged to give the final result.

The ToF covariance maps in the central row of Figure 3.9 have been calculated using a contingent covariance analysis. Each simulated dataset was grouped into five smaller subsets containing equal numbers of laser shots, based on the total ion count per laser shot distribution. Data can be divided into bins based on the distribution of the fluctuating parameter, but the total ion count per laser shot serves as a proxy for any number of fluctuating parameters, eliminating the need to measure each independently.[171,172] After applying a contingent covariance analysis to the dataset with λ proportional to a fluctuating parameter, the result covariance map, shown in panel (e), is free of false correlations.

Overall, contingent covariance analysis is more straightforward to implement than partial covariance analysis, as it does not require calculation of the correction term in Equation 3.6. In addition, the calculation of a contingent covariance map lends itself well to parallel computing, which involves dividing up a calculation into several smaller calculations that can be run simultaneously across several cores of a computer. In this case, the covariance maps for multiple separate subsets can be calculated in parallel to reduce the computation time.

Another advantage of contingent covariance analysis when compared with partial covariance analysis is that it is applicable even when the ionisation rate scales non-linearly with the fluctuating parameter. To demonstrate, the covariance maps in panels (c) and (f) were calculated for a simulated dataset where λ is proportional to the square of the fluctuating parameter. The false correlations in the standard covariance map are more intense, but the contingent covariance map is unchanged in appearance.

For all of the reasons outlined here, contingent covariance analysis was preferred over partial covariance for the work presented in this thesis. As illustrated by Figure 3.2, a contingent covariance analysis always gives the same or better result than a standard covariance analysis, *i.e.* there is no negative consequence of applying contingent covariance analysis. Hence, contingent covariance analysis was used to calculate all of the experimental covariance maps presented in this thesis.

3.5 Covariant momentum mapping

Rather than calculating the covariance map between the 2D spatial coordinates of ion images, it is a more versatile approach to calculate the covariance map between fragment ion momentum vectors. In the current work, this is referred to as covariant momentum mapping. First introduced by Allum *et al.*,[81] this thesis explores the full potential of the technique. Examining the correlations between fragment ions in terms of their relative momenta is the conventional approach for CEI studies that perform coincidence mapping. This is because such studies typically employ DLA detectors, capable of recording the 3D momentum information for each ion. The most immediate advantage of working in terms of 3D fragment momenta is that it allows the relative momentum of fragments to be visualised and transformed in three dimensions.

Figure 3.10(a) is a simulated three-fold covariance map of the correlated fragment momenta for the Coulomb explosion of a prototypical bent triatomic molecule ABC into $A^+ + B^+ + C^+$. Similar to a recoil-frame covariance map, the momentum of A^+ is constrained to one axis, in this case the positive x-axis, and the relative *momenta* of B^+ and C^+ are plotted on the top and bottom halves of the diagram. This representation is known as a Newton diagram.[74] Compared to the recoil-frame covariance maps considered earlier in Section 3.2, the correlated features in Figure 3.10(a) are not smeared towards the origin. This is because each trio of correlated fragment momentum vectors can be orientated in three dimensions to align with the plane of the image, which fully defines the molecular orientation prior to Coulomb explosion.

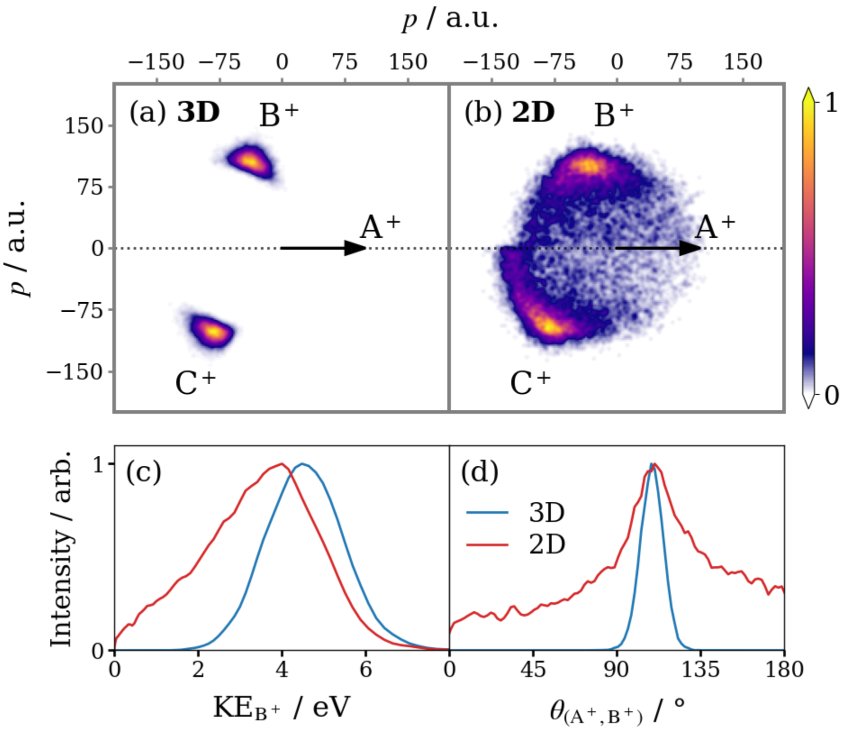

Figure 3.10: Simulated Newton diagram covariance maps for the concerted three-body breakup of a triatomic polycation ABC^{3+} into $A^+ + B^+ + C^+$. Calculated using (a) the 3D fragment momenta and (b) 2D projected fragment momenta. Each panel is normalised separately. Below the (c) B^+ KE and (d) (A^+, B^+) relative recoil angle distributions are overlaid.

Working in terms of fragment momenta greatly expands the array of available analysis tools. As Figure 3.10(a) demonstrates, by considering the momenta of fragments in common units the relative momenta of several ions can be plotted together. This can provide a more intuitive depiction of the Coulomb explosion process. For example, being able to visualise the relative recoil of all three fragments from the breakup of ABC^{3+} illustrates how they mutually repel apart in separate directions.

In addition, the fragment momentum vectors can be used to define new frames of reference. A Newton diagram is defined in a similar way to a recoil-frame covariance map by using the momentum of one ion species to define an axis. An alternative reference frame might define a plane from a pair of momentum vectors, or an axis based on their bisector, etc. In this way, the frame can be tailored for the molecular system under study to provide insight into the dynamics of fragmentation and starting nuclear structure. This thesis makes use of an assortment of different reference frames for presenting momentum correlation maps, which are introduced as required. Section 3.6 describes a specific example that is useful for investigating sequential fragmentation mechanisms.

3.5.1 Two-dimensional projected-momentum mapping

If the timing resolution of the ion detection system is not sufficient to reconstruct the out-of-plane component of an ion's momentum, only a 2D projection of the ion momenta is recorded. This is a limitation of the experimental work described in Chapters 6 and 7. The conventional method of examining the fragment ion correlations for a CEI experiment that employs 2D ion imaging is recoil-frame covariance imaging. To take advantage of the benefits of covariant momentum mapping, the present work introduces 2D protected-momentum covariance mapping as an alternative. The effect of constructing a momentum correlation map from 2D projected-momentum information is demonstrated by Figure 3.10. Whilst the Newton diagram in panel (a) was calculated using the 3D $(p_x,\ p_y,\ p_z)$ momentum information for each simulated ion, panel (b) was calculated using only $(p_x,\ p_y)$ momentum information.

The transformation from 3D to 2D projected fragment momentum information is analogous to crushing a sphere onto a plane, which explains why the projected-momentum distribution is smeared across all angles, but only toward lower radii. Despite the modest blur, the peaks in the distribution remain distinct. From inspection of the integrated distributions in the lower panels of Figure 3.10, the angle of maximum intensity is unchanged, whilst the peak in the radial distribution is shifted down in magnitude slightly. This means fragment KE appear slightly below their true values when measured from 2D projected-momenta.

3.5.2 Application of momentum constraints

This thesis introduces the concept of applying a fragment momentum constraint in a covariance calculation. It is perhaps the most powerful tool that working in terms of fragment momenta gives access to. Filtering the raw dataset based on ion momenta is regularly exploited in coincidence ion imaging studies to identify and remove false coincidence events. The most common approach is to focus on 'complete' coincidence events where the detected fragments together constitute the original molecule. True coincidences can then be isolated by selecting only those combinations of ions whose momenta sum to zero.[13,20,21,76,78,79] The same constraint can be applied prior to performing a covariance calculation. For a dataset acquired at a high count rate, such a filter typically will not remove all combinations of ions that are falsely correlated, but a sizeable percentage. This effectively increases the signal-to-noise ratio of the resulting dataset, thereby reducing noise in the calculated covariance map.

Figure 3.11(a) and (b) are three-fold covariance maps of the correlated fragment momenta for three-body breakup of triatomic ABC^{3+}, simulated for two different values of λ. Whilst covariance mapping is effective at isolating the true correlations from the background of falsely correlated events, the technique has its limitations. When on average five parent molecules are probed per laser shot, the correlated features in the covariance map are clear. If this number is increased by an order of magnitude, the covariance map becomes dominated by noise. This can be understood in terms of the average number of possible ion combinations per laser shot. For $\lambda = 5$ there are on average 210 unique combinations of (A^+, B^+, C^+) that need to be considered in every shot. Increasing λ to 50 raises the number to over 130,000.

If only those ion combinations that approximately obey momentum conservation are considered, the noise in the covariance map can be substantially reduced. Panels (c) and (d) were both calculated using a constraint on the fragment momentum sum of ± 5 a.u. to select the ion combinations used as input for the covariance calculation. This filter reduces the average number of ion combinations per shot to 5.1 and 54 for the $\lambda = 5$ and 50 datasets, respectively, *i.e.* nearly all combinations of falsely correlated ions have been removed. As a result the correlated signal is well resolved even in the covariance map for the high count rate dataset.

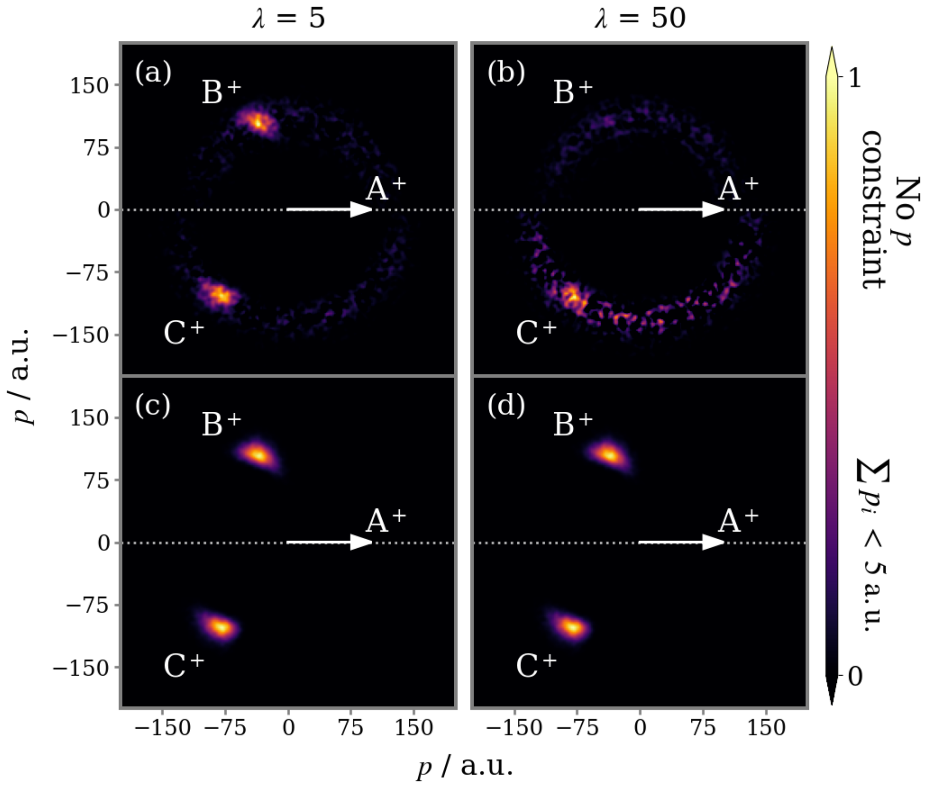

Figure 3.11: Simulated Newton diagram covariance maps for the concerted three-body breakup of triatomic ABC^{3+} into A$^+$ + B$^+$ + C$^+$. Data were simulated for 1×10^4 ionisation events and grouped into laser shots with an average number of parent molecules probed of (a, b) 5 shot^{-1} and (c, d) 50 shot^{-1}. Panels (a) and (c) were calculated from all (A$^+$, B$^+$, C$^+$) combinations, and panels (b) and (d) from only those with an absolute momentum sum < 5 a.u. Each is normalised separately.

This demonstration only scratches the surface of what can be achieved using fragment momentum constraints. An appropriate constraint can also be used, for example, to distinguish between dissociation pathways that yield the same product ions via different mechanisms. These concepts are explored in detail as part of the work described in Chapter 5.

3.6 Covariant native frames analysis

Many-body molecular fragmentation processes are considered to occur in two regimes, sequential and concerted.[73,173] If the bonds are broken within the approximate timescale of a single vibration, the fragmentation is said to be concerted. To use the example of the three-body breakup of triatomic ABC^{3+} again, the concerted mechanism is:

$$\mathrm{ABC^{3+} \rightarrow A^{+} + B^{+} + C^{+}}, \tag{3.7}$$

Alternatively, in a sequential regime the fragmentation occurs in two distinct, independent two-body dissociations. First, a primary fragmentation produces a stable product and a metastable intermediate and, after some finite time, the intermediate fragments further into the secondary products, for example:

$$\begin{aligned} \mathrm{ABC^{3+}} &\rightarrow \mathrm{A^{+} + BC^{2+}}, \\ \mathrm{BC^{2+}} &\rightarrow \mathrm{B^{+} + C^{+}}. \end{aligned} \tag{3.8}$$

Because the concerted and sequential fragmentation mechanisms are two alternative pathways that can yield the same product ions, being able to distinguish between these processes is an important goal in the field of reaction dynamics. This is especially true concerning the technique of CEI, which relies on concerted breakup of the molecular ion in order to extract geometric information from the relative momenta of the fragment ions. Rajput *et al.* introduced a method for disentangling sequential three-body fragmentation events based on analysing each of the fragmentation steps in their own ‘native’ frame of reference.[174] The first step is analysed in the Centre-of-Mass (CoM) frame of the parent ion, and the second in the CoM frame of the intermediate ion. In this thesis, the native frames analysis approach is combined with covariant momentum mapping.

To demonstrate, a simulated Newton diagram three-fold covariance map for the fragmentation mechanism outlined in Equation 3.8 is shown in left panel of Figure 3.12. If the intermediate ion is rotationally excited by the initial dissociation, it causes the momenta of the secondary products to be distributed over an angular span relative to the momentum of the primary product.[174,175] The simulation assumes the lifetime of the intermediate greatly exceeds its rotational period, such that the relative angle can take any value. Full details are provided in Section 4.4.1. The result is the semicircular distributions seen in the Newton diagram, which is a characteristic signature of a sequential three-body breakup.[74,75]

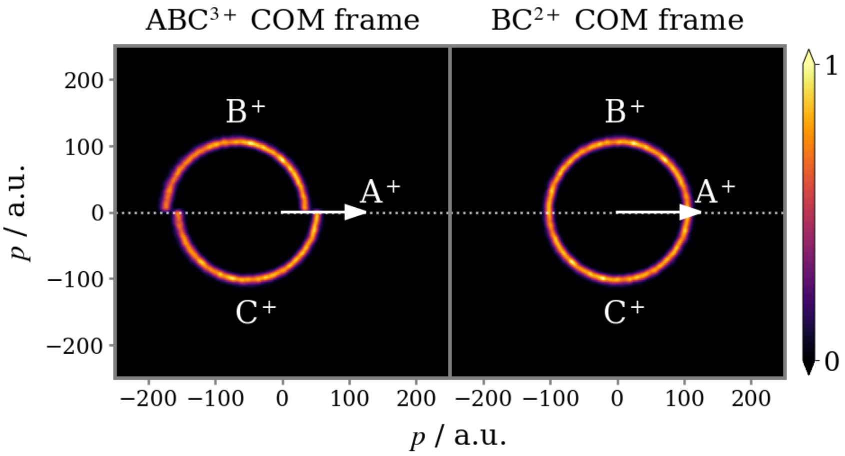

Figure 3.12: Simulated Newton diagram covariance maps for the sequential three-body dissociation scheme described in Equation 3.8. The left panel displays the fragment momenta in the CoM frame of the parent trication, whilst in the right panel the fragment momenta have been transformed into the CoM frame of the BC^{2+} intermediate. Each panel is normalised separately.

The momentum imparted to the intermediate (BC^{2+}) by the primary fragmentation is equal and opposite to the momentum of the primary product (A^+). When applying covariance analysis, the contribution this makes to the momenta of the products of the delayed fragmentation can be calculated based on their respective masses, and subtracted in order to produce a covariance map in the CoM frame of the intermediate ion. This transformation is possible only when working in terms of the fragment momenta, as opposed to their positions on the detector. In resulting covariance map, shown in the right panel of Figure 3.12, the momenta of the secondary products are necessarily equal and opposite.

3.7 Cumulant mapping

For many years, a major disadvantage of covariance mapping when compared with coincidence mapping was that covariance analysis was not established for more than three variables. CEI experiments that utilise coincidence mapping regularly probe the correlation of four or five ions,[13,77,78] and a recent study even extend this as high as eight ions.[20] The intrinsic advantage of being able to probe correlations between a higher number of fragments is that it offers more information about the molecular structure. This is particularly important as CEI is progressively scaled up to study larger molecules with more complex structure.

The issue when considering the covariance of four or more variables is that it is possible to have contributions between individual pairs of variables that are independent of the collective correlation between all the variables. Assuming the number of fragments generated in an experiments follows a Poisson distribution, it can be shown:[155]

$$\begin{aligned}\mathrm{cov}(A,B) &= \langle N_{AB}\rangle,\\ \mathrm{cov}(A,B,C) &= \langle N_{ABC}\rangle,\\ \mathrm{cov}(A,B,C,D) &= \langle N_{ABCD}\rangle + \sum^{3}\langle N_{AB}\rangle\langle N_{DC}\rangle,\end{aligned} \tag{3.9}$$

where N_{AB} denotes the number of events in which A and B are generated together. The values of two- and three-fold covariance are dictated only by the correlation between two and three variables, respectively. The four-fold covariance also contains contributions from pairwise correlations of the four variables, where the sum in Equation 3.9 is over the three ways of pairing the four variables. This means that it is possible to measure a positive covariance between A, B, C and D that are not collectively correlated if, for example, A is independently correlated with B, and C with D.

Recently, a solution was proposed. By introducing a correction factor, the formula can be modified to capture only the collective correlations between n variables, called the nth cumulant (χ_n):[156]

$$\begin{aligned}\chi_2(A,B) &= \mathrm{cov}(A,B),\\ \chi_3(A,B,C) &= \mathrm{cov}(A,B,C), \\ \chi_4(A,B,C,D) &= \mathrm{cov}(A,B,C,D) - \sum^{3} \mathrm{cov}(A,B)\mathrm{cov}(C,D).\end{aligned} \tag{3.10}$$

Note that the 2nd and 3rd cumulants are equivalent to two- and three-fold covariance, respectively. Four-fold cumulant mapping has already been demonstrated on the four-body breakup of quadruply ionised formaldehyde, prepared by an intense NIR femtosecond laser pulse.[176] The correlated momenta of the four fragment ions, plotted in Figure 3.13, bear clear resemblance to the structure of the parent molecule.

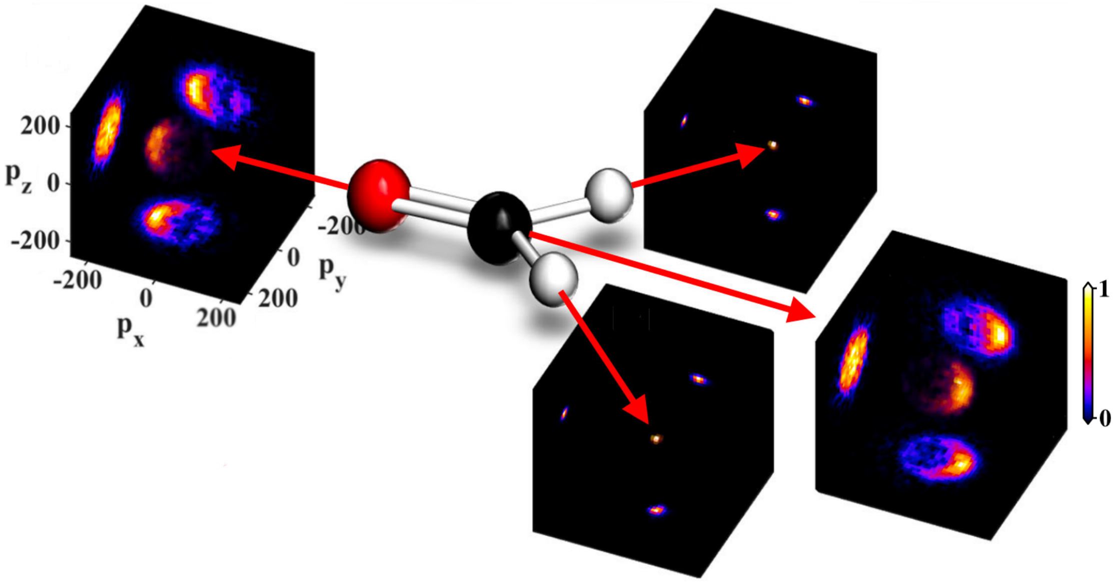

Figure 3.13: Four-fold cumulant map of the correlated momenta of the $C^+ + 2H^+ + O^+$ fragments from the breakup of formaldehyde, following quadruple ionisation by an intense NIR femtosecond laser pulse. The xy-plane is defined by the momenta of the two protons, with the positive x-axis defined by their bisector. Adapted from Reference [176].

3.8 Summary and outlook

This chapter has given a detailed account of covariance mapping applied to the fragmentation of molecular polycations, included all variations of covariance mapping that are utilised as part of the data analysis in later chapters. Specifically, Chapter 5 presents results from a 3D ion imaging study which are analysed using 3D momentum covariance mapping. The study represents the first application of the covariant native frames approach and of fragment momentum constraints in a covariance calculation. Together, these techniques are used to isolate and interrogate specific fragmentation channels in detail. In Chapter 6 a similar analysis is performed for a 2D ion imaging dataset to showcase 2D projected-momentum covariance mapping.

Multi-dimensional cumulant mapping, which extends covariance mapping to four-fold and higher correlations, is anticipated to be of great utility moving forwards. The initial experiments of Cheng *et al.*[176] have demonstrated that cumulant mapping is capable of producing comparable results to contemporary coincidence mapping studies. This raises the question as to what will ultimately prove the most effective method for laser-induced CEI: operating at a low ion count rate and measuring the fragment ions in coincidence, or operating at a higher ion count rate and extracting the correlated ion signals by calculating the nth cumulant.

It is reasonable to expect the latter scenario to produce the same results on a faster timescale due to the increased rate of data acquisition. However, operating at a higher ion count rate increases the proportion of false coincidence events, meaning that a greater number of observations will be required to suppress the noise to an acceptable level. The noise-to-signal-ratio (N:S) as a function of λ, assuming $\eta = 100\%$ and no background counts, is plotted for the first four cumulants in Figure 3.14.[156] As the dimensionality increases, so too does the noise for a given value of λ. The higher order the cumulant, the more subtraction of lower order correlations is required, each of which contributes more noise.

With increasing λ, the noise of the first cumulant (the spectrum) approaches zero. This is intuitive, as it is always advantageous to measure a spectrum at maximum count rate. The N:S of the second cumulant also decreases with λ, approaching a constant value of $\sqrt{2}$. This would suggest it is also optimum to measure a two-fold covariance map at maximum count rate, but only because the impact of a non-uniform detection efficiency has been neglected. Even so, it remains effective to measure two-fold covariance at high count rate.

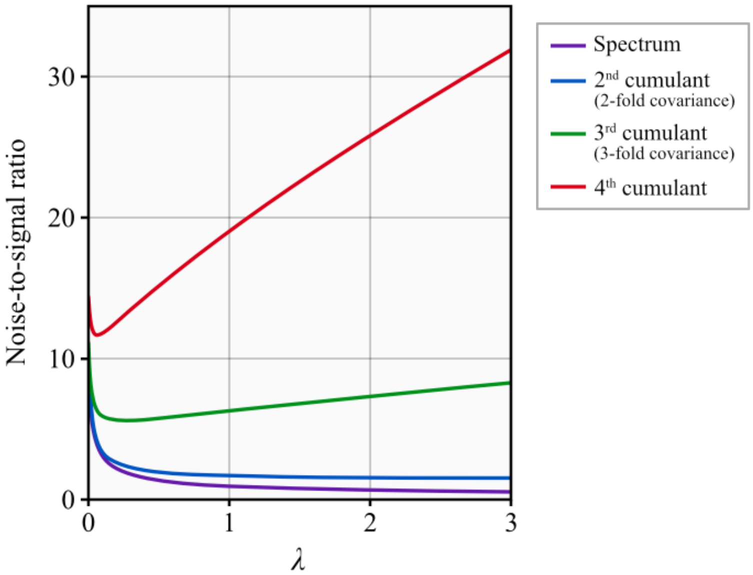

Figure 3.14: Noise-to-signal ratio for the first four cumulants as a function of the average number of parent molecules ionised per laser shot (λ). Calculated for ideal conditions with 100% ion detection efficiency and no background. For third and higher order cumulants, the statistical noise is minimal at low count rate (< 1). Adapted from Reference [156].

For third- and higher-order cumulants the N:S rises with λ, producing a minimum that indicates an optimum count rate. Notably, the optimum λ is below 1 even for three-fold covarianc, hence, it is inefficient to measure correlations between three or more particles at a high count rate. The position of the minimum shifts lower as the cumulant order increases, implying that to measure a many-body correlation it is most appropriate to operate under coincidence conditions.

It remains to be seen how this idealised theory will compare with the results of experiment. Reference [156] contains a discussion of other important factors including detection efficiency and background counts. For example, each time the cumulant order is increased, the signal decreases because it is multiplied by the detection efficiency. The analysis presented here also disregards key techniques such as fragment momentum filtering which, as demonstrated in Section 3.5.2, can effectually reduce the count rate of a dataset by removing false coincidence events. In the future, a study that explores the convergence of the nth cumulant as a function of ion count rate would be of great interest.

Given the limitation that statistics imposes on the count rate of a multi-particle correlation experiment, recent efforts in the field of CEI have focused on increasing the sampling rate. This is especially important as studies endeavour to measure higher-fold correlations in order to study larger and more complex molecular systems. New high repetition rate laser sources have offered the greatest increases in experimental cycle speed, but experiments are now close to reaching a ceiling. Because the average ion ToF in a ion imaging spectrometer is several μs, as the repetition rate approaches $\sim 10^6$ Hz the time interval between laser shots becomes shorter than span of the ToF spectrum, and ions generated in separate laser shots begin to overlap.

4

Classical simulations of Coulomb explosion

Contents

CEI is often described in terms of measuring the momenta of the fragment ions and using this information to reconstruct the molecular structure at the instant of fragmentation. However, working backwards from the final fragment momenta to the starting molecular structure through a 'reverse' Coulomb explosion is not straightforward for polyatomic systems. It is much more practical to use a forward simulation process, where the initial conditions of the system are assumed and the Coulomb explosion process simulated by calculating the ion trajectories. The simulated final fragment momenta may then be compared to the experimentally measured values in order to advise the starting parameters. These are refined and the simulation repeated in an iterative procedure until satisfactory agreement between the simulation and experiment is achieved. At this point, the starting conditions of the simulation should provide an accurate impression of the original molecular structure.

Coulomb explosion is an inherently complex process, involving ionisation, charge redistribution, and molecular fragmentation all occurring on an ultrafast timescale. But as a first approximation, the process can be modelled by classical mechanics calculations of point charges interacting exclusively under Coulomb's law, assuming an instantaneously imposed charge distribution. Such simulations have proven remarkably successful at predicting the relative recoil angle of the fragments from a Coulomb explosion for various molecules of different size and chemical constitution.[19,21,23,177–179] This model will provide a better approximation the more prompt the Coulomb explosion event, which limits the time window for nuclear dynamics to occur during the ionisation process.[62,176] Practically, this is achieved by minimising the duration of the initiating laser pulse and ionising target molecules to a high charge state. The approximation also improves when considering the motion of heavy nuclei, which are less easily perturbed.[18]

A limited number of studies have been performed that utilise more complex modelling methods. Reduced-dimensionality *ab initio* potential energy surfaces have been used to investigate the two-body Coulomb explosion of CH_3I into CH_3^+ + I^+.[151,154] Molecular dynamics simulations have been used to study the Coulomb explosion of aromatic molecules including benzene,[180] hexafluorobenzene[181] and C_{60}.[182] Recently, Zhou *et al.* conducted a comprehensive on-the-fly *an initio* trajectory study of the Coulomb explosion dynamics for prototypical small molecules.[183] This considered all of the relevant chemical binding forces and degrees of freedom in parallel with the Coulomb repulsion, in order to explore how the mapping between the initial atomic positions and final fragment momenta varies as a function of the charge state of the parent polycation (Z). They reported a complex mapping for low Z, which is very sensitive to the initial parameters. For high Z they found that the mapping becomes more straightforward and a purely Coulombic model provides a good first-order description of the Coulomb explosion dynamics.

Throughout this thesis, forward simulations of the Coulomb explosion process are used to guide the interpretation of Coulomb explosion images. Although a comprehensive model that considers all of the relevant chemical interactions would be more accurate, for the sake of efficiency, in this work a simple model that considers only the Coulombic forces acting between ions is applied. The model presented is able to simulate thousands of Coulomb explosion trajectories in minutes in order to simulate a dataset with a realistic distribution of starting conditions. The simulated data can then be processed in the same manner as experimental data for comparison.

To begin, the fundamentals of the model are described. The base version closely resembles the classical model of interacting point charges established by earlier studies.[19,178,179] The focus of this chapter is how this basic framework can be modified to recreate the dynamics of more complex molecular fragmentation processes. Previous applications have mainly attempted to simulate concerted dissociation dynamics. This chapter discusses how sequential dissociation dynamics can be simulated by chaining together trajectory calculations in a manner that recreates the steps of the fragmentation mechanism. This methodology is extended further to design a simple simulation of the molecular dynamics in a TR-CEI experiment.

4.1 Computational details

Coulomb explosion is modelled by assuming instantaneous fragmentation into initially stationary fragments. The fragments are represented by point charges with their starting positions defined by the initial molecular structure and the fragment centres-of-mass. For a given molecule, the equilibrium geometry at the instant of explosion was specified to be the lowest energy neutral ground state geometry, determined with the Gaussian software package using the B3LYP density functional method and 6-311G basis set. The charges assigned to the fragments are chosen to simulate a specific Coulomb explosion channel of interest and are fixed throughout, *i.e.* no charge redistribution occurs.

The interactions between fragment ions are assumed to be entirely Coulombic in nature, with no contribution from the bonding interactions of the molecule. Under these condition, the motions of the ions in each dimension are described by a set of coupled second-order differential equations:[19]

$$\begin{aligned} m_i u \frac{d^2 x_i}{dt^2} &= \frac{e^2}{4\pi\epsilon_0} \sum_{j\neq i}^{N} \frac{q_i q_j (x_i - x_j)}{|x_i - x_j|^3}, \\ m_i u \frac{d^2 y_i}{dt^2} &= \frac{e^2}{4\pi\epsilon_0} \sum_{j\neq i}^{N} \frac{q_i q_j (y_i - y_j)}{|y_i - y_j|^3}, \\ m_i u \frac{d^2 z_i}{dt^2} &= \frac{e^2}{4\pi\epsilon_0} \sum_{j\neq i}^{N} \frac{q_i q_j (z_i - z_j)}{|z_i - z_j|^3}, \end{aligned} \tag{4.1}$$

where the sum is over all pairwise interactions between ions i and j. m_i, q_i and $(x_i,\ y_i,\ z_i)$ are the mass, charge and 3D spatial coordinates of ion i, respectively, with u, e and ϵ_0 being the atomic mass unit, elementary charge and vacuum permittivity constant.

The ion trajectories are solved numerically using an iterative procedure, wherein the equations of motion are solved to determine the ion velocities, the system is allowed to evolve for a short time step, and then the procedure is repeated. This is implemented by an ordinary differential equation solver from the SciPy

Python library[184] using a fourth-order explicit Runge–Kutta algorithm. This method evaluates the function at several points within each time step in order to significantly reduce the cumulative error. The ion trajectories are propagated until they have approximately reached their terminal velocities, which is typically within a few picoseconds. For the first 100 fs, when the ions are close together and their trajectories are very sensitive to their relative positions, the trajectories are propagated using femtosecond steps. Beyond this larger steps of tens of fs are used for computational efficiency.

4.2 Ion trajectories

Figure 4.1 plots the trajectories of the ions from the Coulomb explosion of a prototypical triatomic molecule ABC:

$$\mathrm{ABC}^{3+} \rightarrow \mathrm{A}^{+} + \mathrm{B}^{+} + \mathrm{C}^{+}. \tag{4.2}$$

At the start of the simulation, the three ions are arranged in the positions of the atoms in the original molecule. Specifically, the A-B and B-C bonds were chosen to be the same length, and the A-B-C bond angle was bent at 120°. Because the geometry of molecule at the start of the simulation is confined to the xy plane, the ion trajectories in Figure 4.1 are also confined to this 2D plane.

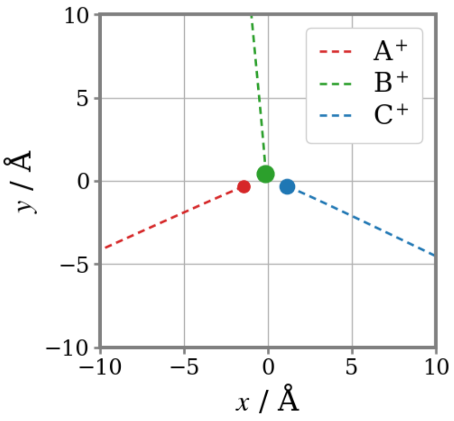

Figure 4.1: Simulated ion trajectories for the concerted three-body breakup of triatomic ABC^{3+} into $\mathrm{A}^+ + \mathrm{B}^+ + \mathrm{C}^+$. The geometry of ABC is planar, hence the ion trajectories are confined to the xy-plane.

The relative recoil directions of the three ions provides a good impression of the triangular geometry of ABC. Although the initial arrangement of the ions is symmetric, their trajectories are asymmetric due to the mass imbalance between A^+ and C^+. The atoms A, B and C were assigned masses of 10, 20 and 15 u respectively. Because A^+ is lighter, it experiences greater acceleration and quickly separates from the other two ions. C^+ spends longer in the vicinity of B^+ and therefore exerts a greater impulse upon it, causing B^+ to recoil slightly into the negative x direction.

Figure 4.2 displays the absolute fragment momenta as a function of time after the start of the simulation. The Coulomb explosion process is characterised by rapid initial acceleration of fragments, which decays as time elapses, their separation increases, and the electrostatic forces between them diminish. The atoms that constitute ABC are relatively light and fly apart fast, so the timescale of the Coulomb explosion is short. Beyond ∼200 fs the ions are separated to an extent that Coulombic interaction is no longer significant. At this point their momenta have visibly plateaued and the simulation is terminated.

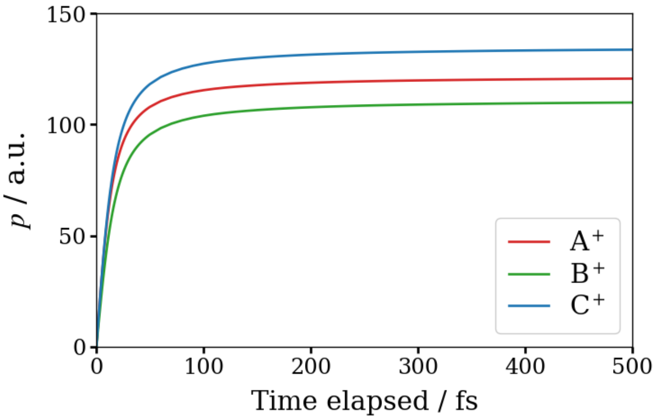

Figure 4.2: Simulated fragment momenta for the concerted three-body breakup of triatomic ABC^{3+} into $A^+ + B^+ + C^+$.

4.3 Simulating experimental data

The model presented in the previous section provides valuable insight into the behaviour of fragment ions during Coulomb explosion. However, the simulation has been concerned with the Coulomb explosion of a single parent molecule, which is to neglect the vast number of initial starting conditions that are possible. Most importantly, in an experiment molecules will exist in one of many configurations due to vibrational motion. In order to achieve an accurate simulation of experimental data it is necessary to run a series of trajectories with an appropriate distribution of starting geometries.

A quantitative method for generating an ensemble of starting geometries is to sample a probability distribution of potential ground-state configurations by allowing for zero-point vibrational motion.[178] In this thesis, a qualitative approach is taken wherein the atomic positions for each trajectory are sampled from a distribution that incorporates key vibrational modes. For example, to recreate a bond stretching mode, the relevant bond length is sampled from a Gaussian distribution which is centred at the equilibrium geometry bond length, and has a width equal to a small fraction of the central value.

Fragment positions are also collectively rotated in three-dimensions by a random angle at the start of each trajectory to simulate an isotropic distribution of molecules. Considering how the molecules are orientated in an experiment is primarily important for simulating accurate laboratory frame ion images. In the current work, simulated data are used exclusively to generate correlated momentum maps. With 3D fragment momentum information, the molecular orientation prior to Coulomb explosion can be fully defined in the molecular frame, in which case the distribution in the laboratory frame has no influence. If the correlation map is calculated using 2D projected fragment momenta, though, the molecular orientation is not fully defined, so the orientation in the laboratory frame is significant.

With these additional layers of averaging included in the ion trajectory simulation routine, it becomes possible to simulate a complete dataset. The simulation is typically run over several thousand trajectories to generate an array of ionisation events. These are grouped according to Poisson statistics to imitate the distribution of parent molecules ionised per laser shot in an experiment. In this way, data can be simulated under idealised coincidence conditions, with exactly one ionisation event per laser shot, or high count rate conditions that demand covariance analysis. In the output dataset, the chemical identity, final $(p_x,\ p_y,\ p_z)$ momentum, and a laser shot identifier are saved for each ion. This is equivalent to the information recorded in an experiment, allowing the simulated data to be processed using the same collection of analysis algorithms.

4.3.1 Momentum correlation maps

For demonstration, the correlated final fragment momenta of $A^+ + B^+ + C^+$ from the trajectory shown in Figure 4.1 are plotted as a Newton diagram in Figure 4.3(a), with A^+ selected as the reference ion. Because the correlation map is constructed from a single set of correlated momentum vectors, these appear as individual points on the diagram. The adjacent panel shows the correlation map constructed from a simulated dataset of 1×10^4 trajectories, where the starting geometry for each trajectory was sampled from a distribution that incorporates the A-B-C bending, symmetric stretching and antisymmetric stretching modes.

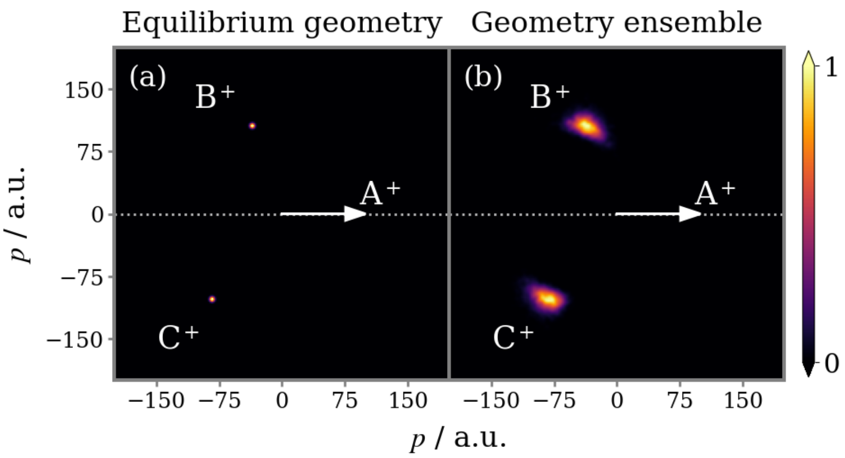

Figure 4.3: Simulated Newton diagram correlation maps for the concerted three-body breakup of triatomic ABC^{3+} into $A^+ + B^+ + C^+$. Panel (a) displays the correlated fragment momenta for a simulation initiated from the equilibrium geometry, whilst panel (b) displays the correlated momenta for an ensemble of starting geometries, intended to approximate ground-state vibrational motion.

The KER of the Coulomb explosion and the relative recoil angles of the fragments are sensitive to the initial atomic positions, hence, the variation of the molecular structure is reflected in the distribution of the correlated signals in the momentum map. Overall, the diffuse appearance of the features in Figure 4.3(b) provides a realistic recreation of an experimentally measured correlation map for a concerted breakup channel.

4.4 Sequential three-body fragmentation model

The Coulomb explosion model described thus far is a model of a concerted fragmentation mechanism, wherein the product ions are all formed concurrently. One of the main reasons why a model that assumes instantaneous fragmentation often fails to reproduce the Coulomb explosion dynamics of low charged parent ions is that such species may fragment via a sequential mechanism.[23,73–75,174,175,177] For example, in a sequential three-body mechanism, an initial fragmentation produces a stable product and a metastable intermediate that, after some finite time, further fragments further into the secondary products.[73]

The approach introduced for simulating sequential three-body fragmentation is to execute the trajectory in two distinct steps, which model the primary and secondary fragmentation steps, respectively. Practically, this is achieved by chaining together two trajectory calculations, where the output parameters of the first are used as input parameters for the second. The model detailed here that involves two stages is the simplest version. It can be extended to include additional stages in order to recreate a fragmentation mechanism involving any number of sequential steps.

4.4.1 Fragmentation into exclusively charged fragments

First, the case of a three-body fragmentation that yields three ionic fragments is considered. To use the example of the Coulomb explosion of triatomic ABC^{3+} again, a potential sequential mechanism is:

$$\begin{aligned} ABC^{3+} &\rightarrow A^{+} + BC^{2+}, \\ BC^{2+} &\rightarrow B^{+} + C^{+}. \end{aligned} \tag{4.3}$$

The first step of the simulation is the Coulomb explosion of A^{+} + BC^{2+}. Initially, it is assumed that the intermediate lifetime is sufficiently long that the two fragmentation steps are isolated events. The trajectories of A^{+} and BC^{2+} are therefore propagated until they have approximately reached their terminal velocities.

The second step is Coulomb explosion of (A^{+} +) B^{+} + C^{+}. This is initiated by replacing BC^{2+} with B^{+} and C^{+} – separated by the same distance as in the initial molecular structure. A key consideration for a sequential three-body fragmentation event is how the intermediate ion is rotationally excited by the primary step. The simulation assumes the lifetime of the intermediate greatly exceeds its rotational period, therefore B^{+} and C^{+} are rotated in-plane through an angle sampled from a uniform distribution. Finally, the trajectories of the A^{+}, B^{+} and C^{+} ions are propagated until they have once again reached tangential velocities.

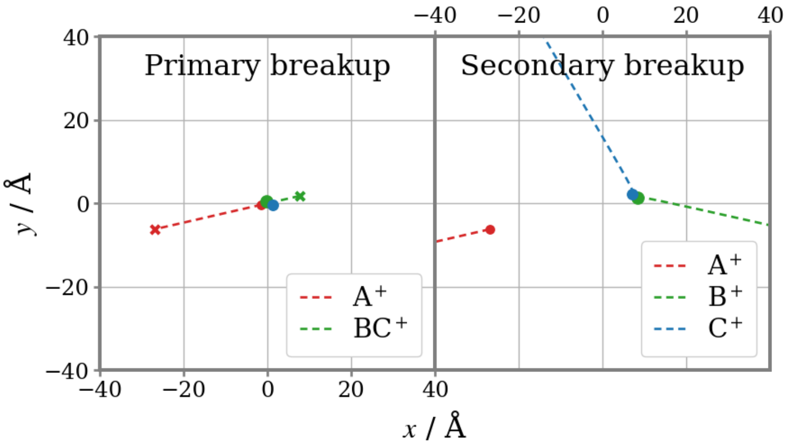

Figure 4.4: Simulated ion trajectories for the sequential three-body dissociation scheme described in Equation 4.3. (a) Coulomb explosion of A^{+} + BC^{2+}. (b) Subsequent breakup of the BC^{2+} into B^{+} + C^{+}. At the beginning of the second step, BC^{2+} is replaced by B^{+} + C^{+}, rotated in the xy-plane to simulate the rotation of BC^{2+} induced by the initial dissociation.

Example ion trajectories for the first and second steps of the simulation are plotted in the left and right panels of Figure 4.4, respectively. The first step is a two-body Coulomb explosion, so the fragments necessarily recoil back-to-back. The trajectories of A^+ and BC^{2+} are propagated for 200 fs. Within this the time, A^+ travels much further than the heavier intermediate. In this particular simulation, BC^{2+} is rotated by ∼180° prior to the start of the second step. As a result, the Coulomb explosion of BC^{2+} ejects B^+ roughly in the direction of travel, whilst C^+ is scattered at a backwards angle. Although this is another Coulomb explosion, the pair of ions do not recoil back-to-back due to the momenta they retain from the initial Coulomb explosion. Meanwhile, A^+ continues undisturbed along its trajectory, as it is already beyond the influence of the other ions.

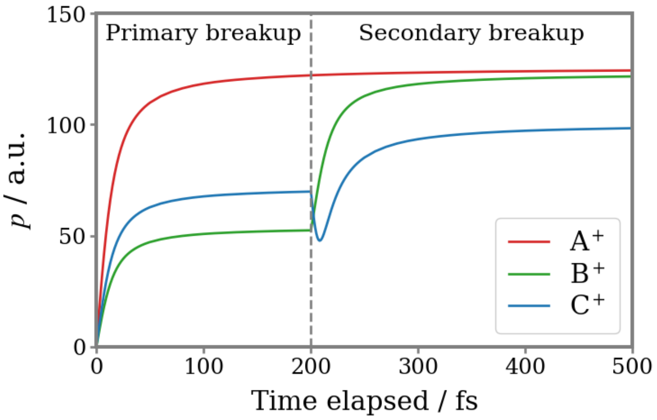

Figure 4.5: Simulated fragment momenta for the sequential three-body dissociation scheme described in Equation 4.3. The dashed line indicates the separation between the two steps of the simulation. The momentum of B^+/C^+ during the primary step is calculated as $\frac{m_{B/C}}{m_{BC}} p_{BC^+}$.

The plot of the fragment momenta as a function of time in Figure 4.5 provides a better impression of the forces acting throughout the simulation. Although B^+ and C^+ are bonded throughout the duration of the first step, for coherence, their individual momenta are plotted. These were calculated from how the momentum of the BC^{2+} is partitioned between B and C based on their relative masses. As soon as the intermediate ion fragments, the Coulombic repulsion accelerates C^+ in a similar direction to its existing momentum vector, causing its momentum to further increase. At the same time, B^+ is accelerated in the y direction, but decelerated in the x direction, the combination of which causes a decrease in momentum. In a narrow time window, the electrostatic force reverses the travel of B^+ in the x direction, and the momentum of the ion again begins to increase. The momentum of A^+ does not perceptibly change during the course of the second step.

The simulation was run for several thousand trajectories to produce the Newton diagram correlation map shown in Figure 4.6. The only parameter that changes between trajectories is the random rotation of BC^{2+}, causing the momenta of secondary products to be distributed over an angular range relative to the momentum of the primary product. The result is the pair of semicircular distributions seen in the figure. The radii of these features is determined by the momentum release of the secondary fragmentation, and their x-axis offsets by the momenta that the secondary ions retain from the primary fragmentation.

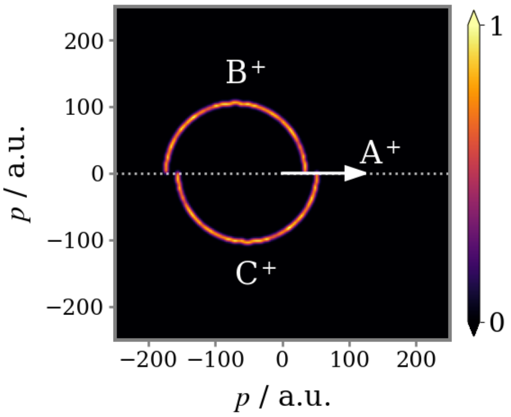

Figure 4.6: Simulated Newton diagram correlation map for the sequential three-body dissociation scheme described in Equation 4.3, assuming the lifetime of the intermediate BC^{2+} far exceeds its rotational period.

Simulation of a variable intermediate lifetime

It is common to observe a non-uniform angular distribution from a sequential three-body fragmentation channel.[75,175] For a triatomic molecule, under the assumption that rotation occurs within the plane of the diatomic intermediate, the angular distribution takes the form of an exponential decay, with a decay constant determined by the ratio of the characteristic lifetime (τ) and the rotational period (T_{R}) of the intermediate.[175] In the current model, the lifetime of the intermediate ion is determined by the duration of the first step. Rather than having a single fixed value, a distribution of lifetimes is modelled by assuming that the population of BC^{2+} decays exponentially as a function of time:

$$n(\mathrm{BC}^{2+}) \propto e^{-t/\tau}, \tag{4.4}$$

where $n(\mathrm{BC}^{2+})$ is the number density of the species. For each individual simulation, the lifetime of BC^{2+} is determined by randomly sampling on this function. The angle of rotation of B^+ and C^+ prior to second step is then given by the product of the lifetime and T_{R}.

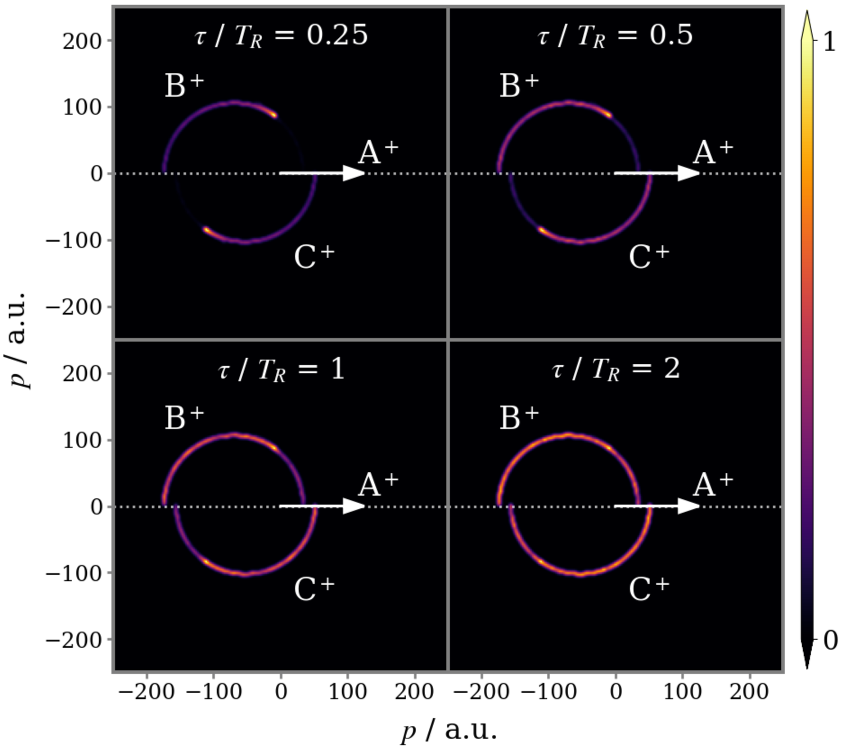

Figure 4.7: Simulated Newton diagram correlation map for the sequential three-body dissociation scheme described in Equation 4.3, as a function of the ratio of the characteristic lifetime (τ) and rotational period (T_{R}) of the intermediate, BC^{2+}.

Figure 4.7 displays results from a series of simulations with fixed T_R (1 ps) and different values of τ. With a short characteristic lifetime, peak intensity coincides with the distribution observed for the concerted Coulomb explosion mechanism (Figure 4.3), *i.e.* a considerable fraction of the intermediate population dissociates before significant rotation occurs. The features curve counter-clockwise as they decay due to the rotation of the intermediate ion induced by the primary dissociation step, which pivots the C atom end of the intermediate towards the recoiling A^+ ion. As τ is increased, the mechanism transitions from concerted to sequential. As expected, for sufficiently long τ the semicircular features become essentially isotropic.

4.4.2 Fragmentation with a neutral cofragment

Next, the sequential three-body fragmentation of a molecular dication is considered. Specifically, the model described here is for a mechanism where the primary step is a Coulomb explosion between two charged fragments, one of which is an unstable intermediate ion that further dissociates by ejecting a neutral fragment.[73] For example:

$$\begin{gathered}\mathrm{ABC}^{2+} \rightarrow \mathrm{A}^+ + \mathrm{BC}^+,\\ \mathrm{BC}^+ \rightarrow \mathrm{B}^+ + \mathrm{C}.\end{gathered} \tag{4.5}$$

The first step of the simulation is the Coulomb explosion of $\mathrm{A}^+ + \mathrm{BC}^+$ and is propagated until both fragments have approximately reached terminal velocity. At this point, BC^+ is replaced in space by B^+. The neutral C fragment is omitted because, in a model that only includes Coulombic forces, it cannot interact with other species.

To account for the impulse of the secondary bond dissociation on B^+, an additional velocity component is added onto its recoil velocity. This velocity component is randomly rotated in-plane to simulate the rotation of the intermediate induced by the primary step. Once again, this assumes that the lifetime of the intermediate greatly exceeds its rotational period. The magnitude of the velocity component is a required input, typically determined from the experimentally measured impulse associated with the secondary dissociation step.

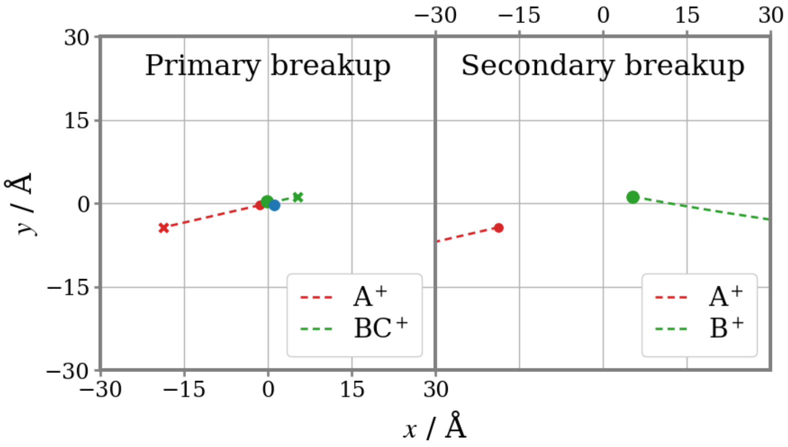

Figure 4.8: Simulated ion trajectories for the sequential three-body dissociation scheme described in Equation 4.5. (a) Coulomb explosion of A^+ + BC^+. (b) Subsequent breakup of the BC^+ into B^+ + C. At the beginning of the second step BC^+ is replaced by B^+, with an additional velocity component added onto its recoil velocity to recreate the impulse of the B-C bond fission. This velocity component is rotated in the xy-plane to simulate the rotation of BC^+ induced by the initial dissociation.

Figure 4.8 plots example ion trajectories for the sequential three-body fragmentation of ABC^{2+}. The simulation is, fundamentally, a two-body Coulomb explosion. B^+ is only perturbed from recoiling back-to-back with A^+ by the impulse of the secondary dissociation. In the figure, this impulse acts into the bottom-right corner and redirects the trajectory of B^+ accordingly. Figure 4.9 displays the fragment momentum over time. Because the secondary bond dissociation is replicated by an instantaneous acceleration, it causes a discontinuous jump in the momentum of B^+ at the onset of the secondary step.

A Newton diagram for the sequential fragmentation of ABC^{2+} is shown in Figure 4.10. This momentum correlation map was constructed from the simulated momenta of the A^+ and B^+ ions, with the relative momentum of the neutral cofragment deduced through momentum conservation in this frame. The uniform rotation of the intermediate ion again produces a pair of semicircular features, similar to the distribution observed for the sequential fragmentation of tricationic ABC (Figure 4.6). However, the radii of the features is smaller because the KER of the dissociation of BC^+ is much lower than the Coulomb explosion of BC^{2+}.

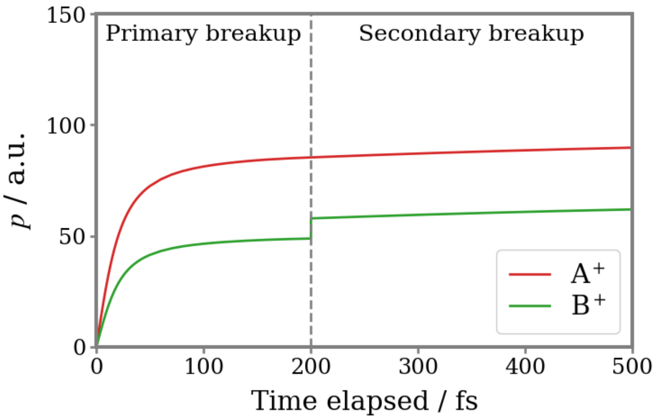

Figure 4.9: Simulated ion fragment momenta for the sequential three-body dissociation scheme described in Equation 4.5. The dashed line indicates the separation between the two steps of the simulation. The momentum of B$^+$ during the primary step is calculated as $\frac{m_\mathrm{B}}{m_\mathrm{BC}} p_{\mathrm{BC}^+}$.

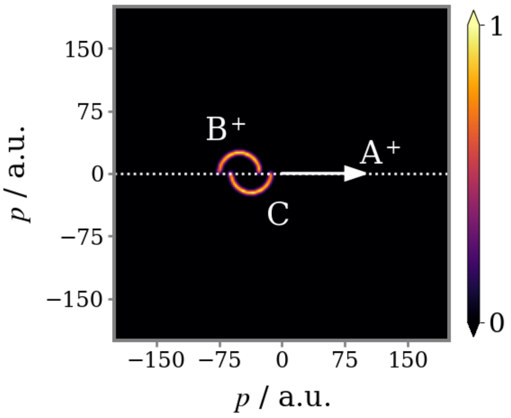

Figure 4.10: Simulated Newton diagram correlation map for the sequential three-body dissociation scheme described in Equation 4.5, assuming the lifetime of the intermediate BC$^+$ far exceeds its rotational period.

4.5 Simulating time-resolved Coulomb explosion imaging data

Until this point, the focus has been on simulating the fragmentation dynamics of molecular polycations in order to recreate data recorded in a CEI experiment, and hence be able to infer the original molecular structure. The next step is to attempt a simulation of a TR-CEI experiment. Once again, this relies on a forward simulation process. The molecular dynamics prompted by the pump pulse are simulated independently, and the nuclear structure at a series of points throughout are sampled, to be used as the starting conditions for a Coulomb explosion simulation. The result is a series of calculated ion trajectories for different pump-probe delays, which together depict how the correlated fragment ion momenta are expected to evolve. The simulated and experimentally measured distributions can then be compared to gauge whether the simulation provides an accurate representation of the dynamics initiated by the pump pulse.

The ideal method of predicting the nuclear dynamics following photoexcitation by the pump pulse would be using *ab initio* non-adiabatic molecular dynamics.[185,186] Such an extensive computational study is beyond the scope of the current thesis, though it remains the long term goal. As an example, the following section presents a simple model of a direct photodissociation process probed by TR-CEI. The photodissociation is modelled classically within the existing framework of the Coulomb explosion model.

4.5.1 Photodissociation dynamics

Consider again the Coulomb explosion of triatomic molecule ABC following triple ionisation, but some time beforehand the A-B bond is cleaved:

$$\begin{gathered}\mathrm{ABC} \rightarrow \mathrm{A} + \mathrm{BC},\\ \mathrm{A} + \mathrm{BC} \rightarrow \mathrm{A}^{+} + \mathrm{B}^{+} + \mathrm{C}^{+}.\end{gathered} \tag{4.6}$$

In this scenario the initial dissociation corresponds to the dynamics initiated by the pump pulse, and the subsequent Coulomb explosion is prompted by the probe pulse. Because it is another two step mechanism, the process can be modelled by chaining together two trajectory calculations.

The first step of the simulation is the dissociation of A + BC. Because the model only includes Coulombic forces, the fragments are not able to interact. Therefore, both are instantaneously accelerated to their recoil velocities at the start of the simulation. The impulse on each fragment is considered to act along the axis of the bond that is broken. The magnitude of their momenta is determined by an input KER value. It is expected that an accurate KER will be extracted from the experimental data. The neutral fragment trajectories are propagated for a predetermined time, which corresponds to the pump-probe delay (Δt). To begin the second step, A is replaced with A^+ and BC with B^+ and C^+ – separated by the same distance as in the initial molecular structure. The trajectories of the ions are then propagated until all three have reached terminal velocity.

Example ion trajectories for a simulation with $\Delta t = 200\,\text{fs}$ are plotted in Figure 4.11. Compared to the case of the sequential three-body fragmentation of ABC^{3+} (Figure 4.4), the fragments do not travel far in the first step as the KER of the dissocation into A + BC is much less than the KER of the Coulomb explosion into $A^+ + BC^{2+}$. At this stage, the simulation assume that the BC moiety is not rotationally excited by the primary dissociation, such that Coulomb explosion of BC^{2+} ejects B^+ and C^+ roughly in opposite directions along the axis of the B–C bond in the original molecule.

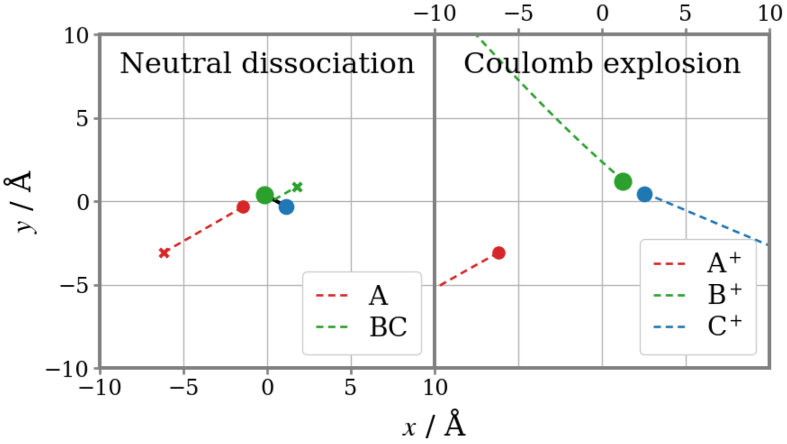

Figure 4.11: Simulated ion trajectories for the three-body dissociation scheme described in Equation 4.6. (a) Neutral dissociation of A + BC. (b) Subsequent ionisation of the fragments and Coulomb explosion. At the beginning of the second step A is replaced by A^+ and BC by $B^+ + C^+$.

Figure 4.12 displays the ion momenta as a function of time elapsed in the simulation. The fragments start with non-zero momentum because they are initiated with their tangential recoil velocities, calculated from the KER of the primary dissociation. Their momenta are constant throughout the first step of the simulation as the neutral fragments do not interact. The fact that the momentum of A^+

increases over the course of the second step demonstrates that upon ionisation it remains close enough to interact with the other fragments. Because A^+ and B^+ exert forces on C^+ that act in a similar direction, C^+ is accelerated to higher momentum than B^+, which experiences opposing forces from A^+ and C^+.

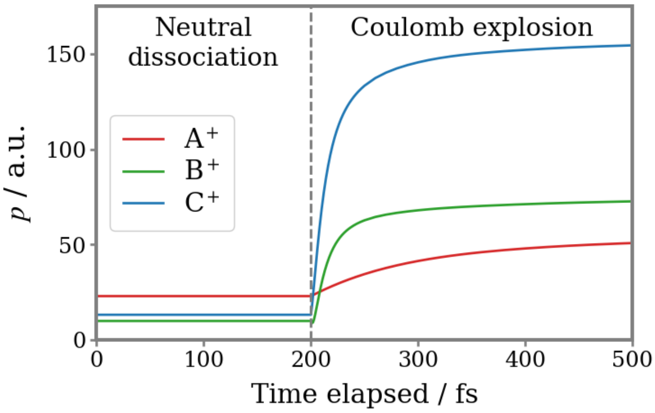

Figure 4.12: Simulated ion fragment momenta for the three-body dissociation scheme described in Equation 4.6. The dashed line indicates the separation between the two steps of the simulation (Δt). The momentum of B^+/C^+ during the primary step is calculated as $\frac{m_{\mathrm{B/C}}}{m_{\mathrm{BC}}} p_{\mathrm{BC}}$.

The series of Newton diagrams in Figure 4.13 have been constructed from datasets simulated with different Δt. The simulations also incorporated an ensemble of starting geometries intended to approximate ground-state vibrational motion of ABC. First, consider a simulation with $\Delta t = 0\,\mathrm{fs}$. There is no movement of the atoms before they are exchanged with atomic ions, so the simulation is nearly identical to the concerted fragmentation model presented in Section 4.3. The only difference is that the ions have non-zero starting velocities, determined by the kinematics of the primary dissociation. A comparison of the correlation maps simulated using the two different models (Figure 4.13(a) and Figure 4.3(b)) shows that the effect is negligible. As Δt is increased the momentum of B^+ shifts in the positive x direction (the recoil direction of A^+) causing the relative recoil angle of B^+ and C^+ to increase. This reflects the fact that A and BC are further apart when Coulomb explosion occurs, so the recoil of B^+ and C^+ becomes dominated by their interaction with one another. At $\Delta t = 1\,\mathrm{ps}$ the pair essentially recoil back-to-back.

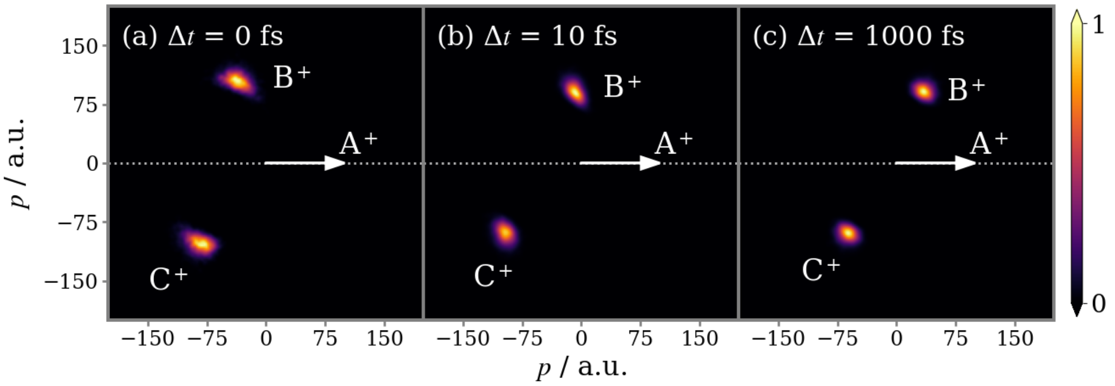

Figure 4.13: Simulated Newton diagram correlation map for the sequential three-body dissociation scheme described in Equation 4.6, as a function of the delay between the initial dissociation event and subsequent Coulomb explosion (Δt).

Finally, consider the case where the bond breaking event induces rotation of the BC moiety. This is modelled by randomly rotating B^+ and C^+ in-plane at the start of the second simulation step, *i.e.* it is assumed that the rotational period of BC is much shorter than Δt. Figure 4.14 is a Newton diagram simulated with this model, using a Δt of 1 ps. The form of the correlation map is familiar for a sequential mechanism. The uniform rotation of BC^{2+} prior to Coulomb explosion produces a pair of semicircular features. The horizontal offset of each is slight because the KER of the initial dissociation is small compared to the KER of the subsequent Coulomb explosion.

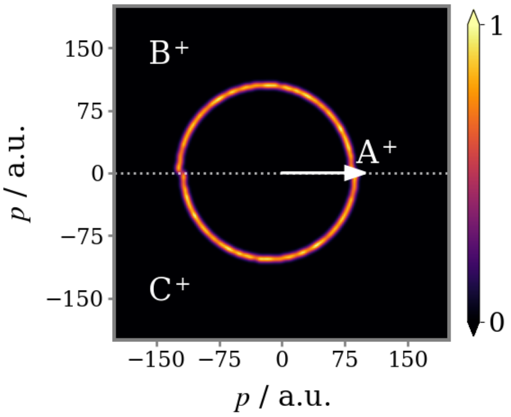

Figure 4.14: Simulated Newton diagram correlation map for the sequential three-body dissociation scheme described in Equation 4.6 where the BC moiety is rotationally excited by the initial dissociation event. It is assumed that Δt (1 ps) far exceeds the rotational period of BC.

4.6 Summary

A simple model for calculating the ion trajectories from a Coulomb explosion event has been introduced. By generating an ensemble of geometries that approximates ground-state vibrational motion and simulating the Coulomb explosion of each, a simulated dataset can be created that is able to be processed in the same manner as experimental data. By chaining together two trajectory calculations, where the output of the first determines the starting conditions of the second, it is possible to recreate a sequential fragmentation mechanism. Here, this approach has been used to construct models of: (i) the sequential three-body fragmentation of a molecular polycation that yields exclusively ionic products, (ii) the sequential three-body fragmentation of a molecular polycation that produces a neutral cofragment, and (iii) the neutral photodissociation of a molecule followed by delayed ionisation and Coulomb explosion, akin to a TR-CEI experiment.

In theory, any number of trajectory calculations can be chained together in order to model even more complex fragmentation processes, involving multiple steps. For example, a fellow student in the Brouard group is currently exploring the potential of a multi-step model to recreate the Coulomb explosion dynamics of a large biphenyl molecule. The molecule breaks up into numerous fragments and the model is being used to simulate different scenarios in order to determine the sequence in which fragments are ejected.

The examples presented here have provided valuable insight into how the fragmentation dynamics can shape the final fragment momenta. In particular, the discussion has focused on how a rotationally excited intermediate produces distinct features in the momentum correlation map, which can be used to identify the fragmentation mechanism. In later chapters, it is considered how other factors can affect the measured fragment momenta, including structural change prior to fragmentation and the excitation of specific vibrational modes. These modifications are introduced as required in order to simulate specific fragmentation channels.

The different versions of the model are relied upon heavily in the results chapters that make up the remainder of this thesis to guide and support the interpretation of fragment momentum correlation maps. The sequential three-body fragmentation model is used in Chapter 5 to simulate the fragmentation dynamics of 1- and 2-iodopropane dications and trications. Chapter 6 applies the sequential three-body fragmentation model to simulate the asynchronous breakup dynamics of *cis*- and *trans*-1,2-dichloroethene trications, as well as the concerted fragmentation model to simulate the Coulomb explosion of highly charged 1,2-dichloroethene polycations. The model for simulating TR-CEI data is used to examine the UV photoexciation dynamics of *trans*-1,2-dichloroethene in Chapter 8.

5

Fragmentation dynamics of extreme-ultraviolet ionised iodopropane

Contents

Declaration of authorship

The work presented in this chapter is based on two publications:

1. **J. W. McManus**,* T. Walmsley,* K. Nagaya, J. R. Harries, Y. Kumagai, H. Iwayama, M. N. Ashfold, M. Britton, P. H. Bucksbaum, B. Downes-Ward, T. Driver, D. Heathcote, P. Hockett, A. J. Howard, E. Kukk, J. W. L. Lee, Y. Liu, D. Milesevic, R. S. Minns, A. Niozu, J. Niskanen, A. J. Orr-Ewing, S. Owada, D. Rolles, P. A. Robertson, A. Rudenko, K. Ueda, J. Unwin, C. Vallance, M. Burt, M. Brouard, R. Forbes, and F. Allum, "Disentangling sequential and concerted fragmentations of molecular polycations with covariant native frame analysis", Phys. Chem. Chem. Phys. **24**, 22699–22709 (2022).
   *These authors contributed equally to this work.

2. T. Walmsley,* **J. W. McManus**,* Y. Kumagai, K Nagaya, J. R. Harries, H. Iwayama, M. N. Ashfold, M. Britton, P. H. Bucksbaum, B. Downes-Ward, T. Driver, D Heathcote, P Hockett, A. J. Howard, J. W. L. Lee, Y. Liu, E. Kukk, D. Milsesevic, R. S. Minns, A. Niozu, J. Niskanen, A. J. Orr-Ewing, S. Owada, P. A. Robertson, D. Rolles, A. Rudenko, K. Ueda, J. Unwin, C. Vallance, M. Brouard, M. Burt, F. Allum, and R. Forbes., "The role of momentum partitioning in covariance ion imaging analysis", J. Phys. Chem. A, **128**, 4548-5460, (2024).
   *These authors contributed equally to this work.

These publications were co-authored by the author of this thesis and another Doctor of Philosophy student, Tiffany Walmsley. Analysis of the experimental data presented in this chapter was jointly performed and interpreted by both students. Therefore, some of the results presented here may also be found in the thesis of Tiffany Walmsley. The simulation work presented in this chapter is the sole work of the author.

Following multiple ionisation, a polyatomic species can dissociate via a complex array of different fragmentation pathways. Because CEI is sensitive to all ionic products, the dataset acquired in such an experiment contains a wealth of information on the fragmentation behaviour of the target species. This chapter presents results from an ion imaging study of the fragmentation dynamics of the isomers of IodoPropane (IP) following interaction with intense XUV femtosecond laser pulses. The analysis is a showcase for how multiple competing fragmentation pathways can be resolved based on the correlated momenta of the fragment ions, thereby providing detailed insight into the dissociation dynamics of individual channels.

The dissociation of IP dications and trications are extensively characterised using 3D momentum covariance mapping. Fragment momentum correlations are interpreted with the support of classical simulations, which use parameters obtained directly from the experimental data. A key theme of the work is how a constraint on the fragment momenta can be incorporated into the covariance analysis procedure to disentangle concurrent dissociation channels that yield the same ion species. This approach is also exploited to examine the momentum exchange relationship between the products, which provides direct insight into the dynamics of molecular fragmentation.

5.1 Background

Experimental studies of the dissociation dynamics of molecular polycations can yield wide-ranging insights, for instance in providing stringent tests for theoretical methods[187–189] and aiding in understanding the chemistry and composition of planetary atmospheres.[190–192] Molecular polycations are generally unstable and decay quickly via an assortment of processes, involving the cleavage of multiple bonds on different time scales to yield charged and neutral fragments.[73–75] In recent years, the fragmentation behaviour of polycations has attracted further interest due to the development of TR-CEI as a method to probe ultrafast photochemistry.[16,17,47,50,57] In order to fully exploit CEI as a structural probe, a detailed understanding of the many-body fragmentation dynamics of polycations is essential.

This chapter explores the complex nature of molecular fragmentation following multiple ionisation, using the isomers of IP as an exemplary system. Molecular polycations were prepared by site-selective ionisation of the iodine atom using intense XUV femtosecond laser pulses. The momenta of the resulting photofragments were recorded using VMI. Covariance mapping is used to isolate correlated fragment momenta for individual fragmentation channels. The analysis focuses on the dynamics of doubly and triply charged parent ions, which are observed to undergo a range of fragmentation pathways, many of which produce the same ionic products via different mechanisms. Being able to distinguish between such processes is an important goal in the field of reaction dynamics.

In the context of CEI, being able to discriminate between concerted and sequential fragmentation is particularly important, as the technique relies on concerted breakup of the molecular ion in order to extract geometric information from the relative momenta of the fragment ions. Sequential fragmentation has primarily been studied in triatomic molecules using coincidence mapping,[73–75,173] due in part to the relative ease of being able to conduct 'kinematically complete' measurements. Sequential mechanisms have also been reported in larger systems, including 1,2-dibromoethane[23] five-membered nitrogen heterocycles[193] and structural isomers of difluoroiodobenzene.[177]

To identify concerted and sequential three-body fragmentation events, the present work employs the native frames approach,[174] introduced in Section 3.6. This method was developed by Rajput *et al.* for coincidence mapping and has been adapted here for covariance mapping. The current analysis builds upon the work of Rajput *et al.* by demonstrating how concerted and sequential three-body fragmentation events can be separated based upon the momentum of primary product. This is an example of applying a fragment momentum constraint in a covariance calculation, a concept that is central to this work.

Filtering the raw dataset based on ion momenta is regularly exploited in coincidence ion imaging studies to identify and remove false coincidence events. For example, if the fragments of a dissociation together constitute the original molecule, the true coincidences can be isolated by selecting only those combinations of ions whose momenta sum to zero.[13,20,21,76,78,79] Two methods for separating overlapping contributions to a covariance map from different dissociation channels are introduced here. The first is to carefully constrain the momentum of one of the ions in the covariance calculation. The second is a more systemic method, which involves constraining the momentum of a pair of ions based upon their expected momentum relationship for a specific fragmentation channel.

The methods presented allow concurrent fragmentation channels leading to the same products to be disentangled and independently investigated. The interpretation of the observed fragment momentum correlations is supported by comparisons with classical simulations of the fragmentation processes. These provide physical insight into the dynamics of sequential fragmentation, including how the initial dissociation step influences rovibrational dynamics in the metastable intermediate ion, and how signatures of this nuclear motion manifest in the measured signals. Collectively, these results shed light on the fragmentation behaviour of 1/2-IP polycations and demonstrate the potential of covariance mapping to study nuclear dynamics induced by ISI.

5.2 Methods

5.2.1 Experimental

Experiments were carried out at SACLA in Hyogo, Japan using the soft X-ray beamline (BL1). The experimental set-up is described in Section 2.6.3. The room temperature vapour pressure of each sample was expanded into the spectrometer without carrier gas to produce a pulsed molecular beam. The FEL was tuned to a central photon energy of 95 eV to coincide with the maximum of the I 4d photoionisation cross section.[194] XUV pulses had an average bandwidth of ∼2%, a pulse duration of ∼30 fs,[138] and a polarisation parallel to the detector plane.

The XUV pulse energy was recorded on a shot-to-shot basis using a gas intensity monitor.[135] On-target pulse energy distributions for both datasets are shown in Figure 5.1. The mean pulse energy was determined to be 33 μJ, which was attenuated to 3.9 μJ at the molecular sample by the expected transmission of the beamline (90%) and a 0.6 μm Zr filter (13%). A Kirkpatrick-Baez mirror system focused the XUV pulses down to a spot size of approximately 10 μm ($1/e^2$), resulting in a Gaussian intensity of $3.3 \times 10^{14}\,\mathrm{W\,cm^{-2}}$.

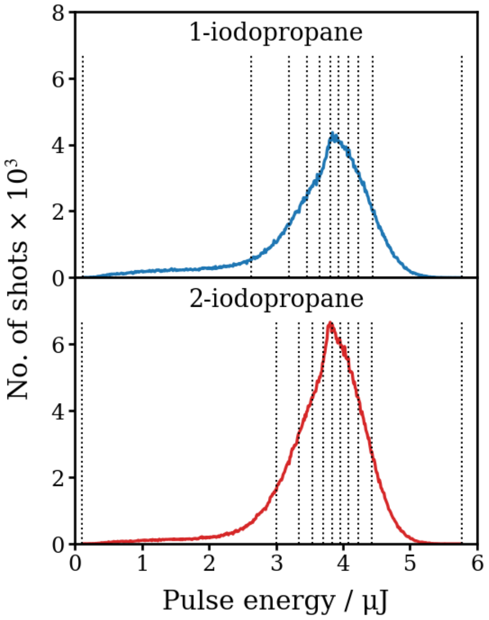

Figure 5.1: Pulse energy distribution for (*top*) 1- and (*bottom*) 2-IP. Vertical dotted lines indicate the boundaries of the bins used for contingent covariance calculations.

5.2.2 Analytical

The VMI spectrometer is equipped with a DLA detector that records the (x, y) spatial position and arrival time of ion hits with high precision, permitting reconstruction of the complete 3D momentum information for each ion. Because of the relatively low repetition rate of the experimental set-up, it was necessary to conduct experiments at a relatively high ion count rate (~12 ions shot^{-1}) to acquire sufficient data in the time available. Therefore, the analysis relies upon covariant momentum mapping[81] to extract the relative momenta of ions produced in the same fragmentation event.

A key feature of the current work is the use of a SASE FEL, which produces laser pulses with properties that fluctuate considerably on a shot-by-shot basis.[93] Most significant are the fluctuations in the pulse energy that cause the yield of all species to rise and fall as one. To avoid false correlations in the calculated covariance maps, contingent covariance analysis was used.[155] See Section 3.4.2 for information. Raw data were grouped into 10 subsets based on the distribution of pulse energy at the molecular sample (Figure 5.1), each containing an equal number of acquisition cycles.

5.3 Time-of-flight data

Ion ToF mass spectra acquired from the XUV ionisation of 1- and 2-IP are overlaid in Figure 5.2. Subtle differences are observed in the relative yields of the $C_nH_x{}^+$ fragments ($n = 1, 2, 3;\ 0 \leq x \leq 2n + 1$), which implies that the fragmentation channels are isomer-dependent. The ToF contingent covariance map for 2-IP, shown in Figure 5.3(b), reveals which pairs of ions are formed in the same fragmentation event. Note that the scale along each axis does not extend to zero as no covariance involving H^+ was observed. Because H^+ is formed with very high velocity, the majority is focused beyond the edges of the detector by the VMI ion optics and is not detected.

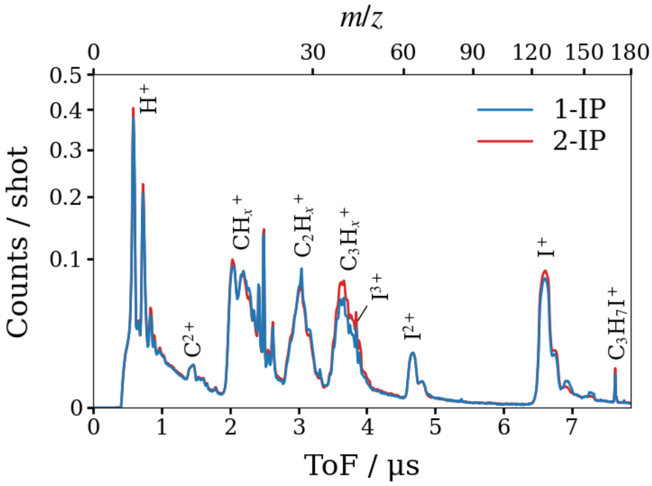

Figure 5.2: Ion ToF spectra of 1- and 2-IP exposed to an intense XUV ultrafast laser pulse. Unlabelled peaks are background gases. Datasets were acquired under comparable experimental conditions and are not otherwise normalised.

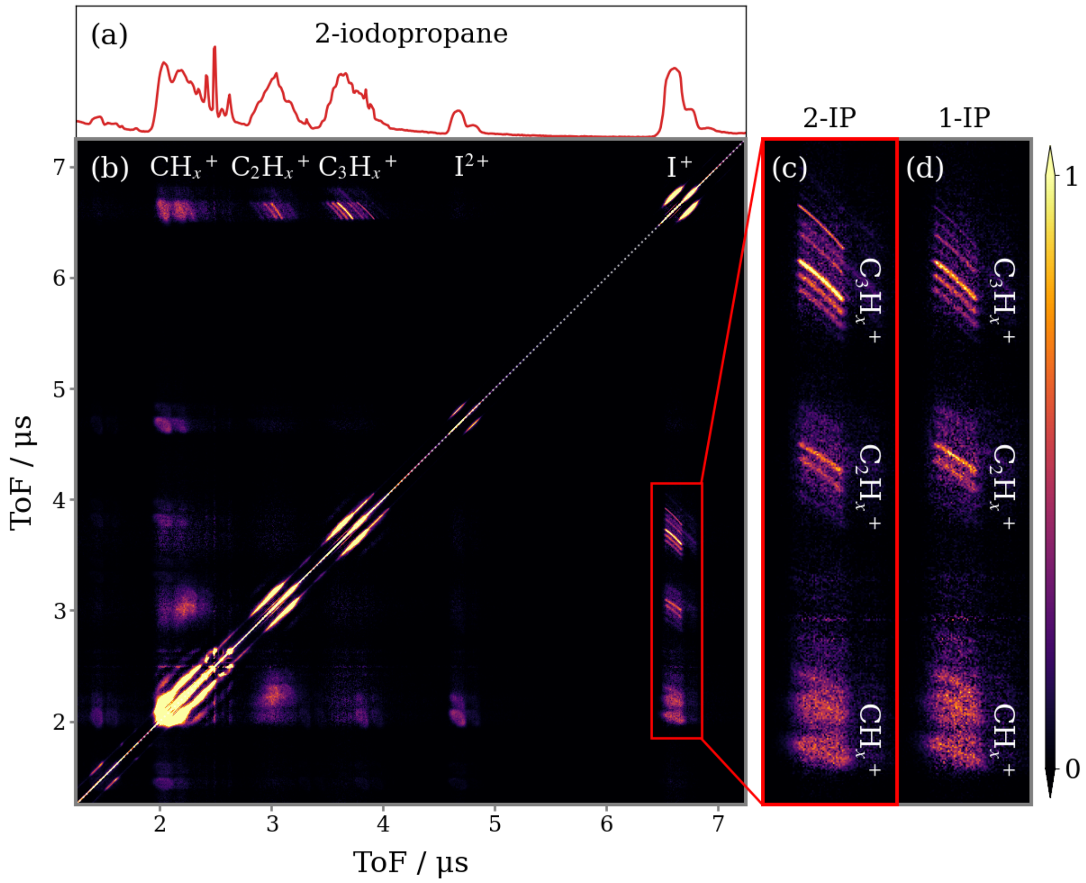

Figure 5.3: (a) Ion ToF spectrum for 2-IP. (b) ToF covariance map for 2-IP. The red box highlights the region containing correlations between I^+ and $C_nH_x{}^+$, which is enlarged in panel (c). (d) The same expanded section from the ToF covariance map for 1-IP. Covariance maps are normalised separately.

Clear correlations between I^+ and various alkyl ions are highlighted by the red box and expanded in panel (c). The high ToF resolution of the DLA detector is sufficient to distinguish correlations between $C_nH_x{}^+$ ions differing by a single hydrogen mass. Panel (f) shows the same expanded section of the covariance map for 1-IP. The two are broadly similar, however with notably different intensities for the various I^+ + $C_3H_x{}^+$ correlations. The sharp structure and −1 gradient of the correlation between I^+ and $C_3H_7^+$ is characteristic of a two-body Coulomb explosion. Other I^+ + $C_3H_x^+$ signals become blurrier as H atoms are removed due to the impulse they impart when they separate. By contrast, the I^+ + CH_x^+ features are significantly more diffuse as these pairs of ions arise from many-body dissociation, in which significant momentum is carried by additional (unidentified) heavy fragments.

5.4 Three-body breakup of parent trications

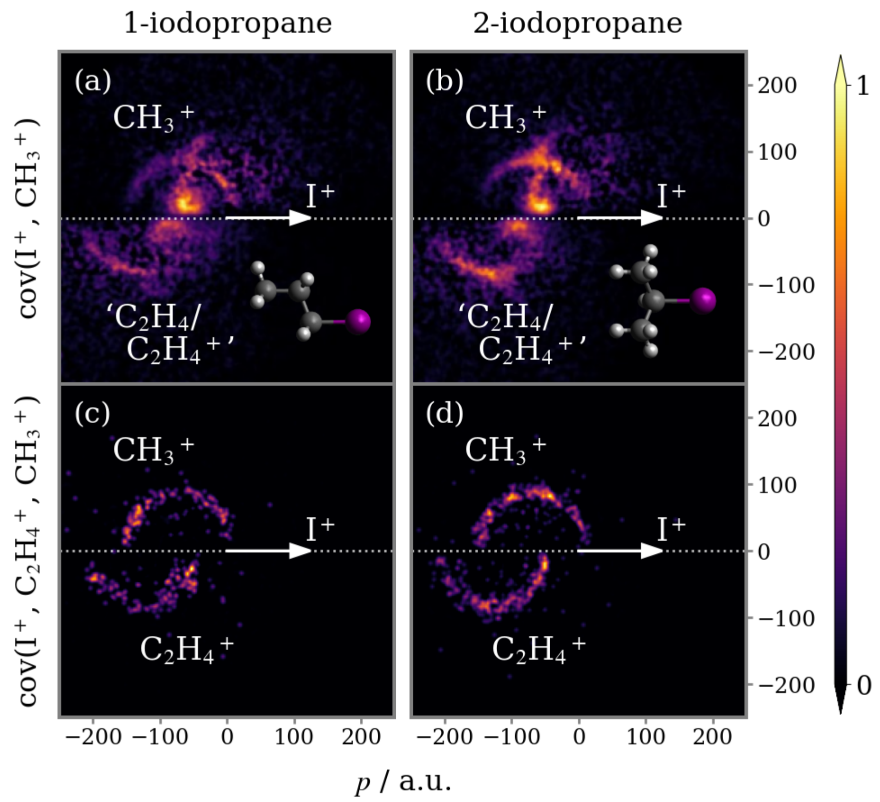

Figure 5.4: Newton diagrams for the three-body breakup of (*left column*) 1-IP$^{2+/3+}$ and (*right column*) 2-IP$^{2+/3+}$ into $I^+ + C_2H_4/C_2H_4^+ + CH_3^+$. *Top row*: The correlated momenta of I^+ and CH_3^+ have been determined via two-fold covariance, wherein the momentum of the third fragment (C_2H_4 or $C_2H_4^+$) is deduced through momentum conservation in this frame. *Bottom row*: The correlated momentum of $I^+ + C_2H_4^+ + CH_3^+$ has been determined via three-fold covariance. Each panel is normalised separately.

This section focuses on the isomer-specific three-body fragmentation pathways of the 1- and 2-IP trications into $I^+ + C_2H_4^+ + CH_3^+$. The correlated momenta for the (I^+, CH_3^+) ion pair, determined via two-fold contingent covariance, are plotted in a Newton diagram in panels (a) and (b) of Figure 5.4 for 1- and 2-IP, respectively. Here, the recoil direction of I^+ is oriented along the positive x-axis and the relative momentum of CH_3^+ is plotted in the upper half. The momentum of the third fragment, deduced through momentum conservation in this frame, is plotted in the lower half. An arc, characteristic of a sequential three-body dissociation process, can be seen in the data for both isomers. This is assigned to the fragmentation of IP^{3+} by loss of I^+ and subsequent dissociation of $C_3H_7^{2+}$:

$$\begin{aligned} C_3H_7I^{3+} &\rightarrow I^+ + C_3H_7{}^{2+}, \\ C_3H_7{}^{2+} &\rightarrow C_2H_4{}^+ + CH_3{}^+. \end{aligned} \tag{I}$$

Rising from the arcing sequential fragmentation feature in each covariance map is a feature assigned to concerted three-body dissociation of the trication:

$$C_3H_7I^{3+} \rightarrow I^+ + C_2H_4{}^+ + CH_3{}^+. \tag{II}$$

In this mechanism, the time between the first and second steps is short such that rotation is limited, and I^+ remains in close enough proximity to influence the KER of the second dissociation. Finally, the low momentum signal close to the x-axis arises from three-body breakup of IP^{2+} into I^+, $CH_3{}^+$ and a neutral cofragment, assumed to be C_2H_4. (The fragmentation behaviour of the parent dication is the focus of the next section). Based on their relative intensities, the yield of I^+ + $CH_3{}^+$ from the breakup of parent dications is approximately half that from trication breakup.

These channel assignments are confirmed using three-fold covariance analysis to determine the correlated momenta of I^+ + $C_2H_4{}^+$ + $CH_3{}^+$, plotted in the lower panels of Figure 5.4. In these Newton diagrams, the low momentum features assigned to breakup of IP^{2+} are completely absent, whilst the high momentum features assigned to breakup of IP^{3+} remain. This analysis also confirms that channels I and II yield $C_2H_4{}^+$, *i.e.* $C_2H_4{}^+$ does not fragment further. Because of the inherently lower probability of detecting three ions in coincidence, the statistics for these three-fold covariance maps are distinctly worse than the two-fold covariance maps, seen in the panels above. Hence, the discussion will focus on the two-fold covariance maps.

To inspect the sequential fragmentation mechanism the momentum correlation map must be transformed into the CoM frame of the $C_3H_7{}^{2+}$ intermediate, *i.e.* the native frame of the second dissociation step of channel I. The resulting Newton diagram for 2-IP is shown Figure 5.5(a). Because the transformation isolates the dynamics of the secondary dissociation, the momentum of the CH_3^+ and $C_2H_4^+$ fragments match in this frame. The overlapping concerted and sequential fragmentation channels can be disentangled by making use of the I^+ momentum information.

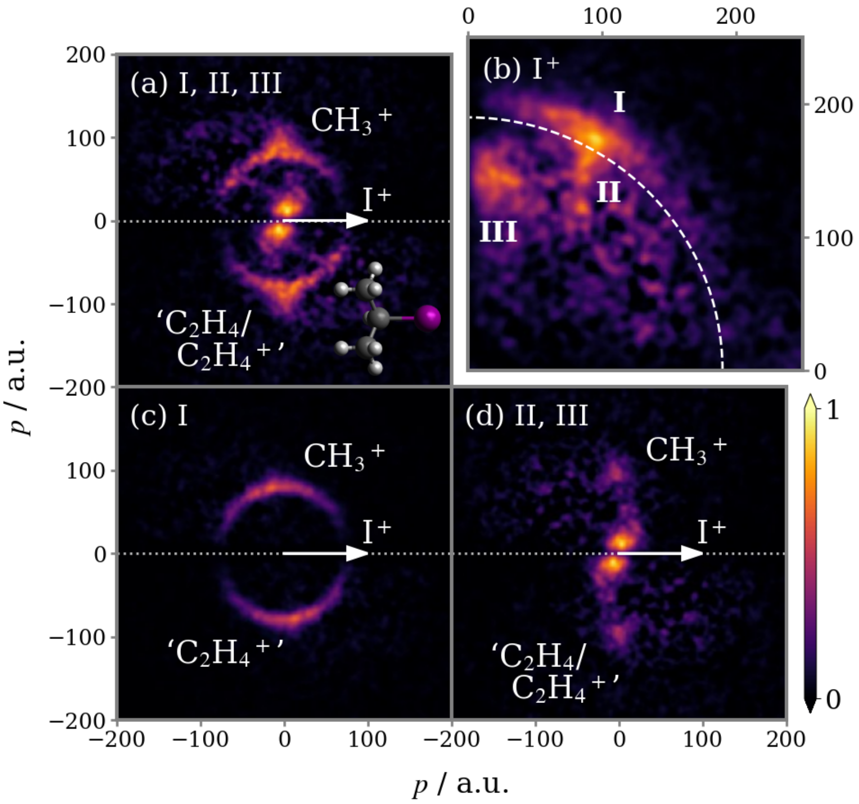

Figure 5.5: (a) Newton diagram two-fold covariance map for the three-body breakup of 2-IP$^{2+/3+}$ into I^+ + $C_2H_4/C_2H_4^+$ + CH_3^+, plotted in the CoM frame of the $C_3H_7^+$ intermediate. (b) The corresponding momentum distribution of I^+. This panel is displaced to highlight the different reference frame in which the data are presented. The labelled features correspond to: (I) sequential and (II) concerted three-body fragmentation of 2-IP^{3+} and (III) sequential three-body fragmentation of 2-IP^{2+}. Filtering the dataset based on the magnitude of the I^+ momentum prior to calculating the covariance map has been used to isolate channel I, shown in panel (c), from the signals for channels II and III, seen in panel (d).

Figure 5.5(b) displays the corresponding momentum distribution of I^+, plotted in a frame where the x-axis bisects the I^+ and CH_3^+ momentum vectors. This information is obscured in the Newton diagram in panel (a) because the momentum of I^+ is constrained to x-axis. Three features are observed, which correspond with the channels already described: (I) the sequential three-body breakup of 2-IP^{3+} produces a high momentum, constant magnitude feature; (II) descending in momentum from the sequential feature is the signal produced by the three-body concerted breakup of 2-IP^{3+}; and (III) the sharp low momentum signal corresponds to three-body breakup of 2-IP^{2+} to produce I$^+$, CH$_3^+$ and a neutral cofragment.

The sequential feature can be completely isolated by filtering the ion imaging data on the absolute magnitude of the I$^+$ momentum, prior to calculating the covariance map. The result is Figure 5.5(c), produced by constraining the I$^+$ momentum to be above 190 a.u. This limit is indicated by the dashed line in panel (b). Channels II and III yield I$^+$ with similar momenta and hence cannot be completely separated using this method. However, as the momenta of CH$_3^+$ produced by the two channels are drastically different, they are well resolved in the Newton diagram in panel (d), wherein the momentum of I$^+$ is restricted between $120 - 190$ a.u.

5.4.1 Sequential three-body fragmentation

Figure 5.6 compares the ion momentum distributions associated with the channel I for 1- and 2-IP. In panels (a) and (b) the correlated fragment momenta are plotted as Newton diagrams in the CoM frame of propyl intermediate, as shown previously in Figure 5.5(c). In panels (c) and (d) the covariance maps are replotted as a function of the KER of the secondary fragmentation ($\mathrm{KER}_{(\mathrm{C_2H_4}^+,\mathrm{CH_3^+})}$) and the relative recoil angle of the (I$^+$, CH$_3$$^+$) ion pair ($\theta_{(\mathrm{I}^+,\mathrm{CH_3}^+)}$). In both molecules, $\mathrm{KER}_{(\mathrm{C_2H_4}^+,\mathrm{CH_3^+})}$ is essentially independent of $\theta_{(\mathrm{I}^+,\mathrm{CH_3}^+)}$. This implies that the fragmentation is truly sequential, *i.e.* at the point of secondary dissociation I$^+$ is so far separated from C$_3$H$_7$$^{2+}$ that the KER of this step does not depend on the orientation with respect to the departing iodine fragment. For both isomers $\mathrm{KER}_{(\mathrm{C_2H_4}^+,\mathrm{CH_3^+})}$ takes a value of 5.3±0.9 eV, determined by fitting Gaussian functions to the distributions in panel (e), where the uncertainty represents the standard deviation of the Gaussian distribution.

Significant differences are observed in the $\theta_{(\mathrm{I}^+,\mathrm{CH_3}^+)}$ distributions, as compared in Figure 5.6(f). For 1-IP a very broad angular distribution is observed, with some degree of asymmetry – more signal is observed close to 180° than close to 0°. A significantly narrower angular distribution is observed for 2-IP, with a peak close to 90°. These angular distributions are notably more complex than observed in previous studies that used the native frames approach,[174,175] which investigated triatomic molecules. In such cases, under the assumption that rotation occurs within the plane of the diatomic intermediate, the angular distribution takes the form of an exponential decay, with a decay constant determined by the ratio of the lifetime and the rotational period of the intermediate.[175] In the limit of a very long lifetime relative to the rotational timescale an isotropic angular distribution is observed.[174]

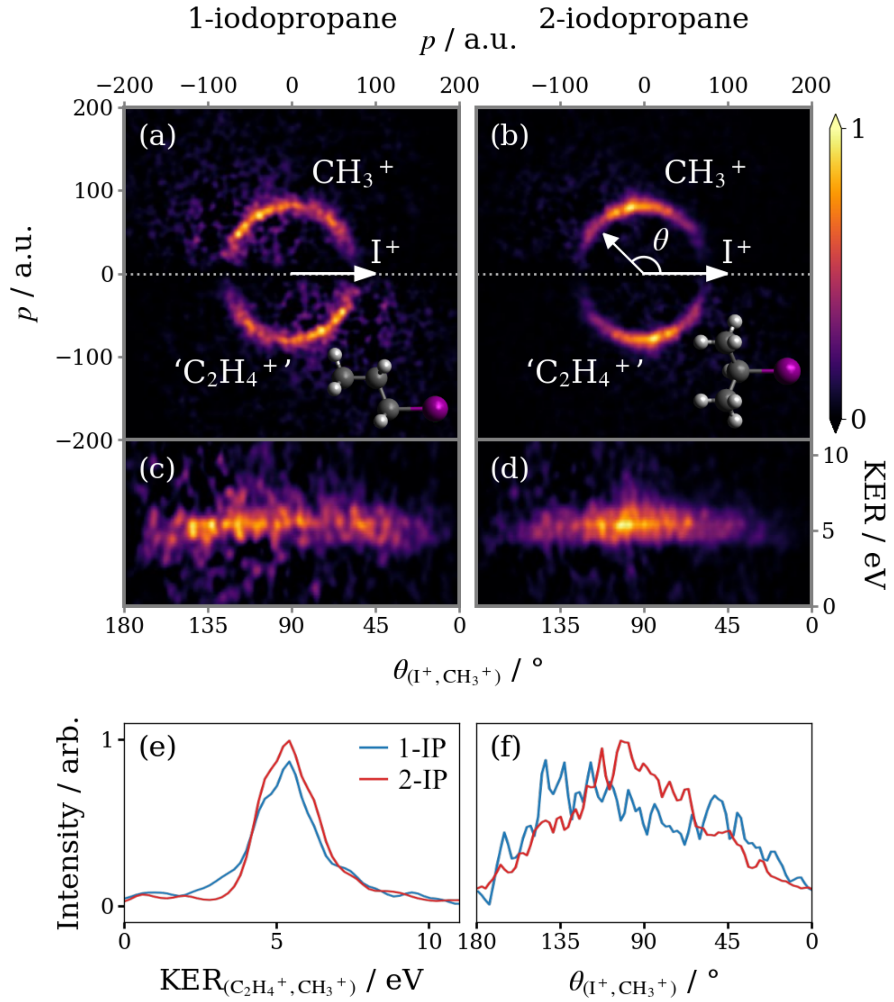

Figure 5.6: Newton diagram two-fold covariance maps for channel I: the sequential breakup of (a) 1-IP^{3+} and (b) 2-IP^{3+} into I$^+$ + $C_2H_4{}^+$ + $CH_3{}^+$, where the primary step is Coulomb explosion into I$^+$ + $C_3H_7{}^{2+}$. Fragment momenta are plotted in the CoM frame of the propyl intermediate. Below, the Newton diagrams are displayed in polar coordinates, where KER$_{(C_2H_4{}^+,CH_3^+)}$ is the KER of the secondary dissociation and $\theta_{(I^+,CH_3{}^+)}$ is the recoil angle of $CH_3{}^+$ relative to I$^+$. Each panel is normalised separately. Below, the integrated (e) KER and (f) angular distributions are overlaid.

In the case of a polyatomic metastable intermediate, the situation is more complex. Additional factors can affect the angular distribution of ion emission within the native frame of the secondary dissociation, including: rotation of the intermediate ion about different axes relative to the initial fragmentation; the relationship between the 3D structure of the intermediate and the recoil direction of ions following its fragmentation; and any other nuclear dynamics occurring (for instance, bending) in the intermediate prior to its dissociation. In order to assess the effects of these dynamics on the measured ion momentum correlations, a series of classical simulations of the sequential Coulomb explosion process were conducted. The results are compared to the experimental data in the following section.

5.4.2 Classical simulations

Classical trajectory calculations of point charges interacting under Coulomb's law can provide a useful guide for interpreting Coulomb explosion images.[19,177–179] However, a model that assumes instantaneous fragmentation and purely electrostatic repulsion is generally only a good approximation for Coulomb explosion of highly charged polycations, which fragment promptly into exclusively ionic products.[183] How this basic framework can be modified to recreate sequential fragmentation dynamics was described in Section 4.4. The basis of the model constructed here is a sequential three-body fragmentation simulation that incorporates a variable intermediate lifetime, taken from Section 4.4.1.

Briefly, the simulation is executed as two separate Coulomb explosion events that model the primary and secondary fragmentation steps of channel I. The first step is propagated for the duration of the intermediate lifetime. At the start of the second step $C_3H_7^{2+}$ is replaced by $C_2H_4^+ + CH_3^+$. A distribution of lifetimes is modelled by assuming the population of the propyl dication decays exponentially as a function of time, with a characteristic lifetime τ. Successive modifications incorporate more tuneable parameters. The input parameters are empirically chosen to reproduce the experimental results, therefore the simulations provide qualitative insights into the possible nuclear dynamics that may occur in the propyl dication, but preclude quantitative comparisons.

Concerted fragmentation

Initially, it is verified that if τ is made very short (for instance, on the order of vibrational motion), the simulation is able to accurately recreate concerted three-body breakup dynamics. In the top panel of Figure 5.7, the covariance map from Figure 5.5(d), which isolates the signal for the concerted three-body breakup of 2-IP^{3+}, has been replotted as a function of $\mathrm{KER}_{(C_2H_4{}^+, CH_3^+)}$ and $\theta_{(I^+, CH_3{}^+)}$. Simulated data for the same process with $\tau = 25$ fs and $T_R = 1$ ps are plotted in the panel below.

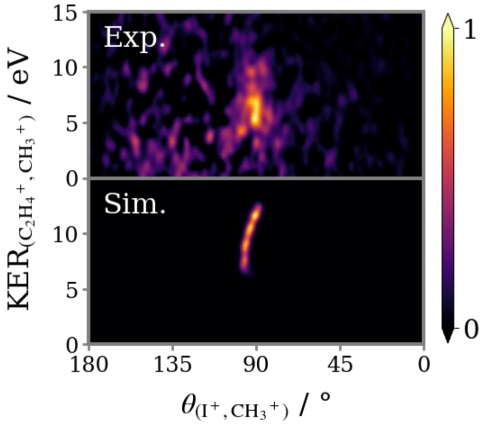

Figure 5.7: (*Top*) The covariance map from Figure 5.5(d) displayed in polar coordinates. (*Bottom*) Simulated correlation map for channel II: the concerted breakup of 2-IP^{3+} into I^+ + $C_2H_4{}^+$ + $CH_3{}^+$. Each panel is normalised separately.

The agreement between the experimentally observed $\theta_{(I^+, CH_3{}^+)}$ distribution and that predicted by simulation is reasonable – both are narrowly distributed around 90°. The broad $\mathrm{KER}_{(C_2H_4{}^+, CH_3^+)}$ range arises due to the range of delays between the first and second dissociation steps, implying that the concerted fragmentation is somewhat asynchronous. The KER decreases to a lower limit when the secondary dissociation occurs more than 200 fs after the first. At this point, the separation between I^+ and $C_3H_7{}^{2+}$ is great enough that the effect of the iodine fragment on the secondary dissociation energetics is negligible.

Sequential fragmentation of 1-iodopropane trications

By increasing the characteristic lifetime of the propyl dication in the model, sequential fragmentation dynamics may be simulated. Figure 5.8 compares the covariance map for the sequential breakup of 1-IP^{3+} into I^{+} + $C_2H_4{}^{+}$ + $CH_3{}^{+}$ with the output of the simulation as successive modifications are implemented that account for a range of physical processes. The impulse from the primary dissociation step is expected to impart a large torque,[195] rotating the intermediate as depicted schematically in Figure 5.8(g). The rotational states populated by this process will be much higher than the thermal population in the skimmed molecular beam. It is therefore predicted that the relative recoil angle between the primary I^{+} product and the secondary $CH_3{}^{+}$ product will decrease as the propyl ion rotates to orient the methyl group towards the recoiling I^{+}.

As can be seen in Figure 5.8(a), the angular distribution peaks at an obtuse angle and decays slightly towards lower values. Performing a simulation with a intermediate lifetime that is half its rotational period ($\tau = 0.75\,\text{ps}$, $T_\text{R} = 1.5\,\text{ps}$), successfully reproduces the qualitative form of this angular decay (Figure 5.8(b)). A demonstration of how the simulated results vary with τ and T_R is given in Appendix C. However, many discrepancies still exist between panels (a) and (b), primarily due to nuclear dynamics occurring in the intermediate ion prior to dissociation, which is neglected in the simulation. Accounting for apparent geometry changes in the propyl ion provides insight into these dynamics.

Firstly, the KER of the secondary dissociation step in Figure 5.8(b) is significantly overestimated and varies dramatically close to 0 and 180°. The experimental value of the $\text{KER}_{(C_2H_4{}^{+},CH_3^{+})}$ was combined with Coulomb's law to calculate an effective CH_3-C_2H_4 separation at the instant of secondary fragmentation of 2.96 Å – approximately double the C-C bond length in the neutral ground state parent molecule. This apparent stretch of the bond length is not solely indicative of changes to the nuclear geometry in the propyl dication intermediate, but also the deviation of the Coulomb explosion dynamics from the limit of two Coulombically repelling point charges, which may be significant in this case. Incorporating this effective separation into the model produces the KER-corrected simulation shown in panel (c). The blurring results in a much broader KER distribution, which varies less dramatically with $\theta_{(\mathrm{I}^+,\mathrm{CH_3}^+)}$.

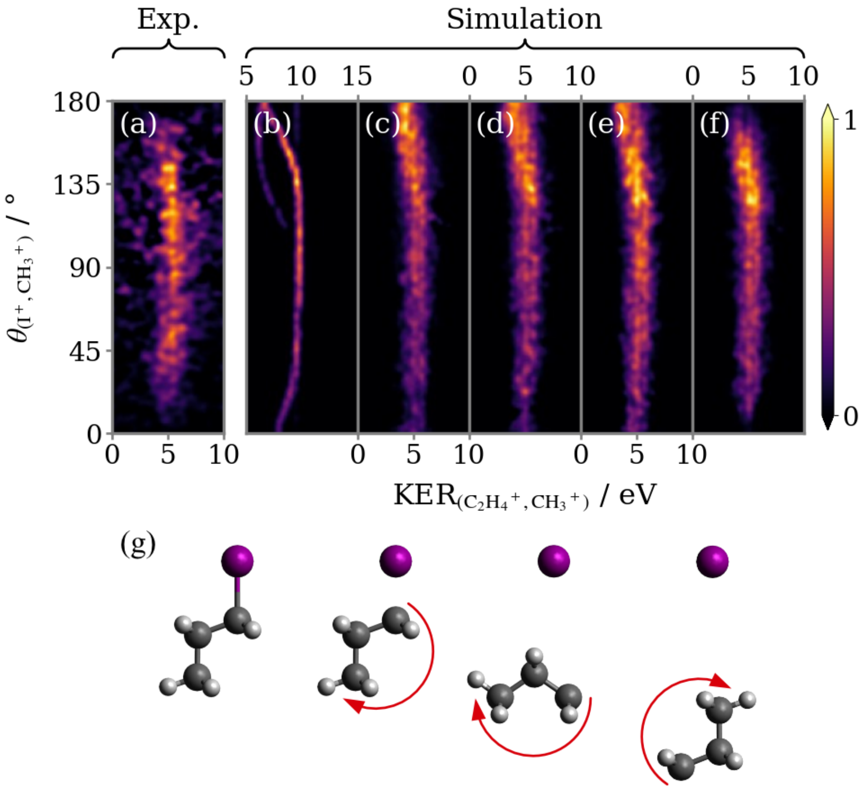

Figure 5.8: (a) The covariance map from Figure 5.6(c). (b-f) Simulated correlation maps for channel I: the sequential breakup of 1-IP^{3+} into I$^+$ + $\mathrm{C_2H_4}^+$ + $\mathrm{CH_3}^+$, where the primary step is Coulomb explosion into I$^+$ + $\mathrm{C_3H_7}^{2+}$. From left to right, the simulated correlation maps display the results of successive modifications. (b) is the basic model, (c) incorporates an effective charge separation for the primary step, (d) simulates bending of the C-C-C bond angle in the propyl dication, (e) increases the average C-C-C bond angle by 20°, and (f) includes a small degree of out-of-plane rotation. (g) Schematic diagram of the rotation of the 1-propyl dication with respect to the emission direction of I$^+$.

Because the intermediate ion in this system is polyatomic, the primary dissociation step may excite the propyl ion vibrationally as well as rotationally. The predominant vibrational modes are expected to be low frequency bending modes. To simulate this motion, a Gaussian variation of the C-C-C bond angle with a width of 30° was included. The result in panel (d) is a blurring of the overall angular distribution, which appears to somewhat decrease the angle of maximum intensity, though it remains noticeably larger than observed in the experimental data.

The next modification is to simulate a relaxation of the C-C-C bond angle in the propyl ion by 20° relative to the optimised neutral ground state 1-IP geometry (panel (f)). Doing so improves the resemblance to the experimental data by decreasing the angle of maximum intensity. This could be the result of changes in the bonding in the propyl dication. The final effect to account for is rotation of the intermediate about different axes relative to the initial fragmentation. The excitation is deemed to be small, so it is simulated using a normal distribution of rotation about a perpendicular axis, with a narrow width of 10°. In panel (e) this reduces the vertical span and consequently shifts the position of the angular maximum to lower theta, which markedly improves the similarity to panel (a).

The modifications to the simulation outlined here have been used to account for the additional behaviours associated with the polyatomic nature of the intermediate radical. Together, they represent a series of refinements to the model. Comparing the first and last panels of Figure 5.8, the end result is an excellent qualitative agreement between the experimental and simulated sequential fragmentation channel feature, given the inherent simplicity of the model employed. The concepts originally developed to describe sequential three-body dissociation of a triatomic trication translate well to describing fragmentation in a larger polyatomic trication through simple modelling of the additional degrees of freedom.

Sequential fragmentation of 2-iodopropane trications

Data simulated for the sequential three-body fragmentation of 2-IP^{3+} are compared with the results of experiment in Figure 5.9. The intensity in the experimental covariance map, displayed in panel (a), peaks around 100°, close to the angle separating the iodine and methyl groups in the parent molecule. The angular distribution is slightly asymmetric about this point, being weighted towards smaller $\theta_{(\mathrm{I}^+,\mathrm{CH}_3{}^+)}$. The motion of the 2-propyl radical following the primary dissociation step is expected to be rather different that of the 1-propyl radical from 1-IP. The impulse of the C-I dissociation acts symmetrically on the 2-propyl dication, with much less torque applied.[195] Because the iodine atom in 2-IP is out-of-plane of the

C atom chain, the ejection of I^+ will initiate rotation of $C_3H_7^{2+}$ such that the two terminal methyl groups pivot towards a minimum methyl-iodine recoil angle after approximately a quarter rotation, followed by a maximum recoil angle after another half rotation. This is depicted schematically in panel (g).

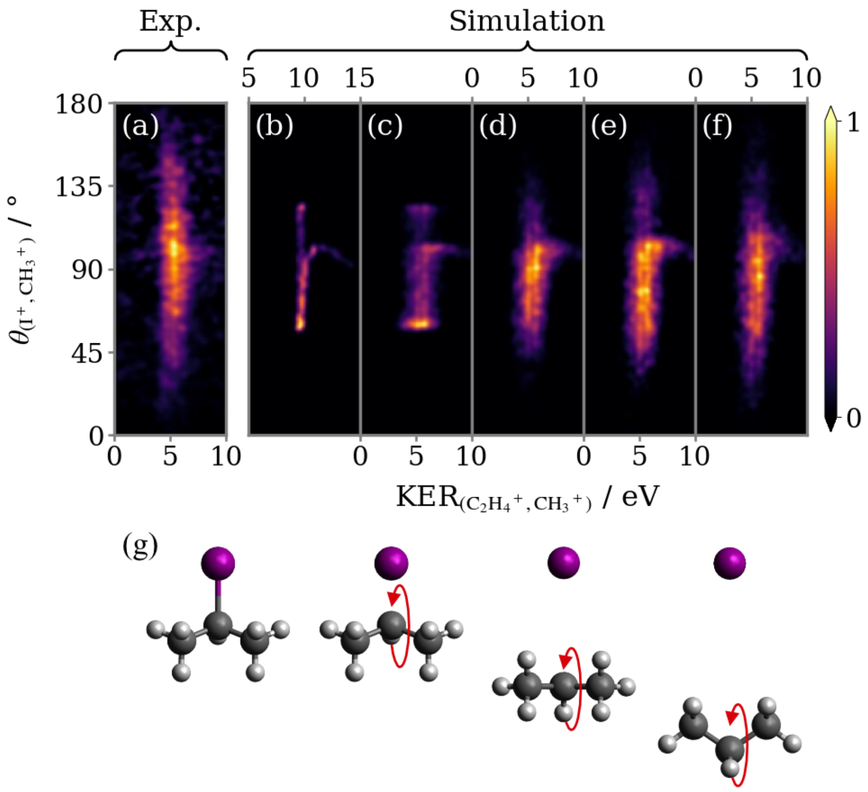

Figure 5.9: (a) The covariance map from Figure 5.6(d). (b-f) Simulated correlation maps for channel I: the sequential breakup of 2-IP^{3+} into $I^+ + C_2H_4^+ + CH_3^+$, where the primary step is Coulomb explosion into $I^+ + C_3H_7^{2+}$. From left to right, the simulated correlation maps display the results of successive modifications. (b) is the basic model, (c) incorporates an effective charge separation for the primary step, (d) simulates bending of the C-C-C bond angle in the propyl dication, (e) compresses the average C-C-C bond angle by 20°, and (f) includes a small degree of out-of-plane rotation. (g) Schematic diagram of the rotation of the 2-propyl dication with respect to the emission direction of I^+.

The data in Figure 5.9(b) have been simulated assuming a intermediate lifetime that is half the rotational period ($\tau = 0.75\,\text{ps}$, $T_\text{R} = 1.5\,\text{ps}$). This reproduces the asymmetry in the angular distribution observed in panel (a), with the methyl fragment predominantly ejected at a relative angle to the I^+ lower than the angle for concerted fragmentation. The KER predicted by the simulation was once again corrected (panel (c)) using Coulomb's law to infer an effective CH_3-C_2H_4 separation at the instant of secondary fragmentation based on the experimental $KER_{(C_2H_4{}^+,CH_3^+)}$ distribution.

At this stage, the simulation outputs a $\theta_{(I^+,CH_3{}^+)}$ range that is limited by the fixed C-C-C bond angle, and is much narrower than observed in experiment. It correctly predicts a local maximum at around 100°, but incorrectly predicts intense features at the limits of the angular range, corresponding to the rotational turn-around points of the propyl dication. To resolve these discrepancies, the same sequence of modifications outlined in the previous section are implemented. The first is excitation of the bending mode in the $C_3H_7{}^{2+}$, shown in panel (d). The bending mode has a much greater impact on the form of the simulated data for 2-IP than was observed for 1-IP. The blurring has the joint effect of removing the maxima at the turn-around points and expanding the angular range, both of which improve the resemblance to the experimental data.

Panel (e) displays the result of distorting the bond angle of the propyl dication, this time decreasing it by 20° relative to the optimised neutral ground state 2-IP geometry in order to increase the angular range of the feature. Again, the final modification made was to model an additional small rotation about an axis perpendicular to the rotation caused by the initial fragmentation (panel (f)). This further increases the vertical span, but suppresses the intensity maximum.

Overall, the model is less successful at capturing the form of the $\theta_{(I^+,CH_3{}^+)}$ distribution for the sequential breakup of 2-IP^{3+}. However, the results are encouraging for a simple point-charge model. In its current form, the model does not account many factors, including: the ensemble of populated starting geometries of the molecule (for instance due to different conformers of the neutral molecule); internal motions of the propyl dication other than bending; variations in the charge distribution of the molecular trication; and any deviations from Coulombic behaviour in the fragmentation, *e.g.* due to residual bonding interaction in the trication.

Despite such limitations, the model reveals the important role of the nuclear dynamics in the intermediate. In particular, the differences observed between 1-IP and 2-IP indicate the important role of rotation in the propyl dication intermediate, which may occur about multiple axes. This is in contrast to the simpler case of triatomic fragmentation, in which rotation may be assumed to occur in the fragmentation plane.[174,175] Evidence also suggests that other nuclear motion – namely C-C stretching and bending – has a significant impact on the sequential photofragmentation dynamics. To further investigate these effects, a full theoretical trajectory calculations on *ab initio* potential energy surfaces would be desirable, albeit a significant theoretical challenge given the possible contributions from many electronic states of the polycation.[183,196,197]

5.5 Three-body breakup of parent dications

The next part of the analysis is concerned with fully characterising the dissociation behaviour of 1- and 2-IP dications. A common dissociation pathway for a polyatomic dication is sequential three-body breakup to yield a pair of charged fragments and a neutral cofragment. Here, a systematic method for identifying and separating the signal from such channels is introduced. Consider the sequential dissociation process where the primary step is a Coulomb explosion between two charged fragments:

$$\mathrm{ABC}^{2+} \rightarrow \mathrm{A}^{+} + \mathrm{BC}^{+}, \tag{5.1}$$

one of which is an unstable intermediate ion that further dissociates by ejecting a neutral fragment:

$$\mathrm{BC}^{+} \rightarrow \mathrm{B}^{+} + \mathrm{C}. \tag{5.2}$$

This process is illustrated schematically in Figure 5.10.

In this mechanism, the intermediate BC^{+} gains momentum equal and opposite to the primary product A^{+} during the initial step, which is then partitioned between the secondary products according to their masses. Neglecting the impulse of the secondary bond dissociation, which is expected to be significantly smaller than the primary step driven by Coulombic repulsion, the relationship between the momenta of the primary and secondary products can be approximated as:

$$\vec{p}_\mathrm{B} \approx -\frac{m_\mathrm{B}\vec{p}_\mathrm{A}}{m_\mathrm{BC}},\ \vec{p}_\mathrm{C} \approx -\frac{m_\mathrm{C}\vec{p}_\mathrm{A}}{m_\mathrm{BC}}. \tag{5.3}$$

Hence, the signal in a covariance map corresponding to a specific fragmentation channel of a molecular dication can be separated by applying the constraint that the momenta of the ion pair must obey Eqution 5.3, within some range to account for the impulse of the secondary bond dissociation.

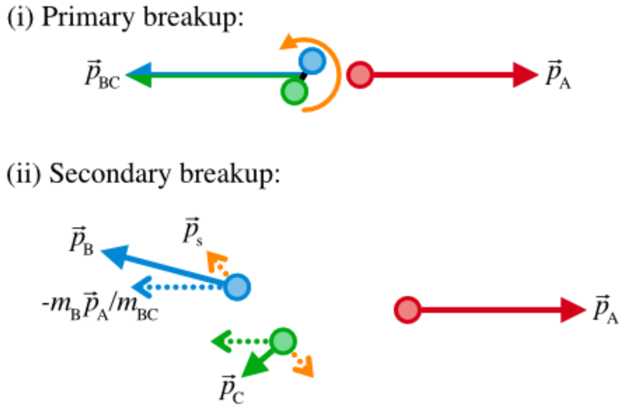

Figure 5.10: Schematic diagram for the sequential three-body dissociation scheme described in Equations 5.1 and 5.2. Panels (i) and (ii) illustrate the primary and secondary steps, respectively. Solid arrows are used to denote the momenta of the products and dotted-line arrows indicate contributions to the total momenta of the secondary products (B^+ + C). The primary Coulomb explosion step induces rotation of the intermediate BC^+, which in the limit that the intermediate lifetime exceeds its rotational period, will randomly distribute the direction of the secondary dissociation impulse $\vec{p}_\mathrm{s}$ relative to the recoil of the primary product (A^+).

To demonstrate how the approach works, consider again the correlated momentum of the (I^+, $CH_3{}^+$) ion pair. The Newton diagrams for 1- and 2-IP from Figures 5.4 are replotted in the top panels of Figure 5.11. The covariance maps contain contributions from: (I) sequential and (II) concerted three-body breakup of IP^{3+}, as well as (III, IV) sequential three-body breakup of IP^{2+}. This latter mechanism involves cleavage of a C-I and C-C bond, but the order in which they can occur gives rise to two distinct channels:

$$\begin{aligned} \mathrm{C_3H_7I^{2+}} &\rightarrow \mathrm{C_3H_7{}^{+} + I^{+}}, \\ \mathrm{C_3H_7{}^{+}} &\rightarrow \mathrm{CH_3{}^{+} + C_2H_4}. \end{aligned} \tag{III}$$

$$\begin{aligned} \mathrm{C_3H_7I^{2+}} &\rightarrow \mathrm{CH_3{}^{+} + C_2H_4I^{+}}, \\ \mathrm{C_2H_4I^{+}} &\rightarrow \mathrm{I^{+} + C_2H_4}. \end{aligned} \tag{IV}$$

Using the momentum constraint described above and assigning ($A^+ = I^+$, $B^+ = CH_3{}^+$) the signal from channel III can be isolated, as shown in panels (c) and (d) of Figure 5.11. (Note that a range of acceptance of 30 a.u. was used to account for the impulse of the C-C bond fission). Although the propyl cation intermediate will be rotationally excited by the initial step, the momenta of both secondary products are roughly in the opposite direction to that of the primary I^+ product since the impulse of the primary Coulomb explosion step is much greater than that of the secondary bond dissociation step. The momenta of the secondary products along the horizontal axis are unequal because the momentum they maintain from the primary step is partitioned according to their masses. By exchanging the assignment of I^+ and $CH_3{}^+$ (i.e. $A^+ = CH_3{}^+$, $B^+ = I^+$), the covariance corresponding to channel IV is instead separated, shown in panels (e) and (f).

Although the dynamics associated with the sequential breakup of the trication show considerable dependence on the isomer, owing to the different rovibrational dynamics of the intermediate, the sequential breakup of the dication gives rise to near-identical fragment momentum correlations for the two isomers. Since the initial step is a two-body Coulomb explosion, the outcome must necessarily be back-to-back recoil in both cases. The rovibrational dynamics of the intermediate are expected to be different in 1-IP/2-IP because the iodine atom is in/out-of-plane of the C-chain. However, as will be later demonstrated using simulation, when the dissociation of the intermediate releases little kinetic energy compared to the initial Coulomb explosion, the fragment momentum correlation is nearly identical for this pair of isomers.

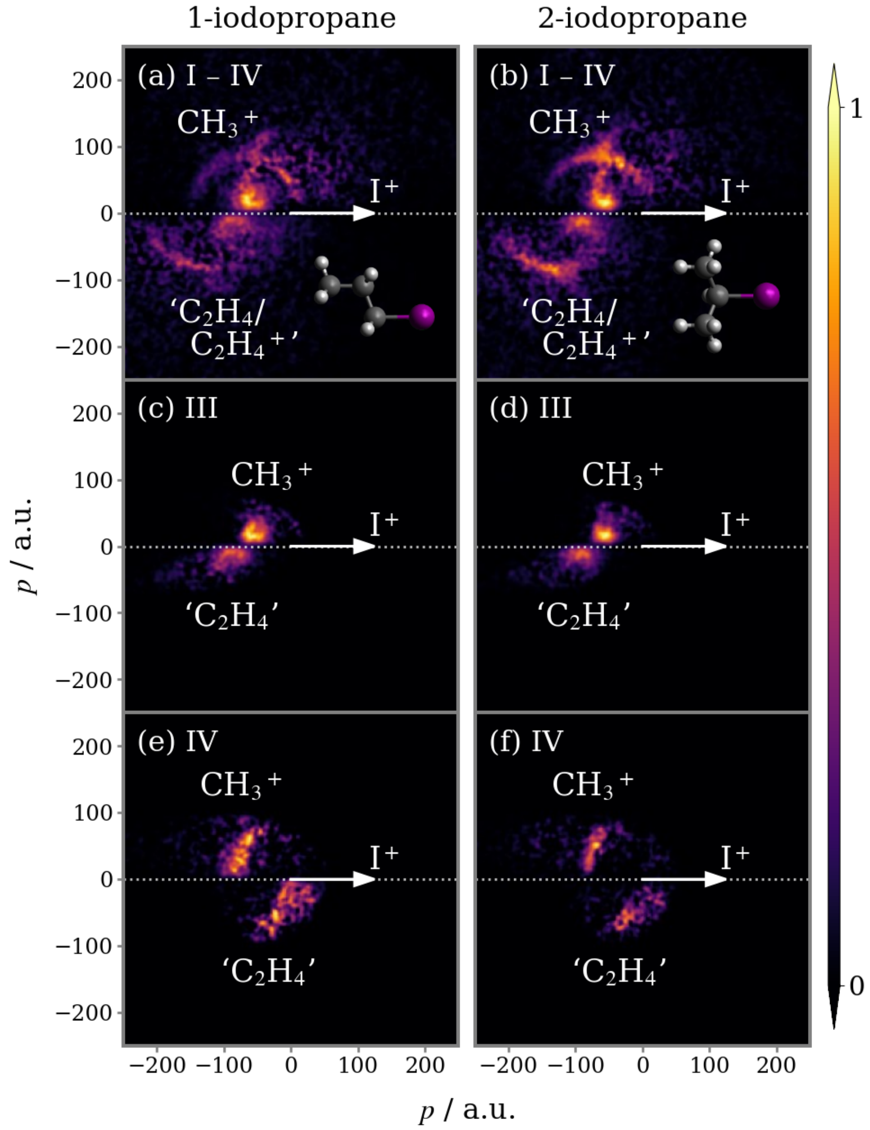

Figure 5.11: Newton diagrams for the three-body breakup of (a) 1-IP$^{2+/3+}$ and (b) 2-IP$^{2+/3+}$ into I$^+$ + C_2H_4/$C_2H_4^+$ + CH_3^+, reproduced from Figures 5.4(a) and (b), respectively. Three dissociation channels contribute: (I) sequential and (II) concerted three-body breakup of IP^{3+}, and (III, IV) sequential three-body breakup of IP^{2+}. In panels (c, d) the signals from the (III) sequential breakup of IP^{2+}, where I$^+$ is the primary fragment, have been separated whilst (e, f) show the isolated signals that correspond to (IV) sequential breakup of IP^{2+} with a primary CH_3^+ product. Each panel is normalised separately.

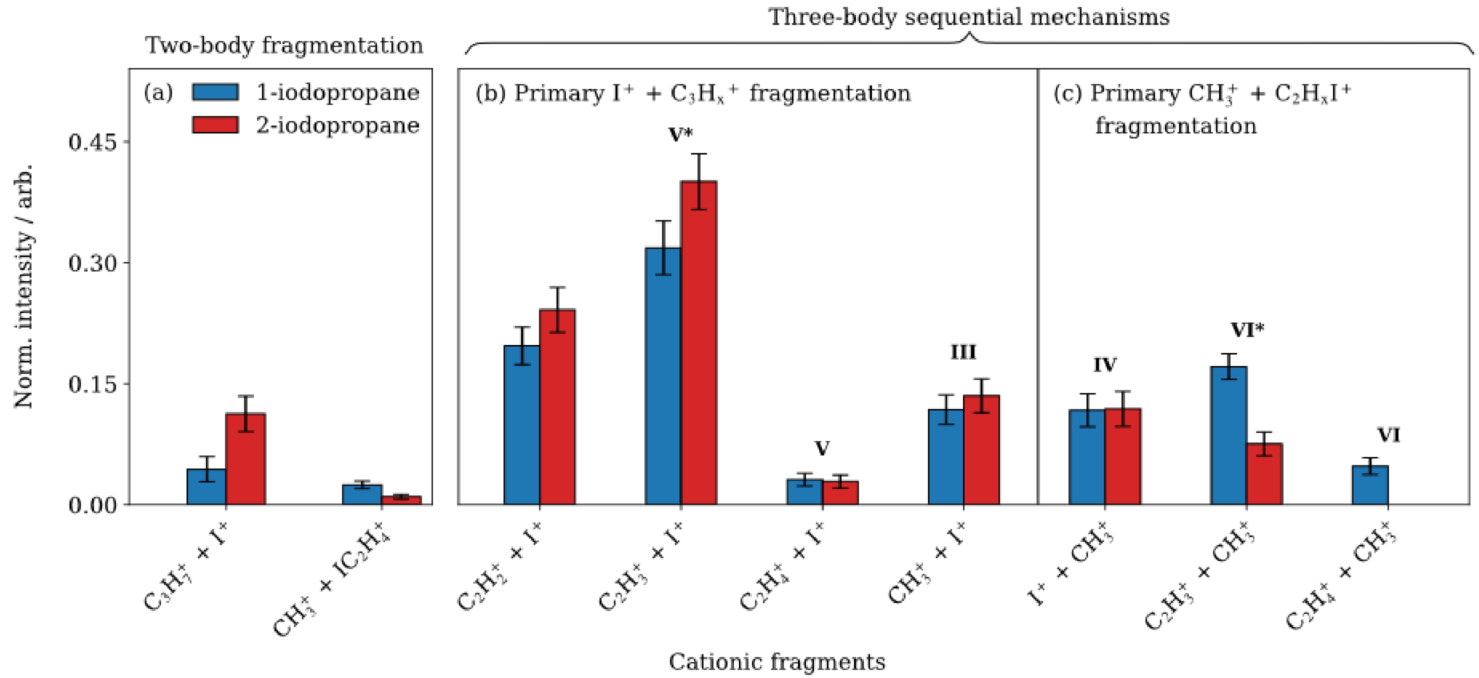

Figure 5.12: Integrated covariance intensity for all observed fragmentation pathways of the parent dication, including (a) two-body fragmentation and sequential three-body fragmentation, where the primary step is Coulomb explosion into (b) $C_3H_7{}^+$ + I^+ or (c) $CH_3{}^+$ + $C_2H_4I^+$. The data are normalised to the summed intensity of all channels for each isomer. No statistically significant covariance was observed for the channel that yields $C_2H_4{}^+$ + $CH_3{}^+$ in 2-IP. Error bars are given by the standard deviation obtained from a bootstrap fitting method, performed on 100 sample sets of 50,000 experimental cycles. Individual channels of interest are discussed within the text and labeled accordingly.

5.5.1 Relative intensity of competing processes

For each observed fragmentation channel of IP^{2+}, the covariance between the pair of ionic products was calculated by considering the momentum partitioning of the products, as outlined above. Assuming a uniform detection efficiency for all ionic fragments, the intensity of the covariance associated with a given fragmentation pathway is proportional to the yield of that process.[80] In Figure 5.12, the relative intensities for the set of covariance maps are plotted together. While the absolute detection efficiency for different ion species cannot easily be determined for these data, it is expected to be of similar magnitude for all those listed in Figure 5.12. Furthermore, the detection efficiency of each ion species is expected to be the same in the datasets recorded for each isomer, as they were acquired under otherwise identical conditions.

The two-body breakup channels listed in panel (a) must correspond to the dissociation of the parent dication. 1-IP is likely to break up via C-C bond cleavage or C-I bond cleavage, whereas breakup of 2-IP occurs predominantly via C-I bond cleavage. This can be attributed to differences between the isomer geometries, which influence the range of charge generation and redistribution processes accessible through AM decay.

Three-body breakup of the molecular dication is always observed to occur via a sequential mechanism involving cleavage of a C-I and a C-C bond, in either order, such as for channels III and IV. Following dissociation of the intermediate, either secondary product can retain the charge, which gives rise to another two distinct channels:

$$\begin{aligned} C_3H_7I^{2+} &\rightarrow C_3H_7{}^{+} + I^{+}, \\ C_3H_7{}^{+} &\rightarrow CH_3 + C_2H_4{}^{+}. \end{aligned} \tag{V}$$

$$\begin{aligned} C_3H_7I^{2+} &\rightarrow CH_3{}^{+} + C_2H_4I^{+}, \\ C_2H_4I^{+} &\rightarrow C_2H_4{}^{+} + I. \end{aligned} \tag{VI}$$

In panels (b) and (c) of Figure 5.12, these processes are separated by whether the primary step is the Coulomb explosion into $I^+ + C_3H_7^+$ or $CH_3^+ + C_2H_4I^+$. No intensity for channel VI in 2-IP is listed in Figure 5.12(c) as no covariance signal was observed above the noise level, indicating that it is a minor process for 2-IP.

Several ion pairs are listed in Figure 5.12(b) and (c) that presumably arise from the fragmentation of the parent molecule into more than three bodies, and for which the initial charge state is uncertain. These have been included because they act as *pseudo* three-body processes and show fragmentation dynamics comparable to the breakup of parent dications. For example, consider the fragmentation pathway that yields $CH_3^+ + C_2H_3^+$. Both I and H are unaccounted for, though it cannot be determined from the data whether they are bound or isolated, *i.e.* whether the process is three- or four-body. This is labelled channel VI*, as the analysis suggests that the fragmentation mechanism is analogous to that of channel VI.

The fragment momentum correlations for channels VI and VI* in 1-IP are compared in Figure 5.13. Aside from the limited statistics for channel VI, they are identical. This indicates that, if H is ejected in the breakup into ($CH_3^+ + C_2H_3^+$), though it cannot be determined at what point in the sequential mechanism this occurs, the nuclear dynamics are not meaningfully altered, *i.e.* the dissociation may be treated as *pseudo* three-body. Similarly, if any other subtle dynamics are involved in channel IV*, for example H migration, the experiment is not sensitive to them.

As discussed in connection with Figure 5.3, because not all H^+ ions reach the detector, there is also the possibility that channel VI* produces H^+, and therefore corresponds to the breakup of a parent trication. Because H is so light relative to the other fragments, if a proton is ejected prior to or simultaneously with the Coulomb explosion into $CH_3^+ + C_2H_3I^+$, it is not expected to significantly affect the KE of other fragments, or meaningfully alter the dynamics compared to the breakup of the parent dication via channel VI.

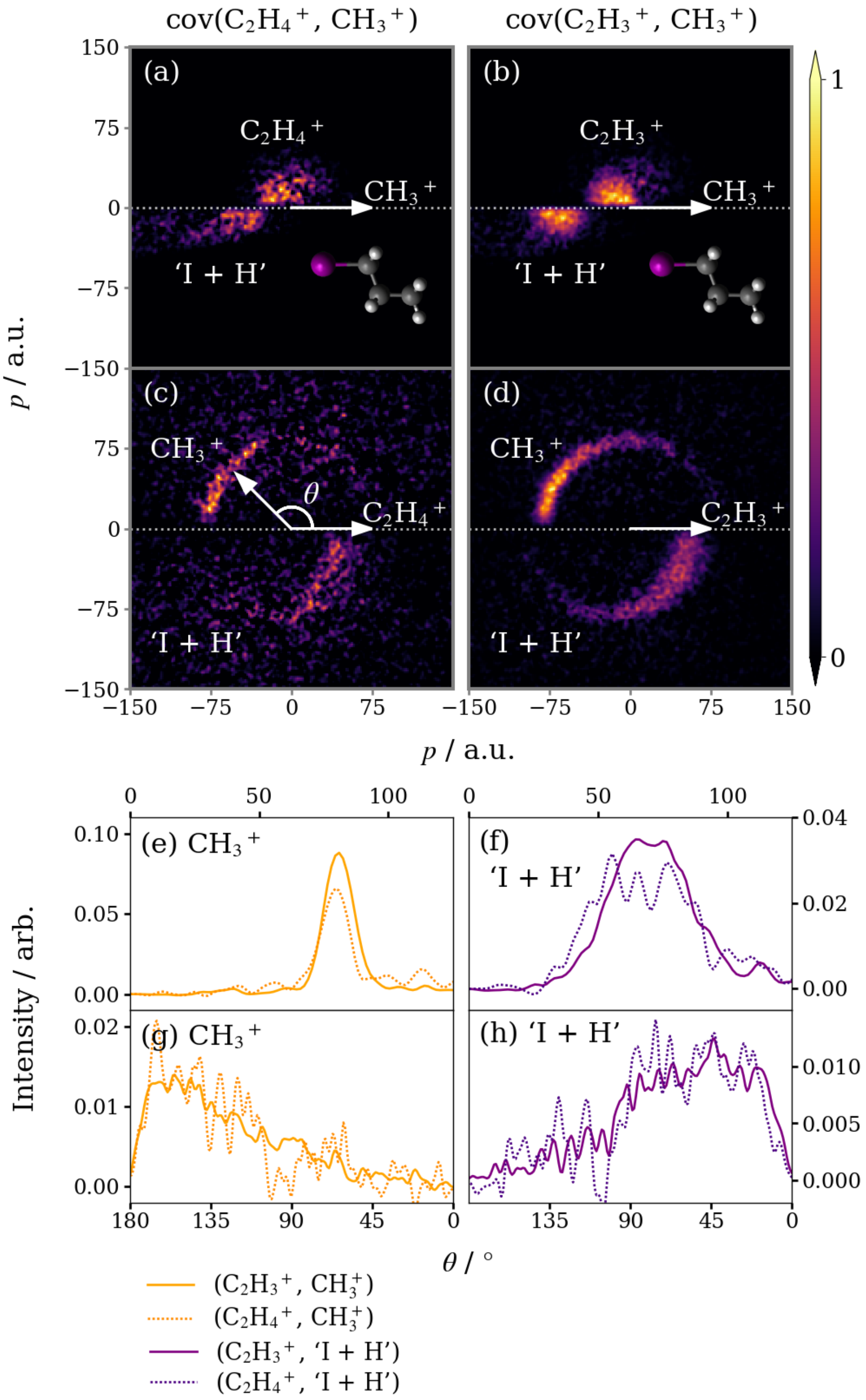

Figure 5.13: Newton diagrams for the sequential breakup of 1-IP^{2+} into (*left column*, channel VI) $CH_3{}^+$ + $C_2H_4{}^+$ and (*right column*, channel VI*) $CH_3{}^+$ + $C_2H_3{}^+$, where the primary step is Coulomb explosion into $CH_3{}^+$ + $C_2H_4I^+$. Panels (a, b) display the momentum distribution of $C_2H_x^+$ relative to the recoil direction of $CH_3{}^+$, and *vice-versa* in (c, d). Each panel is normalised separately. The momentum and angular distributions integrated from panels (c) and (d) are displayed below, indicated by dotted and solid lines, respectively. Distributions are normalised to unit area.

The $C_2H_yI^+$ ($y = 2, 3, 4$) intermediate can, in theory, fragment by C-I or C-C bond cleavage. However, no significant covariance was observed between pairs of ions that would arise from secondary C-C bond cleavage *e.g.* ($CH_3{}^+$, CH_xI^+) or ($CH_3{}^+$, $CH_x{}^+$). Notably, for 1-IP several other possible fragmentation pathways could occur via primary cleavage of a C-C bond closer to iodine, but are not observed. These are outlined in Figure 5.14. Because significant (I^+, $CH_x{}^+$) and ($C_2H_y{}^+$, CH_x^+) covariance is only observed for $x = 3$, it implies that (in the absence of H migration) the C-C bond furthest from the iodine atom is cleaved in the primary step, and hence that breakup into $CH_3{}^+ + C_2H_yI^+$ is a more favorable process. For 2-IP, cleavage of either C-C bond as the primary step also yields $CH_3{}^+ + C_2H_yI^+$.

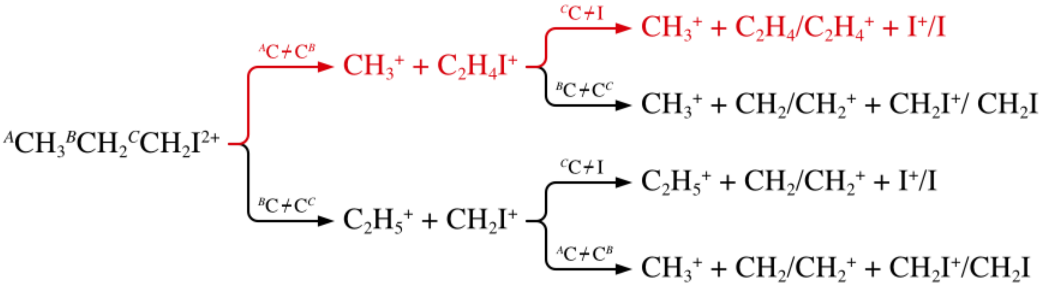

Figure 5.14: The potential sequential three-body dissociation channels of 1-IP^{2+} (disregarding C-H bond cleavage). Highlighted in red are the channels that are observed to be statistically significant and are discussed in the text.

5.5.2 Primary $I^+ + C_3H_7{}^+$ fragmentation

Initial dissociation of the molecular dication by ejection of I^+ is the main pathway for both isomers. This is unsurprising given that ionisation occurs site-selectively at iodine. The fact that no significant isomer-dependent intensity is observed for any of the channels listed in Figure 5.12(b) suggests that the dissociation dynamics are similar for the $C_3H_x{}^+$ intermediates, and independent of the parent isomer. This behaviour could arise for several reasons. For example, the two isomeric forms of $C_3H_7{}^+$ could interconvert through H migration prior to secondary fragmentation.

The Newton diagram covariance maps for the sequential three-body fragmentation of the molecular dication via channel III, which gives rise to a pair of (I^+, $CH_3{}^+$) ions, have been reproduced in Figure 5.15(a) and (b). To extract the kinetic energy release of the secondary dissociation step (KER_s), the data are transformed into the native frame of this step,[174] which is the CoM frame of the $C_3H_7{}^+$ intermediate. The result is the set of Newton diagrams plotted in Figures 5.15(c) and (d). The measured mean KER_s, determined directly from the momenta of the secondary fragments in this frame, is equal within errors for the pair of isomers at 0.22 ± 0.08 eV and 0.15 ± 0.06 eV for 1- and 2-IP, respectively. The high uncertainty in these values derives from the limited momentum resolution of the VMI spectrometer.

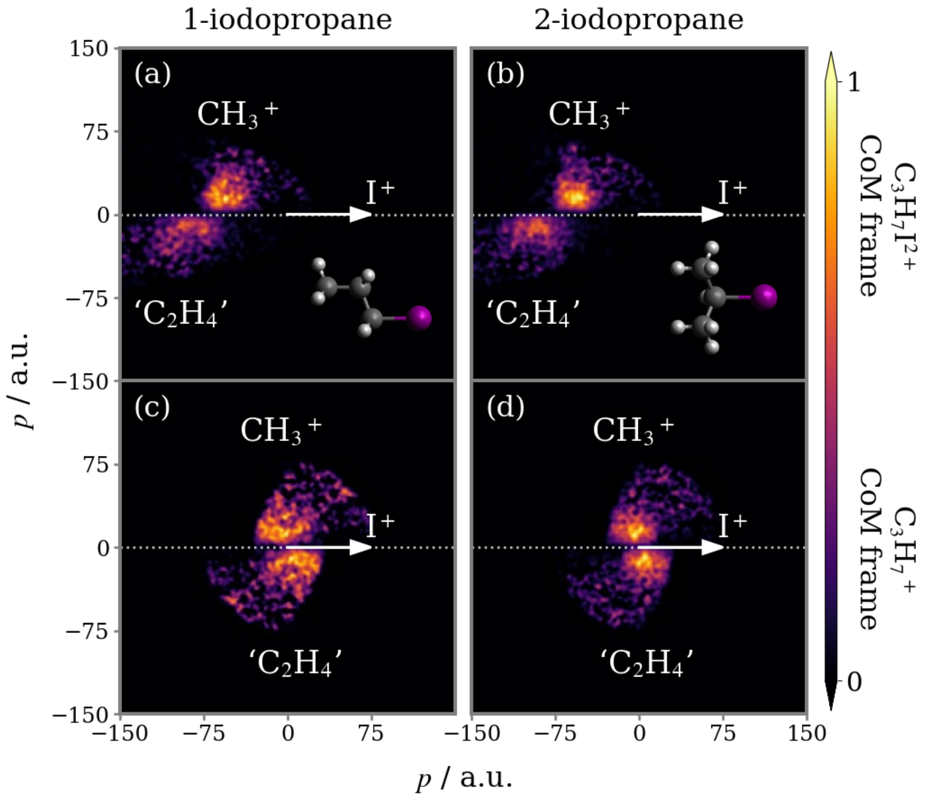

Figure 5.15: Newton diagrams for channel III: the sequential breakup of (*left column*) 1- and (*right column*) 2-IP^{2+} that yields $I^+ + CH_3{}^+$, where the primary step is Coulomb explosion into $I^+ + C_3H_7{}^+$. Panels (a) and (b) display the fragment momenta in the CoM frame of the parent dication. Below, in panels (c) and (d), fragment momenta have been transformed into the CoM frame of the $C_3H_7{}^+$ intermediate intermediate, *i.e.* the native frame of the secondary dissociation step. Each panel is normalised separately.

The sequential three-body fragmentation that yields a pair of (I^+, $C_2H_3{}^+$) ions is, by contrast, an example of the charge remaining on the ethyl fragment following the breakup of the propyl intermediate. The mechanism for this pathway is equivalent to channel V, with the additional loss of H/H^+ or the formation of CH_4 doing little more than slightly blurring the covariances presented in this paper. Hence, it is referred to here as channel V*. From Figure 5.12(b), it is apparent that channel V* is far more prominent than channel V.

The kinetic energy release of the primary Coulomb explosion (KER_p) for channels III and V* is equal, measured at $4.6 \pm 0.5/5.0 \pm 0.4\,\mathrm{eV}$ for 1/2-IP, where the uncertainty in each of these values reflects the standard deviation of a Gaussian distribution. Because the Coulomb explosion product momenta are sensitive to the charge separation, assuming purely Coulombic repulsion, this implies an equivalent charge distribution in the molecular ion leading to both pathways. The observed KER_s for channel V* ($0.17 \pm 0.07\,\mathrm{eV}$ for 1-IP and $0.15 \pm 0.06\,\mathrm{eV}$ for 2-IP) are within error of the values obtained for channel III. Whilst it is difficult to comment on how the dynamics of channels III and V* compare due to the large errors associated with the extracted values, it is assumed that the same C-C bond in the propyl cation intermediate is broken in both processes.

Because the charge is located on different secondary fragments following either channel III or V*, it implies the involvement of different electronic states. These may be populated directly from different AM decay processes, or through non-adiabatic effects en route to dissociation. Though the similar KER_p values for this pair of channels suggest that charge is initially distributed similar on the propyl intermediate, it can redistribute differently during the lifetimes of the corresponding populated excited states. A highly vibrationally excited intermediate ion in a given electronic state could also decay via various pathways. Ultimately both processes may play a role.

5.5.3 Primary CH_3^+ + $C_2H_4I^+$ fragmentation

Sequential three-body breakup via Coulomb explosion into CH_3^+ + $C_2H_4I^+$ is generally less common than sequential three-body breakup via Coulomb explosion into I^+ + $C_3H_7^+$. The occurrence of channel IV, which produces a (CH_3^+, $C_2H_4^+$) ion pair and a neutral iodine fragment, at first sounds surprising given the very high cross section for I 4d ionisation at 95 eV.[194] However, whilst the initial core hole generated by I 4d ionisation is well-localised, AM decay can populate a broad range of electronic and internal energy states of the resultant dication. Given the rapid rate of AM decay relative to photofragmentation, it is the character of these dication states that dictate the fragmentation dynamics and thus product species. Prior work has demonstrated that, in some cases, the dication fragmentation dynamics are largely independent of the initial core-hole site, instead being determined by the electronic character of the two valence-hole states of the dication,[198] or the partitioning of internal energy amongst vibrational modes.[199]

It is also possible that dications that give rise to these photofragmentation dynamics are formed by other photoionisation processes not involving I 4d ionisation, such as single-photon double ionisation[200] or successive single (inner) valence ionisations. However, the cross-sections for these processes is expected to be significantly lower than for I 4d ionisation followed by single AM decay. For instance, Olney *et al.* previously reported a photoabsorption cross-section of ∼30 Mb at 95 eV in CH_3I, with an estimated contribution from valence photoionisation of just ∼1 Mb.[201] The photoabsorption cross-section of CH_4 at this photon energy is ∼0.5 Mb,[202] and the contribution of single-photon double ionisation relative to single ionisation is believed to be on the order of 1%.[203] As such, the prominent photofragmentation channels observed from the molecular dication (including those yielding neutral iodine fragments) are most likely initiated by I 4d ionisation. Future observation of photoelectrons and/or AM electrons produced in correlation with these fragment ions would provide unambiguous evidence for the precise photoionisation process leading to these fragmentation channels.

Channels VI and VI* are the only sequential three-body breakup channels listed in Figure 5.12 that exhibit significantly different intensities for the two isomers. Channel VI is an insignificant pathway for 2-IP, but is common for 1-IP. It is difficult to reason why this should be the case with the available information. If following the primary breakup step the charge on the $C_2H_xI^+$ intermediate is located on the C that has cleaved a bond, this would place the charge further from the iodine substituent for the case of 1-IP, and could make subsequent breakup to yield a neutral iodine cofragment more likely. Ultimately, the dissociation of the dications of both isomers likely takes place on different potential energy surfaces, with topography influenced by various factors that determine the final quantum yield of the processes involved.

As discussed earlier, channel VI* yields CH_3^+ + $C_2H_3^+$ by an equivalent mechanism to channel VI. The loss of H/H^+ or formation of HI does not measurably alter the dynamics. For both isomers, channel VI* is a more significant dissociation pathway than channel VI. Perhaps because loss of neutral iodine is stabilised by formation of HI. Although the current experiment is insensitive to the nature of the neutral fragment(s) formed. Newton diagrams for channel VI* with the primary CH_3^+ product as the reference species are presented in panels (a) and (b) of Figure 5.16. Due to the large mismatch in the mass of the secondary products, $C_2H_3^+$ retains only a small amount of momentum from the initial Coulomb explosion event, the result being that its momentum is localised around the origin.

It is helpful to instead construct the Newton diagrams by selecting $C_2H_3^+$ as the reference ion, as seen in panels (c) and (d). Because the methyl ions have greater momenta, the CH_3^+ momentum distributions are better resolved by the spectrometer, making it easier to visualise the dynamics. In this representation the correlated momenta of CH_3^+ and 'I + H' form opposing arcs. Integrated momentum distributions are shown in panels (e) and (f). The momentum of CH_3^+ is distributed over a narrow range because it is determined solely by the primary process, whereas the 'I + H' momentum distribution is broad because it is the sum of two components that are not aligned (illustrated in Figure 5.10).

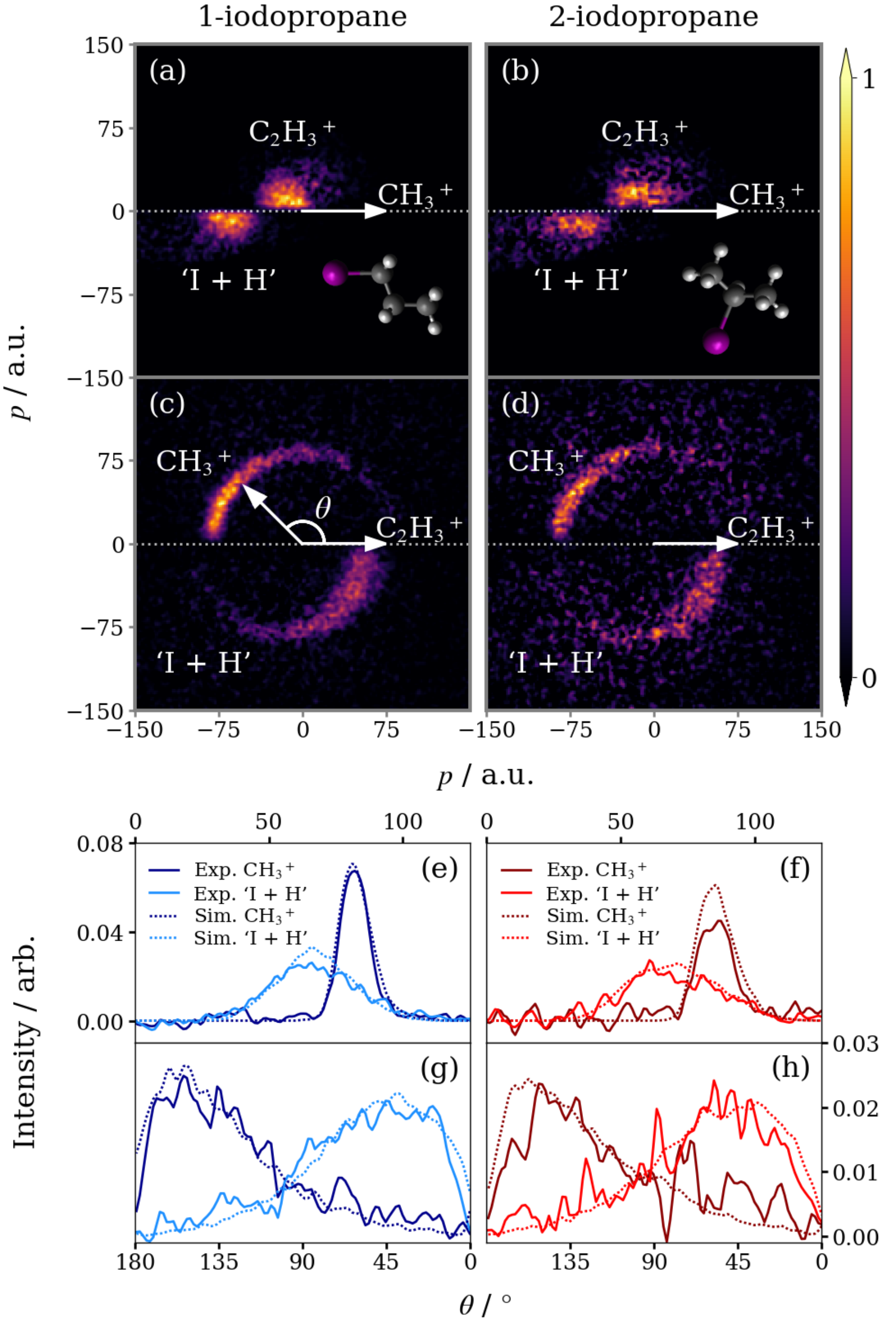

Figure 5.16: Newton diagrams for channel VI*: the sequential breakup of (*left column*) 1-IP^{2+} and (*right column*) 2-IP^{2+} that yields CH_3^+ + $C_2H_3^+$, where the primary step is Coulomb explosion into CH_3^+ + $C_2H_4I^+$. Panels (a, b) display the momentum distribution of $C_2H_3^+$ relative to the recoil direction of CH_3^+, and *vice-versa* in (c, d). Each panel is normalised separately. Below are displayed the integrated CH_3^+ and 'I + H' (e, f) momentum distributions and (g, h) angular distributions relative to the recoil direction of $C_2H_3^+$. Distributions are normalised to unit area. Experimental data, shown by solid lines, are overlaid with data simulated using a classical model of the sequential dissociation process, indicated by dashed lines.

The $C_2H_4I^+$ intermediate is rotationally excited in the initial dissociation event and, if its lifetime far exceeds its rotational period, it will be randomly oriented relative to its recoil direction when it dissociates. However, this would not distribute the secondary ethyl and iodine products over a uniform angular range relative to the primary methyl product if the secondary dissociation barely perturbs the iodine cofragment. In such a dissociation, the iodine cofragment retains the majority of the momentum of the intermediate, and so its recoil direction remains roughly back-to-back with $CH_3{}^+$, as seen in panels (a) and (b) of Figure 5.16. The same impulse has a much greater impact on the trajectory of $C_2H_3{}^+$, as it imparts only slightly less momentum than the fragment retains as a fraction of the intermediate's momentum. This is not enough to reverse the direction of travel of $C_2H_3{}^+$, but can significantly redirect it. The result is a broad recoil distribution of $CH_3{}^+$ relative to $C_2H_3{}^+$ (panels (g) and (h)) that peaks close to 180°.

Simulation of $CH_3{}^+$ + $C_2H_3{}^+$ + HI fragmentation

To support the assigned fragmentation mechanism for channel VI*, a series of classical simulations were conducted using a model based on the one described in Section 4.4.2. The simulation is executed in two steps that replicate the primary and secondary fragmentation steps illustrated in panels (i) and (ii) of Figure 5.10, respectively. It is assumed that the intermediate lifetime is sufficiently long that the two fragmentation steps are isolated events. The ion trajectories are therefore propagated until they have approximately reached their terminal velocities. $C_2H_4I^+$ is then replaced in space by $C_2H_3{}^+$, with an additional velocity component added onto its recoil velocity to account for the impulse of the secondary bond dissociation. This velocity component is randomly rotated to simulate the rotation of the intermediate induced by the primary step. The axis of rotation is determined by considering an impulse along the broken C-C, acting at the CoM of $C_2H_4I^+$.

In panel (a) of Figure 5.17, the experimental ($C_2H_3{}^+$, $CH_3{}^+$) Newton diagram covariance for 1-IP has been reproduced as a function of recoil angle relative to $C_2H_3{}^+$. The neighboring panels are the outputs of the simulation as successive modifications are implemented that incorporate more tunable parameters. To fully reproduce the experimentally observed dynamics, values for many of these parameters were extracted from the experimental data.

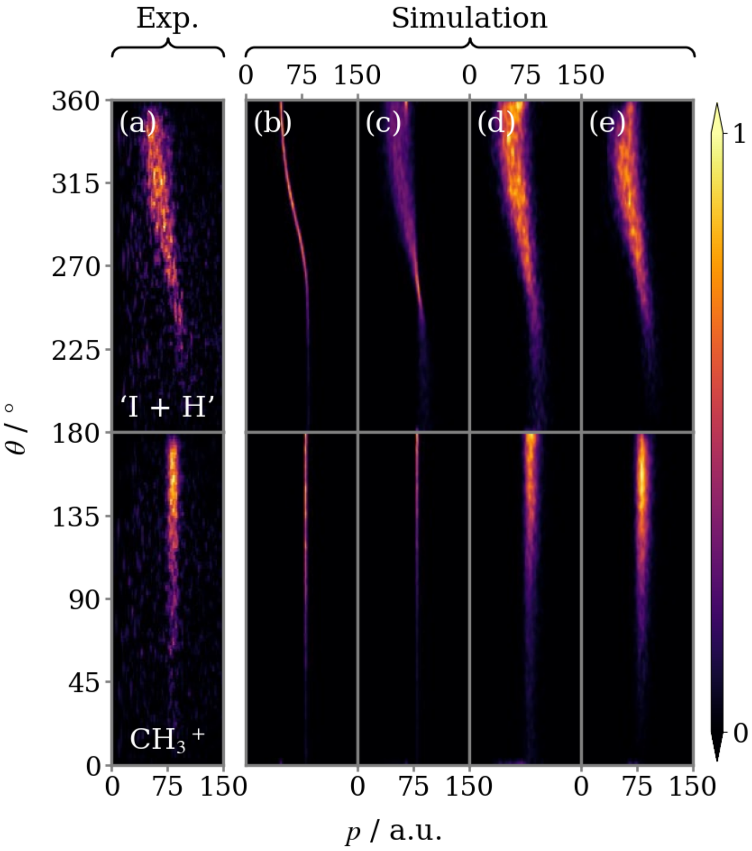

Figure 5.17: (a) The Newton diagram from Figure 5.16(c) displayed in polar coordinates, where θ is the angle relative to the recoil direction of $C_2H_3{}^+$. (b-e) Simulated correaltion maps for channel VI*: the sequential breakup of 1-IP^{2+} that yields $CH_3{}^+$ and $C_2H_3{}^+$, where the primary step is Coulomb explosion into $CH_3{}^+$ + $C_2H_4I^+$. (b) was produced by the model outlined in the methods section, (c) incorporates a distribution for the secondary dissociation KER, (d) uses an effective charge separation distribution for the primary step, and (e) also includes a small degree of out-of-plane rotation.

A Gaussian fitting to the experimental data in the native frame of the $C_2H_4I^+$ intermediate was used to extract a secondary dissociation impulse (p_s) of 18 ± 9 a.u. In the first iteration of the model (Figure 5.17(b)), the mean p_s was used to determine the magnitude of the velocity component v_s superimposed onto the secondary ion product to simulate the dissociation of $C_2H_4I^+$. A demonstration of how the simulated result varies as a function of p_s is provided in Appendix C.

Even in this simple form, the model captures the form of the angular distribution well. This supports the interpretation of the dissociation mechanism, *i.e.* that the intermediate is randomly oriented at the instant of secondary breakup, but the secondary products are not uniformly distributed relative to the recoil direction of the primary product, as the greater portion of their momenta derives from the primary Coulomb explosion step.

Because the KERs of both steps are single-valued, they do not reproduce the momentum distribution of the products. In panel (c) of Figure 5.17, the p_s width has been used to generate a v_s distribution. A second Gaussian fitting to the experimental $CH_3{}^+$ momentum distribution in Figure 5.16(e) was used to determine a KER_p of $3.8 \pm 0.3\,\mathrm{eV}$ for the Coulomb explosion event, equivalent to an effective separation of the charges on the $CH_3{}^+$ and $C_2H_4I^+$ moieties of 3.8 Å. This has been incorporated into the simulation in panel (d). Finally, to account for potential rotational excitation of the intermediate about different axes relative to the rotation induced by the initial fragmentation, a normal distribution of rotation with a narrow width of 10° about a perpendicular rotational axis was applied. This drives the angular distribution towards 90/270° (panel (e)), reproducing the decreased intensity at 180/360° in the experimental plot.

Integrated angular and radial distributions from the final simulation are overlaid with the experimental data in panels (e) and (g) of Figure 5.16 and show strong agreement. Despite the simplicity of such a model, it is possible to recreate the fragmentation dynamics of a relatively low-charge molecular polycation using parameters directly obtained from experimental data. This is a showcase for the general applicability of the classical point charge model for simulating Coulomb explosion processes, even in the low parent ion charge state regime.

The model was also used to simulate the same fragmentation channel in 2-IP, with analogous parameters extracted from the 2-IP experimental data used as input. The output is overlaid with experiment in panels (f) and (h) of Figure 5.16. Although the 2-IP experimental data for this fragmentation channel has limited statistics compared to 1-IP, the agreement between experimental and simulation is once again excellent. It is worth remarking again on the resemblance between fragment correlations for 1- and 2-IP^{2+}, which has been observed in all the fragmentation channels discussed here. The same resemblance is observed in the simulated data. Interestingly, it was important to consider the different axis of rotation of the intermediate for each isomer, otherwise the predicted angular distributions were very different. This suggests that it is in spite of different intermediate dynamics that this pair of isomers produce closely matching final fragment momentum correlations.

5.5.4 Direct imaging of product momentum exchange

The approach of considering the momentum partitioning between an ion pair has so far been applied to disentangle signals arising from the same pairs of ion species generated by different fragmentation channels. This can be taken a step further and used to directly interrogate the dynamics of molecular fragmentation more generally. To demonstrate, consider again the sequential breakup of 1-IP^{2+} via Coulomb explosion into CH_3^+ and $C_2H_4I^+$, producing the (CH_3^+, $C_2H_3^+$) pair. In Figure 5.18, the momentum of the primary CH_3^+ product ($p_{CH_3^+}$) relative to the recoil direction of secondary $C_2H_3^+$ product are plotted as a function of the magnitude of the momentum of this reference ion ($p_{C_2H_3^+}$). The (CH_3^+, $C_2H_3^+$) data were split into subsets based on the momentum of $C_2H_3^+$, and each slice was calculated from a different subset. The sum of these slices is projected onto the xy-plane and exactly equals the data plotted in the top half of Figure 5.16.

When the $C_2H_3^+$ has minimal momentum (the lowest slice), the angular distribution of CH_3^+ ($\theta_{(C_2H_3^+,CH_3^+)}$) sweeps out a broad range. As the momentum of the secondary product increases, the angular distribution becomes focused towards 180°. This shift is a direct visualisation of the rotation of the intermediate. Due to the long lifetime of $C_2H_4I^+$ relative to its rotational period, each intermediate ion is effectively randomly orientated relative to the recoil direction of CH_3^+ at the instant of secondary dissociation. However, the exact orientation of the intermediate affects the momentum exchange in the secondary products. To help illustrate this, complete Newton diagrams for several slices are shown with schematic vector diagrams overlaid.

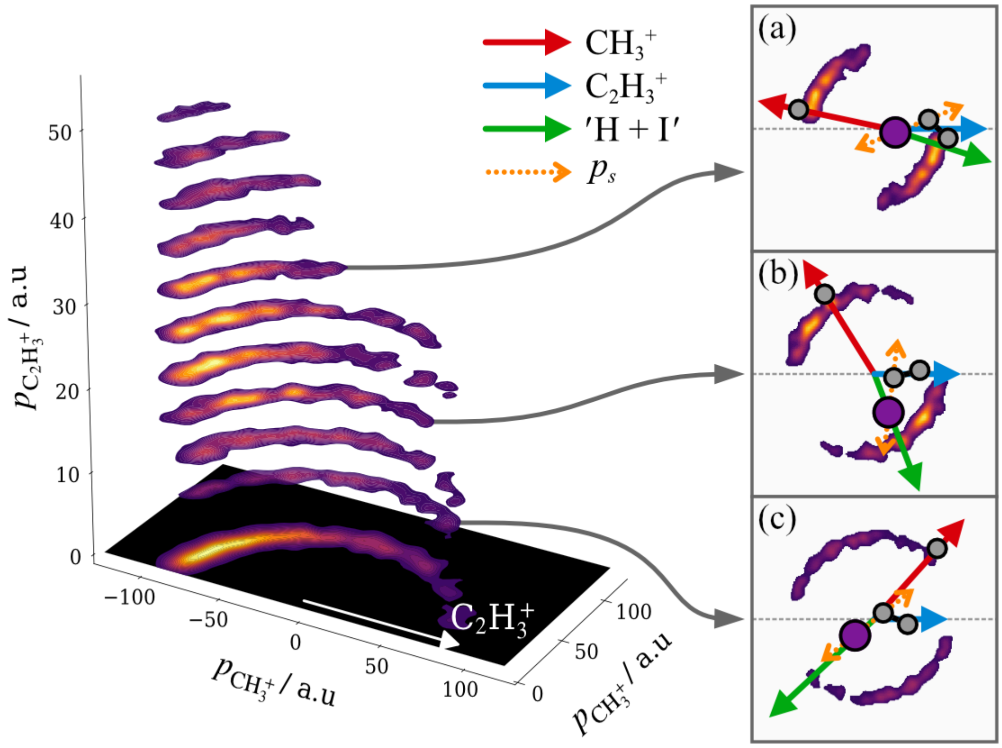

Figure 5.18: Momentum distribution of CH_3^+ relative to the recoil direction of $C_2H_3^+$ for channel VI*: the sequential breakup of 1-IP^{2+} that yields CH_3^+ and $C_2H_3^+$, where the primary step is Coulomb explosion into $CH_3^+ + C_2H_4I^+$. Ascending vertical slices correspond to increasing absolute momentum of $C_2H_3^+$. The projection onto the xy-plane is the sum of these vertical slices. Complete Newton diagrams are shown for several slices, with cartoons superimposed to demonstrate how the rotation of the intermediate prior to secondary fragmentation produces the observed fragment momentum distribution. Vectors are shown in the same colours as their corresponding counterparts in Figure 5.10.

The relationship between $\theta_{(C_2H_3^+,CH_3^+)}$ and $p_{C_2H_3^+}$ is not directly linear because the momentum release of the secondary dissociation takes a range of values. For the orientation of the intermediate illustrated in panel (c), if p_s is large it is enough to redirect the trajectory of $C_2H_3^+$, resulting in a pair of ions that recoil at an acute angle. Whereas if p_s is small, the momentum that $C_2H_3^+$ retains from the primary dissociation dominates, and the ion's trajectory remains roughly opposite to CH_3^+. The angular distribution contracts towards 180° in the upper slices because $C_2H_3^+$ can only be produced with maximum momentum when p_s is maximum and the intermediate is orientated such that p_s aligns with the initial direction of travel.

Fundamentally, the Newton diagrams in Figures 5.16(a) and (c) contain the same information as Figure 5.18. However, this representation provides a more intuitive visualisation of nuclear dynamics and direct insight into the relationships between fragment momenta and relative recoil angle.

Once more, these arguments are corroborated by simulation. To give a clear-cut comparison of the experimental and simulated data, the 3D covariance map in Figure 5.18 has been transformed into a 2D representation by radially integrating each slice. The result is a distribution of $\theta_{(C_2H_3^+,CH_3^+)}$ as a function of $p_{C_2H_3^+}$, plotted in the top panel of Figure 5.19. In the panel below is the simulated data first presented in Figure 5.17(e), now formatted into the same representation. The simulation captures the general form of experimental data well, with a broad distribution that tapers towards 180° with increasing $p_{C_2H_3^+}$. It also able to reproduce the maximum around ∼160° and ∼30 a.u.

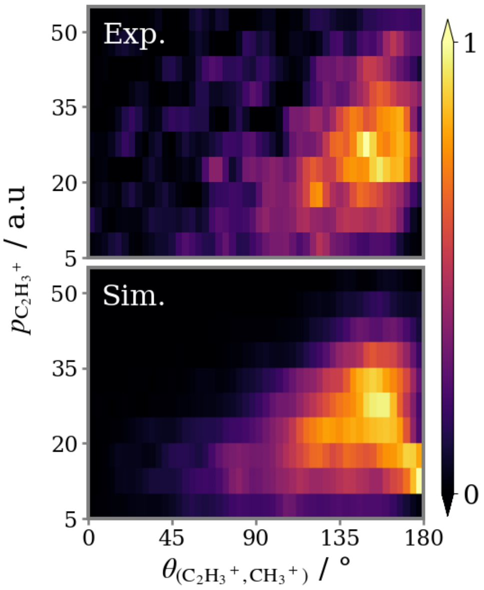

Figure 5.19: *Top*: angular distribution of CH_3^+ relative to the recoil direction of $C_2H_3^+$ as a function of the absolute momentum of $C_2H_3^+$. Integrated from the vertical slices in Figure 5.18. *Bottom*: the simulated dataset from Figure 5.16(e, g) processed in the same manner.

5.6 Conclusions and future work

This chapter has served as a showcase for the utility of incorporating momentum constraints into covariance mapping analysis. The concerted and sequential three-body Coulomb explosion pathways of triply charged 1- and 2-IP into I^+ + $C_2H_4^+$ + CH_3^+ were separated by filtering the I^+ momentum above or below a defined threshold. The isomer-specific dynamics of the three-body dissociation processes were studied in detail using the newly developed covariant native frames analysis approach. A classical Coulomb explosion model of the sequential process was used to interpret the angular distribution of ion emission within the native frame of the secondary dissociation. This model was modified to incorporate possible nuclear motions of the propyl dication intermediate following the primary dissociation. Despite the apparent simplicity of the model, it offers valuable insight into how the torsional and electrostatic forces of the primary dissociation influence the nuclear dynamics in the propyl fragment during its lifetime.

By exploiting the expected momentum partitioning between the products of a three-body breakup, the wide array of different fragmentation channels for 1- and 2-IP dications have been disentangled. Taking this approach further, the momentum exchange relationship between the products of a sequential breakup was studied by calculating the covariance map as a function of the momenta of one of the products. The results provide direct insight into how the rotational dynamics of the intermediate manifests in the measured signal. Again, classical simulations were used to confirm the interpretation of the fragmentation dynamics. They reproduced the experimental results with impressive accuracy, demonstrating the worth of a classical point charge model for simulating a variety of Coulomb explosion processes.

In the present work, the molecular dication predominantly dissociates to give I^+. However, the significant and isomer-dependent intensity observed for covariances between CH_3^+ and $C_2H_3^+$ (generated with a neutral iodine-containing co-fragment) shows that the range and probability of different charge redistribution processes occurring depends on the geometry of the target molecule. A future study would benefit from recording the AM electrons in correlation with the fragment ions in order to be sensitive to the excited electronic states of the dication accessed by the ionisation process. This electronic information would allow the relationship between ionisation and fragmentation dynamics to be explored. The dissociation pathways could then be analyzed in terms of energetics, concerning the internal energy partitioning in the primary and secondary products and the barriers to dissociation. In particular, this could aid in explaining the branching ratios of the various channels listed in Figure 5.12, and hence the reasons for the isomeric differences. Similarly, photoelectron-photoion coincidence experiments ionising above the carbon K-edge would likely shed further information on the extent of any site-selectivity in the dication fragmentation dynamics.

6

Fragmentation dynamics of strong-field ionised *cis* and *trans* isomers of 1,2-dichloroethene

Contents

This chapter describes a 2D ion imaging study of the Coulomb explosion of the *cis* and *trans* isomers of 1,2-dichloroethene (DCE), following SFI by intense NIR femtosecond laser pulse. This work was conducted in the laboratory at the University of Oxford using the Oxford Spectrometer. The data are used to demonstrate projected-momentum covariance mapping, an extension of recoil-frame covariance mapping for 2D ion imaging studies. By considering the 2D projection of the ion momenta as recorded by the detector, it opens the door to a complex suite of analysis tools adapted from 3D momentum imaging studies. Here, this includes the use of different frames of reference to unravel the dynamics of fragmentation, and the application of fragment momentum constraints to isolate specific fragmentation channels.

The analysis explores how parent ion charge state affects the Coulomb explosion dynamics. Two fragmentation pathways of 1,2-DCE polycations are examined in detail: the three-body breakup of a parent trication, and the many body-breakup of a highly charged parent ion that yields, amongst other atomic ions, a pair of chlorine dications. The relationship between the initial molecular geometry and final fragment momenta is shown to be more straightforward for the Coulomb explosion of the more highly charged parent ions, in agreement with a recent theoretical study. The results lay the groundwork for the TR-CEI studies reported in the subsequent chapters, which explore the UV photoexcitation dynamics of this pair of isomers.

6.1 Background

The ability of laser-induced CEI to determine static nuclear structure, such as distinguishing structural isomers, has been demonstrated extensively.[21–23] The next logical step then, is to attempt to use CEI to track the interconversion of a pair of structural isomers in an ultrafast pump-probe experiment. A key goal of this thesis was to use TR-CEI to investigate photo-induced *cis-trans* isomerisation in a simple molecular system. The simplest possible system that exhibits *cis-trans* isomerisation is ethene, but lacking any ‘anchors’ to experimentally track its interconversion, 1,2-DCE is a good alternative.

This chapter reports on the Coulomb explosion of the *cis* and *trans* isomers of 1,2-DCE following SFI by intense NIR femtosecond laser pulse. The experiments were primarily intended to provide a basis for the interpretation of the TR-CEI study that was to follow. Several experimental studies have been conducted on the Coulomb explosion of this pair of geometric isomers in the past.[163,204–206] Ablikim *et al.* used the momentum correlation between the products of a three-body breakup to determine the *cis* and *trans* structures[205]. Crane *et al.* have offered a thorough discussion of the various two-body breakup channels of doubly and triply charged parent ions[163]. Notably, these experiments only investigated the Coulomb explosion of relatively low charge parent polycations (≤ 3). The present study expands upon the previous body of work by examining the Coulomb explosion dynamics of more highly charged parent ions, in order to explore how the fragmentation dynamics vary with parent ion charge state (Z).

A recent *ab initio* trajectory study explored the Z-dependent Coulomb explosion dynamics for *cis*-1,2-DCE and found two distinct regimes of behaviour.[183] For 'low' Z states – defined here as those that dissociate to yield a mixture of atomic and molecular fragments – the mapping from initial molecular geometry to final fragment momenta was complex due to the fragmentation dynamics differing so much between individual channels. By contrast 'high' Z states, for which dissociation results in direct and exclusive formation of atomic ions, had much simpler, Coulomb-interaction dominated mapping. For the purpose of using CEI to probe time-evolving nuclear structure, a straightforward relationship between atomic positions and final fragment momenta is essential.

This work also serves as the first demonstration of projected-momentum covariance mapping, introduced in Section 3.5.1. To recap, in an ion imaging experiment the in-plane components of an ion's momentum can be determined directly from its impact position, whilst the third out-of-plane component must be reconstructed from its arrival time. Recording the ion ToF with sufficient resolution to perform this final step can be a challenge, so it is common to omit the reconstruction of the third momentum component, in which case only a 2D projection of the ion momentum onto the detector is recorded. It generally is not possible to obtain the relative 3D fragment momentum distribution in a CEI experiment that employs 2D projected-momentum imaging, therefore structural information must be deduced from the 2D projected-momentum correlation map.

The conventional method of examining the fragment ion correlations for a CEI experiment that employs 2D ion imaging is recoil-frame covariance imaging.[19,160] It is well suited for studying the Coulomb explosion between a pair of ions, such as a two-body breakup,[50,163] or a three-body breakup involving a neutral cofragment,[163,164] but not for studying Coulomb explosion into many ions. 3D ion imaging studies that utilise more advanced analysis techniques have been able to examine many-body fragmentation dynamics in much greater detail.[13,20,23,78,79,174]

Projected-momentum covariance mapping is a new analysis procedure for 2D projected-momentum imaging data, which expands upon recoil-frame covariance mapping by incorporating techniques adapted from analogous 3D momentum imaging studies. This includes the use of alternative frames of reference, along with different methods of representing the data, which, combined with multi-particle correlation mapping, provide insight into the dynamics of fragmentation. Overall, this analysis methodology offers a deeper understanding of the Coulomb explosion process, producing results that are comparable with leading 3D momentum imaging experiments.

6.2 Methods

6.2.1 Experimental

Experiments were conducted using the Oxford spectrometer, which was described in detail in Section 2.6.1. Isomerically pure samples (97% and 98% purity for *cis* and *trans*) were purchased from a commercial supplier (Sigma-Aldrich). Both samples are liquid at room temperature. A ∼10% gaseous mixture of each was prepared by diluting its room temperature vapour pressure in helium, up to a pressure of 3 bar. The supersonic molecular beam was crossed by the focused, fundamental output of the Ti:Sapphire laser system. NIR pulses were polarised parallel to the face of the detector. Data were recorded with a pulse energy of 35 μJ, corresponding to a peak intensity of $4 \times 10^{14}\,\mathrm{W\,cm^{-2}}$. For each target molecule, data were acquired over ~100,000 experimental cycles. The repetition rate was limited by the PImMS2 camera, which operates at 10 Hz with all four memory registers enabled.

In previous studies using a PImMS2 camera, 3D ion imaging with modest momentum resolution along the ToF axis has been achieved by employing ion optics designed to temporally stretch the ion Newton spheres.[67,105,107] However, in the current experiments high ion optics voltages were required to focus fast moving fragments onto the detector, *e.g.* $\mathrm{Cl^{2+}}$. The spectrometer was operated with voltages of 6.77 and 9.00 kV applied to the extractor and repeller electrodes, respectively, and the other two electrodes held at ground. This effectively 'crushed' the ion Newton spheres onto the detector, making it impossible to reconstruct the out-of-plane ion momenta with the 25 ns time-stamping precision of the PImMS2 camera.

6.2.2 Analytical

Projected-momentum covariance mapping

Because the experimental detection system lacked sufficient time-stamping precision to reconstruct the out-of-plane component of an ion's momentum, the experiments employed 2D projected-momentum imaging. As such, the fragment ion recoil correlations must be calculated using 2D projected-momentum covariance mapping. When calculating the correlation map between fragments that together constitute the original molecule, considering the 2D projected fragment momenta allows only those combinations of ions that approximately fulfil momentum conservation in the plane of the detector to be selected. This can greatly reduce the noise in a calculated covariance map. Filtering based upon 2D projected-momentum sum does not guarantee that out-of-plane momentum conservation is fulfilled, so it is not able to remove all possible falsely correlated combinations of ions. As a result, it is not appropriate to construct a coincidence map from the filtered set of ion combinations. It is still necessary to applying covariance analysis in order to suppress any remaining false correlation events.

In order to isolate signal from the three-body breakup of triply charged 1,2-DCE into ${C_2H_2}^+ + 2Cl^+$ (considered in Section 6.3.2) using three-fold covariance analysis, a constraint on the projected-momentum sum of the fragment ions was essential. A limit of ± 5 a.u. was chosen based on the width of the fragment momentum sum distribution for the two-body breakup into $Cl^+ + C_2H_2Cl^+$, as determined via two-fold covariance analysis. In the dataset for each isomer, the number of combinations of ${C_2H_2}^+ + 2Cl^+$ with a projected-momentum sum within ± 5 a.u. is a very small fraction of the total number (∼0.01%). Using the fragment momentum sum as a filter therefore reduced the number of combinations that needed to be considered from several billion to several million over the ∼100,000 total accumulated laser shots for each target molecule.

Contingent covariance analysis

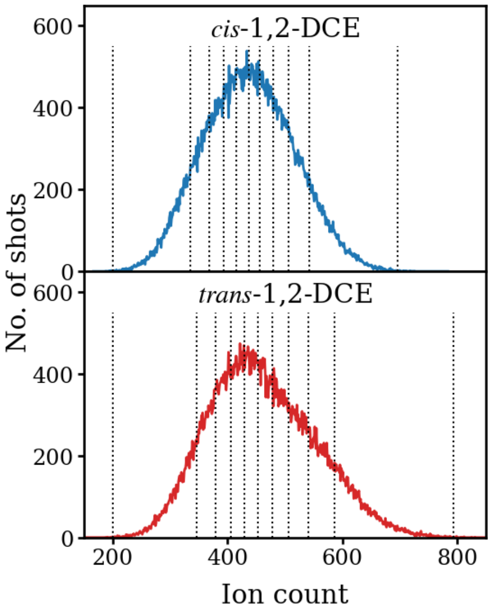

Figure 6.1: Ion count per laser shot distribution for (*top*) *cis*- and (*bottom*) *trans*-1,2-DCE. Vertical dotted lines indicate the boundaries of the bins used for contingent covariance calculations.

A contingent covariance analysis[155] was implemented to prevent false correlations induced by fluctuating experimental conditions from contributing to the calculated covariance maps. The parameter most prone to fluctuations was the target molecule density in the interaction region, due to inconsistent pulsing of the solenoid valve. Raw data were grouped into 10 subsets based on total ion count per laser shot, with each subset containing an equal number of laser shots. Aside from noise, no qualitative differences were observed between the covariance maps calculated across the 10 subsets. The total ion count per laser shot distribution for each molecule is presented in Figure 6.1.

6.3 Results and discussion

6.3.1 Time-of-flight spectra

The ion ToF mass spectra of strong-field ionised *cis*- and *trans*-1,2-DCE recorded by the PImMS2 camera are overlaid in Figure 6.2. The recorded yield of parent ions is very low because under velocity-mapping conditions ions with near-zero transverse momentum are focused to a point on the detector, producing overlapping flashes that saturate the detector. It also possible that the detection efficiency of this central point on the detector is somewhat diminished, but this does not meaningfully affect high KE species of key interest.

The parent ion peak is broad both because there are four different unresolved isotopic masses, due to the various combinations of the two Cl isotopes, and because of the way in which the PImMS2 camera behaves when saturated, which leads to some hits bleeding into later time bins. Contributions from clusters can be ruled out based on the fact that no additional peaks are discernible in the ToF spectra beyond the range shown. In addition, no high KE parent ions are observed in the velocity-map images of the parent ions. If parent dimer was present, for example, Coulomb explosion of the dimer dication would be expected to give rise to a pair of relatively high KE parent ions.

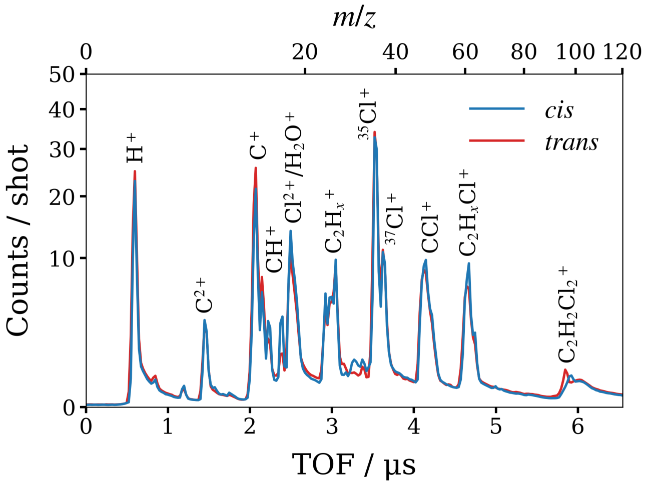

Figure 6.2: Ion ToF spectra of *cis*- and *trans*-1,2-DCE exposed to a NIR laser pulse with a peak intensity of 4 × 10^{14} W cm^{-2}. Unlabelled peaks are background gases. Datasets were acquired under comparable experimental conditions and are not otherwise normalised.

Aside from a slightly higher yield of heavier molecular fragments (and background ions) in the *cis* spectrum, the spectra are similar, implying that the fragmentation pathways are largely isomer-independent. The host of observed ion species represent the full array of molecular fragments conceivable for the breakup of these species. This is indicative of the broad range of parent ion charge states that are generated, and the assortment of different pathways via which they dissociate.

6.3.2 Three-body breakup

The three-body breakup of triply charged 1,2-DCE into $C_2H_2^+$ + $2Cl^+$ is the simplest, lowest total-charge Coulomb explosion channel that is expected to produce isomer-dependent signals. As such, it provides an interesting contrast to ‘complete’ Coulomb explosion that yields exclusively atomic ions, which is examined in the next section. The correlated fragment momenta for this fragmentation channel, determined via three-fold contingent covariance analysis, are plotted in the top panels of Figure 6.3. A constraint on the projected fragment momentum sum of ± 5 a.u. greatly reduced the noise in the covariance maps and was essential to isolate the signal from this fragmentation channel.

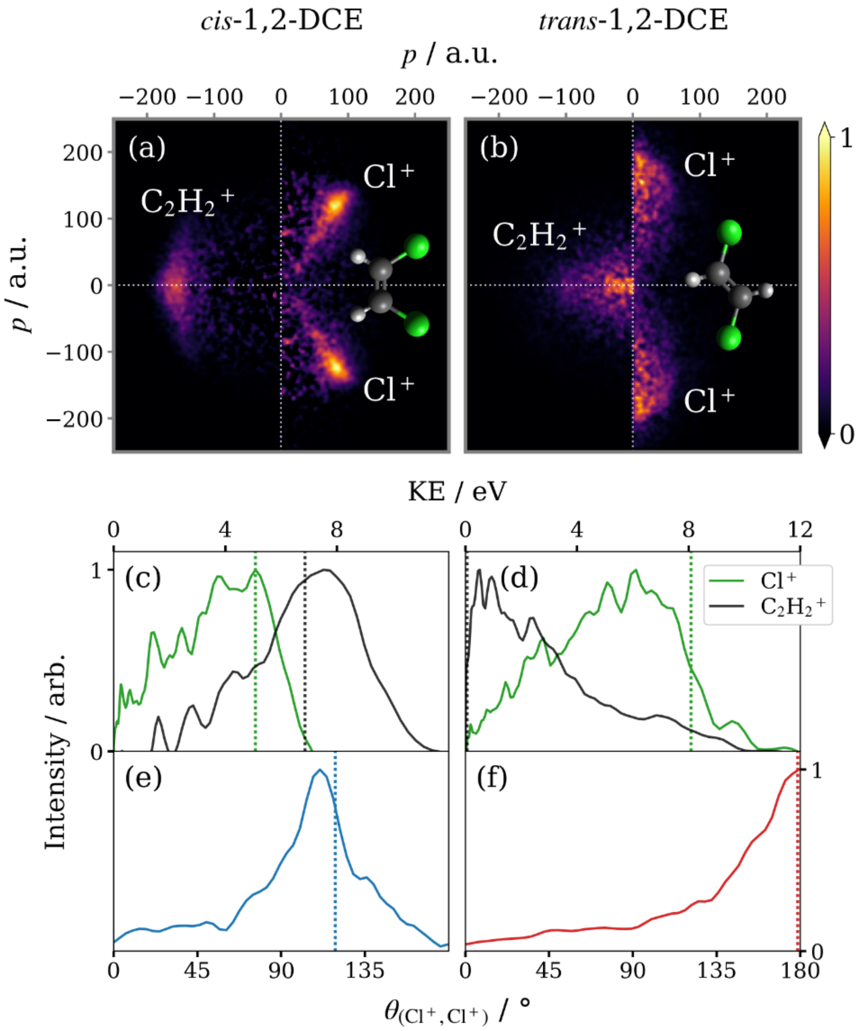

Figure 6.3: 2D projected-momentum three-fold covariance maps for the three-body breakup of (a) *cis*- and (b) *trans*-1,2-DCE^{3+} into $C_2H_2{}^+ + 2Cl^+$. Each panel is normalised separately. Below are overlaid (c, d) the fragment KE and (e, f) (Cl^+, Cl^+) relative recoil angle distributions. Vertical dotted lines indicate the results of a classical simulation of the Coulomb explosion of each molecule in its ground state equilibrium geometry.

The frame of reference in Figure 6.3 is defined by using the the relative momentum of the two Cl^+ ions ($\vec{p}_{Cl^+,1} - \vec{p}_{Cl^+,2}$) to determine the vertical axis. The result is that the horizontal axis bisects the Cl^+ momenta. This demonstrates the use of covariance analysis in a 2D ion imaging study to present fragment ion correlations in an alternative frame of reference to the conventional ‘recoil-frame’. In this instance, the advantage of a different frame of reference is that it allows the relative momenta of all fragment ions to be plotted together, providing an intuitive depiction of the Coulomb explosion process.

It should be noted that in the case of *trans*-1-2-DCE, if $\vec{p}_{\mathrm{Cl}^+,1}$ and $\vec{p}_{\mathrm{Cl}^+,2}$ are directly opposite, their difference (taken as the y-axis) lies parallel to $\vec{p}_{\mathrm{Cl}^+,1}$. The xy-plane will therefore not be uniquely defined as the $\mathrm{C_2H_2}^+$ fragment will have zero momentum perpendicular to y. However, in general $\vec{p}_{\mathrm{Cl}^+,1}$ and $\vec{p}_{\mathrm{Cl}^+,2}$ will not be exactly opposite, and the $\mathrm{C_2H_2}^+$ momentum will be non-zero in the xy plane. In this case the direction of the $\mathrm{C_2H_2}^+$ momentum is used to define the xy-plane.

The covariance maps in panels (a) and (b) of Figure 6.3 closely resemble the nuclear structures of the isomers under study. Because the Cl atoms are adjacent to one another in the *cis* isomer, both Cl^+ recoil in the opposite direction to $\mathrm{C_2H_2}^+$ when the parent trication dissociates. The relative recoil angle distribution for the Cl^+ pair is displayed in panel (e) and peaks at 111°. In the *trans* form, the Cl atoms are located on opposite sides of the C=C double bond, which causes the Cl^+ pair to recoil approximately back-to-back, whilst $\mathrm{C_2H_2}^+$ is caged between them. The mutual repulsion on this species on average cancels out, producing low momentum $\mathrm{C_2H_2}^+$. Comparing this fragmentation channel for this pair of isomers is essentially comparing the repulsion of three charges arranged in a triangle (*cis*), versus a line (*trans*). From the fragment KE distributions shown in panels (c) and (d) it is clear that the linear arrangement accelerates Cl^+ to higher velocity.

Drawn on the fragment KE and relative recoil angle distributions in Figure 6.3 are the results of a classical simulation of the Coulomb explosion of each isomer in its ground state equilibrium geometry. A full description of the model is provided in Chapter 4. The calculated values are generally in good agreement with experiment. Notably, the predicted (Cl^+, Cl^+) relative recoil angles are very close to the peaks in the experimental distributions.

Figure 6.4 shows correlation maps for the three-body concerted dissociation of triply charged 1,2-DCE into $\mathrm{C_2H_2}^+ + 2\mathrm{Cl}^+$ produced from simulated 2D projected fragment momenta. Data were simulated with an ensemble of geometries intended to approximate ground-state vibrational motion. The structure of the $\mathrm{C_2H_2}^+$ moiety is fixed in the same configuration as the equilibrium ground state geometry of the molecule, whilst the positions of the Cl atoms are sampled from a distribution that incorporates relevant vibrational modes. These include C–Cl symmetric/antisymmetric stretching, Cl–C–C–Cl in-plane scissoring/C–C–Cl bending and Cl–C–C–Cl out-of-plane twisting.

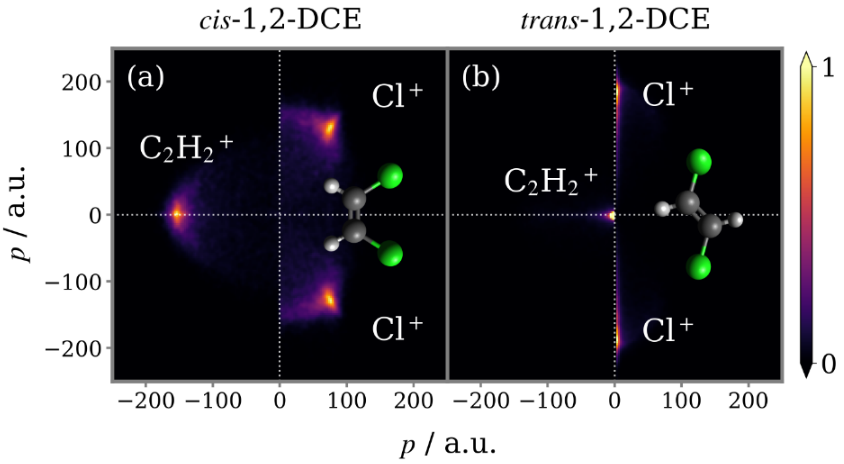

Figure 6.4: Simulated 2D projected-momentum correlation maps for the three-body concerted dissociation of (a) *cis*- and (b) *trans*-1,2-DCE^{3+} into 2Cl$^+$ + $C_2H_2{}^+$. Each panel is normalised separately.

Comparing the covariance map for *cis*-1,2-DCE in Figure 6.3(a) and the simulated correlation map for the same fragmentation channel in Figure 6.4(a), there are distinct differences. The experimental Cl$^+$ momentum distribution possesses a tail, not seen in the simulated data, which trails from the point of maximum intensity down towards the origin, whilst the momentum distribution of $C_2H_2{}^+$ is considerably broader along the vertical axis. The simulated correlation map for the Coulomb explosion of *trans*-1,2-DCE^{3+}, shown in Figure 6.4(b), does not fully reproduce the form of the covariance map in Figure 6.3(b), either. It predicts a distribution that is tightly confined along the vertical axis, *i.e.* the simulated Cl$^+$ ions do not deviate significantly from back-to-back recoil, whereas in the experimental data each fragment has a significant horizontal momentum component.

Such discrepancies are indicative of more complex fragmentation dynamics. The simulation models the dissociation as a strictly concerted process, *i.e.* both C–Cl bonds are broken simultaneously, but that is not the case for this fragmentation channel. To elucidate the Coulomb explosion dynamics more closely, the data needs to be transformed into a different frame of reference.

One popular method for investigating the dynamics of a three-body Coulomb explosion process is to present the data as a Dalitz plot,[207] which depicts the energy sharing amongst the fragments. This method has previously been adapted for the analysis of 2D projected-momentum data.[208–210] Here, a different method is adopted. In the top panels of Figure 6.5, the correlated fragment momenta of Cl^+ + $C_2H_2^+$ + Cl^+ have been re-plotted as Newton diagrams, wherein the momentum of one of the Cl^+ ions is constrained to the positive x-axis, and the relative momenta of the other two fragments are plotted on the top and bottom halves of the diagram.

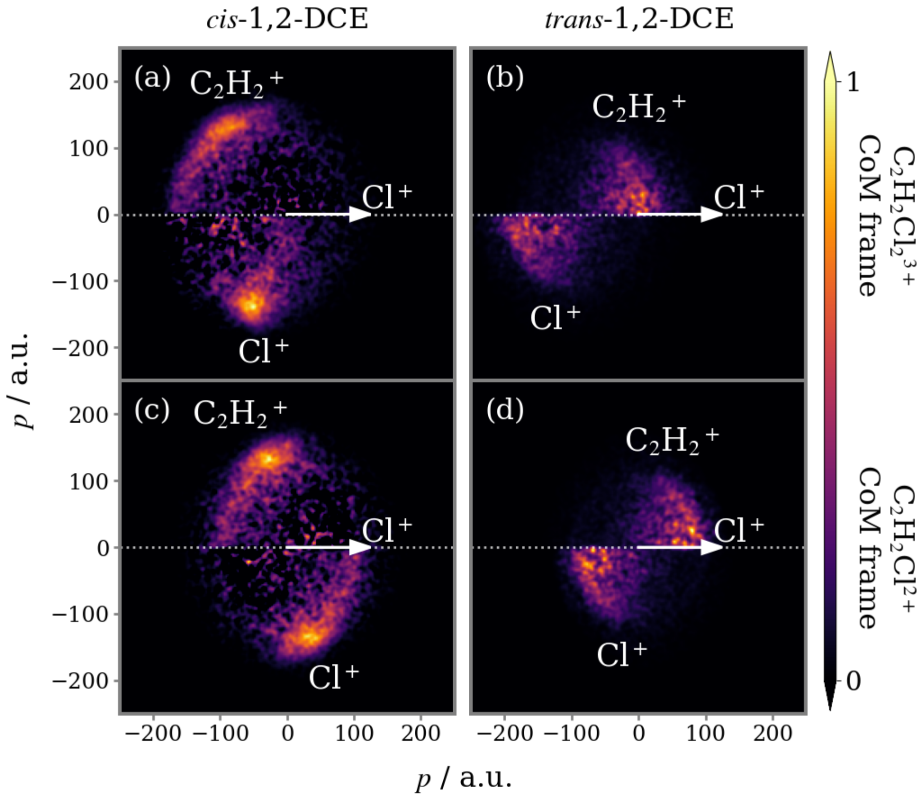

Figure 6.5: 2D projected-momentum Newton diagram three-fold covariance maps for the three-body breakup of (*left column*) *cis*- and (*right column*) *trans*-1,2-DCE^{3+} into $C_2H_2^+$ + $2Cl^+$. Panels (a) and (b) display the fragment momenta in the CoM frame of the parent trication. Below, in panels (c) and (d), fragment momenta have been transformed into the CoM frame of the $C_2H_2Cl^{2+}$ intermediate. Each panel is normalised separately.

This new representation is the same as that used in previous studies that investigated this fragmentation channel.[163,205] The 2D projected momentum, three-fold covariance maps show good resemblance to the 3D momentum, triple coincidence maps in these prior publications. The Cl^+ and $C_2H_2{}^+$ momenta for both isomers now appear as short arcs, curving in opposite directions. This is characteristic of a sequential three-body breakup mechanism:[74,75]

$$\begin{aligned} C_2H_2Cl_2{}^{3+} &\rightarrow Cl^+ + C_2H_2Cl^{2+} \\ C_2H_2Cl^{2+} &\rightarrow C_2H_2{}^+ + Cl^+, \end{aligned} \tag{6.1}$$

and arises when the initial dissociation induces rotation of the intermediate dication before it further fragments, causing the momenta of the secondary products to be distributed over an angular span relative to the momentum of the primary product.

Assuming rotation of the $C_2H_2Cl^{2+}$ intermediate occurs in the plane of the parent molecule, the intensity in the angular distribution of the secondary products will decay exponentially from the angle for concerted breakup. The decay constant is determined by the ratio of the lifetime of the intermediate (τ) and its rotational period (T_R).[175] Maul and Gericke proposed use of the term 'sequential' to describe the limiting case where the delay between the two bond-breaking events exceeds the average rotational period of the intermediate ($\tau/T_R > 1$),[173] resulting in a uniform angular distribution. Because the experimental angular distributions in the present work exhibit a decay component, this fragmentation channel represents an intermediate case, *i.e.* $0 < \tau/T_R < 1$, which is referred to here as 'asynchronous'.

The final step is to apply the covariant native frames analysis approach to transform into the CoM frame of the $C_2H_2Cl^{2+}$ intermediate, shown in the lower panels of Figure 6.5. The transformation is performed by subtracting the momentum that the reference Cl^+ imparts to the plotted species. The momenta of Cl^+ and $C_2H_2{}^+$, which together constitute $C_2H_2Cl^{2+}$, are equal and opposite in this frame. This distinctly enhances the twin arcs in each covariance map, and provides an intuitive picture of the fragmentation dynamics. The initial dissociation step in the asynchronous breakup of the *cis*-1,2-DCE^{3+} induces counter-clockwise rotation of $C_2H_2Cl^{2+}$ in this frame, which pivots the Cl in the intermediate towards the recoiling Cl^+ ion prior to secondary dissociation, thereby reducing the recoil angle between the Cl^+ pair. The covariance maps in panels (c) and (d) of Figure 6.5 are re-plotted in Figures 6.6(a) and (b), respectively, as a function of KER in this frame versus the (Cl^+, Cl^+) relative recoil angle. The dynamics of the *cis* isomer breakup produces a distribution that decays from ∼80° (the angle for concerted breakup) towards 0°. A similar mechanism for *trans* acts to turn around the $C_2H_2Cl^{2+}$ intermediate, giving a distribution that decays from 180° towards smaller angle.

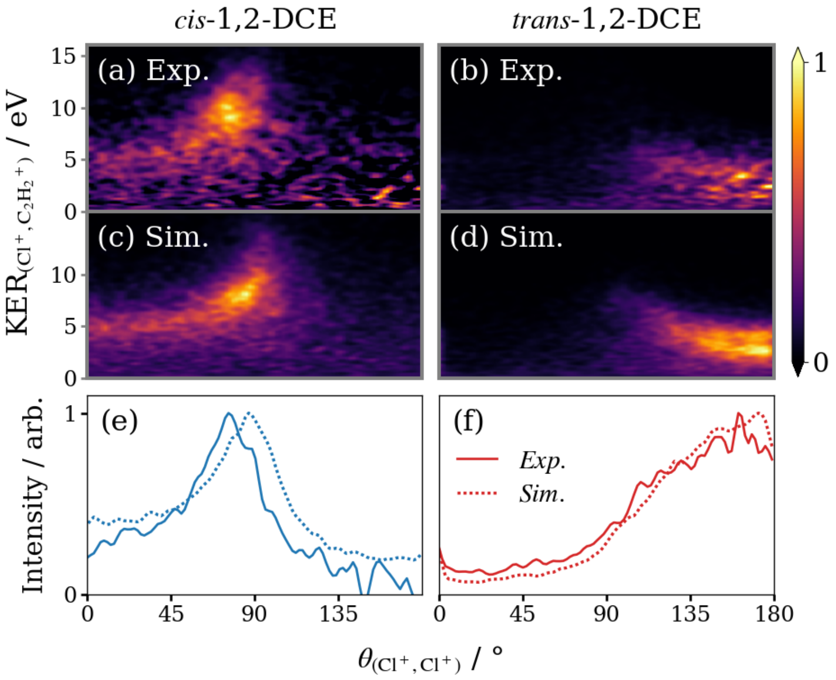

Figure 6.6: (a, b) The covariance maps from Figure 6.5(c) and (d) displayed in polar coordinates, where $\mathrm{KER}_{(Cl^+,C_2H_2^+)}$ is the KER in the CoM frame of the $C_2H_2Cl^{2+}$ intermediate and $\theta_{(Cl^+,Cl^+)}$ is the relative recoil angle between the Cl^+ pair. (c, d) Simulated correlation maps for the asynchronous breakup of 1,2-DCE^{3+} into $C_2H_2{}^+$ + $2Cl^+$. Each panel is normalised separately. Below the (*solid*) experimental and (*dotted*) simulated (Cl^+, Cl^+) relative recoil angle distributions are overlaid.

Simulations of asynchronous fragmentation dynamics

To verify the assigned fragmentation mechanism for this channel, a second series of classical simulations of the three-body breakup of 1,2-DCE^{3+} were conducted using a model appropriate for recreating asynchronous breakup dynamics. The model is broadly similar to the sequential three-body fragmentation model that incorporates a variable intermediate lifetime, described in Section 4.4.1. Briefly, the simulation is executed as two separate Coulomb explosion events that model the primary and secondary fragmentation steps outlined in Equation 6.1. The first step is propagated for the duration of the intermediate lifetime (t), which is determined by randomly sampling on an exponential decay function with a characteristic lifetime τ. $C_2H_2Cl^{2+}$ is then replaced by ${C_2H_2}^+$ + Cl^+, rotated through an angle:

$$\theta = 2\pi \times t/T_{\mathrm{R}}. \tag{6.2}$$

The separation of $C_2H_2^+$ and Cl^+ (r) is scaled to emulate extension of the C–Cl bond, modelled by an inverted exponential decay function:

$$r = r_{\mathrm{f}} - (r_{\mathrm{f}} - 1)\mathrm{e}^{-t/t_{\mathrm{ex}}}. \tag{6.3}$$

The asymptotic separation (r_f) is determined by combining Coulomb's law and the mean KER of the tail of the distribution in Figure 6.6(a) or (b). The input parameters τ, t_{ex} and T_{R} are empirically chosen to reproduce the experimental results. For this reason, the simulations provide only a qualitative insight into the nuclear dynamics of the intermediate dication.

Data simulated for the *cis* and *trans* isomers (using identical values of $\tau = 100\,\mathrm{fs}$, $t_{\mathrm{ex}} = 100\,\mathrm{fs}$, and $T_{\mathrm{R}} = 1\,\mathrm{ps}$) are plotted in panels (c) and (d) of Figure 6.6, respectively. The simulation successfully reproduces the arcing features in the experimental covariance maps, supporting the interpretation of the rotational dynamics of the intermediate. The downward curvature towards smaller angles for the *cis* isomer is caused by the stretch of C–Cl bond in the intermediate as a function of time, and hence rotation of the intermediate. The upward curvature towards smaller angles for the *trans* isomer is produced by a combination of bond extension and rotation of the intermediate, both of which limit caging of the ${C_2H_2}^+$ between the Cl^+ pair, resulting in increased KER. The simulated angular distributions were found to be very sensitive to the ratio τ/T_{R}. To achieve the resemblance to the experiment results seen in panels (e) and (f), it was necessary to tune this ratio to a small fraction, corroborating the statement that the dissociation is asynchronous.

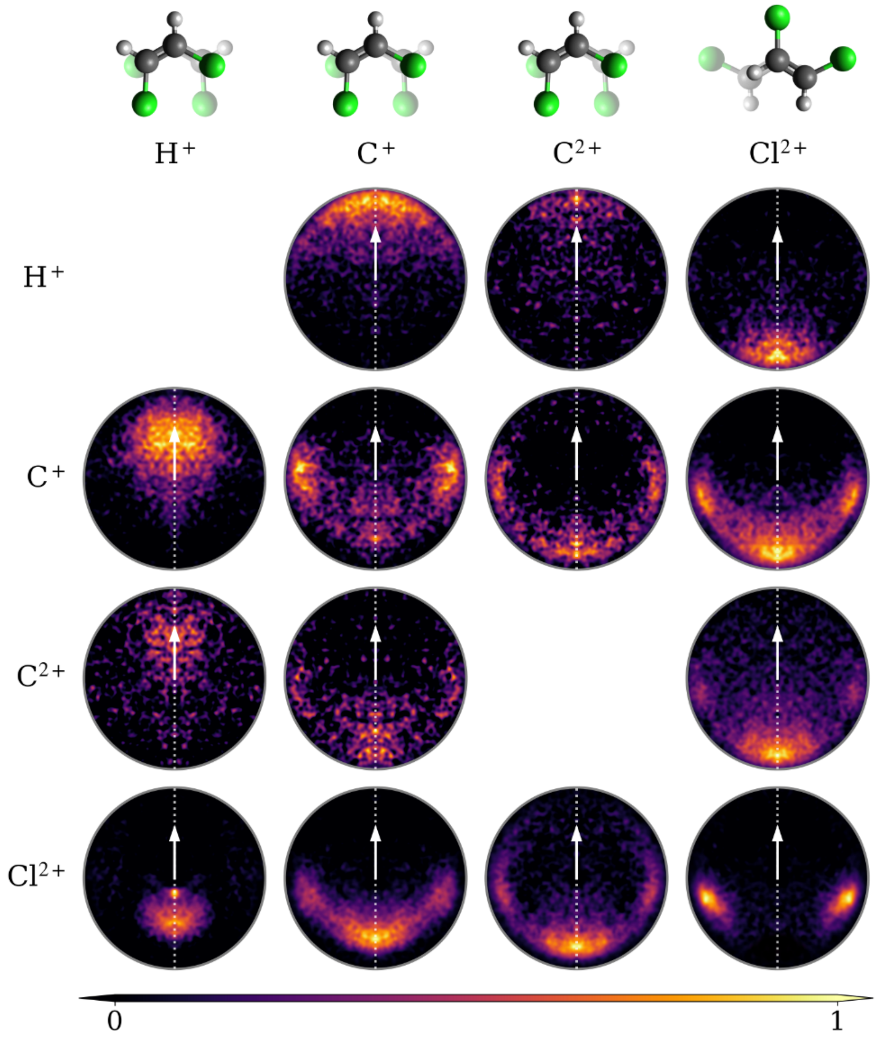

Figure 6.7: Recoil-frame two-fold covariance maps for the Coulomb explosion of *cis*-1,2-DCE. The reference and partner ion for each plot are labelled along the horizontal and vertical axes, respectively. The reference ion is constrained to the positive y-axis, as indicated by the arrow, and the positional distribution of the partner ion on the detector is plotted relative to this direction. Covariance maps with no statistically significant signal have been omitted.

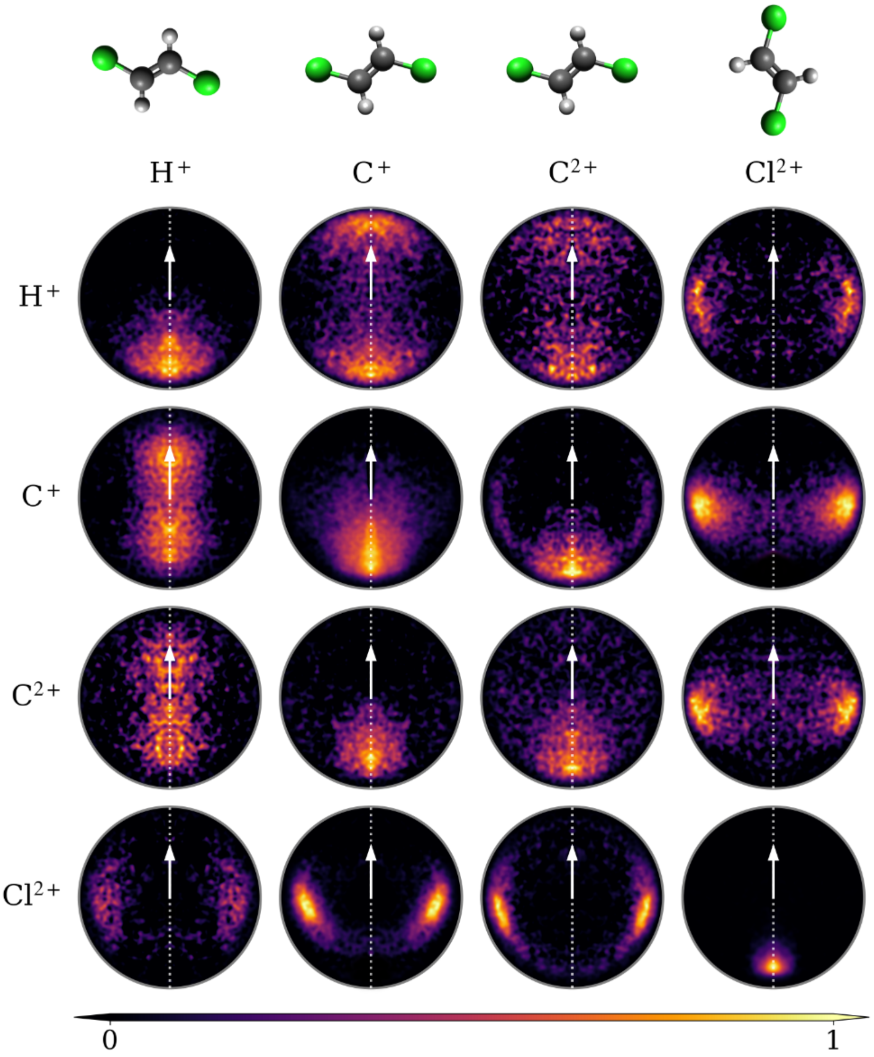

Figure 6.8: Recoil-frame two-fold covariance maps for the Coulomb explosion of *trans*-1,2-DCE. The reference and partner ion for each plot are labelled along the horizontal and vertical axes, respectively. The reference ion is constrained to the positive y-axis, as indicated by the arrow, and the positional distribution of the partner ion on the detector is plotted relative to this direction.

6.3.3 Atomised breakup

Fully mapping the correlated fragment momenta from a ‘complete’ Coulomb explosion of 1,2-DCE into atomic ions would require the determination of a six-fold correlation, which is beyond the capabilities of the current experiments. Neither is it feasible to examine such dissociation pathways using three-fold covariance analysis as the three-body breakup analysis, discussed in the previous section, relied upon using the momentum sum of the fragments to reduce the noise to a reasonable level. Consequently, one must rely on two-fold covariance analysis and study the correlation between individual pairs of fragment ions. This section focuses on the correlated momenta of the chlorine dications.

Through individual two-fold covariance analyses, it can be confirmed that Cl^{2+} is not produced in correlation with any molecular ion fragments. Strong covariance signal is observed between Cl^{2+} and other atomic ions, including H^+, C^+, C^{2+}, Cl^+ and Cl^{2+}, recoil-frame covariance maps for which are presented in Figures 6.7 and 6.8, for the *cis* and *trans* isomers, respectively. It is also possible that Cl^{2+} is produced in correlation with neutral atomic fragments, but it is considered very unlikely that Cl^{2+} is produced in coincidence with any molecular fragments. Hence, the production of Cl^{2+} can confidently be assigned to the dissociation of highly charged parent ions that completely destroys the chemical bonding.

The correlated momenta for a pair of chlorine dications, determined via two-fold contingent covariance, are plotted in the top panels of Figure 6.9. Analogous to Figure 6.3, the vertical axis is defined by the relative momentum of the two Cl^{2+} ions ($\vec{p}_{\mathrm{Cl}^{2+},1} - \vec{p}_{\mathrm{Cl}^{2+},2}$), such that the horizontal axis bisects the Cl^{2+} momenta. Once again, the relative recoil of the Cl^{2+} pair closely resembles the atomic positions of Cl in each isomer. Plotted in the left half of each covariance map is the residual momentum in this frame ($\vec{p}_3 = -(\vec{p}_{\mathrm{Cl}^{2+},1} + \vec{p}_{\mathrm{Cl}^{2+},2})$), which must equal the sum of the momenta of the other fragments (2C + 2H with undetermined charge).

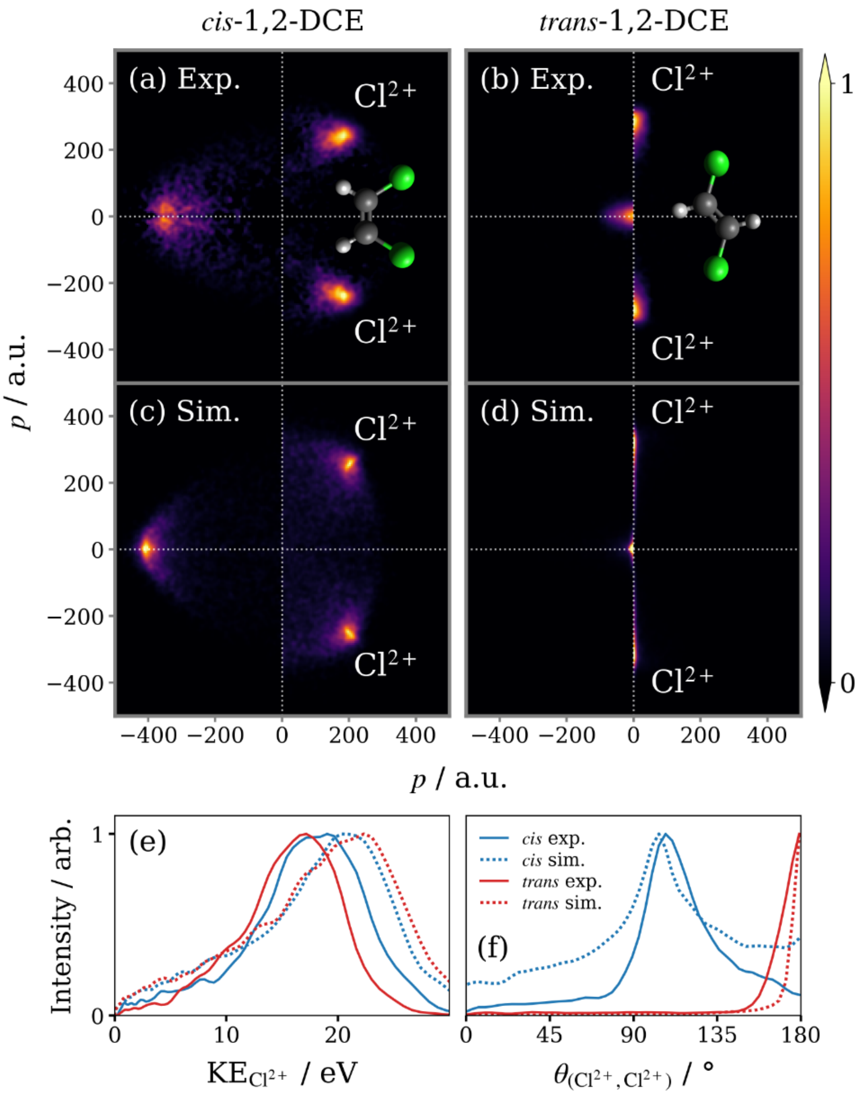

Figure 6.9: 2D projected-momentum two-fold covariance maps for the Coulomb explosion of (a) *cis*- and (b) *trans*-1,2-DCE that yields a pair of Cl^{2+} ions. The unlabelled feature in each covariance map corresponds to the sum of the momenta of all other fragments. Below (c, d) are the results of simulation of the Coulomb explosion of 1,2-DCE^{8+} into $2C^{+} + 2H^{+} + 2Cl^{2+}$. Each panel is normalised separately. In the bottom panels (e) the Cl^{2+} kinetic energy and (f) (Cl^{2+}, Cl^{2+}) relative recoil angle distributions are overlaid.

The residual momentum contains indirect structural information that can be obscured in a different representation, such as the recoil frame. For example, the momentum sum of the missing fragments from the Coulomb explosion of *trans*-1,2-DCE in Figure 6.9(b) is tightly distributed around the origin. This does not necessarily indicate that the fragments have near-zero momentum, but rather that the pair of C fragments must recoil back-to-back, as must the H fragments, and hence that the molecule is symmetric about the line connecting the Cl atoms. This is confirmed by two-fold covariance analysis between H^+ + H^+, and $C^{+/2+}$ + $C^{+/2+}$, also shown in Figure 6.8.

Panels (c) and (d) of Figure 6.9 show correlated fragment momentum maps for the many-body breakup of *cis*- and *trans*-1,2-DCE^{8+} into $2C^+ + 2H^+ + 2Cl^{2+}$, simulated using the concerted Coulomb explosion model. This was the same fragmentation channel predicted for $Z = 8$ by the theoretical study of Zhou *et al.*,[183] and was also the onset of the high Z regime in their study, where complete fragmentation into atomic ions was observed within 50 fs. The left hand side of the simulated plots display the sum of the momenta of $2C^+ + 2H^+$, rather than simply minus the momentum sum of the Cl^{2+} pair. The similarity between these simulated correlation maps and the experimental covariance maps in the panels directly above, supports the claim that the two-fold covariance analysis isolates signal from the complete dissociation of highly charged parent ions into many atomic ions, even though it only specifies the identities of two fragments.

Discrepancies between the experimental and simulated correlation maps can be attributed to the fact that, whilst the simulation emulates a single fragmentation channel, the experimental covariance maps likely contain contributions from several. For example, the intense features in the (a) and (b) are notably more diffuse than simulation predicts. Whilst the charge state of the Cl pair is specified, any combination of C or H with non-matching charge states, *i.e.* $C + C^+$, $C^+ + C^{2+}$, or $H + H^+$, will break the symmetry of the charge distribution. Indeed, the work of Zhou *et al.* predicts that the extra charge in the $Z = 9/10$ channels is accommodated by the C fragments. Contributions from such channels will broaden the relative recoil distribution of the Cl^{2+} pair.

A quantitative comparison between between the experimental and simulated Cl^{2+} KE distributions is not attempted, as a model of point charges initiated from the equilibrium geometry of the molecule routinely overestimates the KE of fragments.[19,21,23] The contribution of fragmentation pathways yielding neutral cofragments is one factor that could explain why the Cl^{2+} KE distributions are shifted down in energy relative to the simulated results, but this could also be the result of the slight extension of bonds on average during the ionisation process.[18,23] It is worth noting that the simulations qualitatively reproduce the similarity between the Cl^{2+} KE distributions for this pair of isomers.

6.4 Comparison of breakup channels

Comparing the correlated momenta of the Cl^{+} pair from three-body breakup of 1,2-DCE^{3+}, seen in Figure 6.3(a, b), and the correlated momenta of the Cl^{2+} pair from atomised breakup of highly charged 1,2-DCE in Figure 6.9(a, b), the features in the latter set of covariance maps are distinctly sharper, with no evidence of additional structure. This indicates that the Coulomb explosion of a highly charged parent ion yielding a Cl^{2+} pair is a concerted, rather than an asynchronous process. Despite this difference in the nature of the fragmentation process, the average relative recoil angle of the Cl ion pair is similar for these two pathways (see Figure 6.3(e, f) vs. Figure 6.9(f)). For the *trans* isomer both angular distributions peak at 180°. In the case of *cis*, maximum intensity occurs at 111° for the Cl^{+} pair and 107° for the Cl^{2+} pair.

The breakup of 1,2-DCE^{3+} occurring via an asynchronous mechanism is to be expected given the relatively low charge state, Z. Similar dynamics have been observed for other small molecular trications.[174,175] It is uncertain whether the theoretical method of Zhou *et al.* predicts three body breakup as the outcome for the triply ionised *cis*-1,2,-DCE as the simulation terminated at 50 fs, at which point only the C–C bond had broken. This certainly is not consistent with the formation of ${C_2H_2}^{+}$, as observed experimentally. However, their work did predict C–Cl bonds being broken in a stepwise rather than a concerted manner for other low Z states.

As already noted, Zhou *et al.* observed the onset of the high Z regime, where the theoretical method predicts direct and exclusive formation of atomic fragments, at $Z = 8$. For lower Z the method predicts that polycationic molecular fragments, *e.g.* $CCCl^{3+}$, remain intact when their simulations finished at 50 fs. No such fragments were observed in the current work. The study calculated the products for the dissociation of parent ions in their respective ground states, but it is likely that parent ions are prepared in a range of excited electronic states by the strong-field ionization process, which will exhibit varied dissociation dynamics.

For the purpose of using CEI to probe molecular structure on an ultrafast timescale, a distinction can be made between those channels in which the mapping between initial atomic positions in the parent molecule and final fragment momenta is straightforward, and those that exhibit more complex mapping, which although often interesting in their own right, are not suitable for structural determination. The three body breakup of 1,2-DCE^{3+} represents an intermediate case. Although the bond breaking events can occur asynchronously, the dynamics of the intermediate during its short lifetime is not dramatic enough to completely obscure the structural information encoded in the fragment momenta. These dynamics lead to additional structure in the fragment momentum correlation map, which complicate interpretation, but the *cis* and *trans* isomers can still clearly be distinguished.

The relationship between initial molecular geometry and final fragment momenta is much more straightforward for the Coulomb explosion of more highly charged 1,2-DCE ions, particularly those producing pairs a Cl^{2+} ions. Such channels can be understood using a model of point charges interacting under Coulomb's law, without additional modification. For a TR-CEI study on this pair of isomers, Coulomb explosion into atomic fragments is the preferred choice to ensure that the Coulomb explosion dynamics do not complicate the interpretation of the dynamics induced by the pump pulse.

6.5 Conclusions and future work

2D projected-momentum covariance mapping has been introduced and demonstrated on 2D ion imaging data of the Coulomb explosion of the *cis* and *trans* isomers of 1,2-DCE. Working in terms of the 2D projected momenta of fragment ions greatly expands the array of available analysis tools. This study has included the application of a fragment momentum sum constraint in a three-fold covariance calculation to isolate a three-body breakup channel, and the use of various frames of reference, which together allowed the fragmentation dynamics in this channel to be fully unraveled. Though commonplace in 3D momentum imaging studies, such techniques are underutilised in analogous 2D studies and have been adapted here to achieve comparable results from a more limited 2D dataset. These results exceed the level of detail typical of 2D ion imaging studies of molecular Coulomb explosion.

Two fragmentation pathways of 1,2-DCE polycations have been examined in detailed. The three-body breakup of triply charged parent ions into $C_2H_2^+$ + $2Cl^+$ was identified as an asynchronous process. This was confirmed by a classical, point charge simulation of the dynamics. The many-body breakup of a highly charged parent ion that yields a Cl^{2+} ion pair, amongst other atomic ions, is a strictly concerted process. Both fragmentation pathways produce distinct signals for the *cis* and *trans* forms of the target molecule, allowing this pair of isomers to be unambiguously distinguished in a CEI experiment. Because it is a concerted process, the relationship between the initial atomic positions in the parent molecule and the relative momenta of the nascent fragments is more straightforward for the Coulomb explosion into atomic fragments. It was therefore identified as the preferred choice of probe for the TR-CEI study which was to follow (reported in the next chapter).

Future work should aim to explore the Z-dependent Coulomb explosion dynamics of these species more thoroughly. The ultimate goal would be to characterise the fragmentation behaviour for the full range of charge states populated by the laser pulse in order to parallel the theoretical results of Zhou *et al.*, which predicted the fragmentation dynamics of *cis*-1,2-DCE for all parent ion charge states between 3–24 (though such high Z is unlikely in an SFI experiment). This can be achieved using a higher-fold correlation mapping technique, such as cumulant mapping, to isolate the complete fragment momentum correlations for higher Z fragmentation channels that yield > 3 products. The results could be used to establish the transition between the asynchronous and concerted Coulomb explosion dynamics observed here.

7

Part I – Ultraviolet photoexcitation dynamics of 1,2-dichloroethene investigated by time-resolved Coulomb explosion imaging

Contents

The culmination of the work of this thesis is an investigation into the photoinduced molecular dynamics of a new system of study using TR-CEI. In this chapter, results are presented from the first in a pair of studies that investigated the ultrafast torsional and photodissociation dynamics of 1,2-DCE. The experimental work was conducted in the laboratory at the University of Oxford using the newly commissioned TR-CEI instrument. *trans*-1,2-DCE was excited at 202 nm, corresponding to a $\pi^* \leftarrow \pi$ transition. Photodissociation within 100 fs is assigned to rapid C–Cl bond cleavage by surface crossing to a repulsive state. Evidence is also observed for potential torsion of the excited molecule about the C–C bond axis, which could provide a pathway for *cis-trans* isomerisation via internal conversion to the ground electronic state.

Unfortunately, the experiments were hindered by a number of issues that impaired the quality of the data, meaning the interpretation of the nuclear dynamics is ambiguous. It was therefore necessary to perform a second round of experiments. These were carried out in a different laboratory and are the subject of the following chapter. In this regard, the experiments conducted in Oxford served largely as preliminary work. Nevertheless, a brief discussion of the results is informative, as it highlights problems with the instrument in its current state that are important to resolve for future studies.

7.1 Background

Photoinduced *cis-trans* isomerisation about a double bond is a straightforward means of converting light into mechanical motion on a molecular scale. Ethene is the simplest molecule in which this process can be studied. Thus, it has attracted considerable attention from both theoreticians[31,32,211,212] and experimentalists.[212–215] Ethene is planar in its ground electronic state, while the two CH_2 moieties are twisted at a dihedral angle of 90° in the first excited (π, π^*) state. $\pi^* \leftarrow \pi$ excitation therefore induces a rapid twisting motion about the C–C bond axis. Subsequent pyramidalisation of one of the CH_2 groups leads to a conical intersection between the excited and ground state PESs, providing a route for *cis-trans* isomerisation.

The photoisomerisation dynamics of ethene have been revealed by a number of time-resolved photoelectron spectroscopy studies. C–C bond torsion is reported to occur within 10 fs, and transfer to the ground electronic state, forming vibrationally hot product, in less than 45 fs.[215] Such experiments are able to infer changes in the nuclear structure based upon comparisons with the predictions of theory. The aim of the current work was to perform a complementary TR-CEI study to directly monitor the nuclear dynamics of *cis-trans* isomerisation. Unfortunately, ethene is not a good candidate for study by TR-CEI. The technique is sensitive to changes in nuclear structure, but the *cis* and *trans* forms of ethene are identical, so it would not be possible to determined whether the molecule has isomerised. Instead, a substituted derivative of ethene is desirable in order to provide 'anchors' that can be used to track the interconversion.

A halogenated form of ethene is the obvious alternative. CEI studies often rely on measuring the relative momenta of the ions of substituent halogen atoms to determine molecular structure,[19,24,47,51,160] including to distinguish between different isomers.[13,21–23,205] Previous studies have demonstrated how the *cis* and *trans* structures of 1,2-dibromoethene[21] and of 1,2-dichloroethene[205] can be distinguished using CEI. The previous chapter provided a thorough discussion for the latter of these species. For the prospect of conducting a TR study, it is highly advantageous to start with a single isomer and measure the process in one direction. Hence, the chlorinated species was preferred as the pure forms of both isomers can be purchased from a commercial supplier, whereas 1,2-dibromoethene is only available as a isomeric mixture.

Chloroethenes have strong absorption bands centered around 200 nm that are assigned to a $\pi^* \leftarrow \pi$ transition.[216] When 1,2-DCE is photoexcited to the (π, π^*) state the CHCl groups are expected to twist at 90°.[217,218] Analogous to ethene, if the perpendicular geometry lends itself to coupling between the excited and ground PESs, *cis-trans* isomerisation could occur on return to the ground electronic state. Evidence for this pathway has been found in the speed distribution of Cl atoms from UV photolysis of trans-1,2-DCE:

$$C_2H_2Cl_2 \xrightarrow{h\nu} C_2H_2Cl + Cl, \tag{7.1}$$

Several experiments have observed a low KE component, characterised by a Boltzmann distribution.[218–223] This is consistent with the dissociation of vibrationally hot molecules relaxed from the (π, π^*) state via internal conversion, suggested by Suzuki *et al.*[221]

Other authors have proposed different mechanisms for the formation of low KE chlorine. Umemoto *et al.* predicted internal conversion to the vibrational excited levels of a low lying bound state.[219] In addition to the slow Boltzmann-like component, the KE distribution also comprises a high energy component with a Gaussian distribution. Amongst all previous works, this is ascribed to rapid predissociation due to surface crossing between the bound (π, π^*) state and a nearby repulsive state.[218–223] Seki *et al.* pointed out that subsequent dissociation of C_2H_2Cl could be responsible for the production of low KE Cl:[224]

$$\begin{aligned} &C_2H_2Cl_2 \xrightarrow{h\nu} C_2H_2Cl^* + Cl, \\ &C_2H_2Cl^* \rightarrow C_2H_2 + Cl. \end{aligned} \tag{7.2}$$

C_2H_2 is a known product from the UV photodissociation of 1,2-DCE,[223–225] which supports this assignment. The alternative mechanism for the formation of C_2H_2 is the elimination of molecular chlorine:

$$C_2H_2Cl_2 \xrightarrow{h\nu} C_2H_2 + Cl_2. \tag{7.3}$$

However, this can be discounted as a minor process based on the failure of several studies to detect Cl_2.[219,223,226]

The other widely studied photodissocation channel of 1,2-DCE is the elimination of HCl:[216,219,223,227,228]

$$C_2H_2Cl_2 \xrightarrow{h\nu} C_2HCl + HCl. \tag{7.4}$$

This mechanism is considered to proceed via the electronic ground state, and therefore would compete with *cis-trans* isomerisation. It is assumed that memory of the original geometry is lost during elimination because of the atom migration processes.[223] Photodissociation by detachment of H:[220,227]

$$C_2H_2Cl_2 \xrightarrow{h\nu} C_2HCl_2 + H, \tag{7.5}$$

and elimination of molecular hydrogen:[226]

$$C_2H_2Cl_2 \xrightarrow{h\nu} C_2Cl_2 + H_2, \tag{7.6}$$

have also been reported. These processes are not discussed as part of the work presented here, but will be the subject of future analysis.

Because of the various dissociative processes identified for $\pi^* \leftarrow \pi$ excited 1,2-DCE, it has been suggested that *cis-trans* isomerisation is not a primary photochemically driven unimolecular rearrangement, but hinges upon secondary collisions.[216,217,219] Ewbank *et al.* studied *trans*-1,2-DCE excited at 193 nm by TR electron diffraction and observed formation of the *cis* isomer on a timescale of several milliseconds.[217] Based on their findings they propose that isomerisation is the result of an intermolecular chain mechanism, involving recombination of Cl atoms released in the primary photolysis.

Herein, results are presented from an investigation into the real-time molecular motion of $\pi^* \leftarrow \pi$ photoexcited *trans*-1,2-DCE by TR-CEI, with an intense NIR probe pulse. The analysis focuses on the correlated properties of pairs of fragment ions, determined by projected-momentum covariance mapping. The TR KE distribution of the $C_2H_2Cl^+$ + Cl^+ ion pair maps the cleavage of the C–Cl bond. The delay-dependent relative recoil angle distribution of the Cl^+ ion pair displays a shift towards reduced angle shortly after photoexcitation, consistent with rapid C–C twisting motion on the (π, π^*) excited state. Overall, the analysis highlights interesting areas for investigation, which are interrogated in detail by the follow up study described in the next Chapter.

7.2 Methods

7.2.1 Experimental

The experimental set-up is largely similar to that reported in the previous chapter, so only the differences in the operating parameters are outlined here. Data was collected exclusively for *trans*-1,2-DCE. The target molecule was irradiated by the 202 nm output of the OPA and 800 nm fundamental output of the Ti:Sapphire laser system, both of which were polarised parallel to the plane of the detector. The broad (π, π^*) absorption band of *trans*-1,2-DCE spans an approximate range of 160–230 nm and peaks close to 198 nm,[229] however, the pulse energy generated by OPA decays towards shorter wavelength. The UV wavelength was therefore chosen as a compromise between these two factors to maximise the signal due to target molecules successively excited by the pump and probe laser pulses. There was minimal risk of UV multi-photon excitation due to the low pulse energies generated by the OPA in this wavelength range.

Ion images were recorded for regular pump-probe delay steps of 33 fs across a range from -0.8 to 1.9 ps, where positive delay corresponds to the UV pulse arriving before the NIR pulse, and vice versa. The position of time zero was established based on the cross correlation peak in the yield of H_2O^+. The temporal resolution was determined to be 175 ± 5 fs based on the cross correlation width, following the procedure described in Section 2.8.2. At each pump-probe delay, data were acquired over ~5000 laser shots. The PImMS2 camera was operated with only two of four memory registers enabled to support a experimental repetition rate of 20 Hz.

The UV and NIR pulse energies were 9 and 220 μJ, respectively. Compared to the experiments reported in Chapter 6, the NIR focal spot size was distinctly larger, such that the peak intensity at the same pulse energy was estimated to be an order of magnitude lower. In addition, the maximum pulse energy was severely limited by an increased ionisation rate of background species – likely related to the larger focal volume. The value of the peak intensity is unknown as the intensity calibration was not repeated, but it is certain that it was lower than the previous experiments.

To operate with a higher NIR pulse energy whilst preventing saturation of the detector by background ion counts, the front face of the front MCP was pulsed on each cycle from ground to 450 V over the arrival window of H_2O^+ – the most numerous background species. This reduced the average counts of H_2O^+ by over 90%. The set-up is only capable of pulsing one per cycle to gate the detection of a single species. The yield of other background ions including ${N_2}^+$, ${O_2}^+$ and ${C_nH_x}^+$ (from oil contamination) were also high, which ultimately limited the maximum NIR pulse energy that could be employed.

7.2.2 Analytical

The spectrometer records the 2D projected momentum of ions, so fragment ion recoil correlations were calculated using projected-momentum covariance mapping. It was necessary to apply a contingent covariance analysis procedure to correct for unstable operating conditions. Because the ion yield itself is delay-dependent, it is not appropriate to define bins for the contingent covariance calculation based upon the total ion count per laser shot distribution for the whole dataset. Instead, the raw data recorded at each delay point were individually grouped into subsets.

7.3 Results and discussion

Ion ToF mass spectra of trans-1,2-DCE ionised by the UV pulse and NIR pulse separately, as well as by both pulses at positive pump-probe delay, are overlaid in Figure 7.1. Because $\pi^* \leftarrow \pi$ excitation is a single photon process it was important that UV multi-photon excitation was minimised. This is reflected in the small amount of ions produced by each UV pulse, relative to the hundreds produced by each NIR pulse. The NIR only mass spectrum is similar to the spectrum shown in Figure 6.2 of the previous chapter. Peaks stemming from ionisation of residual gases are noticeably more prominent, with the exception of H_2O^+, which was gated on each cycle. The combination of both pulses results in an enhanced yield of ions that correspond with the products of UV photodissociation, including ${C_2H_2}^+$, HCl^+, Cl^+ and $C_2H_xCl^+$, while the yield of parent ion slightly decreases.

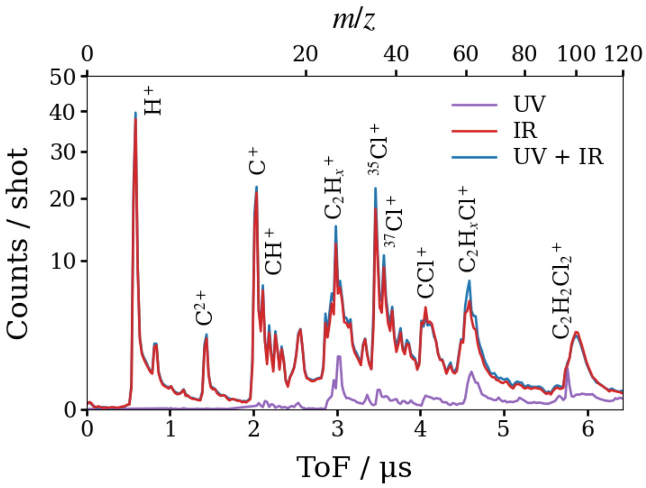

Figure 7.1: Ion ToF mass spectra recorded by the PImMS2 camera for *trans*-1,2-DCE exposed to (*purple*) a UV (202 nm) ultrafast laser pulse, (*red*) an intense NIR (800 nm) ultrafast laser pulse, and (*blue*) both pulses, where the UV precedes the NIR. Unlabelled peaks are background gases.

Compared to the simple case of UV photoinduced C–I bond cleavage in CH_3I, considered in Section 2.8.3, examining the dynamics of *trans*-1,2-DCE is complicated by the fact that there are multiple competing dissociation channels. The most straightforward method of inspecting an individual channel is to focus on the correlated distribution of the ions that correspond with the products of the channel of interest. For example, $C_2H_2Cl^+$ and Cl^+ are produced in combination only by Coulomb explosion of an intact parent molecule, or ionisation of the products of C–Cl bond cleavage.

7.3.1 Cl elimination dynamics

Figure 7.2(a) is a two-fold covariance map of the KE sum of $C_2H_2Cl^+ + Cl^+$, *i.e.* the total KER of two-body breakup, as a function of the pump-probe delay. Total KER was determined from the correlated ion momenta, calculated by projected-momentum covariance mapping, with a constraint of ±5 a.u. on the fragment momentum sum in each dimension. Because the distribution is derived from 2D projected momentum information, features are smeared towards lower KER and appear slightly below their true values (see Section 3.5.1).

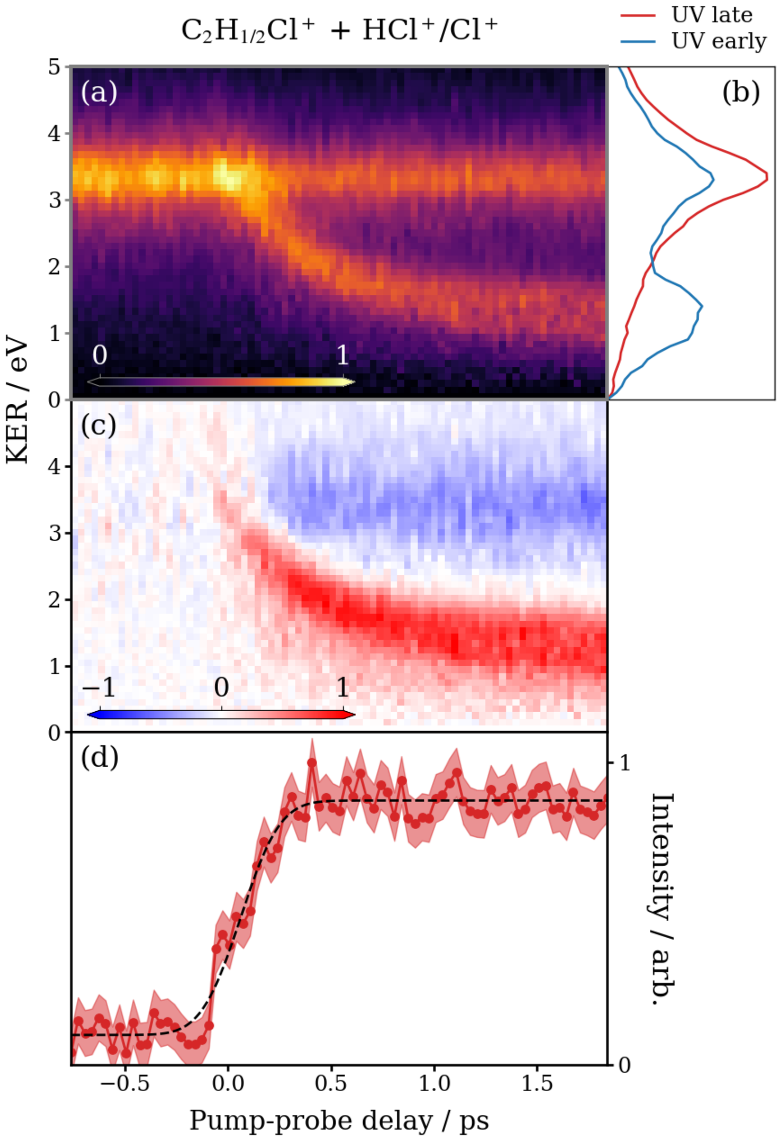

Figure 7.2: (a) Time-resolved two-fold covariance map of the total KER for the two-body breakup of *trans*-1,2-DCE^{2+} into $C_2H_{1/2}Cl^+$ + HCl^+/Cl^+. (b) KER distributions integrated across UV late (< −0.1 ps) and UV early (1.7 – 1.9 ps) pump–probe delays, normalised to unit area. (c) UV late subtracted plot. (d) Integrated ion yield for the Coulomb curve. The dashed black line is a CDF fit to the data. The shaded region represents errors bars.

The ToF resolution of the detection system is relatively low, so fragment ions differing by a single hydrogen mass cannot be distinguished. Considering only those combinations of ions that fulfil (in-plane) momentum conservation ensures that no three-body breakup channels, e.g. $C_2HCl^+ + Cl^+ + H$, contribute to the covariance map. However, the covariance analysis is not able to separate signal from two-body Coulomb explosion into $C_2HCl^+ + HCl^+$. The horizontal band centered at 3.4 eV in Figure 7.2(a) is therefore assigned to the Coulomb explosion of doubly ionised *trans*-1,2-DCE that yields either Cl^+ or HCl^+:

$$C_2H_2Cl_2 \xrightarrow{h\nu_{\mathrm{NIR}}} C_2H_2Cl^+ + Cl^+, \tag{I}$$

$$C_2H_2Cl_2 \xrightarrow{h\nu_{\mathrm{NIR}}} C_2HCl^+ + HCl^+. \tag{II}$$

The Coulomb curve is assigned to photodissociation of $\pi^* \leftarrow \pi$ excited *trans*-DCE by elimination of atomic Cl or HCl, followed by ionisation of both cofragments:

$$C_2H_2Cl_2 \xrightarrow{h\nu_{\mathrm{UV}}} C_2H_2Cl + Cl \xrightarrow{nh\nu_{\mathrm{NIR}}} C_2H_2Cl^+ + Cl^+, \tag{III}$$

$$C_2H_2Cl_2 \xrightarrow{h\nu_{\mathrm{UV}}} C_2HCl + HCl \xrightarrow{nh\nu_{\mathrm{NIR}}} C_2HCl^+ + HCl^+. \tag{IV}$$

Rapid cleavage of the C–Cl bond is expected to follow a curve crossing from the initially excited (π, π^*) state to a repulsive (n, σ^*) or (π, σ^*) state. The angular distribution of the fast recoiling Cl fragments from the photolysis of *trans*-1-2-DCE is strongly anisotropic, indicating that the dissociation lifetime is short compared to the rotational time scale.[218,220,221] The angular distribution of HCl is more isotropic,[219] implying a longer dissociation lifetime. This is in line with elimination proceeding through an internal conversion to the ground electronic state.[219,223,228] Therefore, channel III is likely the dominant at short pump-probe delay, with channel IV representing a greater contribution as more time elapses.

In Figure 7.2(c) the average UV late signal has been subtracted from all delays. This shows that the intensity of the high KER feature decreases at positive pump-probe delay, due to depletion of the parent molecule population by UV induced photodissociation. The Coulomb curve is clearly distinguished based on the enhancement in intensity. By setting all negative values in the distribution equal to zero, then integrating, the TR yield of $C_2H_{1/2}Cl^+$ + HCl^+/Cl^+ associated exclusively with the Coulomb curve can be obtained, seen in panel (d).

The yield of $C_2H_{1/2}Cl^+$ + HCl^+/Cl^+ rises on a very short timescale, which is attributed to rapid C–Cl bond cleavage. Fitting a Cumulative Distribution Function (CDF)[52,66,68] to the data yields a time offset of 60 ± 10 fs, which reflects the time taken for transfer between the (π, π^*) and repulsive states. The width of the CDF fit (150 ± 10 fs) approximately equals the temporal resolution of the instrument. Given the predicted mechanism for HCl elimination, one would expect a second component in the delay-dependent distribution that rises on a longer timescale. The absence of such a feature suggests that HCl is not produced in a significant quantity on the timescale explored in this experiment.

The KER of the Coulomb curve at the longest delay time used in the experiment (1.9 ps) is 1.3 ± 0.5 eV, where the uncertainty refers to the standard deviation of a Gaussian fit to the blue spectrum in panel (b). This is much greater than the KER for HCl elimination reported by Umemoto *et al.* (0.5 eV),[219] but agrees well the KER for Cl detachment measured by Suzuki *et al.* (1.1 ± 0.4 eV).[221] The slight discrepancy can be attributed to a small, lingering Coulombic contribution. It should be noted that Umemoto *et al.* and Suzuki *et al.* performed their measurements at a shorter excitation wavelength (193 nm), alhough other studies have observed that the dissociation kinetics of 1,2-DCE excited in its (π, π^*) absorption band do not vary appreciably with wavelength.[218,221]

7.3.2 Probing time-evolving nuclear structure

The focus of the next section of the analysis is to try and identify whether *trans*-1,2-DCE undergoes structural rearrangement following photoexcitation. The discussion in the previous chapter pinpointed Coulomb explosion into atomic ions as the preferred choice of structural probe, due to the straightforward mapping from initial atomic positions to final fragment momenta. Unfortunately, because the peak intensity of the focused NIR laser pulses was lower for the current experiments, parent ions were formed with lower total charge on average. As a result very few molecules were ionised to a sufficient extent to trigger 'complete' fragmentation.

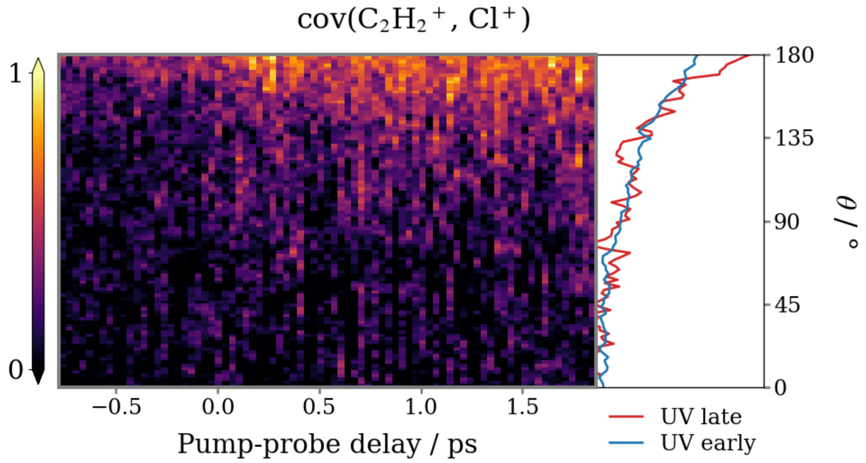

Figure 7.3: Time-resolved two-fold covariance map of the relative recoil angle distribution of $C_2H_2^+ + Cl^+$, produced by the three-body breakup of *trans*-1,2-DCE. Distributions integrated across UV late (< -0.2 ps) and UV early (> 0.2 ps) pump–probe delays are projected on the right. Each is normalised to unit area.

Figure 7.3 is a two-fold covariance map of the recoil angle between $C_2H_2^+$ and Cl^+ as a function of pump-probe delay. This ion pair is produced by the three-body breakup of either a parent dication or trication, yielding Cl or Cl^+ as the third fragment. From the angular distribution it is apparent that the former channel dominates. Peak intensity occurs at 180°, indicative of Coulomb explosion between a pair of charged fragments. The behaviour deviates from strictly back-to-back recoil because of the impulse that the neutral Cl imparts when it separates. Although in Section 6.3.2 a three-fold covariance analysis was able to extract the correlated fragment momenta for the breakup of 1,2-DCE^{3+}, the same approach was not successful here, likely because the yield of the channel is substantially less.

The dication breakup channel does not provide any meaningful structural information. Figure 7.3 shows that the yield of $C_2H_2^+$ + Cl^+ + Cl increases at positive delay, but the angular distribution of the ($C_2H_2^+$, Cl^+) ion pair is invariant with time. The TR KE distribution of Cl^+ measured in covariance with $C_2H_2^+$ is shown in Figure 7.4(a). The distribution is broad, but performing a subtraction of the average UV late signal (panel (b)) reveals the suggestion of a Coulomb curve. The feature appears at approximately the same delay as the Coulomb curve in the $C_2H_2Cl^+$ + Cl^+ covariance map. Hence, it is ascribed to a mechanism similar to channel III, where the $C_2H_2Cl^+$ further fragments into $C_2H_2^+$ + Cl.

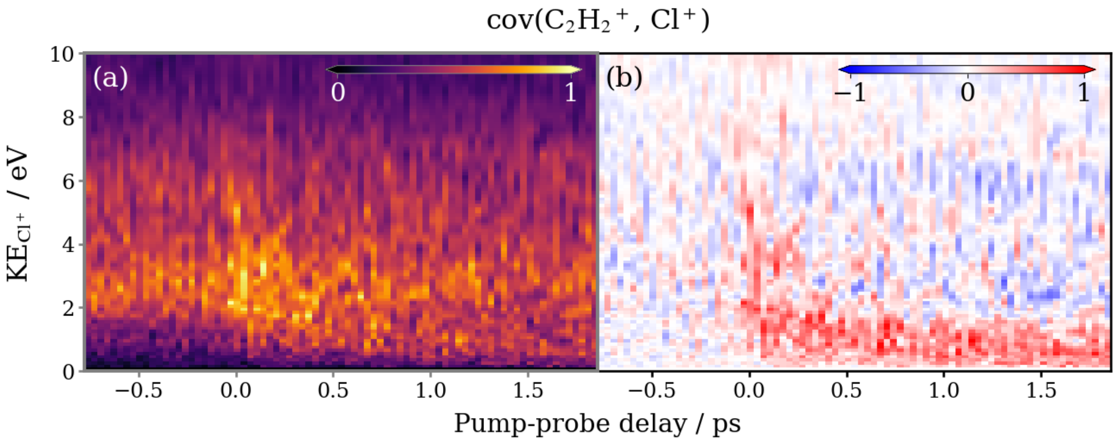

Figure 7.4: (a) Time-resolved two-fold covariance map of the KE distribution of Cl^+ from the three-body breakup of *trans*-1,2-DCE that yields $C_2H_2^+$ + Cl^+. (b) UV late subtracted plot. Each panel is normalised separately.

To deduce information about the time-evolving nuclear structure, it is necessary to explore the Coulomb explosion dynamics of a more highly charged system. Studying the TR correlated momenta of the chlorine dications, akin to Section 6.3.3, is not practical as Cl^{2+} was not detected in a sufficient quantity. A major factor is that Cl^{2+} overlaps in ToF with H_2O^+, which was deliberately gated, so a large portion of the Cl^{2+} Newton sphere was detected with greatly reduced efficiency. The alternative is to focus on the correlated momenta of the Cl^+ ion pair.

The TR KE distribution for the Cl^+ pair, determined via two-fold covariance analysis, is shown in Figure 7.5. Once again, the UV late subtracted distribution reveals a faint Coulomb curve that is offset slightly from time zero, associated with rapid C–Cl bond cleavage prior to ionisation by the probe pulse. Figure 7.6 plots the relative recoil angle of the Cl^+ pair as a function of pump-probe delay. The dominant feature is a horizontal band centered at 180°, which originates from Coulomb explosion of *trans*-1,2-DCE in its ground electronic state. An additional band centered around 130° appears at positive delay. Coulomb explosion of the *cis* geometry causes the Cl^+ ions to recoil at much smaller angle (∼110°), so the feature is not the result of *cis*-*trans* isomerisation.

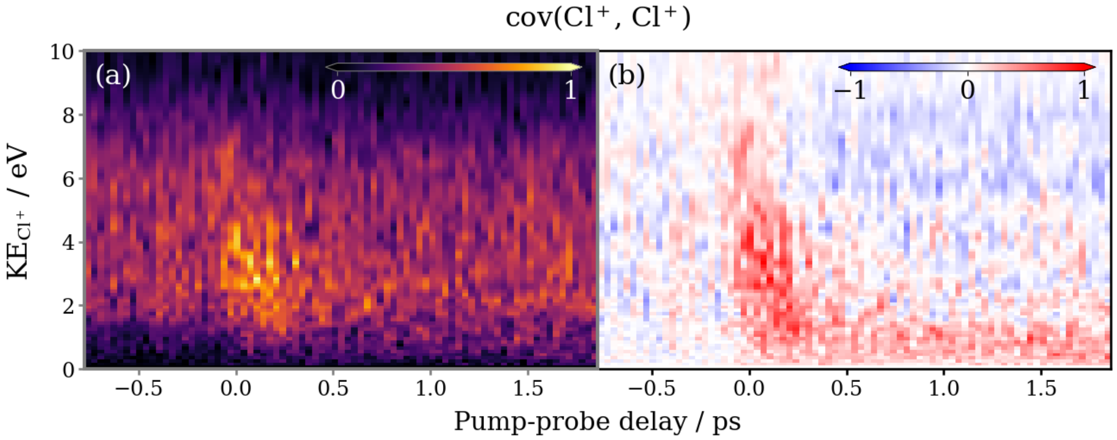

Figure 7.5: (a) Time-resolved two-fold covariance map of the KE distribution of Cl^+ from the Coulomb explosion of trans-1,2-DCE that yields a pair of Cl^+ ions. (b) UV late subtracted plot. Each panel is normalised separately.

Signal at a recoil angle somewhere between the expected values for *cis* and *trans* is consistent with Coulomb explosion initiated from an intermediate geometry, in which the CHCl groups are twisted at a dihedral angle between 0 – 180°. Further, the band develops within a narrow window of time zero. It is probable that the true timescale is obscured due to the limited temporal resolution of the experiment. These observations agree with the picture of ultrafast C–C torsional motion occurring on the excited (π, π^*) PES as the molecule relaxes to a twisted geometry. However, this interpretation is not conclusive. For example, if C–Cl bond cleavage rotationally excites C_2H_2Cl radical, its orientation relative to the detached Cl at the instant of ionisation will affect the relative recoil angle of the chlorine ions.

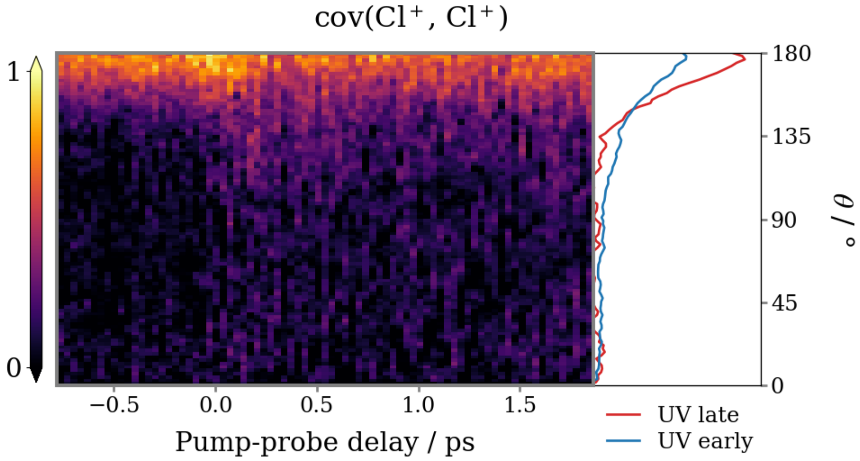

Figure 7.6: Time-resolved two-fold covariance map of the relative recoil angle distribution of the Cl^+ ion pair produced by the Coulomb explosion of *trans*-1,2-DCE. Distributions integrated across UV late (< -0.2 ps) and UV early (> 0.2 ps) pump–probe delays are projected on the right. Each is normalised to unit area.

7.4 Conclusions and future work

The photoexctiation dynamics of *trans*-1,2,DCE have been studied at 202 nm. Photodissociation by Cl elimination was followed by detecting the products in correlation. Based on the measured reaction time and KER, this process occurs on a repulsive state accessed by a surface crossing. Through tracking the relative recoil of the Cl substitutes from the delayed Coulomb explosion of the photoexcited molecule, evidence has been obtained for photoinduced structural change. This has been tentatively ascribed to molecular torsion about the C–C axis. Overall the discussion has been brief. No simulations were performed to support interpretation of the results. This was because a conscious choice was made to focus efforts on the analysis of the follow up experiments, which promised much deeper insight.

Compared to the CEI data presented in the previous chapter, which was acquired using the same instrument, the data discussed here does not provide the same detailed insight. The main difference was the characteristics of the probe laser pulse. Due to an increased increased focal volume the background ion count rate was substantially higher, while the peak intensity was much lower, resulting in the generation of less highly charged parent ions. This particularly impaired the ability to detect changes in the parent molecular structure from the Coulomb explosion images. Since the conclusion of these experiments it was discovered that the cause was astigmatism of the focused beam, which has now been resolved. However, a number of other improvements to the TR-CEI instrument are needed to match the standards of leading experiments in the field, as the next chapter demonstrates.

8

Part II – Ultraviolet photoexcitation dynamics of 1,2-dichloroethene investigated by time-resolved Coulomb explosion imaging

Contents

This chapter continues the discussion on the UV photoexcitation dynamics of 1,2-DCE from the previous chapter. The experiments described in Chapter 7 were repeated in the James R. Macdonald Laboratory at Kansas State University in collaboration with the research group of Professor Daniel Rolles. The TR-CEI apparatus at Kansas State University is more advanced than its counterpart at the University of Oxford in a number of ways. The ToF resolution of the detector is higher, allowing fragments differing by a single hydrogen mass to be distinguished (particularly important for resolving the Cl and HCl elimination channels in chloroethenes). The increased timing precision also makes it possible to reconstruct the complete 3D momentum for each ion, providing a distinct improvement in the clarity of the ion imaging data.

Facilitated by a several orders of magnitude increase in the experimental repetition rate, data could be collected on a similar timescale whilst operating at a much lower average ion count per laser shot. Hence, the correlated properties of fragment ions are determined using coincidence analysis. Coincidence mapping is applied to calculate the correlated momenta of up to four fragments from the Coulomb explosion of the target molecule, providing more information about the molecular structure. The scope of the experimental work was also expanded. The $\pi^* \leftarrow \pi$ photoexcitation dynamics of both *cis* and *trans* forms of 1,2-DCE were investigated and comparisons are made. Data were recorded over an extended pump-probe delay range to capture dissociation processes that occur on a few picosecond timescale.

Overall, the results provide much deeper insight into the UV photoexcitation dynamics of 1,2-DCE. Signals from the Cl and HCl elimination channels are fully resolved. In both isomers, the former process occur within ∼100 fs, while the latter process takes place on a picosecond timescale. The cleavage of both C–Cl bonds via a sequential mechanism is also identified as a prominent process. Conclusive evidence is observed for ultrafast structural rearrangement of photoexcited *trans*-1,2-DCE prior to C–Cl bond cleavage. This motion is attributed to rapid C–C torsion on the (π, π^*) PES, which acts as a precursor to surface crossing to a repulsive PES.

8.1 Methods

8.1.1 Experimental

Experiments were conducted in the James R. Macdonald Laboratory at Kansas State University. The instrument is a COLTRIMS spectrometer coupled to a custom Ti:Sapphire laser system, as described in Section 2.6.2. Samples of the *cis* (97%) and *trans* (98%) forms of 1,2-DCE were purchased from a commercial supplier (Sigma-Aldrich) and used without further purification. Both samples are liquid at room temperature and were first outgassed in a freeze–pump–thaw cycle, before introduction into the gas phase by expansion without carrier gas.

The continuous molecular beam was intersected by the 198 nm fourth harmonic and 790 nm fundamental output of the Ti:Sapphire laser system. Both laser pulses were polarised parallel to the ToF axis. Data were recorded with a UV pulse energy of $0.3\,\mu$J, corresponding to a peak intensity $8 \times 10^{12}\,\mathrm{W\,cm^{-2}}$, and a NIR pulse energy of $30\,\mu$J, corresponding to a peak intensity of $1.4 \times 10^{15}\,\mathrm{W\,cm^{-2}}$. Under these conditions, the count rate from ionisation by the NIR laser was $\sim$11 kHz, with a minimal contribution from the UV laser. This corresponds to an average ion count of 1.1 per laser shot.

The position of temporal overlap and instrument response function (160 ± 4 fs) were determined *in-situ* based on the central position and FWHM of a Gaussian function fit to the cross correlation peak in the TR yield of parent monocations. Ion images were recorded in different intervals across a pump-probe delay range spanning -0.3 to 10 ps. The delay was scanned in 25 fs steps from -0.3 to 0.3 ps, 50 fs steps up to 2 ps, and finally 2 ps steps up to 10 ps.

8.1.2 Analytical

The COLTRIMS instrument is equipped with a DLA detector that records the (x, y) spatial position and arrival time of ion hits with high precision, permitting reconstruction of the complete 3D momentum information for each ion. Because data was recorded with a low ion count rate ($\sim 1\,\mathrm{shot}^{-1}$) the correlated momenta of fragment ions is calculated using coincidence analysis. Strictly speaking, this is not ‘true’ coincidence conditions as the chance that multiple parent molecules are ionised in the same laser shot was not negligible. However, the proportion of false coincidence events is small enough that they can be suppressed by imposing fragment momentum conservation. How this is achieved is outlined as part of the analysis.

8.2 Time-of-flight data

Figure 8.1 displays the ion ToF mass spectrum for *trans*-1,2-DCE when the UV pulse precedes the NIR pulse, and vice versa. Compared to analogous spectra measured by the PImMS2 camera, the recorded yield of parent ions is significantly higher. This is an accurate measure of the yield of parent monocations relative to other species, as the point on the detector where ions with near-zero transverse momentum are focused did not saturate. Accordingly, ions derived from background gases also appear more prominent, even though the overall yield of background ions as a fraction of the total was much less in these experiments. Multiple peaks are resolved for $C_2H_xCl_2^+$ that arise from different combinations of ^{35}Cl and ^{37}Cl and potential loss of hydrogen.

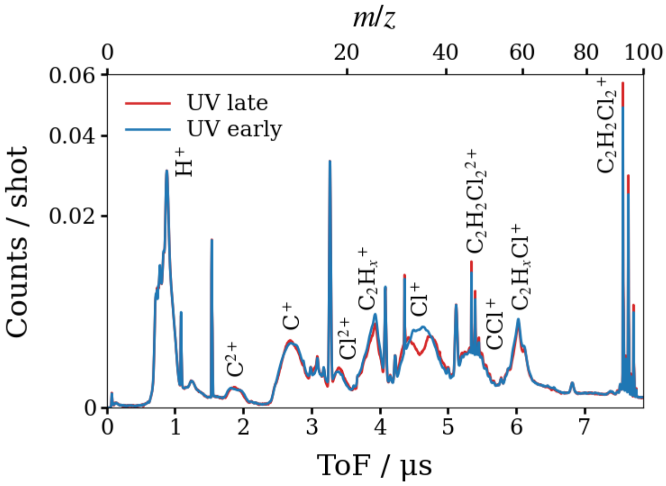

Figure 8.1: Ion ToF spectra of *trans*-1,2-DCE exposed to an UV (198 nm) laser pulse and an intense NIR (790 nm) ultrafast laser pulse. The blue trace is the spectrum when the UV pulse precedes the NIR pulse, and vice versa for the red trace. Unlabelled peaks are background gases.

Because the NIR pulses were polarised parallel rather than perpendicular to the ToF axis, geometric alignment creates two peaks for Cl^+ in the UV late spectrum. The most probable electron-extraction axis for *trans*-1,2-DCE connects the centres of the chlorine atoms,[204] hence, Coulomb explosion typically ejects one Cl^+ towards the detector and the other away from the detector. In the UV early spectrum the space between the Cl^+ peaks is filled in, presumably due to the formation of low KE Cl^+ by photodissociation prior to SFI. The yields of $C_2H_x{}^+$ and $C_2H_xCl^+$ are also enhanced, while the counts of singly and doubly charged parent ions decrease.

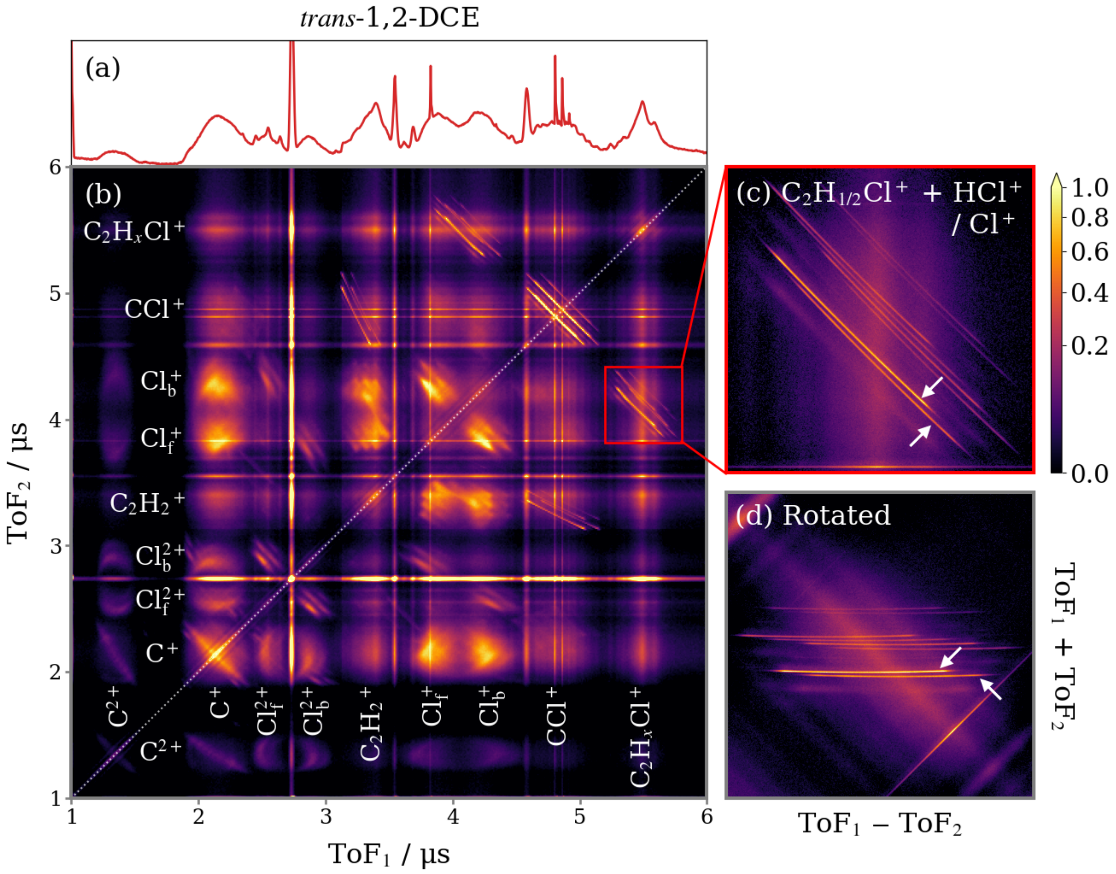

Figure 8.2: (a) Ion ToF spectrum for *trans*-1,2-DCE when the NIR pulse arrives before the UV pulse. (b) The corresponding ToF coincidence map. Laser pulses were polarised parallel to the ToF axis, resulting in pairs of peaks for $Cl^{+/2+}$ due to the Coulomb explosion of geometrically aligned molecules ejecting one ion towards the detector ($_f$) and the other away ($_b$). The red box highlights the region containing correlations between $C_2H_{1/2}Cl^+$ and HCl^+/Cl^+ that is enlarged in panel (c). To filter the different coincidence channels a rotated coincidence map is produced, shown in panel (d), where the correlated features appear as horizontal lines.

The ToF coincidence map for SFI of *trans*-1,2-DCE is shown in Figure 8.2(b). Intense features reveal correlations between pairs of fragment ions. These are visible against a background of false coincidence events, which proves that fragmentation of multiple target molecules in the same laser shot was a common occurrence. It is therefore necessary to apply additional filters to disentangle the true coincidence events, starting with a constraint on the ion ToFs.

Figure 8.2(c) displays an expanded section of the coincidence map containing the $C_2H_2Cl^+$ + Cl^+ and C_2HCl^+ + HCl^+ coincidence channels. Because of momentum conservation, the true coincidence events appears as sharp diagonal lines. Eight such features are observed. Four for each channel due to the various combinations of the two Cl isotopes. The present analysis focuses on the fragmentation channels of the $C_2H_2{}^{35}Cl_2$ isotopologue. In principle, because the small mass difference between the two Cl isotopes has a minor effect on the dynamics, the results for all isotopic combinations could be combined to nearly double the number of events.

The upper and lower arrows in Figure 8.2(c) indicate the $C_2H^{35}Cl^+$ + $H^{35}Cl^+$ and $C_2H_2{}^{35}Cl^+$ + $^{35}Cl^+$ channels, respectively. The method for separating these channels is to produce a plot of the difference between the ion ToFs ($ToF_1 - ToF_2$) versus the sum of the ion ToFs ($ToF_1 + ToF_2$), seen in panel (d). This effectively rotates the coincidence map so that the correlated features are horizontal. Using this plot, a $ToF_1 - ToF_2$ range and a $ToF_1 + ToF_2$ range can defined that capture the true coincidence events exclusively for a single channel, whilst minimising the contribution from false coincidence events.

8.3 Characterisation of photodissociation

The initial focus of the analysis is a re-examination of the photodissociation dynamics of 1,2-DCE. One of the main motivations for doing so is that, in contrast to the previous analysis (Section 7.3.1), signals for $C_2H_2Cl^+$ + Cl^+ and C_2HCl^+ + HCl^+ are clearly distinguished, so the dynamics of the Cl and HCl elimination pathways can be disentangled. Each individual photodissociation channel is interrogated via the coincidence between the ions that correspond with the dissociation products.

Under this approach, the NIR is employed as a universal probe of the product species by inducing single ionisation, rather that acting as a structural probe by inducing further fragmentation.

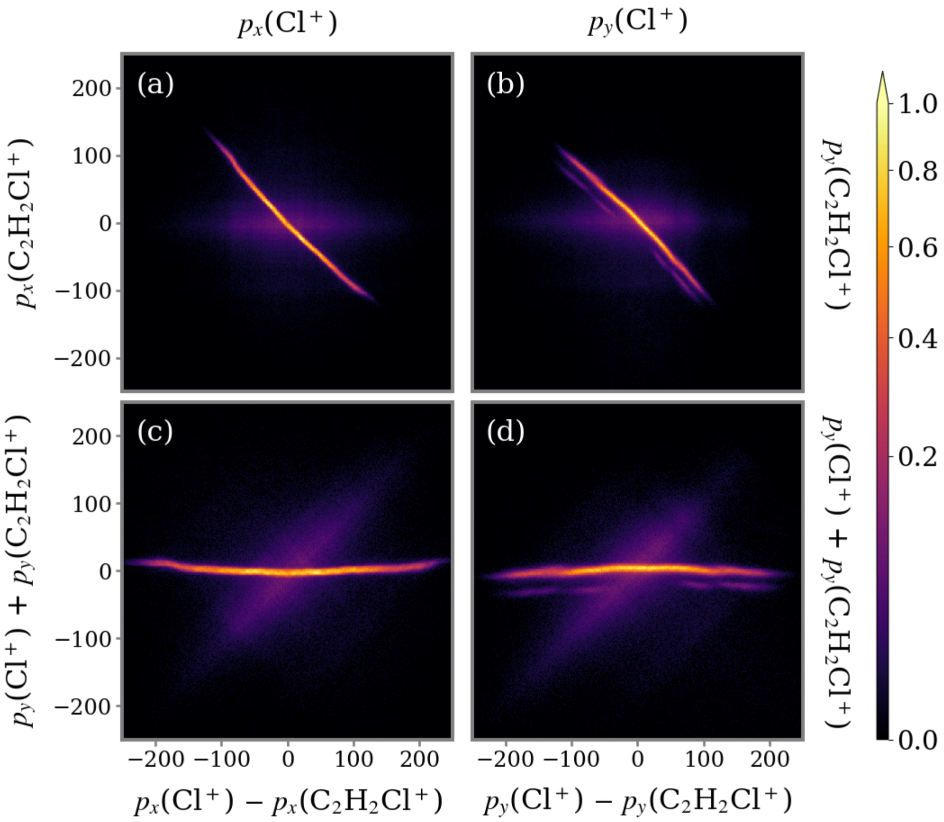

Figure 8.3: Fragment momentum correlation maps for pairs of $C_2H_2Cl^+$ + Cl^+ ions detected in coincidence from the breakup of *trans*-1,2-DCE. Correlation maps for the x and y components of the ion momenta are shown in the left and right columns, respectively. The bottom row displays rotated coincidence maps where the correlated features appear as horizontal lines, used to filter the true coincidence events.

The first stage of isolating a coincidence channel is to apply a constraint on the ion ToFs, as discussed in relation with Figure 8.2(d). This is equivalent to imposing momentum conservation in the z dimension. The second step is to refine the selected subset of events based on the ion momentum sum in the x and y dimensions. As demonstration, a map of how the x momenta of $C_2H_2Cl^+$ and Cl^+ detected in coincidence are correlated is presented in Figure 8.3(a). Analogous to a ToF coincidence map, the coincidence events that satisfy momentum conservation form a roughly diagonal line with negative slope. The set of events has already been filtered based on the ion ToFs, so false coincidences events are few (note the square root colour scale), but not zero.

Again, an appropriate filter to remove false coincidence events is defined based on a rotated coincidence map (panel (c)), produced by computing the sum and difference of the ion x momentum components and plotting one against the other. The panels in the neighbouring column of Figure 8.3 show equivalent plots constructed from the y components of the ion momenta, used to specify a third and final event filter. Following this procedure, it is guaranteed that the correlated ions satisfy momentum conservation in three dimensions.

8.3.1 Cl elimination

In the top row of Figure 8.4, the yield of $C_2H_2Cl^+$ + Cl^+ for *cis* and *trans*-1,2-DCE is plotted as a function of the pump-probe delay and total KE of the ions. To illustrate the dynamics on both short and long timescale, each distribution is plotted in 50 fs steps up to ∼2 ps, then 2 ps steps thereafter. The same key features are observed for both isomers. The horizontal band labelled I arises from double ionisation of intact molecules by the probe pulse:

$$C_2H_2Cl_2 \xrightarrow{h\nu_{\mathrm{NIR}}} C_2H_2Cl^+ + Cl^+. \tag{I}$$

The feature labelled III that curves down with increasing pump-probe delay is assigned to prompt photodissociation into an ethyl chloride radical and a chlorine atom, followed by ionisation of both cofragments:

$$C_2H_2Cl_2 \xrightarrow{h\nu_{\mathrm{UV}}} C_2H_2Cl + Cl \xrightarrow{nh\nu_{\mathrm{NIR}}} C_2H_2Cl^+ + Cl^+. \tag{III}$$

A very low total KER band that develops over several picoseconds is discernible in the UV late subtracted plot for the *cis* isomer in Figure 8.4(c). This corresponds with the Boltzmann-like component that previous studies observed in the Cl KE distribution.[218,219,221–223] The feature is attributed to C–Cl bond cleavage on the ground PES following internal conversion from the initially excited PES,[221] referred to here as channel III*. Unfortunately, the same region in the *trans* isomer spectrum is obscured by trace signal from the $C_2HCl^+ + HCl^+$ coincidence channel (labelled VI), which manifests as a 'shadow' below the Coulomb curve. Saturation of the photodiode that provides the reference time caused distortions in the measured timing signals. Consequently, some coincidence channels slightly intersect.

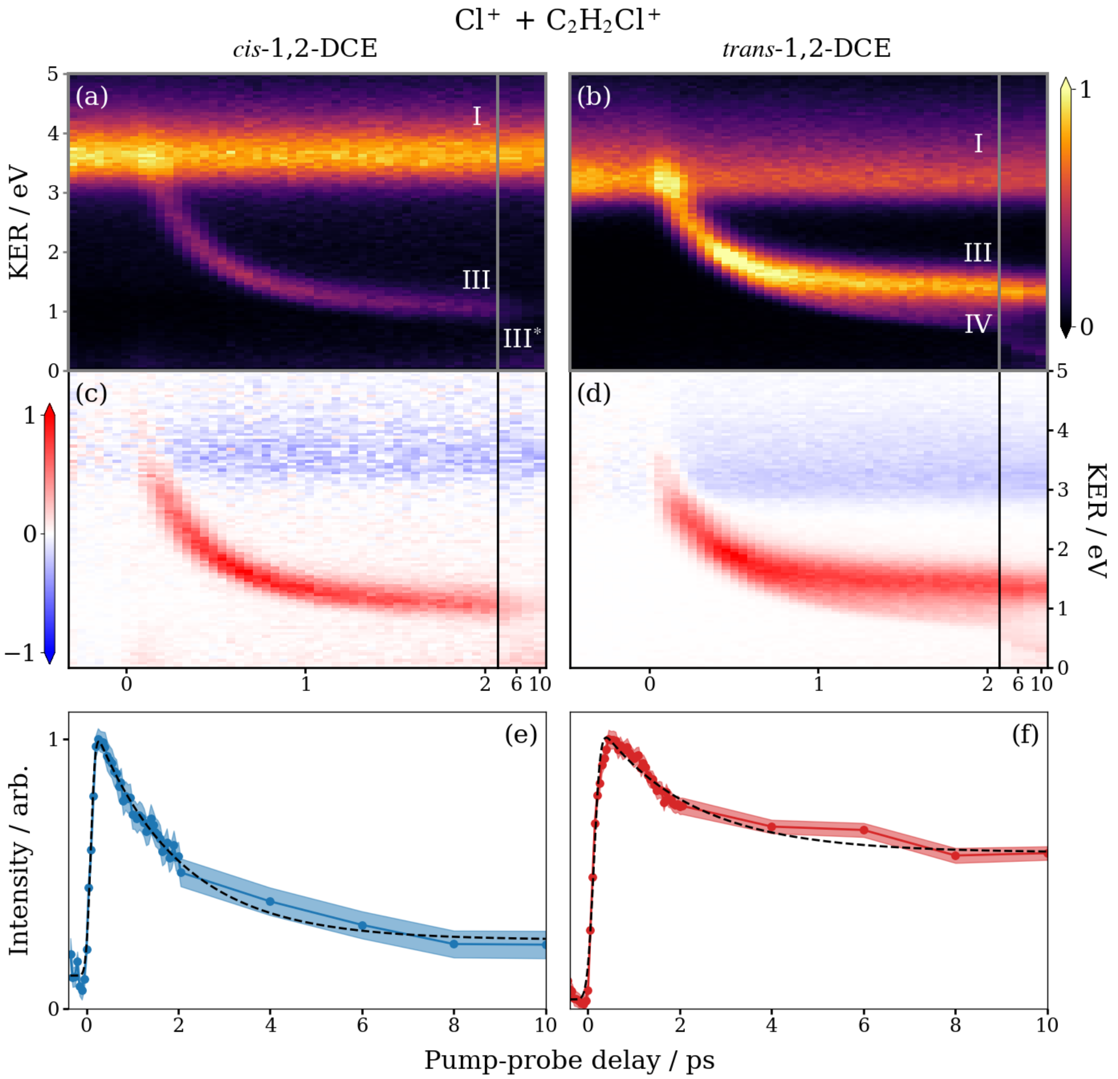

Figure 8.4: Time-resolved total KER distribution for the two-body breakup of (a) *cis*- and (b) *trans*-1,2-DCE^{2+} into $C_2H_2Cl^+ + Cl^+$, normalised to the peak intensity of the probe-only channel. The labelled features are discussed in the main text. UV late subtracted plots are displayed below in panels (c) and (d). (e, f) Integrated ion yields for the Coulomb curve (III), fit using the model described in the text. The shaded regions represent errors bars. Extracted fit parameters are provided in Table 8.1

Table 8.1: Extracted parameters from fitting the data presented in Figures 8.4(e) and (f) with the product of a CDF and an exponential decay function. Uncertainties are given in parentheses.

	τ_0 / fs	τ_d / ps	Φ / %
cis	97 (5)	1.9 (0.1)	13 (4)
trans	133 (7)	2.0 (0.3)	50 (10)

In general, the contrast of the pump-probe features is stronger for *trans*-1,2-DCE. For example, the relative intensity of channel III is noticeably higher. 198 nm lies close to the absorption cross section maximum of the (π, π^*) band for *trans*-1,2-DCE,[229] while the (π, π^*) band of *cis*-1,2-DCE is shifted towards shorter wavelength.[230] Hence, at the chosen wavelength a higher percentage of *trans*-1,2-DCE molecules are photoexcited by the pump pulse.

Integrated total KER spectra for the delay range 4 − 10 ps are presented in Figure 8.5. The low KER region of each spectrum was fit to a Gaussian function to extract the isomer-dependent KER for channel III (listed in Table 8.2). At such long delay fragments are too far apart to interact when they are ionised, so the KER of channel III reflects the KER of the initial photodissociation. Suzuki et al. measured the KER of C–Cl bond fission at 193 nm as 0.8 ± 0.3 and 1.1 ± 0.4 eV for *cis* and *trans*, respectively, which agree within errors with the values in Table 8.2.

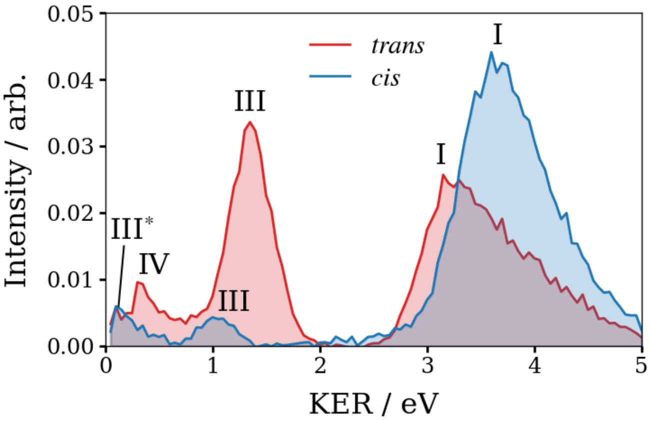

Figure 8.5: Total KER spectra for the two-body breakup of (*blue*) *cis*- and (*red*) *trans*-1,2-DCE^{2+} into $C_2H_2Cl^+$ + Cl^+ when the UV pulse far precedes the NIR pulse (4–10 ps). The labelled features correspond with those in Figure 8.4. Each distribution is normalised to unit area.

Table 8.2: KER for various photodissociation pathways of $\pi^* \leftarrow \pi$ excited 1,2-DCE.

	KER / eV	
	cis	*trans*
Rapid C–Cl bond cleavage	1.0 ± 0.3	1.4 ± 0.2
Sequential cleavage of both C–Cl bonds	1.1 ± 0.3	1.2 ± 0.4
HCl Elimination	0.4 (0.1)	0.4 (0.1)

The TR yield for channel III is plotted in the bottom panels of Figure 8.4. For each isomer, the signal associated with the Coulomb curve was isolated by nullifying the negative values in the UV late subtracted map, then integrating with a minimum total KER boundary to avoid contributions from channels II and III*. The form of both traces is similar: the yield sharply rises as rapid C–Cl bond cleavage establishes a population of C_2H_2Cl and Cl, but slowly decays as more time elapses. This implies that another reaction can occur, most likely further breakup of C_2H_2Cl.

To examine the trend, the traces in Figures 8.4(e) and (f) were fit to a two component function: (i) a CDF representing the step-like enhancement due to formation of C_2H_2Cl + Cl and (ii) an exponential decay function that characterises the depletion due to the further reaction. Best fit parameters are summarised in Table 8.1. These includes the time offset of the rising component (τ_0), the decay time of the exponential (τ_d), and the asymptotic yield at infinite delay (Φ). The width of the CDF was fixed based on the instrument response function.

An offset between temporal overlap and the onset of the Coulomb curve was identified in the previous study. This is interpreted as the time taken for transfer between the (π, π^*) and repulsive states, as well as wave packet motion on the repulsive state. In addition, the present study identifies an isomeric difference in the dissociation time. Given that the kinematics of C–Cl blond cleavage is different for the isomers of 1,2-DCE, it is not surprising that the dissociation time is different too. Further investigation is needed to explain the differences in the primary dissociation dynamics for this pair of geometric isomers.

Compared to the fit of the rise component, the fit of the decay component is considerably less precise. The fitting function struggles to extrapolate based on the limited data available. It has the tendency to predict that Φ is similar to the average value of the final two data points, *i.e.* that the channel yield does not continue to decrease beyond the extent of the data. As a result, it extracts similar τ_d for both isomers, even though from visual inspection it is reasonable to predict that the yield for *trans* follows a gradual decline over a longer period. Refinement of the fitting function is required. It would also be beneficial to collect data at more points extending out to a longer pump-probe delay.

Nevertheless, it is clear that the secondary dissociation dynamics are strongly isomer dependent. Within 10 ps, far more *cis*-C_2H_2Cl dissociates than *trans*-C_2H_2Cl. The fragmentation is reliant upon internal energy gained from the primary dissociation redistributing into the appropriate vibrational mode. The structure of the C_2H_2Cl moiety, whether produced by *cis*- or *trans*-DCE, is in theory identical, so the difference in the secondary dissociation dynamics must derive from an internal energy discrepancy. Considering that the KER of the primary C–Cl bond fission in *cis*-1,2-DCE is lower, it follows that more of the available energy is partitioned into the internal modes of C_2H_2Cl (the Cl atom has no internal degrees of freedom). Future work to model the internal partitioning for this pair of isomers would be highly informative.[231]

Regarding the mechanism of secondary fragmentation, Seki *et al.* conjectured that C_2H_2Cl could dissociate by cleaving another C–Cl bond:

$$\mathrm{C_2H_2Cl} \rightarrow \mathrm{C_2H_2} + \mathrm{Cl}. \tag{8.1}$$

This is confirmed by examining the $C_2H_2^+$ + Cl^+ + Cl^+ coincidence channel. To identify this three-body fragmentation channel, we use a three-fold coincidence map in which the ToF of the first detected ion is plotted against and the sum of the ToFs of the subsequently detected ions. As an example, Figure 8.6(a) shows the region of interest in the coincidence map for *trans*-1,2-DCE. Comparable to a ToF two-fold coincidence map, the coincidence events that satisfy momentum conservation appear as sharp diagonal lines.

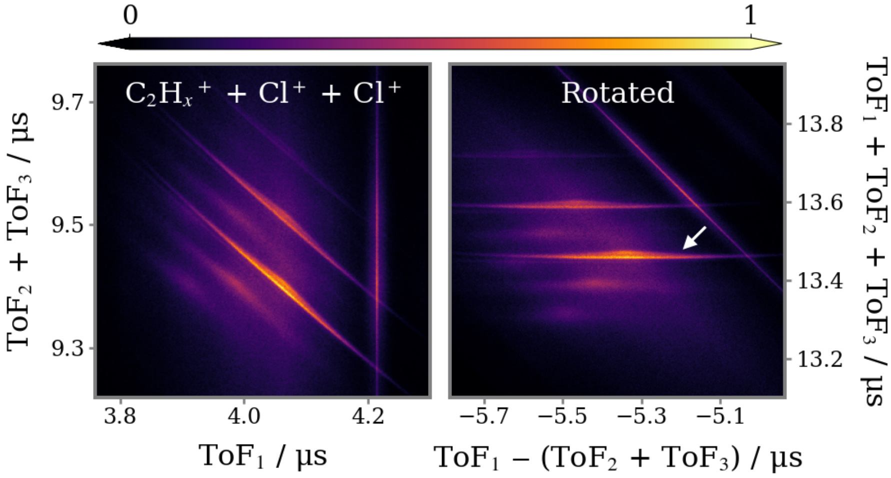

Figure 8.6: (*Left*) A section of the ToF three-fold coincidence map for *trans*-1,2-DCE, displaying the correlations between $C_2H_x{}^+$ and a pair of Cl^+ ions. The ToF of the first detected ion ($C_2H_2{}^+$) is plotted along the x-axis, and the sum of the ToFs of other subsequently detected ions (Cl^+ + Cl^+) is plotted along the y-axis. (*Right*) A rotated version of the coincidence map in which the correlated features for different channels are horizontal, allowing them to be easily separated.

From right to left, the diagonal lines correspond to the $C_2H_2{}^+$ + $2Cl^+$, C_2H^+ + $2Cl^+$ and $C_2{}^+$ + $2Cl^+$. These become progressively blurrier as H atoms are removed. The repetition of features in the vertical direction stems from the different combinations of ^{35}Cl and ^{37}Cl, as explained in Section 8.2 in relation to the two-body fragmentation channels. The analysis focus on the most intense coincidence channel: $C_2H_2{}^+$ + $^{35}Cl^+$ + $^{35}Cl^+$. Signal was isolated using a rotated coincidence map (Figure 8.6(b)) to define $ToF_1 - (ToF_2 + ToF_3)$ and $ToF_1 + ToF_2 + ToF_3$ boundaries. Coincidence events were also filtered based on momentum conservation in the x and y dimensions.

The delay-dependent total KER of $C_2H_2{}^+$ + Cl^+ + Cl^+ is displayed in Figures 8.7(a) and (b) for *cis* and *trans*, respectively. The same three features are common to both distributions. The high KER band is dominated by Coulomb explosion of molecules that have not been excited by the UV pump pulse:

$$C_2H_2Cl_2 \xrightarrow{nh\nu_{\text{NIR}}} C_2H_2{}^+ + 2Cl^+. \tag{V}$$

A pair of Coulomb curves labelled VI and VII descend from this feature. The upper curve is assigned to photodissociation into an ethyl chloride radical and a chlorine atom, followed by single ionisation of Cl and double ionisation of C_2H_2Cl, which subsequently Coulomb explodes:

$$C_2H_2Cl_2 \xrightarrow{h\nu_{UV}} C_2H_2Cl + Cl \xrightarrow{nh\nu_{NIR}} C_2H_2{}^{+} + 2Cl^{+}. \tag{VI}$$

The dynamics induced by the UV pulse are identical to channel III, but the total KER is offset by the KER of the Coulomb explosion of $C_2H_2Cl^{2+}$.

The lower Coulomb curve arises from sequential cleavage of both C–Cl bonds, prior to single ionisation of the each fragment:

$$\begin{aligned} C_2H_2Cl_2 &\xrightarrow{h\nu_{UV}} C_2H_2Cl^{*} + Cl, \\ C_2H_2Cl^{*} &\rightarrow C_2H_2 + Cl, \\ C_2H_2 + 2Cl &\xrightarrow{nh\nu_{NIR}} C_2H_2{}^{+} + 2Cl^{+}. \end{aligned} \tag{VII}$$

The KER of channel VII is consistently lower than channel VI because all three fragments separate as time elapses. When the fragments are far enough apart that they do not repel when ionised, the KER is minimum, and influenced solely by the two C–Cl bond breaking events. Values are listed in Table 8.2 and are effectively equal to the KER for single C–Cl bond cleavage, implying that the impulse of the secondary dissociation is minimal.

The TR yield of channel VII for each isomer is plotted in the bottom row of Figure 8.7. Note that due to the overlap between channels VI and VII in a ∼1 ps window after time zero, intensity data could not be extracted for the complete delay range. Despite the ‘gap’ in the data, the trend can be inferred. Both traces are modelled well by the product of an exponential rise and a Heaviside step function.[67] The fitting function is not considered reliable for extracting accurate physical constants, but serves to demonstrate that the experimental data follows an exponential rise, which mirrors the exponential decay component in channels III and VI.

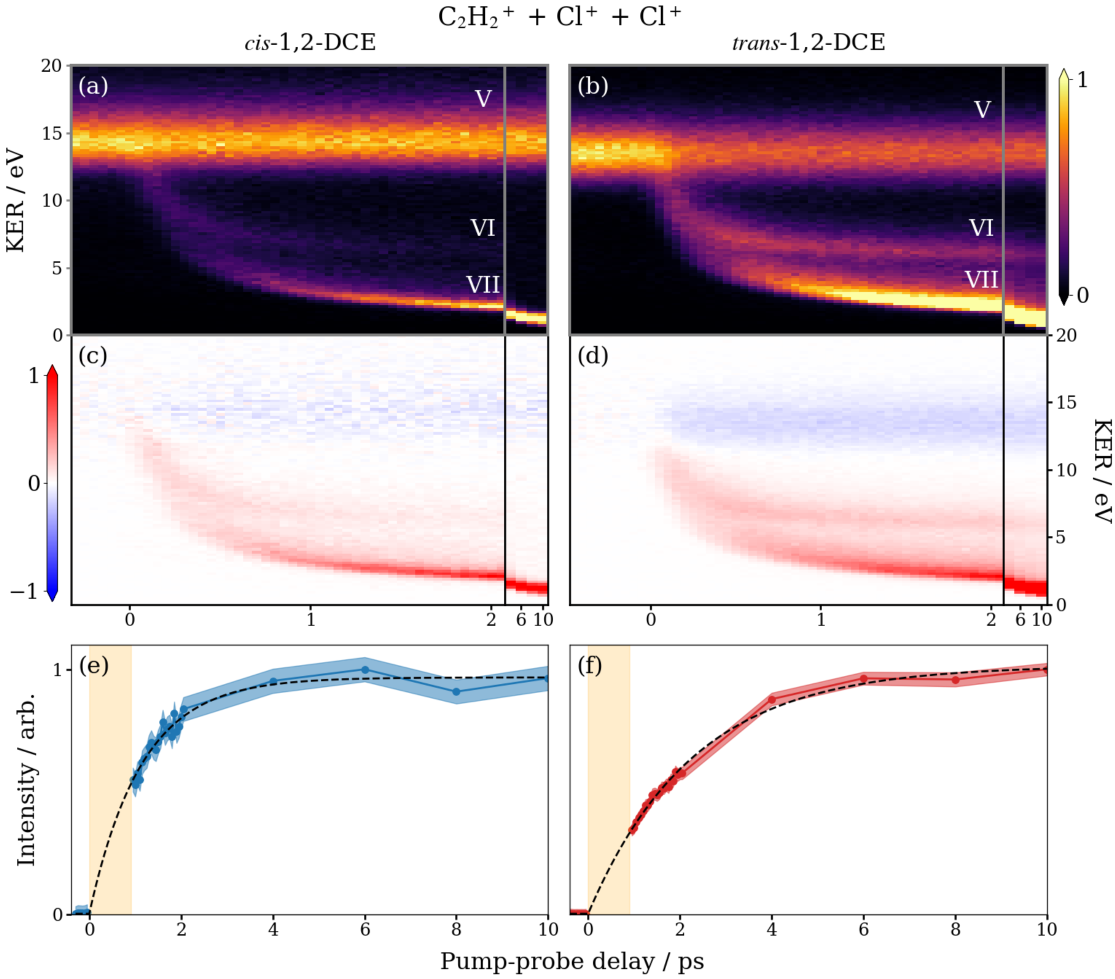

Figure 8.7: Time-resolved total KER distribution for the three-body breakup of (a) *cis*- and (b) *trans*-1,2-DCE^{3+} into $C_2H_2^+ + 2Cl^+$, normalised to the peak intensity of the probe-only channel. The labelled features are discussed in the main text. UV late subtracted plots are displayed below in panels (c) and (d), normalised to the peak intensity at pump-probe delay < 2.1 ps. (e, f) Integrated ion yields for the low KER feature (VII), fit using the model described in the text. The orange shaded regions indicate the delay range where data points cannot be extracted due to overlap between channels VI and VII.

This area of the analysis remains a work in progress. Future work will focus on techniques to disentangle overlapping channels, such as channels VI and VII, and improving the fitting functions. It would also be interesting to consider how the absolute yields of the various channels compare. For example, the yield of channel VII should rise in proportion to the decline in the combined yields of channels III and VI.

8.3.2 HCl elimination

Panels (a) and (b) of Figure 8.8 present the delay-dependent total KER of the C_2HCl^+ + HCl^+ coincidence channel for *cis*- and *trans*-1,2-DCE. These coincidence maps exhibit the same features: (i) a horizontal band of Coulomb explosion events:

$$C_2H_2Cl_2 \xrightarrow{nh\nu_{\mathrm{NIR}}} C_2HCl^+ + HCl^+, \tag{II}$$

and (ii) a broad distribution of low KER events, linked to HCl elimination:

$$C_2H_2Cl_2 \xrightarrow{h\nu_{\mathrm{UV}}} C_2HCl + HCl \xrightarrow{nh\nu_{\mathrm{NIR}}} C_2HCl^+ + HCl^+. \tag{IV}$$

This later feature is only seen clearly in the UV late subtracted distributions in panels (c) and (d). The relative intensity of the two features is different for the isomers, but their form matches exactly. Previous work found that the product energies of HCl elimination are the same for all three isomers of DCE, which is attributed to memory loss of the original geometry due to atom migration.[223]

The elimination of HCl produces a Coulomb curve that appears to be smeared towards higher KER. This form is attributed to two factors. First, the exact time at which HCl separates varies considerably from event to event, so the feature is in essence the combination of manifold Coulomb curves, each with a unique time offset. Second, the velocity distribution of the products of HCl elimination is broad. Those products with low velocity separate much slower and so experience greater Coulomb repulsion. This means that each of the many intersecting Coulomb curves has a different gradient and asymptotic value. The values quoted in Table 8.2 were measured from the peak of the total KER distributions at the longest delay time used in these experiments (10 ps).

The enhancement for the C_2HCl^+ + HCl^+ coincidence channel was fit to the product of an exponential rise and a Heaviside step function. Corresponding plots are shown in panels (e) and (f) of Figure 8.8. This yielded a rise time of 1.1 ± 0.1 ps for *cis* and 1.6 ± 0.1 ps for *trans*. Judging by the noise in panel (c), the error on the former value is likely an underestimate. The measured reaction time reinforces the idea that HCl elimination involves internal conversion to a lower-lying electronic state.

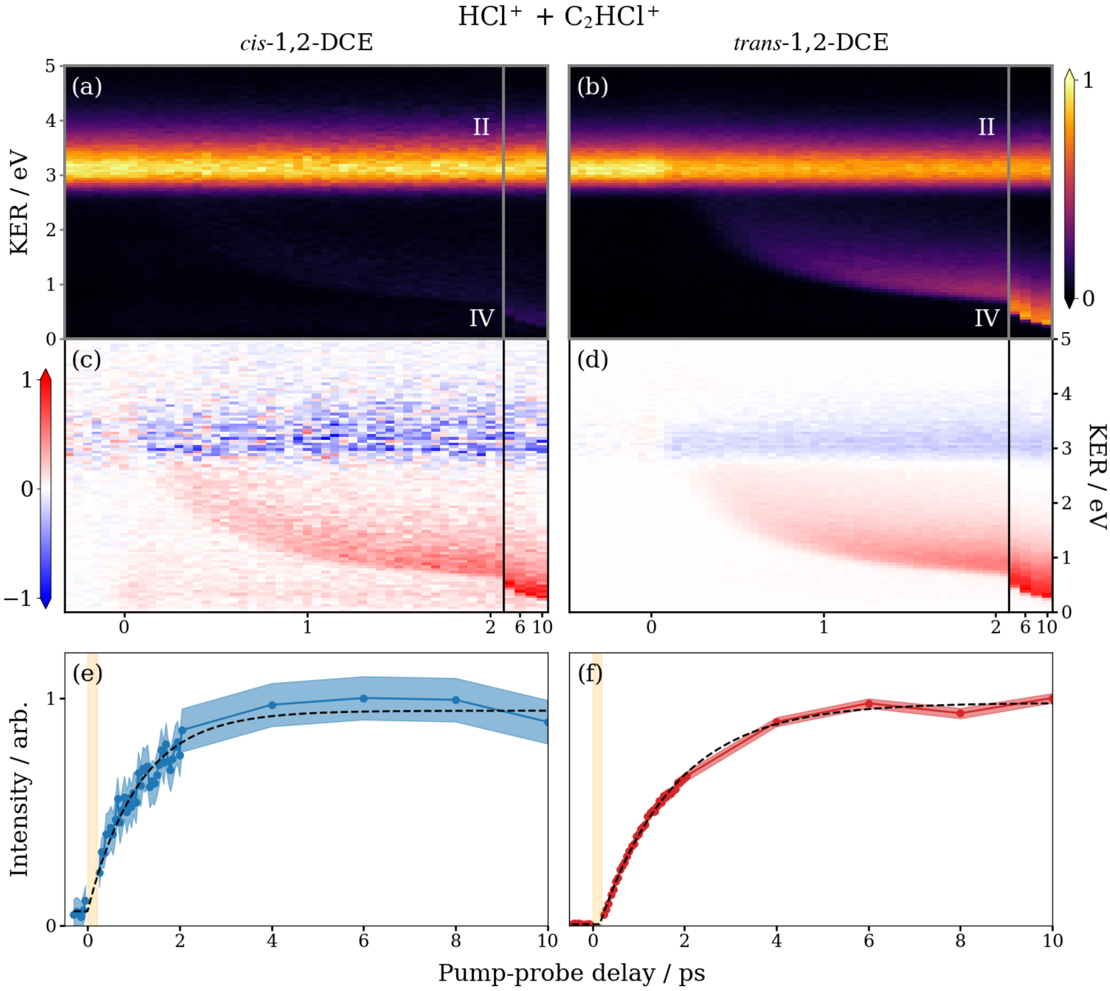

Figure 8.8: Time-resolved total KER distribution for the two-body breakup of (a) *cis*- and (b) *trans*-1,2-DCE^{2+} into $C_2H_2Cl^+$ + HCl^+. UV late subtracted plots are displayed below in panels (c) and (d). (e, f) Integrated ion yields for the low KER feature (IV), fit using the model described in the text. The orange shaded regions indicates the pump-probe delay range where data points cannot be extracted due to overlap with the probe-only channel.

8.3.3 Re-evaluation of previous results

With the information now available, the results presented in Section 7.3.1 can be re-evaluated. In that study, the Cl and HCl elimination channels for *trans*-1,2-DCE could not be resolved, so the TR KER distribution that was extracted (Figure 7.2) is equivalent to the sum of Figure 8.4(b) and Figure 8.8(b). It makes sense that the

Coulomb explosion channels (I and II) could not be distinguished as their KERs are nearly equal at $3.2 \pm 0.3\,\mathrm{eV}$ and $3.3 \pm 0.3\,\mathrm{eV}$. The Cl and HCl elimination channels (III and IV) also overlap within the first few picoseconds, though not completely, which explains why the observed Coulomb curve was broad. Following a rapid initial rise, the yield of channel III decays at roughly the same rate that the yield of channel IV rises. When combined they produced a trace that appeared to plateau. Hence, the previous experiment was blind to the secondary dissociation of C_2H_2Cl.

8.4 Ultrafast torsional dynamics

The introduction to this work highlighted that the (π, π^*) state is predicted to have a potential minimum at a Cl–C–C–Cl dihedral angle of 90°. Therefore, ultrafast C–C torsion is expected to follow from photoexcitation. The results in Section 7.3.2 hinted at this motion, but without the capability to correlate the momenta of more than two fragment ions the interpretation of the data was ambiguous. Using multi-particle coincidence analysis offers more detailed structural information that can shed light on the underlying nuclear dynamics. This begins with an examination of the nuclear dynamics of Cl elimination. The primary C–Cl bond cleavage has been already identified as a rapid process, so it raises the question as to whether the structure of molecules changes beforehand.

8.4.1 $C_2H_2{}^+ + Cl^+ + Cl^+$ coincidence

Figure 8.9(a) shows the total KER spectrum of the $C_2H_2{}^+ + Cl^+ + Cl^+$ coincidence channel for *trans*-1,2-DCE at a pump-probe delay of $\sim$2 ps. The three peaks correspond to the three fragmentation channels identified in Figure 8.7 and are labelled accordingly. In the same way that a coincidence channel is isolated by filtering on the sum of the ion ToFs, coincidence events linked to a particular fragmentation channel are then obtained by filtering on the sum of the ion KEs. As an example, the KER range used to isolate channel VI is highlighted in blue on the figure.

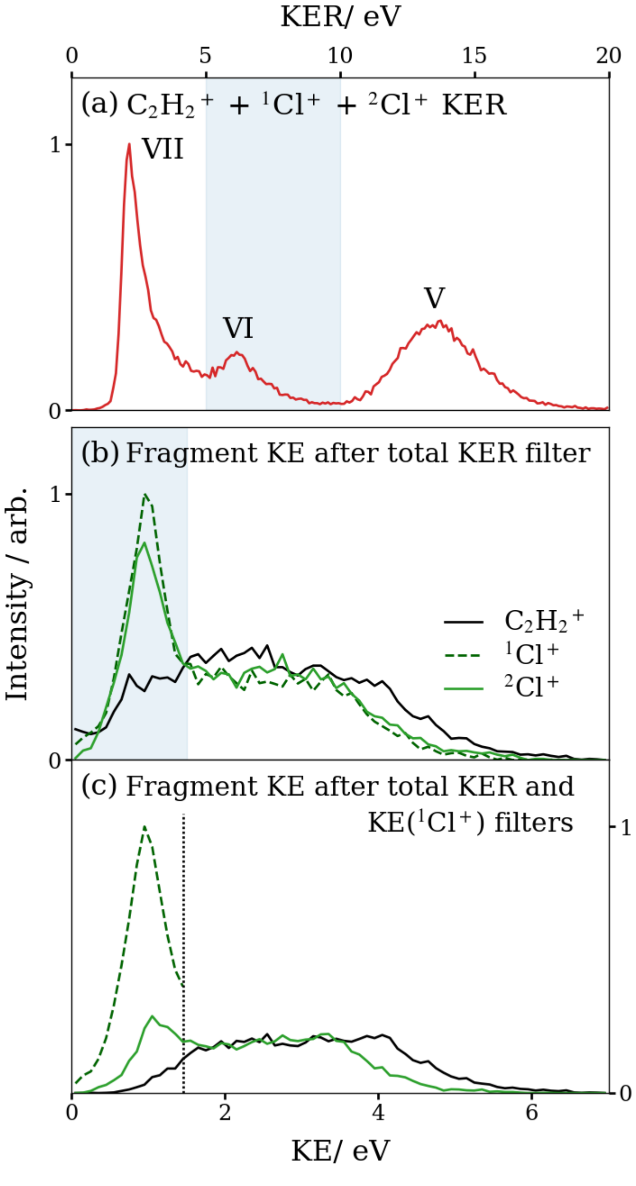

Figure 8.9: (a) Total KER distribution for the three-body breakup of *trans*-1,2-DCE^{3+} into $C_2H_2{}^+$ + 2Cl$^+$ when the UV pulse is early (1.8–2.1 ps). The labelled features correspond with those in Figure 8.7. (b) Individual fragment KE distributions for coincidence events with a total KER between 5–10 eV (the shaded region in (a)). Distributions are normalised to unit area. In panel (c) events have been furthered filtered by selecting those where the KE of the first detected Cl$^+$ is $<$ 1.5 eV.

Briefly, it is worth discussing channel V – the triple ionisation and Coulomb explosion of molecules that are not dissociated by pump pulse. If the UV photoexcitation of *trans*-1,2-DCE induced isomerisation, resulting in the formation of stable *cis* isomer, it would be expected to manifest in the correlated fragment momenta for this channel (see Section 6.3.2 for details). However, no change in the $C_2H_2^+$ + Cl^+ + Cl^+ momenta was observed across the pump-probe delay range studied here. This agrees with the conclusion of Ewbank *et al.* that for 1,2-DCE, in the absence of collisions, *cis*-*trans* isomerisation does not compete with dissociation.

The focus of this section is channel VI – the neutral photodissociation of *trans*-1,2-DCE into C_2H_2Cl + Cl, followed by single ionisation of Cl and double ionisation of C_2H_2Cl, which subsequently Coulomb explodes into $C_2H_2^+$ + Cl^+. The correlated fragment momenta for this channel at a pump-probe delay of ∼2 ps are plotted in a Newton diagram in Figure 8.10. The diagram consist of a pair of arcs overlapped by another pair of irregular features. Disentangling these overlapping contributions requires careful consideration of ‘which’ Cl^+ is chosen as reference: the ‘primary’ Cl^+ product that corresponds to the initially detached Cl, or the ‘secondary’ Cl^+ product from the Coulomb explosion of $C_2H_2Cl^{2+}$.

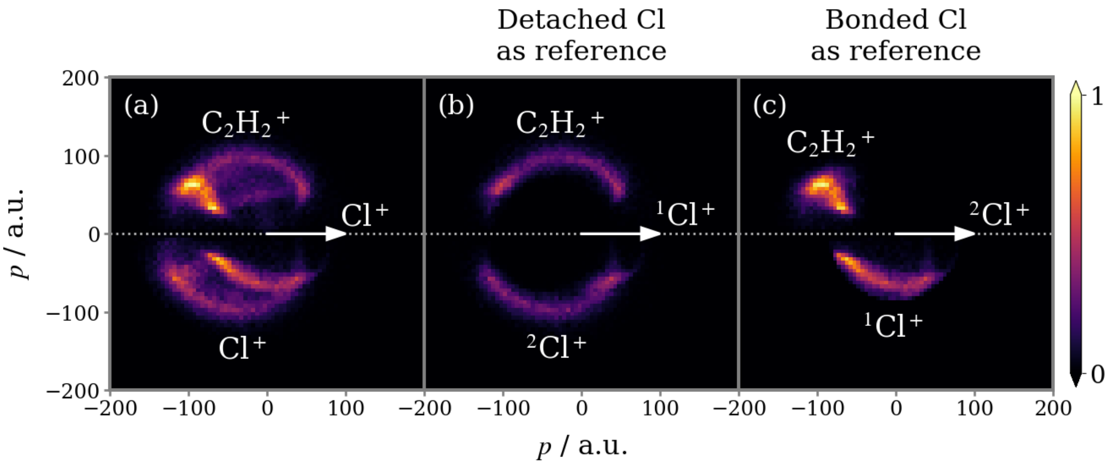

Figure 8.10: Newton diagrams for channel VI: the neutral photodissociation of *trans*-1,2-DCE into C_2H_2Cl + Cl, followed by single ionisation of Cl and double ionisation of C_2H_2Cl, which subsequently Coulomb explodes into $C_2H_2^+$ + Cl^+. The correlation map in (a) has contributions from events in which the isolated Cl^+ is the reference species, and those in which Cl^+ from the Coulomb explosion of $C_2H_2Cl^{2+}$ is the reference. These signals are separated in panels (b) and (c).

To explain, consider the individual fragment KE spectra for channel VI, presented in Figure 8.9(b). The Cl^+ fragments are distinguished by the order in which they were detected, though their KE distributions match. The sharp peak at low KE is attributed to primary Cl^+ product, whose energy derives solely from the neutral photodissociation step (at this delay). The KE of the secondary Cl^+ product is determined by the primary photodissociation and secondary Coulomb explosion. These contributions sum to give a broad distribution, with higher average KE.

Requiring that the first detected chlorine ion ($^1Cl^+$) is the primary product by constraining its KE dictates that the second detected chlorine ion ($^2Cl^+$) must be the secondary product, and vice versa. For demonstration, panel (c) is assembled from the subset of coincidence events where the KE of the first detected Cl^+ is below 1.5 eV. Panels (b) and (c) of Figure 8.10 are Newton diagrams where either the primary or secondary Cl^+ is chosen as the reference species, which completely separates the overlapping features seen in panel (a).

With the primary Cl^+ product as reference, the Newton diagram is the more intuitive representation. The arcing features are reminiscent of a distribution produced by the sequential three-body breakup of a molecular trication. C–Cl bond cleavage induces rotation of the ethyl chloride radical before it is ionised and Coulomb explodes, causing the momenta of $C_2H_2^+$ and $^2Cl^+$ to be distributed over an angular span relative to $^1Cl^+$. It is important to understand that, compared to the sequential breakup mechanism of a molecular polycation, the relative timing of the two dissociation steps for channel IV is well defined by the delay between the pump and probe laser pulses. The fact that the intensity is uniform across the angular range implies that the rotational period of C_2H_2Cl is significantly shorter than the pump-probe delay, such that it is effectively randomly rotated at the instant of Coulomb explosion. The truncated form of the two arcs, *i.e.* they do not extend to the horizontal axis, can be linked to the structure of the excited molecule at the instant that the C–Cl bond is broken.

The Newton diagram in Figure 8.10(b) was transformed into the CoM frame of the Coulomb explosion of $C_2H_2Cl^{2+}$ using the native frames analysis approach, and is re-plotted in Figure 8.11(a) as a function of the KER in this frame and the relative recoil angle of the Cl^+ ions ($\theta_{(Cl^+,Cl^+)}$). Assuming the geometry of *trans*-1,2-DCE is unchanged when it dissociates, an impulse along the C–Cl bond will cause C_2H_2Cl to rotate in the plane of the original molecule. The result of a simulation of this scenario is presented in the adjacent panel (b). TR-CEI data were simulated using the model described in Section 4.5.1, modified to incorporate a distribution for the separation of the charges on $C_2H_2{}^+$ and Cl^+ that reflects the measured KER of the Coulomb explosion.

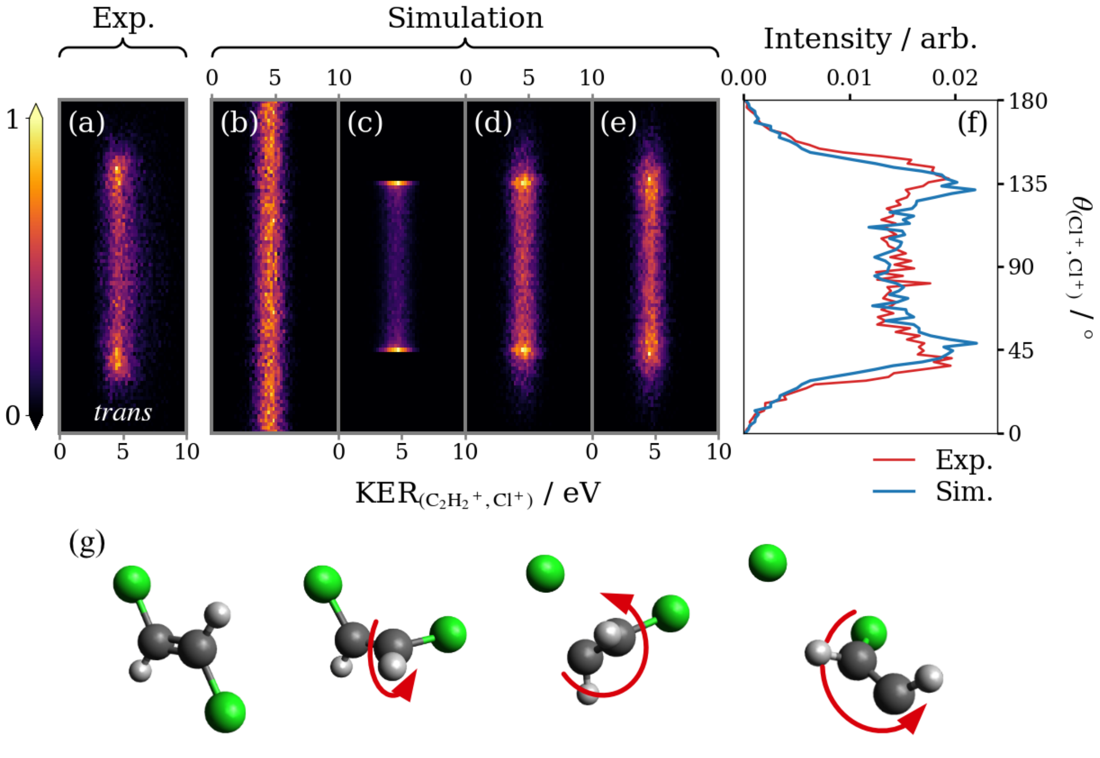

Figure 8.11: (a) The data from Figure 8.10(b) transformed into the CoM frame of $C_2H_2Cl^{2+}$ and displayed in polar coordinates, where KER$_{(C_2H_2{}^+,Cl^+)}$ is the KER of the Coulomb explosion of $C_2H_2Cl^{2+}$ and $\theta_{(Cl^+,Cl^+)}$ is the relative recoil of the Cl^+ ion pair. (b–e) Simulated correlation maps for channel VI. (b) is initiated from the equilibrium geometry of *trans*-1,2-DCE and (c) from an orthogonal twisted geometry, as described in the text. (d) Incorporates a distribution of torsional angles. (e) Also models slight variation of other molecular coordinates. (f) Integrated angular distributions for the experimental and final simulated data. (g) Schematic diagram of the rotation of the ethyl chloride dication with respect to the emission direction of Cl.

Because the fragments are confined to the plane of the original molecule in the simulation, the secondary Cl^+ can be ejected at any angle relative to the recoil direction of the primary product. The result is a uniform $\theta_{(\mathrm{Cl}^+,\mathrm{Cl}^+)}$ distribution in this frame. The discrepancy with the experimental data implies that rotation of ethyl chloride is not in-plane. Panel (c) is the result of a simulation of the scenario illustrated schematically in (g), that is, where the molecules relaxes on the (π, π^*) PES to a geometry in which the CHCl groups are twisted at 90° prior to dissociation. To recreate this process, the simulation is initiated from the orthogonal twisted geometry. Because rotation of $\mathrm{C_2H_2Cl}$ never orients the attached Cl atom directly towards or away from the detached Cl atom, the simulated $\theta_{(\mathrm{Cl}^+,\mathrm{Cl}^+)}$ distribution is truncated at high and low angle, similar to the experimental data.

It is reasonable to expect that torsion about the C–C bond axis will produce an ensemble of twisted geometries, where 90° is the most likely angle. Therefore, the simulation was repeated and for each trajectory the Cl–C–C–Cl dihedral angle in the starting geometry was sampled from a Gaussian distribution with a central value of 90° and a width of 45°. In panel (d) this has blurs out the sharp features at the turning points, which markedly improves the resemblance to the experiment data. Finally, the simulation in panel (e) also models slight variation in the molecular geometry due to other motions, including C–Cl symmetric/antisymmetric stretching, Cl–C–C–Cl scissoring and C–C–Cl bending. The end result is an excellent qualitative agreement between simulation and experiment.

The success of a model that invokes C–C torsional motion in reproducing the correlated fragment momenta for this channel is strong evidence that *trans*-1,2-DCE undergoes structural rearrangement to a non-planar geometry following excitation in its (π, π^*) absorption band. The nuclear motion must be rapid if it precedes C–Cl bond cleavage, which was clocked at $133 \pm 7\,\mathrm{fs}$. Previous authors postulated that rearrangement to a twisted geometry could access a conical intersection with the ground PES, analogous to the $\pi^* \leftarrow \pi$ excitation dynamics of ethene. The findings of the current work suggest that structural rearrangement is also a precursor to surface crossing to the repulsive PES on which Cl elimination takes place.

8.4.2 $C^+ + C^+ + Cl^+ + Cl^+$ coincidence

Having found evidence for torsional motion of 1,2-DCE on the (π, π^*) PES, the natural next question is whether this motion can be perceived in real time. The best approach for tracking changes in molecular structure using TR-CEI is to monitor the Coulomb explosion of highly charged parent ions that fully fragment, as the initial atomic positions are mapped onto the final fragment momenta in a straightforward manner. As a demonstration, Figure 8.12 depicts the 3D correlated momentum distribution of $C^+ + C^+ + Cl^+ + Cl^+$ from the Coulomb explosion of *cis* and *trans*-1,2-DCE, induced solely by NIR laser pulse.

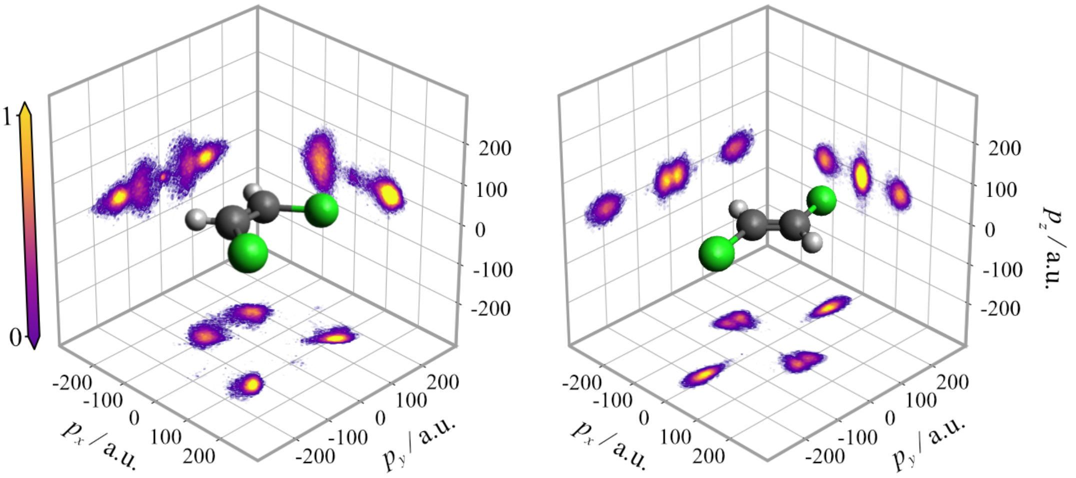

Figure 8.12: 2D projections of the 3D correlated momenta of $C^+ + C^+ + Cl^+ + Cl^+$ from the Coulomb explosion of (*left*) *cis*- and (*right*) *trans*-1,2-DCE.

There are many ways in which to represent multi-dimensional correlated momentum distributions. Here, the frame of reference introduced in Chapter 6 for visualising the correlated 2D fragment momenta from the Coulomb explosion of 1,2-DCE is extended to three dimensions. The y-axis is defined by the relative momentum of the Cl^+ ions $((\vec{p}_{\mathrm{Cl}^+,1} - \vec{p}_{\mathrm{Cl}^+,2})$, and the xy-plane by the relative momentum of the C^+ ions $((\vec{p}_{\mathrm{C}^+,1} - \vec{p}_{\mathrm{Cl}^+,2})$. In each panel of Figure 8.12, the 3D correlated momentum distribution is projected onto the xy, xz and yz planes. The nuclear structure of each isomer is superimposed at the origin. Immediately, the resemblance between the correlated fragment momenta and the atomic positions of C and Cl in each isomer is striking.

The $C^+ + C^+ + Cl^+ + Cl^+$ coincidence channel is not suitable for dissecting the nuclear dynamics that unfold on a long timescale as the many competing photodissociation channels of 1,2-DCE cannot be cleanly separated in the way achieved in the previous section. However, it is an effective probe of the molecular structure on a short timescale, before many excited molecules dissociate. Within the first few hundred femtoseconds after $\pi^* \leftarrow \pi$ excitation the only photodissociation channel that needs to be considered is cleavage of a C–Cl bond.

Figure 8.13 presents delay-dependent angular distributions for the $C^+ + C^+ + Cl^+ + Cl^+$ coincidence channel. This includes the relative recoil angle of the Cl^+ ion pair ($\theta_{(Cl^+,Cl^+)}$) and C^+ ion pair ($\theta_{(C^+,C^+)}$). In order to concentrate on the short term dynamics, the plots span the narrow pump-probe delay range where ion images were acquired in fine (25 fs) steps. Both distributions are dominated by a strip of intensity close to 180°. In the planar geometry of *trans*-1,2-DCE the charges on the C and Cl atoms are essentially arranged in a quadrilateral. The mutual repulsion of the ions causes them to recoil into four corners, such that the two Cl^+ ions recoil in opposite directions, as do the two C^+ ions. Inspecting the UV late subtracted plots, a broad obtuse angle component is seen at positive pump-probe delay in the $\theta_{(Cl^+,Cl^+)}$ distribution, and a similar feature in the $\theta_{(C^+,C^+)}$ distribution. Both features are inherently linked to the same change in nuclear geometry induced by the UV pulse.

Drawn on panels (b) and (e) are the results of a classical simulation of the Coulomb explosion of each isomer in its ground state equilibrium geometry, as well as a geometry with a 90° Cl–C–C–Cl dihedral angle. In general, the comparison between the enhancement in each distribution and the calculated values supports the theory that torsional motion on the (π, π^*) PES generates an ensemble of twisted, non-planar geometries. The region of enhancement in each plot covers an angular span above the calculated value for *cis*-1,2-DCE, which encompasses the calculated value for the twisted orthogonal geometry. The *cis* geometry represents the closest that the Cl atoms can approach through molecular torsion, and therefore should correspond with the lower boundary of $\theta_{(Cl^+,Cl^+)}$ and $\theta_{(C^+,C^+)}$.

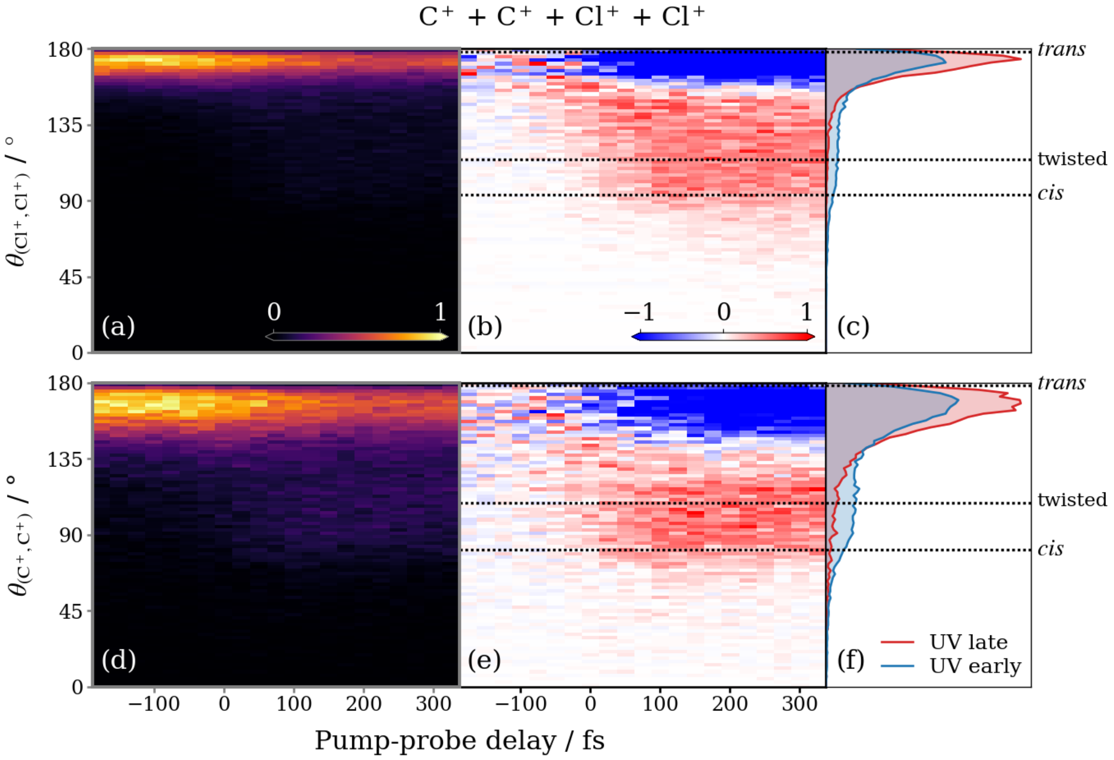

Figure 8.13: Time-resolved relative recoil angle distributions for the Coulomb explosion of *trans*-1,2-DCE that yields $2C^{+} + 2Cl^{+}$. Panel (a) plots the recoil angle between the Cl^{+} ion pair, and (d) the angle between the C^{+} ion pair. UV late subtracted plots are displayed in the adjacent column. Angular distributions integrated across UV late (< -100 fs) and UV early (> 100 fs) pump–probe delays are projected in panels (c) and (f). Distributions are normalised to unit area. Horizontal dotted lines indicate values predicted by Coulomb explosion simulations initiated from different starting geometries.

Assuming that the structural change is associated with molecular torsion, one might expect to see oscillations in the angular distributions as a function of pump-probe delay. The lack of any such features implies that either the wave packet decoheres within a vibrational period, or more likely that the vibrational period is shorter than the instrument response function. There is some structure in the rising component in the $\theta_{(Cl^{+},Cl^{+})}$ distribution, which expands down from 180° until it reaches its full angular span. The profile is undoubtedly obscured by the limited temporal resolution. Nevertheless, the results suggest that the Cl–C–C–Cl backbone of the molecule adjusts within approximately 100 fs – surprisingly fast given how heavy the Cl atoms are.

The rise of the enhancement in each plot appears to coincide with temporal overlap, indicating that either there is no barrier to structural rearrangement, or that the barrier is easily surmounted. This observation is also consistent with structural change occurring prior to Cl elimination, which displays a time offset. Interestingly, the angular distributions do not perceptibly change after the dissociation is known to occur, demonstrating that rotation of C_2H_2Cl does not significantly affect the fragment recoil distribution for at least 200 fs.

Future simulation work should focus on predicting the dihedral angle distribution based on the measured angular distributions. The calculated values for the three different geometries demonstrate that the relationship between dihedral angle and relative recoil angle is non-linear, *i.e.* the Coulomb explosion of a molecule twisted halfway between *cis* and *trans* produces a fragment momentum distribution that bears more resemblance to the structure of the *cis* isomer. Hence, even though the intensity is roughly constant across the angular span of the pump-probe features, this does not correlate with a geometry ensemble that has a uniform dihedral angle distribution. It is also important to considered other plausible scenarios, such as pyramidalisation of the CHCl end groups and out-of-plane adjustment of the hydrogen atoms.

8.5 Conclusions and future work

The photoexcitation dynamics of the *cis* and *trans* isomers of 1,2,DCE have been studied at 198 nm. The results presented are a work in progress as the data analysis is ongoing. Much of the analysis methodology needs refinement and there are many avenues for investigation that are yet to be explored. Coincident detection of the photodissociation products was used characterise the Cl elimination and HCl elimination processes. The former process is observed to proceed mainly via a two-step mechanism, involving cleavage of both C–Cl bonds. The first event is prompt and imparts high KE, while the second event on average takes several picoseconds and imparts minimal KE. The reaction time for HCl elimination is also on the order of picoseconds.

Future work will search for signatures of the other reported photodissociation channels of 1,2-DCE in the dataset, including Cl_2 elimination, H atom detachment and H_2 elimination. The advantage of TR-CEI with a SFI probe compared to other techniques that have been used to study the photodissociation dynamics of 1,2-DCE is that it is capable of detecting all of the photofragment species simultaneously. Exploiting this fact, it would be interesting to analyse the coincidence yield of competing photodissociation channels in order to establish branching ratios, and hence formulate a view of the global dynamics.

trans-1,2-DCE undergoes ultrafast structural rearrangement on the (π, π^*) state, ascribed here to torsion about the C–C axis into a twisted, non-planar geometry, though it should be stressed that further work is needed to substantiate this claim. This structural change precedes the C–Cl bond cleavage and manifests in the dynamics of the dissociation, including how the C_2H_2Cl moiety rotates relative to the departing Cl atom. Future analysis should focus on the nuclear dynamics of other dissociation channels. For example, evidence suggests that HCl elimination follows from atom migration processes that scramble the different 1,2-DCE isomer geometries. A detailed analysis is also needed for *cis*-1,2-DCE.

To fully comprehend the photoinduced molecular dynamics more simulation work is required. Here, inferences were made by assuming the structural change and simulating the Coulomb explosion dynamics for a representative ensemble of geometries. This is a helpful guide for interpreting what molecular motions might play a role, but does not predict the time-evolving nuclear structure. A more informative method is to model the molecular dynamics using *ab initio* calculations[31,185,186] and sample the geometry at regular intervals throughout to perform a Coulomb explosion simulation. In this way the TR correlated fragment momentum distribution can be simulated. Efforts to simulate the molecular dynamics of this system are currently underway by a fellow student in the Brouard group.

Performing the same experiment back-to-back at two different facilities provides the unique opportunity to compare the experimental set-ups and weigh up their respective strengths and weaknesses. In this case, judging the quality of the data by the insight that results provide, the TR-CEI instrument in the James R. MacDonald laboratory is the superior apparatus. Learning from the design of this instrument, there are a number of ways in which the Oxford spectrometer can be improved without needing to change its fundamental components, including the laser system, optical set-up, vacuum chamber and ion optics.

The first factor that sets the COLTRIMS spectrometer apart is the ability to perform 3D momentum imaging. The Oxford spectrometer is unable to record 3D ion momenta due to the limited time stamping precision of the PImMS2 camera, but this is set to change soon. At the time of writing, a Txp3cam is being tested on the Oxford spectrometer for 3D momentum imaging. The increased timing resolution of the Txp3cam should also make it possible to resolve fragment correlations where one of the fragments differ by a single hydrogen mass.

The other key factor that differentiates the experiments conducted in Kansas is that they typically operate at much lower ion count rate and rely on measuring the fragment ions in coincidence. As demonstrated in Section 8.4.2, examining the correlated momenta of a higher number of fragments is crucial for extracting more detailed structural information, and using coincidence mapping this is straightforward to calculate. The Oxford spectrometer is typically operated at much higher ion count rate, necessitating covariance analysis. However, with the current suite of analysis routines the highest-fold correlation than can be calculated is between three fragments. To explore higher-order correlations cumulant mapping mapping will need to be implemented.

Even so, it is likely that data acquired using the Oxford spectrometer will need to be acquired at lower count rate in order to facilitate the measurement of higher order fragment correlations, *i.e.* several rather than several hundred ions of interest per shot. See Section 3.8 for a full discussion. Fortunately, the Txp3cam runs continuously, and so the detection system will no longer limit the experimental repetition rate. Provided an appropriate molecular beam source is installed, experiments could be run at the 1 kHz repetition rate of Ti:Sapphire laser system in order to compensate for a reduced ion count rate.

9

Conclusions and outlook

In this thesis, results have been presented from a range of experimental studies that investigated the photoinduced molecular dynamics of small molecules in the gas phase. Ion imaging techniques including VMI and COLTRIMS were used to measure the momenta of ionic fragments produced by the interaction of molecules with femtosecond laser pulses. A key aspect of the data analysis was the application of coincidence/covariance mapping to inspect the correlated momenta of multiple ions that arise from the breakup of same molecule. This was primarily used to monitor the relative recoil directions of the fragments from a molecular Coulomb explosion, which provides insight into the original molecular structure.

CEI is a powerful method for determining static nuclear structure, demonstrated here for distinguishing the isomers of IP, and the isomers of 1,2-DCE. The beauty of the technique lies in how the molecular configuration can be visualised directly from the measured fragment momenta, which makes the data clear and comprehensible even for a layman. For example, the correlated momentum maps measured for the Coulomb explosion of *cis*- and *trans*-1,2-DCE show striking resemblance to the atomic positions of C and Cl in each isomer. Further, combining CEI with pump-probe spectroscopy offers a straightforward means of monitoring molecular structure on a femtosecond timescale. This approach was applied here to identify structural rearrangement in photoexcited *trans*-1,2-DCE.

In order to fully exploit CEI as a structural probe, a detailed understanding of the many-body fragmentation dynamics of polycations is essential. Working towards this goal, Chapter 5 examined the fragmentation behaviour of iodopropane dications and trications. The analysis was a showcase for how multiple competing fragmentation pathways can be disentangled using a tailored correlation mapping approach that considers the momentum partitioning between fragments. The work highlighted how future studies would benefit from recording the photoelectrons and fragment ions in correlation, in order to explore the relationship between ionisation and fragmentation dynamics. Chapter 6 provided insight into the progression from fragmentation dynamics where the chemical bonding plays an important role, to dynamics dominated by Coulombic interactions with increasing charge. More studies are needed to identify the ways in which this varies with molecular size and composition.

Ab initio electronic structure and molecular dynamics calculations for molecular polycations is a significant theoretical challenge given the many electronic states populated by ionisation in an intense laser field, and the diverse range of possible fragmentation pathways. Hence, the present work relied upon classical trajectory calculations of point charges interacting exclusively under Coulomb's law to provide insight into the behaviour of the fragment ions during Coulomb explosion. Despite the simplicity of the model, it proved remarkably successful at reproducing the experimental signatures of a variety of observed fragmentation channels. The base model provides a good description of the Coulomb explosion dynamics of highly charged molecular polycations. Through appropriate modifications, more complex fragmentation processes could be simulated, including the sequential three-body breakup of doubly and triply charged species. A future study that compares experimental data, the predictions of the simple model employed here, and the predictions of a comprehensive model that considers all the relevant chemical binding forces, would be of great interest. Such an investigation could help identify scenarios in which the purely Coulombic model is appropriate, versus where other forces are important.

A new TR-CEI instrument in the Brouard group laboratory at the University of Oxford has been introduced. Results were presented from characterisation experiments, followed by an investigation into the photoinduced molecular dynamics of a new system of study. The instrument is fully functioning, however, a number of improvements are needed to achieve comparable results to leading experiments, such as the TR-CEI instrument in the James R. MacDonald laboratory at Kansas State University. This includes implementing a detection system with higher timing precision, making it possible to reconstruct the complete 3D momentum information for each ion. It is also important to upgrade the detection system and molecular beam source so that they can match the 1 kHz repetition rate of the Ti:Sapphire laser system. Acquiring data at a higher repetition rate will make it feasible to operate under conditions where on average fewer parent molecules are ionised per laser pulse, which is anticipated to be critical for determining higher order fragment correlations.[156] To calculate four fold and potentially higher-order correlations, cumulant mapping can be used.[176]

TR-CEI is a developing technique that, so far, has mainly been applied to study simple photodissociation processes in small molecules. The scope of experiments is expected to increase over the next decade as researchers turn their attention towards molecules with more complex photochemistry. For example, the UV photolysis of 1,2-DCE, involving structural rearrangement and multiple competing photodissociation pathways, makes it amongst the most complicated molecular dynamics yet studied using TR-CEI. Nevertheless, the prospects for the ongoing analysis are exciting. The data should provide detailed insight into all of the dissociative processes, including any isomeric differences.

The natural trend within the field of TR-CEI is to scale up to larger molecular targets, gradually working towards chemical systems with practical applications. This raises the question as to how large of a molecule is feasible to study using the technique. The main obstacle is photoionising the molecule to a high enough charge state that fragmentation is dominated by Coulomb repulsion, and the initial atomic positions map onto the final fragment momenta in a straightforward manner.

It is also crucial that the probe pulse duration is kept as short as possible since large molecules are more flexible, and therefore more susceptible to structural distortions within the time window of the ionisation process. For experiments that use a NIR probe pulse, additional measures to achieve sub-10 fs pulses such as spectral broadening in a hollow core fiber and pulse compression might be essential.[59] The latest generation of X-ray FELs are already capable of producing few femtosecond pulses.[232]

The Coulomb explosion of a larger molecule will inherently yield more fragment ions, so it becomes a challenge to measure enough fragments in correlation to be able to accurately monitor the molecular structure. The probability of detecting n ions from a single dissociation event decreases exponentially as n increases due to imperfect detection efficiency. Therefore, it will be important to maximise detection efficiency through measures such as installing funnel MCPs.[117,118] Experiments can also compensate by increasing sampling rate through the use of high repetition rate laser sources, such as PULSAR in the James R. MacDonald laboratory.[132] The next generation of X-ray FELs are capable of delivering pulses at an effective repetition rate of several kHz.[90] The ultimate limit is around 100 kHz because the time interval between laser pulses starts to become shorter than span of the ToF spectrum, causing ions generated in separate laser shots to overlap.

Due to their limited multi-hit capacity, DLA detectors may not be suitable for CEI of larger molecules. The technology will likely be superseded by fast time-stamping cameras that offer comparable temporal and spatial resolution, but essentially unlimited multi-hit capacity, such as Timepix4.[128] The innately higher ion count rate may also render coincidence analysis ineffective. At present, cumulant mapping seems the more practical way forward for extracting high-order particle correlations, but the technique has not been tested beyond an initial demonstration.[176] In the future, a study that compares the convergence of the n-fold coincidence map and nth cumulant map as a function of ion count rate would be of great interest.

Appendices

A

Oxford spectrometer calibrations

A.1 Peak laser intensity calibration

When conducting a CEI experiment where the target molecules are ionised by SFI, the key parameter that dictates the ionisation conditions is the peak laser intensity. For details, see Section 1.4.1. The peak intensity is proportional to the pulse energy, inversely proportional to the pulse duration, and inversely proportional to the square of the focused beam diameter. Of these parameters, the pulse energy is by far the easiest to change on-the-fly, *e.g.* using a variable attenuator. It is also straightforward to measure using an optical power meter. Therefore, it is important to establish a calibration between pulse energy and peak intensity.

Assuming a Gaussian beam profile, it is possible to estimate the peak intensity from the measured pulse energy, pulse duration and focused beam width (determined from the unfocused beam width and knowledge of the focusing geometry).[233] A number of free calculators are available online for this purpose. However, the more accurate method is to measure the intensity of the electric field at the interaction of the spectrometer *in situ*. There are several established methods for doing so.[166,234,235] Here, the peak laser intensity was intrinsically calibrated from the ponderomotive shift of the ATI peaks in the photoelectron spectrum of argon, following the method described in Reference [236].

A neat beam of argon was expanded into the spectrometer and intersected by the 800 nm fundamental output of the Ti:Sapphire laser system. The spectrometer was operated with negative voltages applied to the ion optics in order to project nascent photoelectrons towards the detector. The repeller and extractor plates were held at -8.00 and -6.02 kV, respectively, while the other plates were grounded. Photoelectron images were recorded for 5 μJ NIR pulse energy increments across a range from 60 – 120 μJ. An example photoelectron image is shown in Figure A.1. The distribution is complex, but two kinds of features can be distinguished along the (vertical) laser polarisation axis: (i) sharp features known as Freeman resonances[61] and (ii) broad features that repeat with with integer multiples of the photon energy (1.55 eV), caused by ATI.

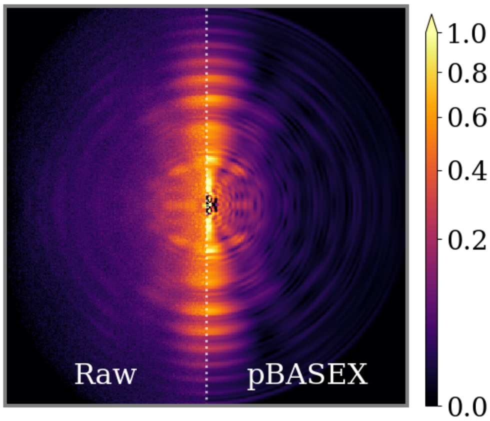

Figure A.1: Example photoelectron image for Ar exposed to a NIR pulse with an energy of 75 μJ, corresponding to a peak intensity of $7.5 \times 10^{13}\,\mathrm{W\,cm^{-2}}$. The laser polarisation axis was vertical in this image. The left and right halves show the raw and pBASEX inverted image, respectively.

Figure A.2(a) is a plot of the photoelectron kinetic energy (KE$_e$) spectrum extracted from each pBASEX inverted photoelectron image as a function of pulse energy (E_p). As E_p is increased, more ATI peaks become visible at higher KE$_e$ due to the absorption of additional photons. The position of the peaks is given by:

$$KE_e = nh\nu_{800\,\mathrm{nm}} - I_p - U_p, \tag{A.1}$$

where n is the number of photons absorbed, $h\nu$ is the photon energy (1.55 eV), I_p is the first ionisation potential of Ar (15.76 eV[143]) and U_p is the ponderomotive potential. U_p is proportional to peak intensity (I), thus the ATI peak positions are expected to shift as a function of pulse energy. The shift is given by:

$$U_p = 9.33 \times 10^{-8}\, I\lambda^2. \tag{A.2}$$

where λ is the laser wavelength, and U_p, I and λ are given in units of eV, TW cm^{-2} and nm, respectively.

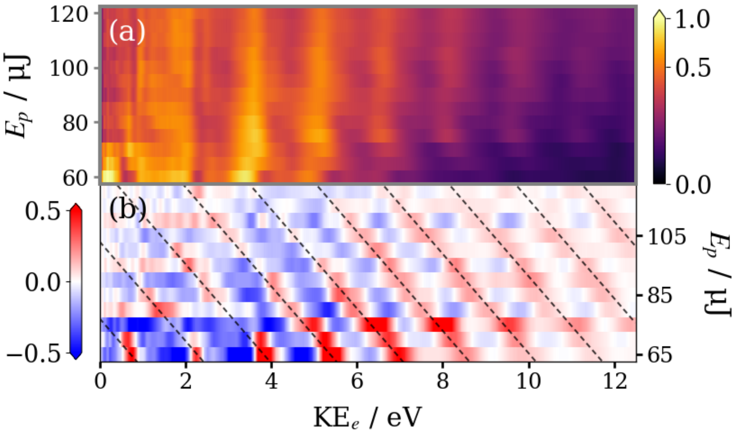

Figure A.2: (a) Photoelectron kinetic energy spectrum for Ar as a function of NIR pulse energy. (b) Intensity-difference spectra depicting the ponderomotive shift in the ATI peaks as a function of NIR pulse energy (*dashed black lines*).

However, the ponderomotive shift of the ATI peaks cannot be clearly seen in Figure A.2(a) because averaging over all intensities present in the focal volume effectively washes out the ponderomotive energy contribution. The contributions from the peak laser intensity at a given pulse energy are isolated by calculating pulse energy difference spectra. Spectra were normalised to unit area and for each a difference spectrum was calculated by subtracting the spectrum with the next lowest pulse energy, *e.g.* the 60 μJ spectrum was subtracted from the 65 μJ spectrum. The result is the distribution seen in Figure A.2(b), plotted on a colour scale that displays enhancement in red and depletion in blue. The ponderomotive shifts are clearly visible from the regions of enhancement.

From Equations A.1 and A.2, it can be shown that the gradient of the ponderomotive shift as a function of pulse energy (E_p) is equal to:

$$m = -\frac{1}{9.33 \times 10^{-8}\,\gamma\lambda^2}, \tag{A.3}$$

where γ is the sought after conversion factor between pulse energy in μJ and peak intensity in TW cm^{-2}:

$$I = \gamma E_p. \tag{A.4}$$

$m = 17 \pm 2$ μJ eV^{-1} for the black dashed lines drawn on Figure A.2(b), which corresponds to a value of $\gamma = 1.0 \pm 0.1$ TW cm^{-2} μJ^{-1}. As such, the peak intensity range covered by the data shown in Figure A.2 is 65 – 120 TW cm^{-2}.

A.2 Absolute kinetic energy calibration

The ATI peaks in the photoelectron spectrum for argon provides a reliable calibration from radius on the detector to KE. The KE$_e$ spectrum recorded at a peak NIR intensity of 75 TW cm^{-2} is presented in Figure A.3(a). The spectrum was fit to a series of Gaussian contributions to extract the centre of each ATI peak. In panel (b), these values are plotted against KE$_e$, calculated using Equation A.1. The error bars for each value represents the standard deviation of the Gaussian profile. A linear fit through the origin yields a radius to KE calibration constant of 2.17 ± 0.03 pixels^2 eV^{-1}. This was value was used to determine a radius to momentum conversion factor $\alpha = (2.39 \pm 0.03) \times 10^{-4}$ pixels^{-1}, which appears in Equation 2.8 for calibrating particle momentum.

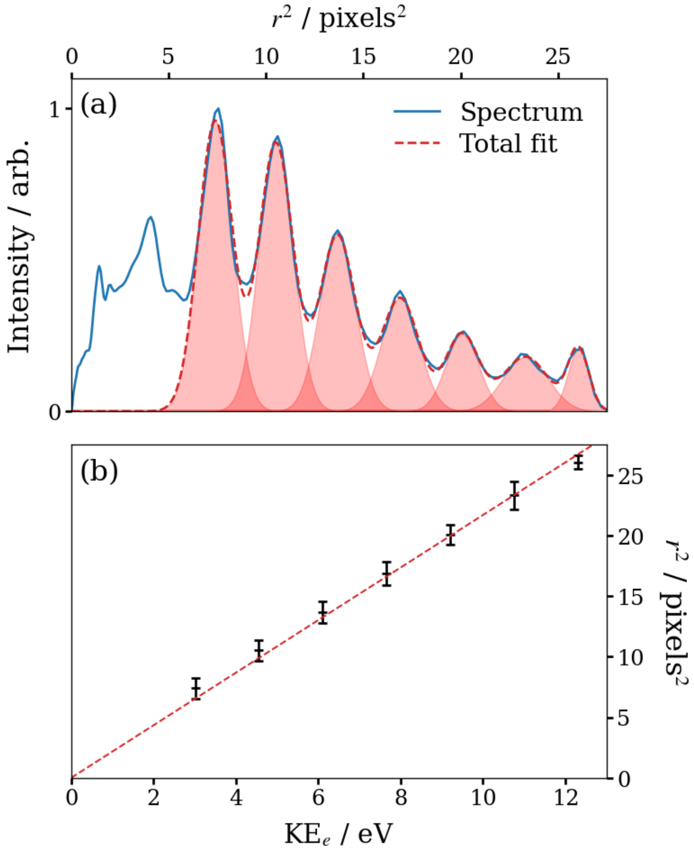

Figure A.3: (a) The photoelectron kinetic energy spectrum in units of pixels^2 for Ar exposed to a NIR pulse with a peak intensity of $7.5 \times 10^{13}\,\mathrm{W\,cm^{-2}}$. The spectrum is fit to a series of Gaussian functions, each shaded in *red*. (b) The relationship between the centre of each Gaussian component and KE$_e$ calculated using Equation A.1. A linear fit to the data (*red dash*) yields a calibration constant of $2.17 \pm 0.03\,\mathrm{pixels^2\,eV^{-1}}$.

B
Covariance mapping algorithm

Covariance analysis was implemented in Python using custom functions developed by the author of this thesis. The covariance analysis algorithm is based upon the work of previous members of the Brouard group, including Dr Craig Slater and Dr Felix Allum. The algorithim relies upon the Numba package to significantly increase computational speed.[237] Numba is a compiler that translates Python functions to optimised machine code and is particularly adept at accelerating the copious number of loops inherent to a covariance calculation.

B.1 Two-fold covariance mapping

Generating a two-fold covariance map typically takes less a minute. To demonstrate how the algorithm works, consider the case of constructing a Newton diagram from the momentum vectors of a pair of ions: A and B. The correlated term ($\langle AB \rangle$) is calculated from all pairs of ions A and B detected in the same laser shot. For each laser shot, the algorithm considers the relative momentum of the first A ion and first B ion. The angle between their momentum vectors is calculated using the scalar product:

$$\theta_{AB} = \cos^{-1}\left(\frac{\vec{p}_A \cdot \vec{p}_B}{|\vec{p}_A||\vec{p}_B|}\right), \tag{B.1}$$

and used to determine the components of $\vec{p}_B$ parallel and perpendicular to $\vec{p}_A$:

$$p_{B,||} = |\vec{p}_B| \cos\theta_{AB}, \tag{B.2}$$

$$p_{B,\perp} = |\vec{p}_B| \sin\theta_{AB}. \tag{B.3}$$

The momentum scalars are divided by the desired size of the momentum bins to determine a set of x and y coordinates and the value of the $\langle AB \rangle$ output array at these coordinates in increased by 1.

For a two-fold covariance calculation it is necessary to derive the momentum of the third body (C) from momentum conservation in the molecular frame:

$$\vec{p}_C = -(\vec{p}_A + \vec{p}_B). \tag{B.4}$$

Again, the angle relative to $\vec{p}_A$ is calculated:

$$\theta_{AC} = \cos^{-1}\left(\frac{\vec{p}_A \cdot \vec{p}_C}{|\vec{p}_A||\vec{p}_C|}\right), \tag{B.5}$$

and used to determine the parallel and perpendicular components of $\vec{p}_C$ in the recoil frame of A:

$$p_{C,||} = |\vec{p}_C| \cos\theta_{AC}, \tag{B.6}$$

$$p_{C,\perp} = -|\vec{p}_C| \sin\theta_{AC}. \tag{B.7}$$

Note that $p_{C,\perp}$ is negative in order to project the momentum distribution of C into the bottom half on the Newton diagram. Finally, a value of 1 is added to the output array at the corresponding (x, y) coordinates.

The same operation is repeated for the first A ion and the second B ion, and so on for all B ions in the laser shot. Then the combinations of the second A ion with every B ion in the laser shot are considered, et cetera. After the final A ion in the laser shot, the algorithm moves onto the second laser shot and the process starts again. The sequence of nested loops is depicted in Figure B.1. To increase computational efficiency, the algorithm only iterates through the laser shots in which both A and B ions were detected.

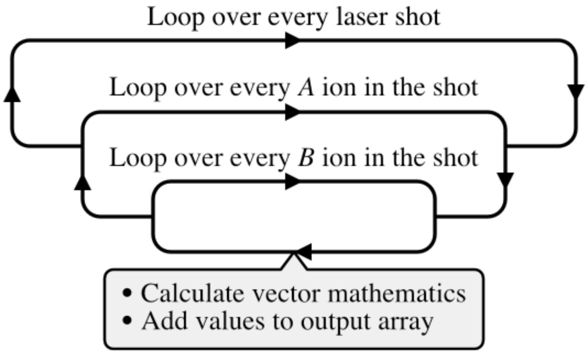

Figure B.1: The series of nested 'for' loops that constitute the algorithm for computing each term of the two-fold covariance.

To calculate the uncorrelated term ($\langle A\rangle\langle B\rangle$) one must in principle consider all pairs of A and B ions across the entire dataset, independent of whether they are detected in the same laser shot or not. This is achieved by repeating the process outlined above, but for each A ion in each laser shot combinations with all B ions in every laser shot need to be considered. Unsurprisingly, this is very computational expensive. A much more efficient approach is to approximately calculate the uncorrelated term based on a smaller subset of the data.

The method used here is to 'shift' the B ions to the next shot along, *i.e.* the B ions recorded in the first laser shot are moved to the second, B ions recorded in the second laser shot are moved to the third, and so on until the B ions in the last laser shot, which are moved to first. Then the procedure for calculating $\langle AB\rangle$ is repeated. It is guaranteed that the output array will be composed entirely of false coincidence events, and thereby approximates $\langle A\rangle\langle B\rangle$. The B ions in the dataset can be shifted again to calculate another '$\langle A\rangle\langle B\rangle$' array (in practice the shift amount is chosen randomly). This process is repeated many times and the resulting sets of arrays is averaged to give the final output. Around 10 iterations is normally sufficient to accurately approximate the $\langle A\rangle\langle B\rangle$ term.

The covariance map is calculated simply by subtracting the $\langle A \rangle \langle B \rangle$ array from the $\langle AB \rangle$ array. Because the total covariance has been calculated across all observations (laser shots), the covariance map needs to be normalised by dividing by the total number of laser shots. Examples of $\langle AB \rangle$ and $\langle A \rangle \langle B \rangle$ are presented in Figure B.2. Data was simulated for the Coulomb explosion of a prototypical bent triatomic molecule ABC into $A^+ + B^+ + C^+$, with an average ionisation rate of $3\,\text{shot}^{-1}$.

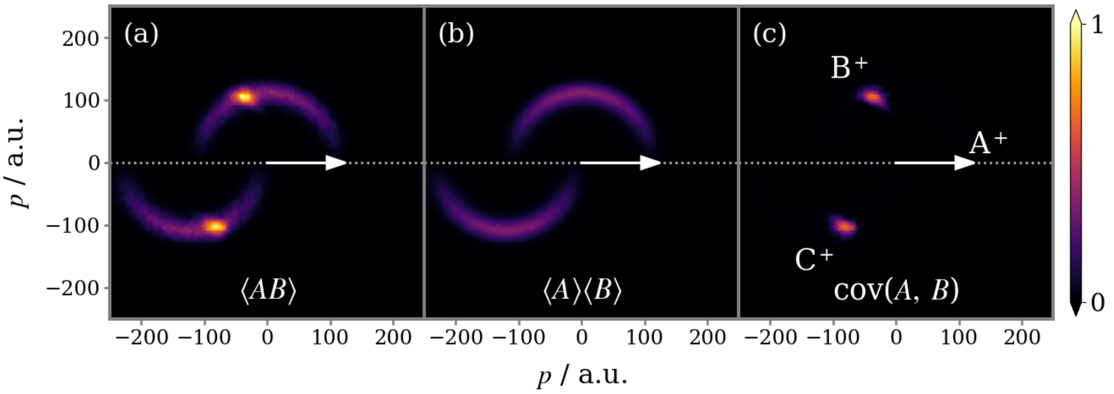

Figure B.2: (a, b) The individual terms calculated as part of the two-fold covariance calculation that produced the Newton diagram covariance map seen in panel (c).

B.2 Three-fold covariance mapping

Generating a three-fold covariance map is a slightly longer process, typically taking around 10 minutes. The algorithm for calculating a three-fold covariance map is an extension of the algorithm described above, so relies on the same approximations and shortcuts to speed up the calculation. To demonstrate, consider the case of constructing the same Newton diagram from the momentum vectors of three ions: A, B and C.

The correlated term ($\langle ABC \rangle$) is calculated from all combinations of A, B and C detected in the laser shot. A illustration of the process is given in Figure B.3. For each laser shot, the algorithm considers the relative momentum of the first A ion, first B ion and first C ion, then the first A ion, first B ion and second C ion, and so on for all C ions in the shot. Then the combinations of the first

A ion and second B ion with every C ion are considered. Once this loop has iterated through every B ion, it moves onto the second A ion and repeats the whole process. From describing this sequence, it is easy to appreciate how the number of combinations and hence calculation time grows exponentially as the order of the covariance map increases. Once again, the algorithm only needs to iterate through the laser shots in which A, B and C were all detected.

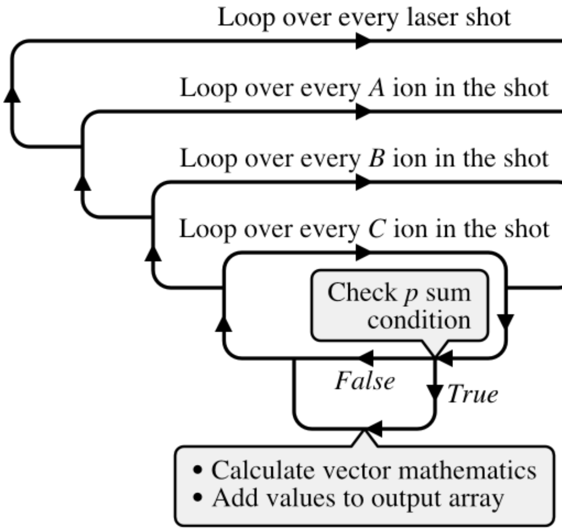

Figure B.3: The series of nested 'for' loops that constitute the algorithm for computing each term of the three-fold covariance.

The vector mathematics performed on each loop is unchanged, with the exception that $\vec{p}_C$ no longer needs to be deduced through momentum conversation. Provided that the three fragments together constitute the original molecule, it is appropriate to filter the ion combinations that do not obey momentum conservation. Practically, this is done by comparing the fragment momentum sum along each axis to a predetermined limit:

$$p_{A,x} + p_{B,x} + p_{C,x} \leq p_{lim}, \tag{B.8}$$

$$p_{A,y} + p_{B,y} + p_{C,y} \leq p_{lim}, \tag{B.9}$$

$$p_{A,z} + p_{B,z} + p_{C,z} \leq p_{lim}. \tag{B.10}$$

If any of these conditions is not satisfied, the algorithm simply skips to the next ion combination without adding any values to the $\langle ABC \rangle$ output array. (If the fragment momentum vectors are 2D, only the p_x and p_y sums are calculated). p_{lim} is typically estimated from the momentum resolution of the spectrometer, but can also be arbitrarily increased, for example to account for momentum carried away by a fourth body.

There are four uncorrelated terms to calculate. Computing these terms in full, *i.e.* by considering all relevant combinations in the dataset, is impractically long for most applications, often requiring days of computation time. Therefore, each uncorrelated term is estimated from a smaller subset of the data via the same method used to approximate the two-fold uncorrelated term. The first uncorrelated term ($\langle AB \rangle \langle C \rangle$) represents the correlation of A and B ions that originate from the same parent molecule, with a C ion that originates from a different parent molecule. It is calculated by shifting the C ions to the next shot along, whilst leaving the A and B ions untouched, then applying the same procedure used to calculate $\langle ABC \rangle$. The C ions are shifted again to calculate another '$\langle AB \rangle \langle C \rangle$' array as many time as necessary until the average of the individual arrays has converged, which is typically around 50 iterations.

The second ($\langle AC \rangle \langle B \rangle$) and third ($\langle BC \rangle \langle A \rangle$) uncorrelated terms are calculated via the same process, but shifting the B or A ions, respectively. The final uncorrelated term ($\langle A \rangle \langle B \rangle \langle C \rangle$) represents the coincidence of three ions that all originate from different parent molecules. Hence, the B and C ions are both shifted between shots *by different amounts* before calculating the output array. Examples of $\langle ABC \rangle$, $\langle AB \rangle \langle C \rangle$, $\langle AC \rangle \langle B \rangle$, $\langle BC \rangle \langle A \rangle$ and $\langle A \rangle \langle B \rangle \langle C \rangle$ calculated from the same simulated dataset are presented in Figure B.4.

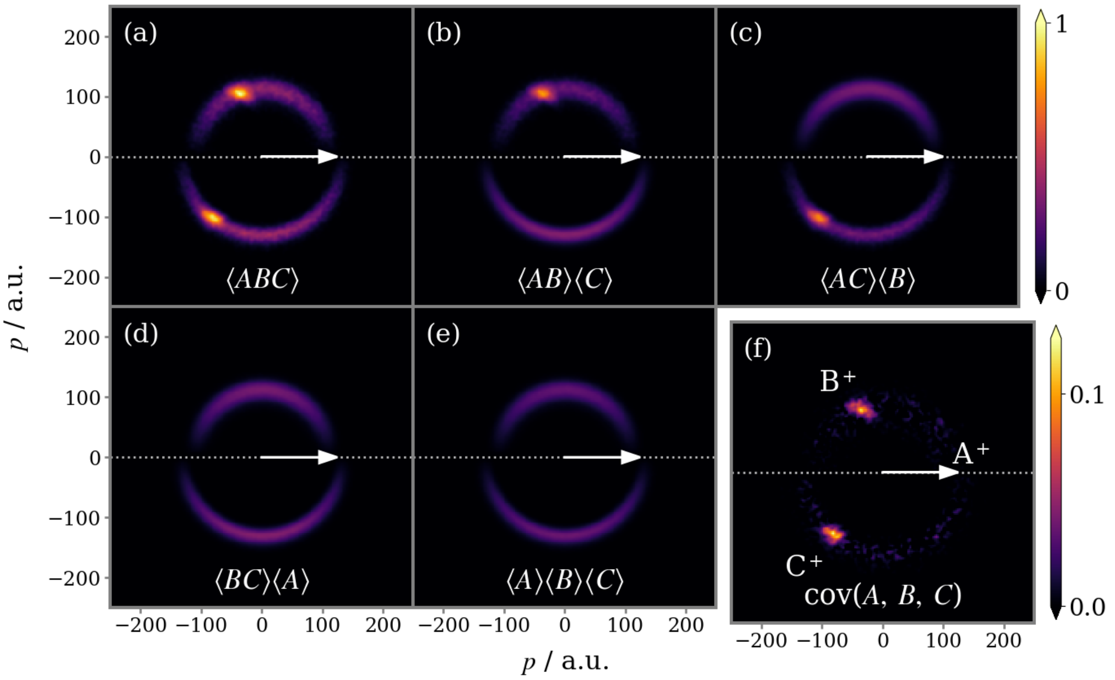

Figure B.4: (a–e) The individual terms calculated as part of the three-fold covariance calculation that produced the Newton diagram covariance map seen in panel (f). This panel is displaced to highlight the different intensity scaling.

C

The effect of Coulomb explosion model parameters

C.1 Simulations of the sequential fragmentation of iodopropane trications

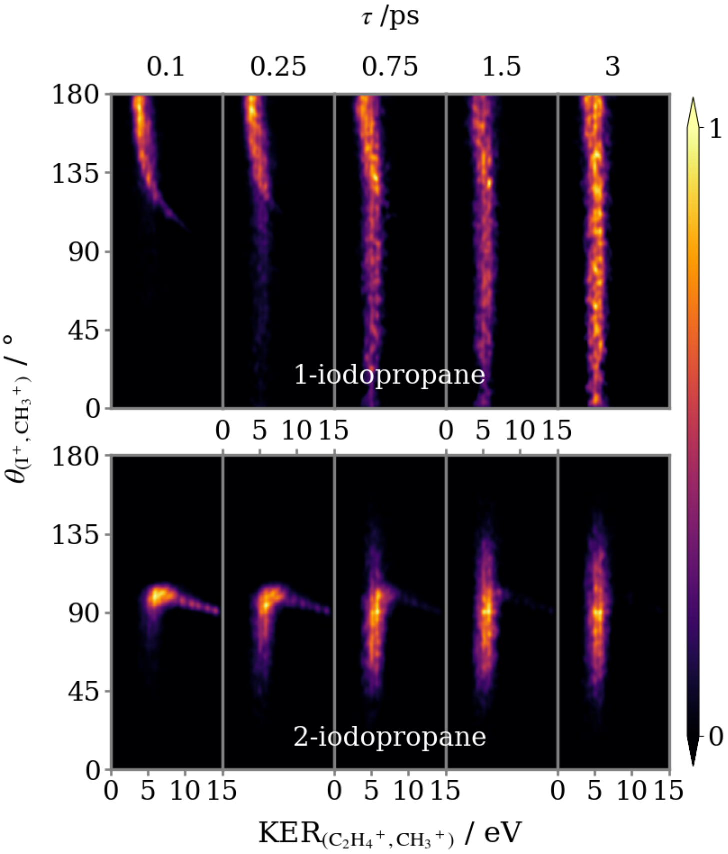

Figure C.1: Simulated correlation maps for the sequential breakup of (*top row*) 1-IP^{3+} and (*bottom row*) 2-IP^{3+} into I$^+$ + $C_2H_4^+$ + CH_3^+, where the primary step is Coulomb explosion into I$^+$ + $C_3H_7^{2+}$. The panels in each row demonstrate how the output of the simulation varies as the lifetime of the propyl dication (τ) is increased. For all simulations $\tau = T_R/2$. Each panel is normalised separately.

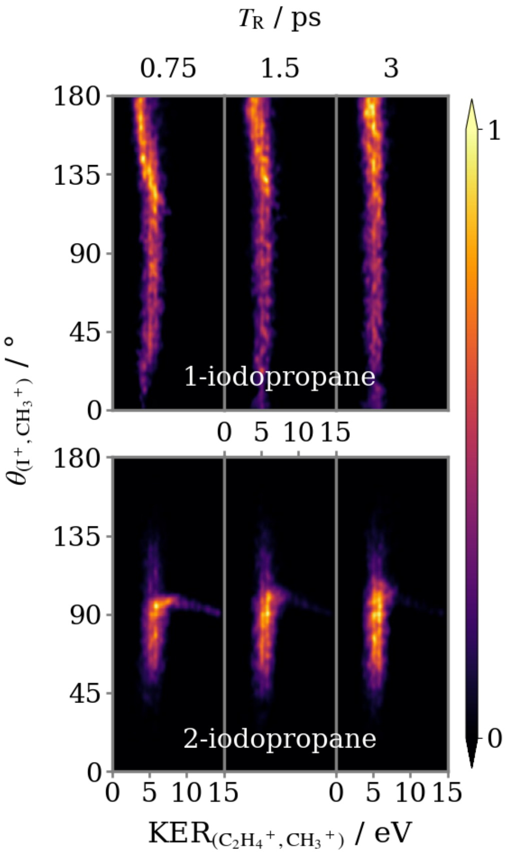

Figure C.2: Simulated correlation maps for the sequential breakup of (*top row*) 1-IP^{3+} and (*bottom row*) 2-IP^{3+} into I$^+$ + $C_2H_4{}^+$ + $CH_3{}^+$, where the primary step is Coulomb explosion into I$^+$ + $C_3H_7{}^{2+}$. The panels in each row demonstrate how the output of the simulation varies as lifetime (τ) and rotational period (T_R) of the propyl dication are increased in proportion. For all simulations $T_R = 0.75$ ps. Each panel is normalised separately.

C.2 Simulation of the sequential fragmentation of 1-iodopropane dications

Because the simulation does not consider a distribution of initial molecular geometries, the KER of the Coulomb explosion is fixed. Therefore, so is the momentum imparted to the fragments by this initial step. The key parameter that controls the output of the simulation is the impulse of the secondary dissociation (p_s). This is demonstrated in Figure C.3.

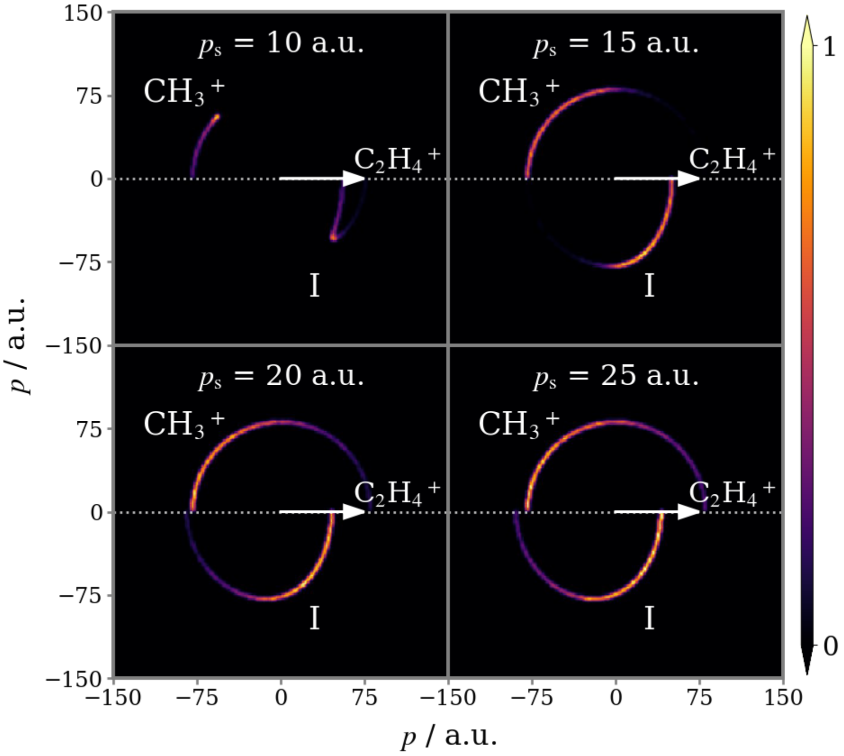

Figure C.3: Simulated Newton diagram correlation maps for the sequential breakup of 1-IP^{2+} into HI + $C_2H_3{}^+$ + $CH_3{}^+$, where the primary step is Coulomb explosion into $CH_3{}^+$ + $C_4H_4I^+$. The successive panels demonstrate how the output of the simulation varies as the secondary dissociation impulse (p_s) is increased. Each panel is normalised separately.

If p_s was equal to zero, $C_2H_3{}^+$ and $CH_3{}^+$ would recoil back-to-back, as the only influence on their trajectories would be Coulomb repulsion. The greater the value of p_s, the more significantly is can perturb the trajectory of $C_2H_3{}^+$ relative to the recoil direction of $CH_3{}^+$, which causes the angular span of the distribution to extend towards lower relative recoil angles. It is worth emphasizing that, whilst $C_2H_4I^+$ is randomly rotated in all of the simulations, only when p_s is large enough to exceed the momentum retained by $C_2H_3{}^+$ from the primary Coulomb explosion is the observed direction of travel of the $C_2H_3{}^+$ reversed by the secondary dissociation, generating ion pairs that recoil at an acute angle. Incorporating a distribution of p_s (see Figure 5.17(c)) is akin to summing several of the single-valued distributions shown here.

References

[1] R. E. Blankenship, *Molecular mechanisms of photosynthesis*, 2nd ed. (Wiley Blackwell, 2014).

[2] S. Chapman, “XXXV. on ozone and atomic oxygen in the upper atmosphere”, Lond. Edinb. Dublin Philos. Mag. J. Sci. **10**, 369–383 (1930).

[3] H. Tong, S. Ouyang, Y. Bi, N. Umezawa, M. Oshikiri, and J. Ye, “Nano-photocatalytic materials: Possibilities and challenges”, Adv. Mater. **24**, 229–251 (2012).

[4] M. Born and R. Oppenheimer, “Zur quantentheorie der molekeln”, Ann. Phys. **389**, 457–484 (1927).

[5] M. Brouard and C. Vallance, *Tutorials in molecular reaction dynamics* (Royal Society of Chemistry, 2015).

[6] D. R. Yarkony, “Conical intersections: Diabolical and often misunderstood”, Acc. Chem. Res. **31**, 511–518 (1998).

[7] D. Polli, P. Altoè, O. Weingart, K. M. Spillane, C. Manzoni, D. Brida, G. Tomasello, G. Orlandi, P. Kukura, R. A. Mathies, M. Garavelli, and G. Cerullo, “Conical intersection dynamics of the primary photoisomerization event in vision”, Nature **467**, 440–443 (2010).

[8] M. S. Schuurman and A. Stolow, “Dynamics at conical intersections”, Ann. Rev. Phys. Chem. **69**, 427–450 (2018).

[9] R. Schinke, *Photodissociation dynamics: Spectroscopy and fragmentation of small polyatomic molecules* (Cambridge university press, 1995).

[10] R. de Nalda, J. Durá, A. García-Vela, J. G. Izquierdo, J. González-Vázquez, and L. Bañares, “A detailed experimental and theoretical study of the femtosecond A-band photodissociation of CH_3I”, J. Chem. Phys. **128**, 244309 (2008).

[11] G. Gitzinger, M. E. Corrales, V. Loriot, G. A. Amaral, R. de Nalda, and L. Bañares, “A femtosecond velocity map imaging study on B-band predissociation in CH_3I. I. The band origin”, J. Chem. Phys. **132**, 234313 (2010).

[12] G. Gitzinger, M. E. Corrales, V. Loriot, R. de Nalda, and L. Bañares, “A femtosecond velocity map imaging study on B-band predissociation in CH_3I. II. The $2^1_0 2^1$ and $3^0_1 3^1$ vibronic levels”, J. Chem. Phys. **136**, 074303 (2012).

[13] M. Pitzer, M. Kunitski, A. S. Johnson, T. Jahnke, H. Sann, F. Sturm, L. P. H. Schmidt, H. Schmidt-Böcking, R. Dörner, J. Stohner, J. Kiedrowski, M. Reggelin, S. Marquardt, A. Schießer, R. Berger, and M. S. Schöffler, “Direct determination of absolute molecular stereochemistry in gas phase by Coulomb explosion imaging”, Science **341**, 1096–1100 (2013).

[14] Z. Vager, R. Naaman, and E. P. Kanter, “Coulomb explosion imaging of small molecules”, Science **244**, 426–431 (1989).

[15]D. S. Gemmell, “Determining the stereochemical structures of molecular ions by "Coulomb-explosion" techniques with fast (MeV) molecular ion beams”, Chem. Rev. **80**, 301–311 (1980).

[16]H. Stapelfeldt, E. Constant, and P. B. Corkum, “Wave packet structure and dynamics measured by Coulomb explosion”, Phys. Rev. Lett. **74**, 3780–3783 (1995).

[17]H. Stapelfeldt, E. Constant, H. Sakai, and P. B. Corkum, “Time-resolved Coulomb explosion imaging: A method to measure structure and dynamics of molecular nuclear wave packets”, Phys. Rev. A **58**, 426–433 (1998).

[18]F. Légaré, K. F. Lee, I. V. Litvinyuk, P. W. Dooley, S. S. Wesolowski, P. R. Bunker, P. Dombi, F. Krausz, A. D. Bandrauk, D. M. Villeneuve, and P. B. Corkum, “Laser Coulomb-explosion imaging of small molecules”, Phys. Rev. A **71**, 013415 (2005).

[19]C. S. Slater, S. Blake, M. Brouard, A. Lauer, C. Vallance, C. S. Bohun, L. Christensen, J. H. Nielsen, M. P. Johansson, and H. Stapelfeldt, “Coulomb-explosion imaging using a pixel-imaging mass-spectrometry camera”, Phys. Rev. A **91**, 053424 (2015).

[20]R. Boll, J. M. Schäfer, B. Richard, K. Fehre, G. Kastirke, Z. Jurek, M. S. Schöffler, M. M. Abdullah, N. Anders, T. M. Baumann, S. Eckart, B. Erk, A. De Fanis, R. Dörner, S. Grundmann, P. Grychtol, A. Hartung, M. Hofmann, M. Ilchen, L. Inhester, C. Janke, R. Jin, M. Kircher, K. Kubicek, M. Kunitski, X. Li, T. Mazza, S. Meister, N. Melzer, J. Montano, V. Music, G. Nalin, Y. Ovcharenko, C. Passow, A. Pier, N. Rennhack, J. Rist, D. E. Rivas, D. Rolles, I. Schlichting, L. P. H. Schmidt, P. Schmidt, J. Siebert, N. Strenger, D. Trabert, F. Trinter, I. Vela-Perez, R. Wagner, P. Walter, M. Weller, P. Ziolkowski, S.-K. Son, A. Rudenko, M. Meyer, R. Santra, and T. Jahnke, “X-ray multiphoton-induced Coulomb explosion images complex single molecules”, Nat. Phys. **18**, 423–428 (2022).

[21]U. Ablikim, C. Bomme, H. Xiong, E. Savelyev, R. Obaid, B. Kaderiya, S. Augustin, K. Schnorr, I. Dumitriu, T. Osipov, R. Bilodeau, D. Kilcoyne, V. Kumarappan, A. Rudenko, N. Berrah, and D. Rolles, “Identification of absolute geometries of cis and trans molecular isomers by Coulomb explosion imaging”, Sci. Rep. **6**, 1–8 (2016).

[22]M. Burt, K. Amini, J. W. L. Lee, L. Christiansen, R. R. Johansen, Y. Kobayashi, J. D. Pickering, C. Vallance, M. Brouard, and H. Stapelfeldt, “Communication: Gas-phase structural isomer identification by Coulomb explosion of aligned molecules”, J. Chem. Phys. **148**, 091102 (2018).

[23]S. Pathak, R. Obaid, S. Bhattacharyya, J. Bürger, X. Li, J. Tross, T. Severt, B. Davis, R. C. Bilodeau, C. A. Trallero-Herrero, A. Rudenko, N. Berrah, and D. Rolles, “Differentiating and quantifying gas-phase conformational isomers using Coulomb explosion imaging”, J. Phys. Chem. Lett. **11**, 10205–10211 (2020).

[24]L. Christensen, J. H. Nielsen, C. S. Slater, A. Lauer, M. Brouard, and H. Stapelfeldt, “Using laser-induced Coulomb explosion of aligned chiral molecules to determine their absolute configuration”, Phys. Rev. A **92**, 033411 (2015).

[25]J. D. Pickering, B. Shepperson, B. A. K. Hübschmann, F. Thorning, and H. Stapelfeldt, “Alignment and imaging of the CS_2 dimer inside helium nanodroplets”, Phys. Rev. Lett. **120**, 113202 (2018).

[26]J. D. Pickering, B. Shepperson, L. Christiansen, and H. Stapelfeldt, “Femtosecond laser induced Coulomb explosion imaging of aligned OCS oligomers inside helium nanodroplets”, J. Chem. Phys. **149**, 154306 (2018).

[27] C. Schouder, A. S. Chatterley, M. Johny, F. Hübschmann, A. F. Al-Refaie, F. Calvo, J. Küpper, and H. Stapelfeldt, “Laser-induced Coulomb explosion imaging of $(C_6H_5Br)_2$ and $C_6H_5Br–I_2$ dimers in helium nanodroplets using a Tpx3Cam”, J. Phys. B **54**, 184001 (2021).

[28] B. C. Arruda and R. J. Sension, “Ultrafast polyene dynamics: The ring opening of 1,3-cyclohexadiene derivatives”, Phys. Chem. Chem. Phys. **16**, 4439–4455 (2014).

[29] H. M. D. Bandara and S. C. Burdette, “Photoisomerization in different classes of azobenzene”, Chem. Soc. Rev. **41**, 1809–1825 (2012).

[30] G. Wald, “Molecular basis of visual excitation”, Science **162**, 230–239 (1968).

[31] M. Ben-Nun and T. J. Martínez, “Ab initio molecular dynamics study of cis–trans photoisomerization in ethylene”, Chem. Phys. Lett. **298**, 57–65 (1998).

[32] M. Ben-Nun and T. J. Martínez, “Photodynamics of ethylene: ab initio studies of conical intersections”, Chem. Phys. **259**, 237–248 (2000).

[33] R. L. Fork, B. I. Greene, and C. V. Shank, “Generation of optical pulses shorter than 0.1 psec by colliding pulse mode locking”, App. Phys. Lett. **38**, 671–672 (1981).

[34] D. E. Spence, P. N. Kean, and W. Sibbett, “60-fsec pulse generation from a self-mode-locked Ti:sapphire laser”, Opt. Lett. **16**, 42–44 (1991).

[35] R. G. W. Norrish and G. Porter, “Chemical reactions produced by very high light intensities”, Nature **164**, 658 (1949).

[36] G. Porter and R. G. W. Norrish, “Flash photolysis and spectroscopy. A new method for the study of free radical reactions”, Proc. R. Soc. Lond. A **200**, 284–300 (1950).

[37] A. H. Zewail, “Femtochemistry: Atomic-scale dynamics of the chemical bond using ultrafast lasers (Nobel lecture)”, Angew. Chem. **39**, 2586–2631 (2000).

[38] J. D. Pickering, *Ultrafast lasers and optics for experimentalists* (IOP Publishing, 2021).

[39] T. S. Rose, M. J. Rosker, and A. H. Zewail, “Femtosecond real-time observation of wave packet oscillations (resonance) in dissociation reactions”, J. Chem. Phys. **88**, 6672–6673 (1988).

[40] T. S. Rose, M. J. Rosker, and A. H. Zewail, “Femtosecond real-time probing of reactions. IV. the reactions of alkali halides”, J. Chem. Phys. **91**, 7415–7436 (1989).

[41] D. Zhong and A. H. Zewail, “Femtosecond real-time probing of reactions. 23. Studies of temporal, velocity, angular, and state dynamics from transition states to final products by femtosecond-resolved mass spectrometry”, J. Phys. Chem. A **102**, 4031–4058 (1998).

[42] A. Stolow, A. E. Bragg, and D. M. Neumark, “Femtosecond time-resolved photoelectron spectroscopy”, Chem. Rev. **104**, 1719–1758 (2004).

[43] R. Berera, R. van Grondelle, and J. T. M. Kennis, “Ultrafast transient absorption spectroscopy: Principles and application to photosynthetic systems”, Photosynth. Res. **101**, 105–118 (2009).

[44] A. Bhattacherjee and S. R. Leone, “Ultrafast X-ray transient absorption spectroscopy of gas-phase photochemical reactions: A new universal probe of photoinduced molecular dynamics”, Acc. Chem. Res. **51**, 3203–3211 (2018).

[45]B. Stankus, H. Yong, J. Ruddock, L. Ma, A. M. Carrascosa, N. Goff, S. Boutet, X. Xu, N. Zotev, A. Kirrander, M. P. Minitti, and P. M. Weber, "Advances in ultrafast gas-phase X-ray scattering", J. Phys. B **53**, 234004 (2020).

[46]D. Filippetto, P. Musumeci, R. K. Li, B. J. Siwick, M. R. Otto, M. Centurion, and J. P. F. Nunes, "Ultrafast electron diffraction: Visualizing dynamic states of matter", Rev. Mod. Phys. **94**, 045004 (2022).

[47]L. Christensen, J. H. Nielsen, C. B. Brandt, C. B. Madsen, L. B. Madsen, C. S. Slater, A. Lauer, M. Brouard, M. P. Johansson, B. Shepperson, and H. Stapelfeldt, "Dynamic stark control of torsional motion by a pair of laser pulses", Phys. Rev. Lett. **113**, 073005 (2014).

[48]E. T. Karamatskos, S. Raabe, T. Mullins, A. Trabattoni, P. Stammer, G. Goldsztejn, R. R. Johansen, K. Długołecki, H. Stapelfeldt, M. J. J. Vrakking, S. Trippel, A. Rouzée, and J. Küpper, "Molecular movie of ultrafast coherent rotational dynamics of OCS", Nat. Commun. **10**, 3364 (2019).

[49]M. Burt, R. Boll, J. W. L. Lee, K. Amini, H. Köckert, C. Vallance, A. S. Gentleman, S. R. Mackenzie, S. Bari, C. Bomme, S. Düsterer, B. Erk, B. Manschwetus, E. Müller, D. Rompotis, E. Savelyev, N. Schirmel, S. Techert, R. Treusch, J. Küpper, S. Trippel, J. Wiese, H. Stapelfeldt, B. C. de Miranda, R. Guillemin, I. Ismail, L. Journel, T. Marchenko, J. Palaudoux, F. Penent, M. N. Piancastelli, M. Simon, O. Travnikova, F. Brausse, G. Goldsztejn, A. Rouzée, M. Géléoc, R. Geneaux, T. Ruchon, J. Underwood, D. M. P. Holland, A. S. Mereshchenko, P. K. Olshin, P. Johnsson, S. Maclot, J. Lahl, A. Rudenko, F. Ziaee, M. Brouard, and D. Rolles, "Coulomb-explosion imaging of concurrent CH_2BrI photodissociation dynamics", Phys. Rev. A **96**, 043415 (2017).

[50]F. Allum, M. Burt, K. Amini, R. Boll, H. Köckert, P. K. Olshin, S. Bari, C. Bomme, F. Brauße, B. Cunha de Miranda, S. Düsterer, B. Erk, M. Géléoc, R. Geneaux, A. S. Gentleman, G. Goldsztejn, R. Guillemin, D. M. P. Holland, I. Ismail, P. Johnsson, L. Journel, J. Küpper, J. Lahl, J. W. L. Lee, S. Maclot, S. R. Mackenzie, B. Manschwetus, A. S. Mereshchenko, R. Mason, J. Palaudoux, M. N. Piancastelli, F. Penent, D. Rompotis, A. Rouzée, T. Ruchon, A. Rudenko, E. Savelyev, M. Simon, N. Schirmel, H. Stapelfeldt, S. Techert, O. Travnikova, S. Trippel, J. G. Underwood, C. Vallance, J. Wiese, F. Ziaee, M. Brouard, T. Marchenko, and D. Rolles, "Coulomb explosion imaging of CH_3I and CH_2ClI photodissociation dynamics", J. Chem. Phys. **149**, 204313 (2018).

[51]T. Walmsley, J. Unwin, F. Allum, S. Bari, R. Boll, K. Borne, M. Brouard, P. Bucksbaum, N. Ekanayake, B. Erk, R. Forbes, A. J. Howard, P. Eng-Johnsson, J. W. L. Lee, Z. Liu, B. Manschwetus, R. Mason, C. Passow, J. Peschel, D. Rivas, D. Rolles, A. Rörig, A. Rouzée, C. Vallance, F. Ziaee, and M. Burt, "Characterizing the multi-dimensional reaction dynamics of dihalomethanes using XUV-induced Coulomb explosion imaging", J. Chem. Phys. **159**, 144302 (2023).

[52]K. Amini, E. Savelyev, F. Brauße, N. Berrah, C. Bomme, M. Brouard, M. Burt, L. Christensen, S. Düsterer, B. Erk, H. Höppner, T. Kierspel, F. Krecinic, A. Lauer, J. W. L. Lee, M. Müller, E. Müller, T. Mullins, H. Redlin, N. Schirmel, J. Thøgersen, S. Techert, S. Toleikis, R. Treusch, S. Trippel, A. Ulmer, C. Vallance, J. Wiese, P. Johnsson, J. Küpper, A. Rudenko, A. Rouzée, H. Stapelfeldt, D. Rolles, and R. Boll, "Photodissociation of aligned CH_3I and $C_6H_3F_2I$ molecules probed with

time-resolved Coulomb explosion imaging by site-selective extreme ultraviolet ionization", Struct. Dyn. **5**, 014301 (2018).

[53] H. Ibrahim, B. Wales, S. Beaulieu, B. E. Schmidt, N. Thiré, E. P. Fowe, É. Bisson, C. T. Hebeisen, V. Wanie, M. Giguére, J.-C. Kieffer, M. Spanner, A. D. Bandrauk, J. Sanderson, M. S. Schuurman, and F. Légaré, "Tabletop imaging of structural evolutions in chemical reactions demonstrated for the acetylene cation", Nat. Commun. **5**, 4422 (2014).

[54] C. E. Liekhus-Schmaltz, I. Tenney, T. Osipov, A. Sanchez-Gonzalez, N. Berrah, R. Boll, C. Bomme, C. Bostedt, J. D. Bozek, S. Carron, R. Coffee, J. Devin, B. Erk, R. W. Field, L. Foucar, L. J. Frasinski, J. M. Glownia, M. Gühr, A. Kamalov, J. Krzywinski, H. Li, J. P. Marangos, T. J. Martinez, B. K. McFarland, S. Miyabe, A. Murphy Brendanand Natan, D. Rolles, A. Rudenko, M. Siano, E. R. Simpson, L. Spector, M. Swiggers, D. Walke, T. Wang Songand Weber, P. H. Bucksbaum, and V. S. Petrovic, "Ultrafast isomerization initiated by X-ray core ionization", Nat. Commun. **6**, 8199 (2015).

[55] I. Luzon, E. Livshits, K. Gope, R. Baer, and D. Strasser, "Making sense of Coulomb explosion imaging", J. Phys. Chem. Lett. **10**, 1361–1367 (2019).

[56] N. G. Kling, S. Díaz-Tendero, R. Obaid, M. R. Disla, H. Xiong, M. Sundberg, S. D. Khosravi, M. Davino, P. Drach, A. M. Carroll, T. Osipov, F. Martín, and N. Berrah, "Time-resolved molecular dynamics of single and double hydrogen migration in ethanol", Nat. Commun. **10**, 2813 (2019).

[57] T. Endo, S. P. Neville, V. Wanie, S. Beaulieu, C. Qu, J. Deschamps, P. Lassonde, B. E. Schmidt, H. Fujise, M. Fushitani, A. Hishikawa, P. L. Houston, J. M. Bowman, M. S. Schuurman, F. Légaré, and H. Ibrahim, "Capturing roaming molecular fragments in real time", Science **370**, 1072–1077 (2020).

[58] M. Zhang, Z. Guo, X. Mi, Z. Li, and Y. Liu, "Ultrafast imaging of molecular dynamics using ultrafast low-frequency lasers, X-ray free electron lasers, and electron pulses", J. Phys. Chem. Lett. **13**, 1668–1680 (2022).

[59] A. Catanese, B. Kaufman, C. Cheng, E. Jones, M. G. Cohen, and T. Weinacht, "Acousto-optic modulator pulse-shaper compression of octave-spanning pulses from a stretched hollow-core fiber", OSA Contin. **4**, 3176–3183 (2021).

[60] M. Protopapas, C. H. Keitel, and P. L. Knight, "Atomic physics with super-high intensity lasers", Rep. Prog. Phys. **60**, 389 (1997).

[61] R. R. Freeman, P. H. Bucksbaum, H. Milchberg, S. Darack, D. Schumacher, and M. E. Geusic, "Above-threshold ionization with subpicosecond laser pulses", Phys. Rev. Lett. **59**, 1092–1095 (1987).

[62] A. J. Howard, C. Cheng, R. Forbes, G. A. McCracken, W. H. Mills, V. Makhija, M. Spanner, T. Weinacht, and P. H. Bucksbaum, "Strong-field ionization of water: Nuclear dynamics revealed by varying the pulse duration", Phys. Rev. A **103**, 043120 (2021).

[63]K. Amini, J. Biegert, F. Calegari, A. Chacón, M. F. Ciappina, A. Dauphin, D. K. Efimov, C. Figueira de Morisson Faria, K. Giergiel, P. Gniewek, A. S. Landsman, M. Lesiuk, M. Mandrysz, A. S. Maxwell, R. Moszyński, L. Ortmann, J. A. Pérez-Hernández, A. Picón, E. Pisanty, J. Prauzner-Bechcicki, K. Sacha, N. Suárez, A. Zaïr, J. Zakrzewski, and M. Lewenstein, "Symphony on strong field approximation", Rep. Prog. Phys. **82**, 116001 (2019).

[64]L. Meitner, "Über den zusammenhang zwischen β- und γ-strahlen", Z. Phys. **9**, 145–152 (1922).

[65]P. Auger, "Sur l'effet photoélectrique composé", J. Phys. Radium **6**, 205–208 (1925).

[66]B. Erk, R. Boll, S. Trippel, D. Anielski, L. Foucar, B. Rudek, S. W. Epp, R. Coffee, S. Carron, S. Schorb, K. R. Ferguson, M. Swiggers, J. D. Bozek, M. Simon, T. Marchenko, J. Küpper, I. Schlichting, J. Ullrich, C. Bostedt, D. Rolles, and A. Rudenko, "Imaging charge transfer in iodomethane upon X-ray photoabsorption", Science **345**, 288–291 (2014).

[67]R. Forbes, F. Allum, S. Bari, R. Boll, K. Borne, M. Brouard, P. H. Bucksbaum, N. Ekanayake, B. Erk, A. J. Howard, P. Johnsson, J. W. L. Lee, B. Manschwetus, R. Mason, C. Passow, J. Peschel, D. E. Rivas, A. Rörig, A. Rouzée, C. Vallance, F. Ziaee, D. Rolles, and M. Burt, "Time-resolved site-selective imaging of predissociation and charge transfer dynamics: The CH_3I B-band", J. Phys. B **53**, 224001 (2020).

[68]"Direct momentum imaging of charge transfer following site-selective ionization", Phys. Rev. A **108**, 043113 (2023).

[69]R. E. Continetti, "Coincidence spectroscopy", Annu. Rev. Phys. Chem. **52**, 165–192 (2001).

[70]K. E. McCulloh, T. E. Sharp, and H. M. Rosenstock, "Direct observation of the decomposition of multiply charged ions into singly charged fragments", J. Chem. Phys. **42**, 3501–3509 (1965).

[71]A. Hishikawa, A. Iwamae, and K. Yamanouchi, "Ultrafast structural deformation of NO_2 in intense laser fields studied by mass-resolved momentum imaging", J. Chem. Phys. **111**, 8871–8878 (1999).

[72]H. Hasegawa, A. Hishikawa, and K. Yamanouchi, "Coincidence imaging of Coulomb explosion of CS_2 in intense laser fields", Chem. Phys. Lett. **349**, 57–63 (2001).

[73]J. H. D. Eland, "The dynamics of three-body dissociations of dications studied by the triple coincidence technique PEPIPICO", Mol. Phys. **61**, 725–745 (1987).

[74]S. Hsieh and J. H. D. Eland, "Reaction dynamics of three-body dissociations in triatomic molecules from single-photon double ionization studied by a time- and position-sensitive coincidence method", J. Phys. B **30**, 4515 (1997).

[75]N. Neumann, D. Hant, L. P. H. Schmidt, J. Titze, T. Jahnke, A. Czasch, M. S. Schöffler, K. Kreidi, O. Jagutzki, H. Schmidt-Böcking, and R. Dörner, "Fragmentation dynamics of ${CO_2}^{3+}$ investigated by multiple electron capture in collisions with slow highly charged ions", Phys. Rev. Lett. **104**, 103201 (2010).

[76]E. Kukk, K. Motomura, H. Fukuzawa, K. Nagaya, and K. Ueda, "Molecular dynamics of XFEL-induced photo-dissociation, revealed by ion-ion coincidence measurements", Appl. Sci. **7**, 531 (2017).

[77]X. Yu, X. Zhao, Z. Wang, Y. Yang, X. Zhang, P. Ma, X. Li, C. Wang, X. Xu, C. Wang, D. Zhang, S. Luo, and D. Ding, “Determining the stereo configuration of carbonyl sulfide dimers using Coulomb-explosion imaging”, Phys. Rev. A **104**, 053104 (2021).

[78]S. Bhattacharyya, K. Borne, F. Ziaee, S. Pathak, E. Wang, A. S. Venkatachalam, X. Li, N. Marshall, K. D. Carnes, C. W. Fehrenbach, T. Severt, I. Ben-Itzhak, A. Rudenko, and D. Rolles, “Strong-field-induced Coulomb explosion imaging of tribromomethane”, J. Phys. Chem. Lett. **13**, 5845–5853 (2022).

[79]S. Bhattacharyya, K. Borne, F. Ziaee, S. Pathak, E. Wang, A. S. Venkatachalam, N. Marshall, K. D. Carnes, C. W. Fehrenbach, T. Severt, I. Ben-Itzhak, A. Rudenko, and D. Rolles, “Two- and three-body fragmentation of multiply charged tribromomethane by ultrafast laser pulses”, Phys. Chem. Chem. Phys. **24**, 27631–27644 (2022).

[80]L. J. Frasinski, K. Codling, and P. A. Hatherly, “Covariance mapping: A correlation method applied to multiphoton multiple ionization”, Science **246**, 1029–1031 (1989).

[81]F. Allum, C. Cheng, A. J. Howard, P. H. Bucksbaum, M. Brouard, T. Weinacht, and R. Forbes, “Multi-particle three-dimensional covariance imaging: “Coincidence” insights into the many-body fragmentation of strong-field ionized D_2O”, J. Phys. Chem. Lett. **12**, 8302–8308 (2021).

[82]L. E. Hargrove, R. L. Fork, and M. A. Pollack, “Locking of He–Ne laser modes induced by synchronous intracavity modulation”, App. Phys. Lett. **5**, 4–5 (1964).

[83]M. Piché, “Beam reshaping and self-mode-locking in nonlinear laser resonators”, Opt. Commun. **86**, 156–160 (1991).

[84]D. Strickland and G. Mourou, “Compression of amplified chirped optical pulses”, Opt. Commun. **56**, 219–221 (1985).

[85]G. Mourou, “Nobel lecture: Extreme light physics and application”, Rev. Mod. Phys. **91**, 030501 (2019).

[86]D. Strickland, “Nobel lecture: Generating high-intensity ultrashort optical pulses”, Rev. Mod. Phys. **91**, 030502 (2019).

[87]W. Ackermann et al., “Highly coherent and stable pulses from the FERMI seeded free-electron laser in the extreme ultraviolet”, Nat. Photon. **1**, 336–342 (2007).

[88]P. Emma, R. Akre, J. Arthur, R. Bionta, C. Bostedt, J. Bozek, A. Brachmann, P. Bucksbaum, R. Coffee, F.-J. Decker, Y. Ding, D. Dowell, S. Edstrom, A. Fisher, J. Frisch, S. Gilevich, J. Hastings, G. Hays, P. Hering, Z. Huang, R. Iverson, H. Loos, M. Messerschmidt, A. Miahnahri, S. Moeller, H.-D. Nuhn, G. Pile, D. Ratner, J. Rzepiela, D. Schultz, T. Smith, P. Stefan, H. Tompkins, J. Turner, J. Welch, W. White, J. Wu, G. Yocky, and J. Galayda, “First lasing and operation of an ångstrom-wavelength free-electron laser”, Nat. Photon. **4**, 641–647 (2010).

[89]T. Ishikawa, H. Aoyagi, T. Asaka, Y. Asano, N. Azumi, T. Bizen, H. Ego, K. Fukami, T. Fukui, Y. Furukawa, S. Goto, H. Hanaki, T. Hara, T. Hasegawa, T. Hatsui, A. Higashiya, T. Hirono, N. Hosoda, M. Ishii, T. Inagaki, Y. Inubushi, T. Itoga, Y. Joti, M. Kago, T. Kameshima, H. Kimura, Y. Kirihara, A. Kiyomichi, T. Kobayashi, C. Kondo, T. Kudo, H. Maesaka, X. M. Maréchal, T. Masuda, S. Matsubara, T. Matsumoto, T. Matsushita, S. Matsui, M. Nagasono, N. Nariyama, H. Ohashi, T. Ohata, T. Ohshima, S. Ono, Y. Otake, C. Saji, T. Sakurai, T. Sato, K. Sawada,

T. Seike, K. Shirasawa, T. Sugimoto, S. Suzuki, S. Takahashi, H. Takebe, K. Takeshita, K. Tamasaku, H. Tanaka, R. Tanaka, T. Tanaka, T. Togashi, K. Togawa, A. Tokuhisa, H. Tomizawa, K. Tono, S. Wu, M. Yabashi, M. Yamaga, A. Yamashita, K. Yanagida, C. Zhang, T. Shintake, H. Kitamura, and N. Kumagai, "A compact X-ray free-electron laser emitting in the sub-ångström region", Nat. Photon. **8**, 540–544 (2012).

[90] W. Decking et al., "A MHz-repetition-rate hard X-ray free-electron laser driven by a superconducting linear accelerator", Nat. Photon. **14**, 391–397 (2020).

[91] E. M. McMillan, "The synchrotron - a proposed high energy particle accelerator", Phys. Rev. **68**, 143–144 (1945).

[92] B. W. J. McNeil and N. R. Thompson, "X-ray free-electron lasers", Nat. Photon. **4**, 814–821 (1945).

[93] R. Bonifacio, L. De Salvo, P. Pierini, N. Piovella, and C. Pellegrini, "Spectrum, temporal structure, and fluctuations in a high-gain free-electron laser starting from noise", Phys. Rev. Lett. **73**, 70–73 (1994).

[94] E. Allaria, R. Appio, L. Badano, W. Barletta, S. Bassanese, S. Biedron, A. Borga, E. Busetto, D. Castronovo, P. Cinquegrana, S. Cleva, D. Cocco, M. Cornacchia, P. Craievich, I. Cudin, G. D'Auria, M. Dal Forno, M. Danailov, R. De Monte, P. De Ninno G.and Delgiusto, A. Demidovich, S. Di Mitri, B. Diviacco, A. Fabris, R. Fabris, W. Fawley, M. Ferianis, E. Ferrari, S. Ferry, L. Froehlich, P. Furlan, G. Gaio, F. Gelmetti, L. Giannessi, M. Giannini, R. Gobessi, R. Ivanov, E. Karantzoulis, M. Lonza, A. Lutman, B. Mahieu, M. Milloch, S. Milton, M. Musardo, I. Nikolov, S. Noe, F. Parmigiani, G. Penco, M. Petronio, L. Pivetta, M. Predonzani, F. Rossi, L. Rumiz, A. Salom, C. Scafuri, C. Serpico, P. Sigalotti, S. Spampinati, C. Spezzani, M. Svandrlik, C. Svetina, S. Tazzari, M. Trovo, R. Umer, A. Vascotto, M. Veronese, R. Visintini, M. Zaccaria, D. Zangrando, and M. Zangrando, "Highly coherent and stable pulses from the FERMI seeded free-electron laser in the extreme ultraviolet", Nat. Photon. **6**, 699–704 (2012).

[95] W. Wmrath, *Fundamentals of vacuum technology*, Leybold GmbH (Bonner Strasse 498, Cologne, Germany, 2015).

[96] W. Becker, "The turbomolecular pump, its design, operation and theory; calculation of the pumping speed for various gases and their dependence on the forepump", Vacuum **16**, 625–632 (1966).

[97] G. L. Weissler and R. W. Carlson, *Vacuum physics and technology* (Academic Press, 1979).

[98] G. Scoles, *Atomic and molecular beam methods* (Oxford University Press, 1988).

[99] D. W. Chandler and P. L. Houston, "Two-dimensional imaging of state-selected photodissociation products detected by multiphoton ionization", J. Chem. Phys. **87**, 1445–1447 (1987).

[100] A. T. J. B. Eppink and D. H. Parker, "Velocity map imaging of ions and electrons using electrostatic lenses: Application in photoelectron and photofragment ion imaging of molecular oxygen", Rev. Sci. Instrum, **68**, 3477–3484 (1997).

[101] D. H. Parker and A. T. J. B. Eppink, "Photoelectron and photofragment velocity map imaging of state-selected molecular oxygen dissociation/ionization dynamics", J. Chem. Phys. **107**, 2357–2362 (1997).

[102]C. Bordas, F. Paulig, H. Helm, and D. L. Huestis, “Photoelectron imaging spectrometry: Principle and inversion method”, Rev. Sci. Instrum, **67**, 2257–2268 (1996).

[103]J. J. Lin, J. Zhou, W. Shiu, and K. Liu, “Application of time-sliced ion velocity imaging to crossed molecular beam experiments”, Rev. Sci. Instrum. **74**, 2495–2500 (2003).

[104]D. Townsend, M. P. Minitti, and A. G. Suits, “Direct current slice imaging”, Rev. Sci. Instrum. **74**, 2530–2539 (2003).

[105]K. Amini, S. Blake, M. Brouard, M. B. Burt, E. Halford, A. Lauer, C. S. Slater, J. W. L. Lee, and C. Vallance, “Three-dimensional imaging of carbonyl sulfide and ethyl iodide photodissociation using the pixel imaging mass spectrometry camera”, Rev. Sci. Instrum. **86**, 103113 (2015).

[106]J. W. Lee, H. Köckert, D. Heathcote, D. Popat, R. T. Chapman, G. Karras, P. Majchrzak, E. Springate, and C. Vallance, “Three-dimensional covariance-map imaging of molecular structure and dynamics on the ultrafast timescale”, Commun. Chem. **3**, 72 (2020).

[107]F. Allum, R. Mason, M. Burt, C. S. Slater, E. Squires, B. Winter, and M. Brouard, “Post extraction inversion slice imaging for 3d velocity map imaging experiments”, Mol. Phys. **119**, 1842531 (2021).

[108]L. Dinu, A. T. J. B. Eppink, F. Rosca-Pruna, H. L. Offerhaus, W. J. van der Zande, and M. J. J. Vrakking, “Application of a time-resolved event counting technique in velocity map imaging”, Rev. Sci. Instrum. **73**, 4206–4213 (2002).

[109]S. K. A. I. Chichinin K.-H. Gericke and C. Maul, “Imaging chemical reactions – 3D velocity mapping”, Int. Rev. Phys. Chem. **28**, 607–680 (2009).

[110]S. Kauczok, N. Gödecke, A. I. Chichinin, M. Veckenstedt, C. Maul, and K.-H. Gericke, “Three-dimensional velocity map imaging: Setup and resolution improvement compared to three-dimensional ion imaging”, Rev. Sci. Instrum. **80**, 083301 (2009).

[111]J. Long, F. J. Furch, J. Durá, A. S. Tremsin, J. Vallerga, C. P. Schulz, A. Rouzée, and M. J. J. Vrakking, “Ion-ion coincidence imaging at high event rate using an in-vacuum pixel detector”, J. Chem. Phys. **147**, 013919 (2017).

[112]A. Zhao, M. van Beuzekom, B. Bouwens, D. Byelov, I. Chakaberia, C. Cheng, E. Maddox, A. Nomerotski, P. Svihra, J. Visser, V. Vrba, and T. Weinacht, “Coincidence velocity map imaging using Tpx3cam, a time stamping optical camera with 1.5 ns timing resolution”, Rev. Sci. Instrum **88**, 113104 (2017).

[113]J. Ullrich, R. Moshammer, A. Dorn, R. Dörner, L. P. H. Schmidt, and H. Schmidt-Böcking, “Recoil-ion and electron momentum spectroscopy: Reaction-microscopes”, Rep. Prog. Phys. **66**, 1463 (2003).

[114]R. Dörner, V. Mergel, O. Jagutzki, L. Spielberger, J. Ullrich, R. Moshammer, and H. Schmidt-Böcking, “Cold target recoil ion momentum spectroscopy: A ‘momentum microscope’ to view atomic collision dynamics”, Phys. Rep. **330**, 95–192 (2000).

[115]X. Li, A. Rudenko, M. S. Schöffler, N. Anders, T. M. Baumann, S. Eckart, B. Erk, A. De Fanis, K. Fehre, R. Dörner, L. Foucar, S. Grundmann, P. Grychtol, A. Hartung, M. Hofmann, M. Ilchen, C. Janke, G. Kastirke, M. Kircher, K. Kubicek, M. Kunitski, T. Mazza, S. Meister, N. Melzer, J. Montano, V. Music, G. Nalin, Y. Ovcharenko, C. Passow, A. Pier, N. Rennhack, J. Rist, D. E. Rivas, I. Schlichting, L. P. H. Schmidt, P. Schmidt, J. Siebert, N. Strenger, D. Trabert, F. Trinter, I. Vela-Perez, R. Wagner, P. Walter, M. Weller, P. Ziolkowski, A. Czasch, D. Rolles, M. Meyer, T. Jahnke, and R. Boll, "Coulomb explosion imaging of small polyatomic molecules with ultrashort X-ray pulses", Phys. Rev. Res. **4**, 013029 (2022).

[116]F. Allum, V. Music, L. Inhester, R. Boll, B. Erk, P. Schmidt, T. M. Baumann, G. Brenner, M. Burt, P. V. Demekhin, S. Dörner, A. Ehresmann, A. Galler, P. Grychtol, D. Heathcote, D. Kargin, M. Larsson, J. W. L. Lee, Z. Li, B. Manschwetus, L. Marder, R. Mason, M. Meyer, H. Otto, C. Passow, R. Pietschnig, D. Ramm, K. Schubert, L. Schwob, R. D. Thomas, C. Vallance, I. Vidanović, C. von Korff Schmising, R. Wagner, P. Walter, V. Zhaunerchyk, D. Rolles, S. Bari, M. Brouard, and M. Ilchen, "A localized view on molecular dissociation via electron-ion partial covariance", Commun. Chem. **5**, 42 (2022).

[117]S. Matoba, R. Takahashi, C. Io, T. Koizumi, and H. Shiromaru, "Absolute detection efficiency of a high-sensitivity microchannel plate with tapered pores", Jpn. J. Appl. Phys. **50**, 112201 (2011).

[118]K. Fehre, D. Trojanowskaja, J. Gatzke, M. Kunitski, F. Trinter, S. Zeller, L. P. H. Schmidt, J. Stohner, R. Berger, A. Czasch, O. Jagutzki, T. Jahnke, R. Dörner, and M. S. Schöffler, "Absolute ion detection efficiencies of microchannel plates and funnel microchannel plates for multi-coincidence detection", Rev. Sci. Instrum. **89**, 045112 (2018).

[119]J. H. D. Eland and A. H. Pearson, "Simple radial position-sensitive detector with short deadtime for time-of-flight and coincidence experiments", Meas. Sci. Technol. **1**, 36 (1990).

[120]J. H. D. Eland, "Simple two-dimensional position sensitive detector with short dead-time for coincidence experiments", Meas. Sci. Technol. **5**, 1501 (1994).

[121]O. Jagutzki, V. Mergel, K. Ullmann-Pfleger, L. Spielberger, U. Spillmann, R. Dörner, and H. Schmidt-Böcking, "A broad-application microchannel-plate detector system for advanced particle or photon detection tasks: Large area imaging, precise multi-hit timing information and high detection rate", Nucl. Instrum. Methods Phys. Res. A **477**, 244–249 (2002).

[122]O. Jagutzki, A. Cerezo, A. Czasch, R. Dorner, M. Hattas, M. Huang, V. Mergel, U. Spillmann, K. Ullmann-Pfleger, T. Weber, H. Schmidt-Bocking, and G. Smith, "Multiple hit readout of a microchannel plate detector with a three-layer delay-line anode", IEEE Trans. Nucl. Sci. **49**, 2477–2483 (2002).

[123]A. Nomerotski, M. Brouard, E. Campbell, A. Clark, J. Crooks, J. Fopma, J. J. John, A. J. Johnsen, C. Slater, R. Turchetta, C. Vallance, E. Wilman, and W. H. Yuen, "Pixel imaging mass spectrometry with fast and intelligent pixel detectors", J. Instrum. **5**, C07007 (2010).

[124] J. J. John, M. Brouard, A. Clark, J. Crooks, E. Halford, L. Hill, J. W. L. Lee, A. Nomerotski, R. Pisarczyk, I. Sedgwick, C. S. Slater, R. Turchetta, C. Vallance, W. Wilman, B. Winter, and W. H. Yuen, "PImMS, a fast event-triggered monolithic pixel detector with storage of multiple timestamps", J. Instrum. **7**, C08001 (2012).

[125] T. Poikela, J. Plosila, T. Westerlund, M. Campbell, M. De Gaspari, X. Llopart, V. Gromov, R. Kluit, M. van Beuzekom, F. Zappon, V. Zivkovic, C. Brezina, K. Desch, Y. Fu, and A. Kruth, "Timepix3: A 65K channel hybrid pixel readout chip with simultaneous ToA/ToT and sparse readout", J. oInstrum. **9**, C05013 (2014).

[126] E. Frojdh, M. Campbell, M. De Gaspari, S. Kulis, X. Llopart, T. Poikela, and L. Tlustos, "Timepix3: First measurements and characterization of a hybrid-pixel detector working in event driven mode", J. Instrum. **10**, C01039 (2015).

[127] A. Nomerotski, "Imaging and time stamping of photons with nanosecond resolution in Timepix based optical cameras", Nucl. Instrum. Methods Phys. Res. A **937**, 26–30 (2019).

[128] X. Llopart, J. Alozy, R. Ballabriga, M. Campbell, R. Casanova, V. Gromov, E. H. M. Heijne, T. Poikela, E. Santin, V. Sriskaran, L. Tlustos, and A. Vitkovskiy, "Timepix4, a large area pixel detector readout chip which can be tiled on 4 sides providing sub-200 ps timestamp binning", J. Instrum. **17**, C01044 (2022).

[129] B. Winter, S. J. King, M. Brouard, and C. Vallance, "A fast microchannel plate-scintillator detector for velocity map imaging and imaging mass spectrometry", Rev. Sci. Instrum. **85**, 023306 (2014).

[130] M.-J. Lee and E. Charbon, "Progress in single-photon avalanche diode image sensors in standard CMOS: from two-dimensional monolithic to three-dimensional-stacked technology", Jpn. J. Appl. Phys. **57**, 1002A3 (2018).

[131] C. Weeraratna, C. Amarasinghe, S. K. Lee, W. Li, and A. G. Suits, "Demonstration of multi-hit and multi-mass capability of 3d imaging in a conventional velocity map imaging experiment", J. Chem. Phys. **149**, 084202 (2018).

[132] X. Ren, A. M. Summers, K. P. Raju, A. Vajdi, V. Makhija, C. W. Fehrenbach, N. G. Kling, K. J. Betsch, Z. Wang, M. F. Kling, K. D. Carnes, I. Ben-Itzhak, C. Trallero-Herrero, and V. Kumarappan, "Single-shot carrier-envelope-phase tagging using an f–2f interferometer and a phase meter: A comparison", J. Opt. **19**, 124017 (2017).

[133] K. W. DeLong, D. N. Fittinghoff, R. Trebino, B. Kohler, and K. Wilson, "Pulse retrieval in frequency-resolved optical gating based on the method of generalized projections", Opt. Lett. **19**, 2152–2154 (1994).

[134] S. Linden, H. Giessen, and J. Kuhl, "XFROG — a new method for amplitude and phase characterization of weak ultrashort pulses", Phys. Status Solidi B **206**, 119–124 (1998).

[135] S. Owada, K. Togawa, T. Inagaki, T. Hara, T. Tanaka, Y. Joti, T. Koyama, K. Nakajima, H. Ohashi, Y. Senba, T. Togashi, K. Tono, M. Yamaga, H. Yumoto, M. Yabashi, H. Tanaka, and T. Ishikawa, "A soft X-ray free-electron laser beamline at SACLA: The light source, photon beamline and experimental station", J. Synchrotron Rad. **25**, 282–288 (2018).

[136]H. Fukuzawa, K. Nagaya, and K. Ueda, “Advances in instrumentation for gas-phase spectroscopy and diffraction with short-wavelength free electron lasers”, Nucl. Instrum. Methods Phys. Res. A **907**, 116–131 (2018).

[137]P. Kirkpatrick and A. V. Baez, “Formation of optical images by X-rays”, J. Opt. Soc. Am. **38**, 766–774 (1948).

[138]S. Owada, M. Fushitani, A. Matsuda, H. Fujise, Y. Sasaki, Y. Hikosaka, A. Hishikawa, and M. Yabashi, “Characterization of soft X-ray FEL pulse duration with two-color photoelectron spectroscopy”, J. Synchrotron Rad. **27**, 1362–1365 (2020).

[139]K. Motomura, L. Foucar, A. Czasch, N. Saito, O. Jagutzki, H. Schmidt-Böcking, R. Dörner, X. J. Liu, H. Fukuzawa, G. Prümper, K. Ueda, M. Okunishi, K. Shimada, T. Harada, M. Toyoda, M. Yanagihara, M. Yamamoto, H. Iwayama, K. Nagaya, M. Yao, A. Rudenko, J. Ullrich, M. Nagasono, A. Higashiya, M. Yabashi, T. Ishikawa, H. Ohashi, and H. Kimura, “Multi-coincidence ion detection system for EUV–FEL fragmentation experiments at SPring-8”, Nucl. Instrum. Methods Phys. Res. A **606**, 770–773 (2009).

[140]D. Manura and D. Dahl, *SIMION (R) 8.1 user manual*, Adaptas Solutions (9 Second Street, Palmer, MA 01069, USA, 2008).

[141]R. Trebino, *Frequency-resolved optical gating: The measurement of ultrashort laser pulses* (Springer Science & Business Media, 2012).

[142]D. Kane and R. Trebino, “Characterization of arbitrary femtosecond pulses using frequency-resolved optical gating”, IEEE J. Quantum Electron. **29**, 571–579 (1993).

[143]P. Linstrom and W. Mallard, *NIST Chemistry WebBook* (NIST Standard Reference Database Number 69, 2024) Chap. Ion Energetics Data.

[144]A. T. J. B. Eppink and D. H. Parker, “Methyl iodide A-band decomposition study by photofragment velocity imaging”, J. Chem. Phys. **109**, 4758–4767 (1998).

[145]A. T. J. B. Eppink and D. H. Parker, “Energy partitioning following photodissociation of methyl iodide in the A band: A velocity mapping study”, J. Chem. Phys. **110**, 832–844 (1999).

[146]A. B. Alekseyev, H.-P. Liebermann, R. J. Buenker, and S. N. Yurchenko, “An ab initio study of the CH_3I photodissociation. I. Potential energy surfaces”, J. Chem. Phys. **126**, 234102 (2007).

[147]A. B. Alekseyev, H.-P. Liebermann, and R. J. Buenker, “An ab initio study of the CH_3I photodissociation. II. Transition moments and vibrational state control of the i* quantum yields”, J. Chem. Phys. **126**, 234103 (2007).

[148]A. García-Vela, R. de Nalda, J. Durá, J. González-Vázquez, and L. Bañares, “A 4D wave packet study of the CH_3I photodissociation in the A-band. Comparison with femtosecond velocity map imaging experiments”, J. Chem. Phys. **135**, 154306 (2011).

[149]E. M. Warne, B. Downes-Ward, J. Woodhouse, M. A. Parkes, D. Bellshaw, E. Springate, P. Majchrzak, Y. Zhang, G. Karras, A. S. Wyatt, R. T. Chapman, A. Kirrander, and R. S. Minns, “Photodissociation dynamics of CH_3I probed via multiphoton ionisation photoelectron spectroscopy”, Phys. Chem. Chem. Phys. **21**, 11142–11149 (2019).

[150]E. M. Warne, B. Downes-Ward, J. Woodhouse, M. A. Parkes, E. Springate, P. A. J. Pearcy, Y. Zhang, G. Karras, A. S. Wyatt, R. T. Chapman, and R. S. Minns, “Photodissociation dynamics of methyl iodide probed using femtosecond extreme ultraviolet photoelectron spectroscopy”, Phys. Chem. Chem. Phys. **22**, 25695–25703 (2020).

[151]M. E. Corrales, J. González-Vázquez, R. de Nalda, and L. Bañares, “Coulomb explosion imaging for the visualization of a conical intersection”, J. Chem. Phys. Lett. **10**, 138–143 (2019).

[152]F. Ziaee, K. Borne, R. Forbes, K. R. P., Y. Malakar, B. Kaderiya, T. Severt, I. Ben-Itzhak, A. Rudenko, and D. Rolles, “Single- and multi-photon-induced ultraviolet excitation and photodissociation of CH_3I probed by coincident ion momentum imaging”, Phys. Chem. Chem. Phys. **25**, 9999–10010 (2023).

[153]G. A. Garcia, L. Nahon, and I. Powis, “Two-dimensional charged particle image inversion using a polar basis function expansion”, Rev. Sci. Instrum. **75**, 4989–4996 (2004).

[154]M. E. Corrales, G. Gitzinger, J. González-Vázquez, V. Loriot, R. de Nalda, and L. Bañares, “Velocity map imaging and theoretical study of the coulomb explosion of CH_3I under intense femtosecond IR pulses”, J. Phys. Chem. A **116**, 2669–2677 (2012).

[155]V. Zhaunerchyk, L. J. Frasinski, J. H. D. Eland, and R. Feifel, “Theory and simulations of covariance mapping in multiple dimensions for data analysis in high-event-rate experiments”, Phys. Rev. A **89**, 053418 (2014).

[156]L. J. Frasinski, “Cumulant mapping as the basis of multi-dimensional spectrometry”, Phys. Chem. Chem. Phys. **24**, 20776–20787 (2022).

[157]L. J. Frasinski, P. A. Hatherly, and K. Codling, “Multiphoton multiple ionisation of N_2O probed by three-dimensional covariance mapping”, Phys. Lett. A **156**, 227–232 (1991).

[158]P. A. Hatherly, M. Stankiewicz, K. Codling, L. J. Frasinski, and G. M. Cross, “The multielectron dissociative ionization of molecular iodine in intense laser fields”, J. Phys. B **27**, 2993 (1994).

[159]V. R. Bhardwaj, K. Vijayalakshmi, and D. Mathur, “Dissociative ionization of benzene in intense laser fields of picosecond duration”, Phys. Rev. A **59**, 1392–1398 (1999).

[160]C. S. Slater, S. Blake, M. Brouard, A. Lauer, C. Vallance, J. J. John, R. Turchetta, A. Nomerotski, L. Christensen, J. H. Nielsen, M. P. Johansson, and H. Stapelfeldt, “Covariance imaging experiments using a pixel-imaging mass-spectrometry camera”, Phys. Rev. A **89**, 011401 (2014).

[161]J. L. Hansen, J. H. Nielsen, C. B. Madsen, A. T. Lindhardt, M. P. Johansson, T. Skrydstrup, L. B. Madsen, and H. Stapelfeldt, “Control and femtosecond time-resolved imaging of torsion in a chiral molecule”, J. Chem. Phys. **136**, 204310 (2012).

[162]F. Allum, “Studying ultrafast photodynamics using charged particle imaging and covariance analysis”, PhD thesis (University of Oxford, 2021).

[163]S. W. Crane, J. W. L. Lee, M. N. R. Ashfold, and D. Rolles, “Molecular photodissociation dynamics revealed by Coulomb explosion imaging”, Phys. Chem. Chem. Phys. **25**, 16672–16698 (2023).

[164] J. W. L. Lee, D. S. Tikhonov, P. Chopra, S. Maclot, A. L. Steber, S. Gruet, F. Allum, R. Boll, X. Cheng, S. Düsterer, B. Erk, D. Garg, L. He, D. Heathcote, M. Johny, M. M. Kazemi, H. Köckert, J. Lahl, A. K. Lemmens, D. Loru, R. Mason, E. Müller, T. Mullins, P. Olshin, C. Passow, J. Peschel, D. Ramm, D. Rompotis, N. Schirmel, S. Trippel, J. Wiese, F. Ziaee, S. Bari, M. Burt, J. Küpper, A. M. Rijs, D. Rolles, S. Techert, P. Eng-Johnsson, M. Brouard, C. Vallance, B. Manschwetus, and M. Schnell, "Time-resolved relaxation and fragmentation of polycyclic aromatic hydrocarbons investigated in the ultrafast XUV-IR regime", Nat. Commun. **12**, 6107 (2021).

[165] J. H. Posthumus, J. Plumridge, M. K. Thomas, K. Codling, L. J. Frasinski, A. J. Langley, and P. F. Taday, "Dynamic and geometric laser-induced alignment of molecules in intense laser fields", J. Phys. B **31**, L553 (1998).

[166] F. Rosca-Pruna, E. Springate, H. L. Offerhaus, M. Krishnamurthy, N. Farid, C. Nicole, and M. J. J. Vrakking, "Spatial alignment of diatomic molecules in intense laser fields: I. Experimental results", J. Phys. B **34**, 4919 (2001).

[167] F. Allum, J. McManus, O. Denby, M. Burt, and M. Brouard, "Photoionization and photofragmentation dynamics of I_2 in intense laser fields: A velocity-map imaging study", J. Phys. Chem. A **126**, 8577–8587 (2022).

[168] J. D. Pickering, K. Amini, M. Brouard, M. Burt, I. J. Bush, L. Christensen, A. Lauer, J. H. Nielsen, C. S. Slater, and H. Stapelfeldt, "Communication: Three-fold covariance imaging of laser-induced Coulomb explosions", J. Chem. Phys. **144**, 161105 (2016).

[169] L. J. Frasinski, V. Zhaunerchyk, M. Mucke, R. J. Squibb, M. Siano, J. H. D. Eland, P. Linusson, P. v.d. Meulen, P. Salén, R. D. Thomas, M. Larsson, L. Foucar, J. Ullrich, K. Motomura, S. Mondal, K. Ueda, T. Osipov, L. Fang, B. F. Murphy, N. Berrah, C. Bostedt, J. D. Bozek, S. Schorb, M. Messerschmidt, J. M. Glownia, J. P. Cryan, R. N. Coffee, O. Takahashi, S. Wada, M. N. Piancastelli, R. Richter, K. C. Prince, and R. Feifel, "Dynamics of hollow atom formation in intense X-ray pulses probed by partial covariance mapping", Phys. Rev. Lett. **111**, 073002 (2013).

[170] O. Kornilov, M. Eckstein, M. Rosenblatt, C. P. Schulz, K. Motomura, A. Rouzée, J. Klei, L. Foucar, M. Siano, A. Lübcke, F. Schapper, P. Johnsson, D. M. P. Holland, T. Schlathölter, T. Marchenko, S. Düsterer, K. Ueda, M. J. J. Vrakking, and L. J. Frasinski, "Coulomb explosion of diatomic molecules in intense XUV fields mapped by partial covariance", J. Phys. B **46**, 164028 (2013).

[171] T. Driver, B. Cooper, R. Ayers, R. Pipkorn, S. Patchkovskii, V. Averbukh, D. R. Klug, J. P. Marangos, L. J. Frasinski, and M. Edelson-Averbukh, "Two-dimensional partial-covariance mass spectrometry of large molecules based on fragment correlations", Phys. Rev. X **10**, 041004 (2020).

[172] D. Heathcote and C. Vallance, "Partial and contingent recoil-frame covariance-map imaging", J. Phys. Chem. A **125**, 7092–7098 (2021).

[173] C. Maul and K. H. Gericke, "Photo induced three body decay", Int. Rev. Phys. Chem. **16**, 1–79 (1997).

[174] J. Rajput, T. Severt, B. Berry, B. Jochim, P. Feizollah, B. Kaderiya, M. Zohrabi, U. Ablikim, F. Ziaee, K. Raju P., D. Rolles, A. Rudenko, K. D. Carnes, B. D. Esry, and I. Ben-Itzhak, "Native frames: Disentangling sequential from concerted three-body fragmentation", Phys. Rev. Lett. **120**, 103001 (2018).

[175] J. Rajput, H. Kumar, P. Bhatt, and C. P. Safvan, "A new technique for measurement of subrotational lifetime of molecular ions", Sci. Rep. **10**, 20301 (2020).

[176] C. Cheng, L. J. Frasinski, G. ç. Mo ğol, F. Allum, A. J. Howard, D. Rolles, P. H. Bucksbaum, M. Brouard, R. Forbes, and T. Weinacht, "Multiparticle cumulant mapping for Coulomb explosion imaging", Phys. Rev. Lett. **130**, 093001 (2023).

[177] U. Ablikim, C. Bomme, E. Savelyev, H. Xiong, R. Kushawaha, R. Boll, K. Amini, T. Osipov, D. Kilcoyne, A. Rudenko, N. Berrah, and D. Rolles, "Isomer-dependent fragmentation dynamics of inner-shell photoionized difluoroiodobenzene", Phys. Chem. Chem. Phys. **19**, 13419–13431 (2017).

[178] L. Minion, J. W. L. Lee, and M. Burt, "Predicting Coulomb explosion fragment angular distributions using molecular ground-state vibrational motion", Phys. Chem. Chem. Phys. **24**, 11636–11645 (2022).

[179] J. Unwin, F. Allum, M. Britton, I. Gabalski, H. Bromberger, M. Brouard, P. H. Bucksbaum, T. Driver, N. Ekanayake, D. Garg, E. Gougoula, D. Heathcote, A. J. Howard, P. Hockett, D. M. P. Holland, S. Kumar, C.-s. Lam, J. W. L. Lee, J. McManus, J. Mikosch, D. Milesevic, R. S. Minns, C. C. Papadopoulou, C. Passow, W. O. Razmus, A. Röder, A. Rouzée, M. Schuurman, A. Simao, A. Stolow, A. Tul-Noor, C. Vallance, T. Walmsley, D. Rolles, B. Erk, M. Burt, and R. Forbes, "X-ray induced Coulomb explosion imaging of transient excited-state structural rearrangements in CS_2", Commun. Phys. **6**, 309 (2023).

[180] S. Shimizu, V. Zhakhovskii, F. Sato, S. Okihara, S. Sakabe, K. Nishihara, Y. Izawa, T. Yatsuhashi, and N. Nakashima, "Coulomb explosion of benzene induced by an intense laser field", J. Chem. Phys. **117**, 3180–3189 (2002).

[181] S. Shimizu, V. Zhakhovskii, M. Murakami, M. Tanaka, T. Yatsuhashi, S. Okihara, K. Nishihara, S. Sakabe, Y. Izawa, and N. Nakashima, "Coulomb explosion of hexa-fluorobenzene induced by an intense laser field", Chem. Phys. Lett. **404**, 379–383 (2005).

[182] J. Kou, V. Zhakhovskii, S. Sakabe, K. Nishihara, S. Shimizu, S. Kawato, M. Hashida, K. Shimizu, S. Bulanov, Y. Izawa, Y. Kato, and N. Nakashima, "Anisotropic Coulomb explosion of C_60 irradiated with a high-intensity femtosecond laser pulse", J. Chem. Phys. **112**, 5012–5020 (2000).

[183] W. Zhou, L. Ge, G. A. Cooper, S. W. Crane, M. H. Evans, M. N. Ashfold, and C. Vallance, "Coulomb explosion imaging for gas-phase molecular structure determination: An ab initio trajectory simulation study", J. Chem. Phys. **153**, 184201 (2020).

[184] P. Virtanen et al., "SciPy 1.0: fundamental algorithms for scientific computing in Python", Nat. Methods **17**, 261–272 (2022).

[185] M. Ben-Nun, J. Quenneville, and T. J. Martínez, "Ab initio multiple spawning: Photochemistry from first principles quantum molecular dynamics", J. Phys. Chem. A **104**, 5161–5175 (2000).

[186] B. F. E. Curchod and T. J. Martínez, "Ab initio nonadiabatic quantum molecular dynamics", Chem. Rev. **118**, 3305–3336 (2018).

[187] M. Hochlaf and J. H. D. Eland, "A theoretical and experimental study of the ${SO_2}^{2+}$ dication", J. Chem. Phys. **120**, 6449–6460 (2004).

[188]G. L. Gutsev, S. L. McPherson, H. A. López Peña, D. A. Boateng, L. G. Gutsev, B. R. Ramachandran, and K. M. Tibbetts, "Dissociation of singly and multiply charged nitromethane cations: Femtosecond laser mass spectrometry and theoretical modeling", J. Phys. Chem. A **124**, 7427–7438 (2020).

[189]T. Jahnke, R. Guillemin, L. Inhester, S.-K. Son, G. Kastirke, M. Ilchen, J. Rist, D. Trabert, N. Melzer, N. Anders, T. Mazza, R. Boll, A. De Fanis, V. Music, T. Weber, M. Weller, S. Eckart, K. Fehre, S. Grundmann, A. Hartung, M. Hofmann, C. Janke, M. Kircher, G. Nalin, A. Pier, J. Siebert, N. Strenger, I. Vela-Perez, T. M. Baumann, P. Grychtol, J. Montano, Y. Ovcharenko, N. Rennhack, D. E. Rivas, R. Wagner, P. Ziolkowski, P. Schmidt, T. Marchenko, O. Travnikova, L. Journel, I. Ismail, E. Kukk, J. Niskanen, F. Trinter, C. Vozzi, M. Devetta, S. Stagira, M. Gisselbrecht, A. L. Jäger, X. Li, Y. Malakar, M. Martins, R. Feifel, L. P. H. Schmidt, A. Czasch, G. Sansone, D. Rolles, A. Rudenko, R. Moshammer, R. Dörner, M. Meyer, T. Pfeifer, M. S. Schöffler, R. Santra, M. Simon, and M. N. Piancastelli, "Inner-shell-ionization-induced femtosecond structural dynamics of water molecules imaged at an X-ray free-electron laser", Phys. Rev. X **11**, 041044 (2021).

[190]R. Thissen, O. Witasse, O. Dutuit, C. S. Wedlund, G. Gronoff, and J. Lilensten, "Doubly-charged ions in the planetary ionospheres: A review", Phys. Chem. Chem. Phys. **13**, 18264–18287 (2011).

[191]M. Alagia, N. Balucani, P. Candori, S. Falcinelli, F. Pirani, R. Richter, M. Rosi, S. Stranges, and F. Vecchiocattivi, "Production of ions at high energy and its role in extraterrestrial environments", Rendiconti Lincei **24**, 53–65 (2013).

[192]S. Falcinelli, F. Pirani, M. Alagia, L. Schio, R. Richter, S. Stranges, N. Balucani, and F. Vecchiocattivi, "Molecular dications in planetary atmospheric escape", Atmosphere **7**, 112 (2016).

[193]S. Hsieh and J. H. D. Eland, "Secondary dissociation reactions of $C_2H_2N^+$ and $CHN_2{}^+$ ions in the charge separation mass spectra of five-membered nitrogen heterocycles", J. Mass Spectrom. **31**, 1054–1060 (1996).

[194]D. W. Lindle, P. H. Kobrin, C. M. Truesdale, T. A. Ferrett, P. A. Heimann, H. G. Kerkhoff, U. Becker, and D. A. Shirley, "Inner-shell photoemission from the iodine atom in ch_3i", Phys. Rev. A **30**, 239–244 (1984).

[195]M. E. Corrales, V. Loriot, G. Balerdi, J. González-Vázquez, R. de Nalda, L. Bañares, and A. H. Zewail, "Structural dynamics effects on the ultrafast chemical bond cleavage of a photodissociation reaction", Phys. Chem. Chem. Phys. **16**, 8812–8818 (2014).

[196]Z. Li, L. Inhester, C. Liekhus-Schmaltz, B. F. E. Curchod, J. W. Snyder, N. Medvedev, J. Cryan, T. Osipov, S. Pabst, O. Vendrell, P. Bucksbaum, and T. J. Martinez, "Ultrafast isomerization in acetylene dication after carbon K-shell ionization", Nat. Commun. **8**, 453 (2017).

[197]Z. L. Streeter, F. L. Yip, R. R. Lucchese, B. Gervais, T. N. Rescigno, and C. W. McCurdy, "Dissociation dynamics of the water dication following one-photon double ionization. I. Theory", Phys. Rev. A **98**, 053429 (2018).

[198]L. Inhester, B. Oostenrijk, M. Patanen, E. Kokkonen, S. H. Southworth, C. Bostedt, O. Travnikova, T. Marchenko, S.-K. Son, R. Santra, M. Simon, L. Young, and S. L. Sorensen, "Chemical understanding of the limited site-specificity in molecular inner-shell photofragmentation", J. Phys. Chem. Lett. **9**, 1156–1163 (2018).

[199] E. Kukk, D. T. Ha, Y. Wang, D. G. Piekarski, S. Diaz-Tendero, K. Kooser, E. Itälä, H. Levola, M. Alcamí, E. Rachlew, and F. Martín, “Internal energy dependence in X-ray-induced molecular fragmentation: An experimental and theoretical study of thiophene”, Phys. Rev. A **91**, 043417 (2015).

[200] T. A. Carlson, “Double electron ejection resulting from photo-ionization in the outermost shell of He, Ne, and Ar, and its relationship to electron correlation”, Phys. Rev. **156**, 142–149 (1967).

[201] T. N. Olney, G. Cooper, and C. E. Brion, “Quantitative studies of the photoabsorption (4.5˘488 eV) and photoionization (9˘59.5 ev) of methyl iodide using dipole electron impact techniques”, Chem. Phys. **232**, 211–237 (1998).

[202] J. A. R. Samson, G. N. Haddad, T. Masuoka, P. N. Pareek, and D. A. L. Kilcoyne, “Ionization yields, total absorption, and dissociative photoionization cross sections of CH_4 from 110 to 950 Å”, J. Chem. Phys. **90**, 6925–6932 (1989).

[203] G. Dujardin, D. Winkoun, and S. Leach, “Double photoionization of methane”, Phys. Rev. A **31**, 3027–3038 (1985).

[204] T. Yatsuhashi, N. Nakashima, and J. Azuma, “Coulomb explosion of dichloroethene geometric isomers at 1 PW cm^{-2}”, J. Phys. Chem. A **117**, 1393–1399 (2013).

[205] U. Ablikim, C. Bomme, T. Osipov, H. Xiong, R. Obaid, R. C. Bilodeau, N. G. Kling, I. Dumitriu, S. Augustin, S. Pathak, K. Schnorr, D. Kilcoyne, N. Berrah, and D. Rolles, “A coincidence velocity map imaging spectrometer for ions and high-energy electrons to study inner-shell photoionization of gas-phase molecules”, Rev. Sci. Instrum. **90**, 055103 (2019).

[206] Y. Wada, H. Akagi, T. Kumada, R. Itakura, and T. Wakabayashi, “Mass-resolved momentum imaging of three dichloroethylene isomers by femtosecond laser-induced Coulomb explosion”, Photochem **2**, 798–809 (2022).

[207] R. H. Dalitz, “CXII. on the analysis of τ-meson data and the nature of the τ-meson”, London, Edinburgh, Dublin Philos. Mag. J. Sci. **44**, 1068–1080 (1953).

[208] D. Strasser, L. Lammich, H. Kreckel, S. Krohn, M. Lange, A. Naaman, D. Schwalm, A. Wolf, and D. Zajfman, “Breakup dynamics and the isotope effect in H_3^+ and D_3^+ dissociative recombination”, Phys. Rev. A **66**, 032719 (2002).

[209] K. Gope, I. Luzon, and D. Strasser, “N–NO & NN–O bond cleavage dynamics in two- and three-body Coulomb explosion of the N_2O^{2+} dication”, Phys. Chem. Chem. Phys. **21**, 13730–13737 (2019).

[210] K. Gope, E. Livshits, D. M. Bittner, R. Baer, and D. Strasser, “An “inverse” harpoon mechanism”, Sci. Adv. **8**, eabq8084 (2022).

[211] J. Quenneville and T. J. Martínez, “Ab initio study of cis-trans photoisomerization in stilbene and ethylene”, J. Phys. Chem. A **107**, 829–837 (2003).

[212] H. Tao, T. K. Allison, T. W. Wright, A. M. Stooke, C. Khurmi, J. van Tilborg, Y. Liu, R. W. Falcone, A. Belkacem, and T. J. Martinez, “Ultrafast internal conversion in ethylene. I. the excited state lifetime”, J. Chem. Phys. **134**, 244306 (2011).

[213] V. Stert, H. Lippert, H. H. Ritze, and W. Radloff, “Femtosecond time-resolved dynamics of the electronically excited ethylene molecule”, Chem. Phys. Lett. **388**, 144–149 (2004).

[214]T. Kobayashi, T. Horio, and T. Suzuki, “Ultrafast deactivation of the $\pi\pi^*$(V) state of ethylene studied using sub-20 fs time-resolved photoelectron imaging”, J. Phys. Chem. A **119**, 9518–9523 (2015).

[215]S. Karashima, A. Humeniuk, W. J. Glover, and T. Suzuki, “Ultrafast photoisomerization of ethylene studied using time-resolved extreme ultraviolet photoelectron spectroscopy”, J. Phys. Chem. A **126**, 3873–3879 (2022).

[216]M. J. Berry, “Chloroethylene photochemical lasers: Vibrational energy content of the HCl molecular elimination products”, J. Chem. Phys. **61**, 3114–3143 (1974).

[217]J. D. Ewbank, J. Y. Luo, J. T. English, R. Liu, W. L. Faust, and L. Schafer, “Time-resolved gas electron diffraction study of the 193 nm photolysis of 1,2-dichloroethenes”, J. Phys. Chem. **97**, 8745–8751 (1993).

[218]L. Hua, X. Zhang, W.-B. Lee, M.-H. Chao, B. Zhang, and K.-C. Lin, “Photodissociation of cis-, trans-, and 1,1-dichloroethylene in the ultraviolet range: Characterization of Cl(^{2}p$_J$) elimination”, J. Phys. Chem. A **114**, 37–44 (2010).

[219]M. Umemoto, K. Seki, H. Shinohara, U. Nagashima, N. Nishi, M. Kinoshita, and R. Shimada, “Photofragmentation of mono- and dichloroethylenes: Translational energy measurements of recoiling Cl and HCl fragments”, J. Chem. Phys. **83**, 1657–1666 (1985).

[220]Y. Mo, K. Tonokura, Y. Matsumi, M. Kawasaki, T. Sato, T. Arikawa, P. T. A. Reilly, Y. Xie, Y.-a. Yang, Y. Huang, and R. J. Gordon, “Mechanism of the ultraviolet photodissociation of chloroethylenes determined from the Doppler profiles, spatial anisotropy, and power dependence of the photofragments”, J. Chem. Phys. **97**, 4815–4826 (1992).

[221]T. Suzuki, K. Tonokura, L. S. Bontuyan, and N. Hashimoto, “Photodissociation of *trans*-dichloroethylene: State-resolved speed and angular distributions of Cl atoms”, J. Phys. Chem. **98**, 13447–13451 (1994).

[222]Y. Huang, Y.-A. Yang, G. He, S. Hashimoto, and R. J. Gordon, “State resolved translational energy distributions of Cl and HCl in the ultraviolet photodissociation of chloroethylenes”, J. Chem. Phys. **103**, 5476–5487 (1995).

[223]K. Sato, S. Tsunashima, T. Takayanagi, G. Fujisawa, and A. Yokoyama, “Translational energy distributions of the products of the 193 and 157 nm photodissociation of chloroethylenes”, J. Chem. Phys. **106**, 10123–10133 (1997).

[224]K. Seki, T. Kobayashi, and K. Ebata, “Laser photolysis of trans-dichloroethylene at 193 nm: Quantum yields of photoproducts”, J. Photochem. and Photobiol. A: Chem. **219**, 200–203 (2011).

[225]R. Ausubel and M. H. J. Wijnen, “The primary process in the photolysis of trans-1,2-$C_2H_2Cl_2$”, J. Photochem. **4**, 241–248 (1975).

[226]G. He, Y.-A. Yang, Y. Huang, S. Hashimoto, and R. J. Gordon, “Ultraviolet elimination of H_2 from chloroethylenes”, J. Chem. Phys. **103**, 5488–5498 (1995).

[227]G. He, Y.-A. Yang, Y. Huang, and R. J. Gordon, “Distribution of rotational states in half-collisions: 193 nm photolysis of dichloroethylene isomers”, J. Phys. Chem. **97**, 2186–2193 (1993).

[228]K. Sato, Y. Shihira, S. Tsunashima, H. Umemoto, T. Takayanagi, K. Furukawa, and S.-i. Ohno, “The photodissociation dynamics of dichloroethenes at 214 and 220 nm”, J. Chem. Phys. **99**, 1703–1709 (1993).

[229]R. Locht, D. Dehareng, and B. Leyh, “The vacuum UV photoabsorption spectroscopy of the trans-dichloroethylene (1,2-ClHC=CClH) in the 5–20 eV range: Experiment and theory”, J. Quant. Spectrosc. Radiat. Transfer **251**, 107048 (2020).

[230]R. Locht, D. Dehareng, and B. Leyh, “The vacuum UV photoabsorption spectroscopy of the cis-1,2-dichloroethylene (1,2-ClHC=CHCl) in the 5-20 eV range. An experimental and theoretical investigation”, AIP Adv. **9**, 015305 (2019).

[231]C. C. Womack, “The effect of internal energy partitioning on the reactivity of radical intermediates”, PhD thesis (University of Chicago, 2013).

[232]R. Khubbutdinov, N. Gerasimova, G. Mercurio, D. Assalauova, J. Carnis, L. Gelisio, L. Le Guyader, A. Ignatenko, Y. Y. Kim, B. E. Van Kuiken, R. P. Kurta, D. Lapkin, M. Teichmann, A. Yaroslavtsev, O. Gorobtsov, A. P. Menushenkov, M. Scholz, A. Scherz, and I. A. Vartanyants, “High spatial coherence and short pulse duration revealed by the Hanbury Brown and Twiss interferometry at the European XFEL”, Struct. Dyn. **8**, 044305 (2021).

[233]F. Ziaee, “Imaging nuclear motion during the photofragmentation of halomethane molecules triggered by ultraviolet light”, PhD thesis (Kansas State University, 2022).

[234]C. Guo, M. Li, J. P. Nibarger, and G. N. Gibson, “Single and double ionization of diatomic molecules in strong laser fields”, Phys. Rev. A **58**, R4271–R4274 (1998).

[235]A. Rudenko, K. Zrost, C. D. Schröter, V. L. B. de Jesus, B. Feuerstein, R. Moshammer, and J. Ullrich, “Resonant structures in the low-energy electron continuum for single ionization of atoms in the tunnelling regime”, J. Phys. B **37**, L407 (2004).

[236]J. Wiese, J.-F. Olivieri, A. Trabattoni, S. Trippel, and J. Küpper, “Strong-field photoelectron momentum imaging of OCS at finely resolved incident intensities”, New J. Phys. **21**, 083011 (2019).

[237]S. K. Lam, A. Pitrou, and S. Seibert, “Numba: a LLVM-based Python JIT compiler”, in Proceedings of the Second workshop on the LLVM Compiler Infrastructure in HPC (2015).